Influence of Welding Conditions on Microstructure and Defect Generation in 316 Stainless Steels: Experimentation and Modeling

by

Mohammad MAROUFKHANI

MANUSCRIPT-BASED THESIS PRESENTED TO ÉCOLE DE TECHNOLOGIE SUPÉRIEURE
IN PARTIAL FULFILLMENT FOR THE DEGREE OF
DOCTOR OF PHILOSOPHY
Ph.D.

MONTREAL, DECEMBER 19TH,2025

ÉCOLE DE TECHNOLOGIE SUPÉRIEURE
UNIVERSITÉ DU QUÉBEC

BOARD OF EXAMINERS

THIS THESIS HAS BEEN EVALUATED

BY THE FOLLOWING BOARD OF EXAMINERS

Mr. Mohammad Jahazi, Thesis supervisor
Department of Mechanical Engineering at École de technologies supérieure

Mr. Alireza Khodabandeh, Thesis Co-Supervisor
Department of Mechanical Engineering at École de technologies supérieure

M. Ambrish Chanta, Chair, Board of Examiners
Department of Electrical Engineering at École de technologie supérieure

Mr. Jean-Luc Fihey, Member of the Jury
Department of Mechanical Engineering at École de technologie supérieure

Mr. Tan Pham, Member of the Jury
Department of Mechanical Engineering at École de technologie supérieure

Mr. Iulian Radu, External Examiner
PCL construction

Mr. Gil Trigo, External Examiner
Department of Mechanical Engineering at École Polytechnique de Montreal

THIS THESIS WAS PRESENTED AND DEFENDED

IN THE PRESENCE OF A BOARD OF EXAMINERS AND THE PUBLIC

ON NOVEMBER 18TH, 2025

AT ÉCOLE DE TECHNOLOGIE SUPÉRIEURE

ACKNOWLEDGEMENTS

I would like to begin by expressing my heartfelt appreciation to my academic advisor, Prof. Mohammad Jahazi, whose insightful guidance, steady encouragement, and unwavering belief in my potential have shaped my doctoral journey. His expertise, professionalism, and approachable nature created a supportive environment that allowed me to thrive both intellectually and personally. His mentorship has not only influenced the success of this research but has also served as a model for my future academic and professional path.

I am equally grateful to Prof. Alireza Khodabandeh, my co-supervisor, for his thoughtful feedback, constructive criticism, and consistent support throughout this work. His input was instrumental in refining my experimental approach and deepening my understanding of the underlying phenomena. My sincere thanks also extend to Dr. Iulian Radu, my industrial co-supervisor and collaborator, for his practical insights and continuous support from our partner organization. His contributions helped bridge the gap between academic research and industrial applications.

I extend my gratitude to the members of my examination committee for their time, valuable feedback, and suggestions during the DGA 1033 oral defense. I am especially thankful to Prof. Elmira Moosavi for her assistance and insightful guidance on the thermodynamic aspects of the project—her expertise significantly enriched the quality of this research.

I acknowledge the Natural Sciences and Engineering Research Council (NSERC) of Canada for funding this research through the Collaborative Research and Development Grant (CRD 542299-19). This financial support was pivotal in enabling the advancement of this work.

My sincere thanks to PCL, the industry partner for this project, for their collaboration and assistance throughout the experimental phase. Their support with welding procedures and technical input, especially in the characterization of the chemical and macrostructural profiles, was vital for achieving the objectives of this study. I also want to express appreciation to the engineers at PCL Construction Inc., particularly Dr. Iulian Radu and Mrs. Joyce Lam, for their technical guidance and helpful contributions.

I would like to acknowledge the members of the CM2P group at ÉTS. Their collaboration, insightful discussions, and friendship created a motivating and enjoyable research environment. Special thanks to Dr. Morteza Sadeghifar for his assistance with the initial geometry of the welding setup, support in ABAQUS simulations, and Fortran code implementation. I am deeply grateful to Dr. Mohammad Saadati for his generous support and training on SEM, LEXT, EBSD, and the Spectromax analysis. I also sincerely thank Alireza Tirehkar for his valuable help with MATLAB coding, which significantly contributed to the data analysis and modeling aspects of this research.

I also thank Mr. Radu Romanica for his training and support with laboratory instrumentation, and Mr. Saleh Rasouli for his guidance on operating and calibrating the STA machine. My appreciation goes to Mr. Hamza Sofiane for his help with the hot stage setup and training, and Mr. Soroosh Hakimian for his valuable assistance with corrosion testing and analysis. I also want to extend warm thanks to Mrs. Fatemeh Jafari for her support in finite volume simulation and her collaboration throughout the project.

On a personal note, I am immensely thankful to my father and mother for their unconditional love, support, and encouragement during every phase of my academic journey. Their strength and sacrifices have always been the foundation of my motivation.

Finally, a very special thank you to my wife, whose patience, understanding, and unwavering support were invaluable throughout this demanding journey. Her companionship and encouragement gave me the strength to persevere, and I am truly blessed to have had her by my side.

To my mother, for her everlasting love.

To my father, for his constant strength.

And to my wife, for being my unwavering support.

INFLUENCE DES CONDITIONS DE SOUDAGE SUR LA MICROSTRUCTURE ET LA FORMATION DE DÉFAUTS DANS LES ACIERS INOXYDABLES 316 : EXPÉRIMENTATION ET MODÉLISATION

Mohammad MAROUFKHANI

RÉSUMÉ

Le soudage à l'arc au tungstène sous gaz (GTAW) est une technique largement utilisée pour l'assemblage des conduites en acier inoxydable, mais il entraîne souvent une décoloration et la formation d'une couche d'oxyde dans la zone affectée thermiquement (ZAT). Cette étude examine l'impact de la concentration d'oxygène dans le gaz de protection sur la résistance à la corrosion par piqûres et le comportement à l'oxydation des soudures en acier inoxydable AISI 316L. Une approche combinant analyses expérimentales et simulations numériques a été employée pour étudier la cinétique d'oxydation et la distribution thermique pendant le soudage.

L'analyse expérimentale a été réalisée sur des tuyaux en acier inoxydable 316L soudés sous différentes concentrations d'oxygène (50, 200, 500 et 5000 ppm) dans le gaz de protection. De plus, l'effet de la rugosité de surface (40 et 60-grains) sur la décoloration et la résistance à la corrosion a été étudié. La formation de la couche d'oxyde et la susceptibilité à la corrosion par piqûres ont été caractérisées par microscopie électronique à balayage (MEB), diffraction des rayons X (XRD) et tests électrochimiques (polarisation cyclique et spectroscopie d'impédance électrochimique). Les résultats ont révélé qu'une augmentation de la concentration d'oxygène dans le gaz de protection améliore initialement la résistance à la corrosion jusqu'à un seuil critique, au-delà duquel la formation de couches d'oxyde poreuses riches en fer et de zones appauvries en chrome entraîne une diminution de la résistance. Les surfaces plus lisses ont montré une meilleure résistance à la corrosion, soulignant l'importance de la préparation de surface pour atténuer la corrosion localisée.

Pour mieux comprendre les mécanismes d'oxydation, la cinétique d'oxydation non isotherme de l'acier inoxydable 316L a été étudiée entre 1100 K et 1373 K en utilisant l'analyse thermogravimétrique (TGA) à des taux de chauffage de 5, 10, 15, 20 et 25 K/min. L'énergie d'activation (E_a) a été déterminée en utilisant des méthodes isoconversionnelles sans modèle (Friedman, Flynn-Wall-Ozawa, Starink et Kissinger-Akahira-Sunose) et des méthodes d'ajustement de modèle (Coats-Redfern et Kennedy-Clark). Les énergies d'activation obtenues variaient de 224,79 à 233,81 kJ/mol, les modèles F2 (réaction d'ordre deux) et F3 (réaction d'ordre trois) étant les mieux adaptés aux données expérimentales. La méthode de Criado a confirmé l'adéquation de ces modèles réactionnels. Les simulations thermodynamiques réalisées avec *FactSage* ont prédit la formation de couches d'oxyde protectrices, principalement composées de spinelle et de corindon, à des températures allant jusqu'à 1373 K.

Les simulations numériques ont été réalisées à l'aide de la modélisation par éléments finis (EF) et volumes finis (VF) pour prédire la distribution de la chaleur et la formation de la couche d'oxyde pendant le soudage. Le modèle à double ellipsoïde de Goldak a été implémenté dans *Abaqus* pour simuler l'apport de chaleur transitoire, tandis que la cinétique d'oxydation a été

analysée en utilisant une équation du taux d'oxydation basée sur le modèle d'Arrhenius. Les valeurs d'énergie d'activation dérivées des méthodes isoconversionnelles et sans modèle ont été intégrées aux simulations pour améliorer la précision des prédictions du comportement à l'oxydation.

Ces résultats soulignent l'importance d'optimiser la concentration d'oxygène dans le gaz de protection et de contrôler la rugosité de surface afin d'améliorer la résistance à la corrosion et de réduire la décoloration des soudures. En intégrant les résultats expérimentaux à la modélisation numérique, cette étude offre une compréhension approfondie de la cinétique d'oxydation et de l'optimisation du procédé de soudage pour une meilleure durabilité et fiabilité des conduites en acier inoxydable dans des environnements corrosifs.

Mots-clés: Acier inoxydable 316L, Corrosion par piqûres, Décoloration, Teneur en oxygène, Rugosité de surface, Soudage à l'arc, Calculs thermodynamiques, Simulation numérique

Influence of Welding Conditions on Microstructure and Defect Generation in 316 Stainless Steels: Experimentation and Modeling

Mohammad MAROUFKHANI

ABSTRACT

Gas Tungsten Arc Welding (GTAW) is a widely used technique for joining stainless steel pipelines, yet it often results in discoloration and oxide layer formation in the heat-affected zone (HAZ). This study investigates the impact of oxygen concentration in the backing gas on the pitting corrosion resistance and oxidation behavior of AISI 316L stainless steel welds. Experimental and numerical approaches were combined to analyze oxidation kinetics and heat distribution during welding.

Experimental analysis was conducted on 316L stainless steel pipes welded under different oxygen levels (50, 200, 500, and 5000 ppm) in the purging gas. Additionally, the effects of surface roughness (40- and 60-grit) on discoloration and corrosion resistance were examined. Scanning Electron Microscopy (SEM), X-ray Diffraction (XRD), and electrochemical testing (cyclic polarization and Electrochemical Impedance Spectroscopy) were utilized to characterize oxide layer formation and pitting susceptibility. Results revealed that increasing oxygen concentration in the backing gas initially enhanced corrosion resistance up to a critical threshold, beyond which the formation of porous iron oxide layers and chromium-depleted zones led to a decrease in resistance. Smoother surfaces exhibited improved corrosion resistance, emphasizing the role of surface preparation in mitigating localized corrosion.

To further understand the oxidation mechanisms, non-isothermal oxidation kinetics of 316L stainless steel were investigated between 1100 K and 1373 K using Thermogravimetric Analysis (TGA) at heating rates of 5, 10, 15, 20, and 25 K/min. Activation energy (E_a) was determined using model-free isoconversional methods (Friedman, Flynn-Wall-Ozawa, Starink, and Kissinger-Akahira-Sunose) and model-fitting methods (Coats-Redfern and Kennedy-Clark). The determined activation energies ranged from 224.79 to 233.81 kJ/mol, with the F2 (second-order reaction) and F3 (third-order reaction) models providing the best fit to experimental data. The Criado method further confirmed the suitability of these reaction models. *FactSage* thermodynamic simulations predicted the formation of protective oxide layers, primarily composed of spinel and corundum, at temperatures up to 1373 K.

Numerical simulations were conducted using Finite Element (FE) and Finite Volume (FV) methods to predict heat distribution and oxidation layer formation during welding. The Goldak double ellipsoid model was implemented in *Abaqus* to simulate transient heat input, while oxidation kinetics were analyzed using an Arrhenius-based oxidation rate equation. Activation energy values derived from isoconversional and model-free methods were incorporated into the simulations to enhance accuracy in predicting oxidation behavior.

The findings of this research highlight the importance of optimizing oxygen concentration in the backing gas and controlling surface roughness to enhance corrosion resistance and mitigate

weld discoloration. By integrating experimental results with numerical modeling, a better understanding was developed on oxidation kinetics and welding process optimization for improved longevity and reliability of stainless steel pipelines in corrosive environments.

Keywords: 316L SS, Pitting corrosion, Discoloration, Oxygen content, Surface roughness, Arc welding, Thermodynamic caculation, Numerical simulation

TABLE OF CONTENTS

LIST OF TABLES

LIST OF FIGURES

LIST OF ABBREVIATIONS

316L SS	316 low carbon Stainless Steel
AISI	American Iron and Steel Institute
ASTM	American Society for Testing and Materials
AWS	American Welding Society
BCC	Body Centered Cubic
C	Carbon
CCP	Cubic Close Packed
CE	Counter Electrode
CFD	Complementary Computational Fluid Dynamics
CFH	Cubic Feet per Hour
CL	Weld Centerline
Co-Kα	Cobalt K-alpha Radiation
Cr	Chromium
CR	Coats-Redfern
DTA	Differential Thermal Analysis
DTG	Differential Thermogravimetric
EBSD	Electron Backscatter Diffraction
EIS	Electrochemical Impedance Spectroscopy
ETS	École de Technologie Supérieure

FCAW	Flux-Cored Arc Welding
FCC	Face Centered Cubic
FEM	Finite Element Method
FVM	Finite Volume Method
FWO	Flynn-Wall-Ozawa
FZ	Fusion Zone
GTAW	Gas Tungsten Arc Welding
HAZ	Heat-Affected Zone
HCP	Hexagonal Close Packed
ICP-OES	Inductively Coupled Plasma Optical Emission Spectrometry
IM	Ion Milling
KAS	Kissinger-Akahira-Sunose
KC	Kennedy-Clark
LFA	Laser Flash Analysis
LHAW	Laser Hybrid Arc Welding
LTE	Local Thermodynamic Equilibrium
MFR	Modified Friedman
MHD	Magneto-Hydrodynamic
MIG	Metal Inert Gas Welding
Mn	Manganese

Mo	Molybdenum
NaCl	Sodium Chloride
Ni	Nickel
OCP	Open circuit Potential
OPD	Optical Path Difference
P	Phosphorus
PAP	Potentiodynamic Anodic Polarization
PREN	Pitting Resistance Equivalent Number
R2	Correlation Coefficient
RE	Reference Electrode
S	Sulfur
SAW	Submerged Arc Welding
SEM	Scanning Electron Microscopy
Si	Silicon
SMAT	Surface Mechanical Attrition Treatment
SS	Stainless Steel
TGA	Thermogravimetric Analysis
TIG	Tungsten Inert Gas
UDF	User-Defined Functions
WE	Working Electrode
XRD	X-ray Diffraction

LIST OF SYMBOLS AND UNITS OF MEASUREMENTS

α	m^2/s	Thermal diffusivity
β	K/min	Heating rate
C_p	J/kg·K	Specific heat capacity
E_a	J/mol	Activation energy
E_{pit}	V	Pitting potential
h	$W/m^2·K$	Heat transfer coefficient
I_{pit}	A/cm^2	Pitting current density
I_{pass}	A/cm^2	Passive current density
K_p	$mg^2/cm^4·s$	Parabolic oxidation rate constant
λ	W/m·K	Thermal conductivity
ρ	kg/m^3	Density
R	J/mol·K	Gas constant (8.314 J/mol·K)
R_a	µm	Surface roughness
T	K	Temperature
t	s	Time
V	V	Voltage
η	%	Welding efficiency
σ	–	Sigma phase
Δm	g	Weight gain

C	–	Constant
$K_{\log}, K_{ilog}$	–	Rate constant
ΔG	J/mol	Gibbs energy
ΔS	J/mol·K	Entropy
ΔH	J/mol	Enthalpy
P_{O_2}	atm	Oxygen partial pressure
T_p	K	Peak temperature
W	mm	Bead width
H	mm	Height of reinforcement
D	mm	Depth of penetration
A_d	mm^2	Electrode deposit area
A_m	mm^2	Plate fusion area
I	A	Welding current
F	$C \cdot mol^{-1}$	Faraday constant (96.585 C/mol)
E_{eq}	V	Equilibrium potential
β_A	–	Tafel slope
K	g/s	Rate of corrosion
θ	°	Refraction angle
λ	nm	Wavelength of light
D_{eff}	m^2/s	Effective diffusivity

D_L	m^2/s	Lattice diffusion
D_{GB}	m^2/s	Grain boundary diffusion
f	–	Volume fraction of grain boundaries
δ	nm	Grain boundary width
R_s	Ω	Solution resistance
R_{ct}	Ω	Charge transfer resistance
W	$\Omega \cdot s^{-1/2}$	Warburg impedance
CPE	$\mu s^{\circ}/\Omega$	Constant Phase Element
C	μF	Capacitance
α	–	Degree of conversion
A	s^{-1}	Pre-exponential factor
V	m^3	Volume
S	m^2	Surface area
ρ	kg/m^3	Material density
U	J	Rate of change of internal energy
q	W/m^2	Surface heat flux
f_f, f_r	–	Fractions of heat deposited in the front and rear quadrants
r	W/m^3	Volumetric rate of internal heat generation
ω	rad/s	Angular velocity
h	J·s	Planck's constant (6.626×10^{-34} J·s)

u	m/s	Velocity vector
μ	Pa·s	Dynamic viscosity
B	T	Magnetic flux density
J	A/m^2	Electric current density
μ_0	H/m	Magnetic permeability of free space
Ψ	–	Scalar Coulomb gauge function
σ	S/m	Electrical conductivity
ε_p	$W/m^3 \cdot K^4$	Radiative emission coefficient
ω_i	–	Mass fraction of species
D_i^o	m^2/s	Molecular diffusion coefficient
D_i^T	m^2/s	Thermal diffusion coefficient
μ_t	m^2/s	Turbulent kinematic viscosity
Sc_t	Dimensionless	Turbulent Schmidt number
$\Delta S^{\neq}$	kJ/mol	Entropy of activation
$\Delta H^{\neq}$	kJ/mol	Enthalpy of activation
$\Delta G^{\neq}$	kJ/mol	Gibbs energy of activation
k_B	J/K	Boltzmann's constant (1.381×10^{-23} J/K)

INTRODUCTION

Introduction

In recent years, the demand for stainless steel pipelines has significantly increased across various industries, including oil and gas, chemical processing, and power generation. Among the various stainless steel grades, AISI 316L, an austenitic alloy known for its high corrosion resistance, mechanical strength, and durability, is widely used in these applications. However, achieving optimal weld integrity while preserving the corrosion resistance of welded joints remains a major challenge, as improper welding conditions can lead to structural defects, oxidation, and corrosion-related failures.

Gas Tungsten Arc Welding (GTAW) is a preferred welding technique for stainless steel pipelines due to its precise control over heat input and ability to produce high-quality welds. Despite its advantages, one of the key challenges associated with GTAW is the formation of oxide layers in the heat-affected zone (HAZ), which can cause discoloration and degrade the corrosion resistance of the welded joint. The presence of oxygen in the backing gas plays a critical role in oxide layer formation, affecting both the weld appearance and long-term corrosion performance of the pipeline.

The American Welding Society (AWS) has established two standards, AWS D18.1 and AWS D18.2, to regulate acceptable levels of discoloration in stainless steel welds. According to the AWS weld discoloration criteria, there are ten levels of discoloration, and any weld exhibiting discoloration above level 5 (light blue) is subject to rejection. Additionally, oxide islands exceeding 1.6 mm in size render the weld unacceptable based on AWS standards.

However, the above two standards were specifically developed for sanitary and food processing applications and require very low oxygen levels in the backing gas to attain discoloration levels that are acceptable according to these two standards. Interestingly, no official standard

currently exists for oil and gas pipeline welding and consequently, pipelines welded for oil and gas applications may be rejected based on AWS D18.1 and AWS D18.2, even if they meet the required materials properties, especially corrosion resistance. Additionally, achieving low oxygen levels in the backing gas requires high-purity argon, which significantly increases production costs.

Therefore, a thorough understanding of oxide layer formation, severity of discoloration, and their impact on corrosion sensitivity is essential for developing guidelines that balance weld integrity and cost-efficiency for the oil and gas industry.

Beyond the influence of oxygen content, surface roughness also plays a key role in oxide layer stability and pitting corrosion resistance. The impact of different surface roughness conditions on the electrochemical behavior of welded joints remains underexplored and requires further investigation.

An important missing information in this framework is to predict the oxidation kinetics of 316L stainless steel at high temperatures and accurately calculate activation energy for subsequent oxide layer thickness predictions in numerical simulations. Traditional oxidation models often fail to capture complex reaction pathways influenced by temperature and heating rates. Advanced isoconversional and model-fitting kinetic analysis methods provide a more accurate understanding of oxidation mechanisms.

Objectives

The primary objective of this study is to investigate the effect of oxygen concentration in the backing gas on the oxidation behavior and corrosion resistance of GTAW-welded AISI 316L stainless steel. This objective is addressed using a combination of experimental and numerical approaches, focusing on:

(a) Experimental analysis of oxidation behavior and corrosion resistance

- Investigating the influence of different oxygen concentrations in backing gas (50, 200, 500, and 5000 ppm) on the formation of oxide layers.
- Evaluating the impact of surface roughness (40 and 60-grit) on pitting corrosion resistance.
- Characterizing oxide layer composition using Scanning Electron Microscopy (SEM) and X-ray Diffraction (XRD).
- Conducting electrochemical testing (cyclic polarization and Electrochemical Impedance Spectroscopy) to assess corrosion performance.

(b) Kinetic analysis of oxidation mechanisms

- Performing non-isothermal oxidation studies using Thermogravimetric Analysis (TGA) over the temperature range of 1100 K to 1373 K.
- Determining activation energy (E_a) using isoconversional methods (Friedman, Flynn-Wall-Ozawa, Starink, and Kissinger-Akahira-Sunose) and model-fitting methods (Coats-Redfern and Kennedy-Clark).
- Validating reaction models using the Criado method to identify dominant oxidation mechanisms.

(c) Numerical modeling of the welding process

- Simulating heat distribution using Finite Element (FE) and Finite Volume (FV) modeling.
- Implementing the Goldak double-ellipsoid heat source model in *Abaqus* for transient heat input simulation.
- Incorporating oxidation kinetics into the numerical model using an Arrhenius-based oxidation rate equation.
- Using activation energy values from kinetic analysis to improve the accuracy of oxidation predictions.

By achieving these objectives, this study contributes to a better understanding of the oxidation behavior of 316L stainless steel welds and offers guidelines for the development of new standards adapted to the realities of the oil and gas industry.

Thesis Structure

Chapter 1 provides a comprehensive literature review on welding-induced oxidation and corrosion behavior of AISI 316L stainless steel. The chapter discusses the challenges associated with oxidation in GTAW-welded stainless steels, highlighting the role of oxygen concentration in the backing gas, the formation of protective and non-protective oxide layers, and their effects on corrosion resistance. Additionally, the chapter presents an overview of oxidation kinetics, including traditional and advanced kinetic analysis methods. The role of numerical modeling in predicting heat distribution and oxidation behavior during welding is also discussed, emphasizing the need for integrating experimental data into computational models. The chapter concludes by identifying key scientific and technical gaps in the existing literature, forming the foundation for the main objective and sub-objectives.

Chapter 2 outlines the experimental methodology used in this study. It details the materials and specimen preparation process, including the welding parameters and gas compositions used for the GTAW process. The characterization techniques employed for analyzing oxide layer composition, surface roughness, and corrosion resistance are described. The chapter also presents the procedures for kinetic analysis using TGA and the numerical modeling approach, including the implementation of heat source models and oxidation kinetics in *Abaqus*.

Chapter 3 presents the experimental investigation of oxide layer formation and pitting corrosion resistance in four passes of GTAW welded joints. The effects of oxygen concentration in the backing gas on oxide composition and electrochemical performance are analyzed. The chapter discusses how different oxidation conditions influence corrosion behavior and provides

recommendations for optimizing welding parameters. The findings from this chapter have been published in the journal *Materials* in August 2023.

Chapter 4 examines whether 500 ppm oxygen remains optimal for GTAW/FCAW welding and evaluates the influence of surface roughness on corrosion resistance in AISI 316L stainless steel welded joints. This chapter provides insights for industries seeking to optimize welding parameters while maintaining cost-effectiveness.

Chapter 5 focuses on the oxidation kinetics of 316L stainless steel at high temperatures. The experimental results obtained from Thermogravimetric Analysis (TGA) are analyzed to determine the activation energy (E_a) using both isoconversional and model-fitting methods. These activation energy values are later incorporated into Chapter 6 for numerical simulations of oxidation behavior during welding. The findings highlight the influence of heating rate on oxidation mechanisms, providing valuable insights into the dominant reaction models governing high-temperature oxidation. The research has been submitted for consideration to the journal *Results in Materials* in April 2025.

Chapter 6 describes the development and validation of numerical models for predicting heat distribution and oxidation kinetics in welded joints. The implementation of the Goldak double-ellipsoid heat source model and the integration of activation energy values into oxidation simulations are detailed. A comparative analysis of experimental and numerical findings is presented. The relationship between oxygen concentration and oxidation kinetics is discussed, and key insights gained from integrating experimental data with numerical modeling are highlighted.

Conclusion: This study provides a comprehensive analysis of the oxidation behavior of GTAW-welded AISI 316L stainless steel by integrating experimental observations with advanced numerical simulations. The research demonstrates how oxygen concentration in the

backing gas, surface roughness, and high-temperature oxidation kinetics significantly influence oxide layer composition and pitting corrosion resistance. Through detailed kinetic analysis and the incorporation of activation energy values into thermal models, a better understanding of oxidation mechanisms has been achieved.

CHAPTER 1

LITERATURE REVIEW

1.1 Stainless Steel and 316L Alloy Composition

1.1.1 General Properties of Stainless Steel

Stainless steel is a highly versatile and corrosion-resistant alloy primarily composed of iron, chromium, nickel, and other alloying elements. Its key characteristic is the ability to form a self-repairing passive oxide layer (Cr_2O_3) when exposed to oxygen, which enhances its resistance to oxidation and corrosion in various environments. TThe addition of nickel stabilizes the austenitic phase, while molybdenum enhances resistance to pitting and crevice corrosion in marine environments. Nitrogen further increases strength and overall corrosion resistance, making the alloy well-suited for demanding applications across aerospace, medical, food-processing, and marine industries. (Sedriks, 1996; Abiodun, Ayoola, Olajire, Oluwajire & Abidakun, 2020).

Among stainless steels, the 300-series austenitic stainless steels are the most widely used, offering exceptional corrosion resistance, high toughness, and excellent weldability (Abiodun *et al.*, 2020).

1.1.2 Microstructure of 316L Stainless Steel

316L stainless steel exhibits a fully austenitic microstructure at room temperature, characterized by a face-centered cubic (FCC) crystal structure (Gholizadeh, Yuen & George, 2024). At elevated temperatures (above 1000°C), delta ferrite (δ-ferrite) may form, particularly in cast or weld metal structures. The formation of δ-ferrite can improve resistance to solidification cracking but may also influence mechanical properties and corrosion resistance (Wang, Chen & Rong, 2020). The presence of secondary phases such as sigma (σ) phase and

carbides at grain boundaries can reduce corrosion resistance in long-term high-temperature applications (Perron *et al.*, 2014).

1.2 Arc Welding

Arc welding is a fusion welding process that utilizes an electric arc to generate heat for melting and joining materials. The process involves creating an arc between an electrode and the workpiece, producing intense heat that melts both the base metal and the filler material, forming a weld pool. Upon cooling and solidification, a strong metallurgical bond is established. This welding technique is prevalent in industrial applications due to its efficiency in producing high-strength joints. Depending on the specific method employed, arc welding can utilize either consumable or non-consumable electrodes. To protect the weld pool from atmospheric contamination and ensure weld quality, shielding gases or flux-coated electrodes are commonly used (Babu *et al.*, 2013).

1.2.1 Gas Tungsten Arc Welding (GTAW)

GTAW, also known as Tungsten Inert Gas (TIG) welding, is a precision welding process that uses a non-consumable tungsten electrode to generate the arc and is normally used for the root pass of welding (Stewart, 2021) (see Figure 1.1). A shielding gas, typically argon or helium, is used to protect the weld pool from oxidation and contamination. GTAW is widely used for welding stainless steels due to its ability to produce high-quality, defect-free welds (Sonar, Ivanov, Trofimov, Tingaev & Suleymanova, 2024).

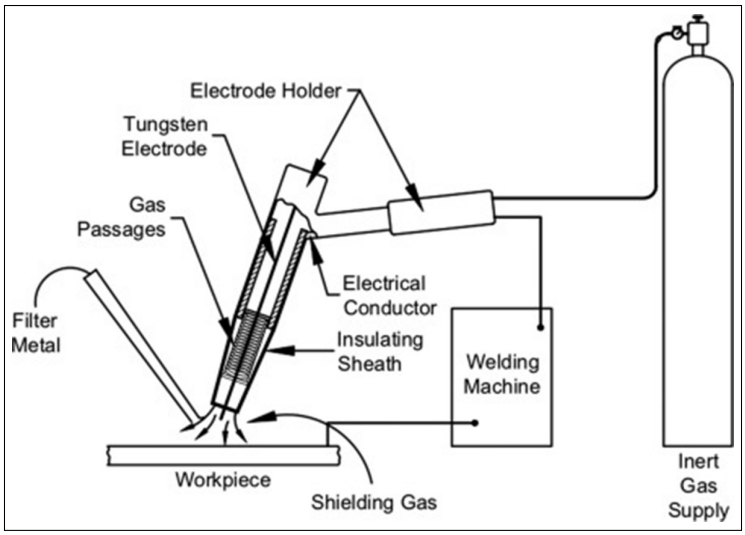

Figure 1.1 Schematic view of GTAW
Taken from Stewart (2021, p. 211)

1.2.2 Flux-Cored Arc Welding (FCAW)

Flux-Cored Arc Welding (FCAW) is a semi-automatic or automatic welding process that utilizes a continuously fed tubular electrode filled with flux. This flux generates a shielding gas during welding, reducing or eliminating the need for an external shielding gas. FCAW is known for its deep penetration capability, high deposition rates, and suitability for outdoor applications (Singh, Pramanik, Basak & Chattopadhyay, 2020).

There are two main types of FCAW, as shown in Figure 1.2: self-shielded FCAW (FCAW-S) and gas-shielded FCAW (FCAW-G). In FCAW-S, the flux within the electrode provides complete shielding, making it ideal for fieldwork and construction sites where wind conditions make gas shielding difficult. FCAW-G, on the other hand, uses an external shielding gas in addition to the flux, improving weld quality and reducing spatter Taken from (Stewart, 2021).

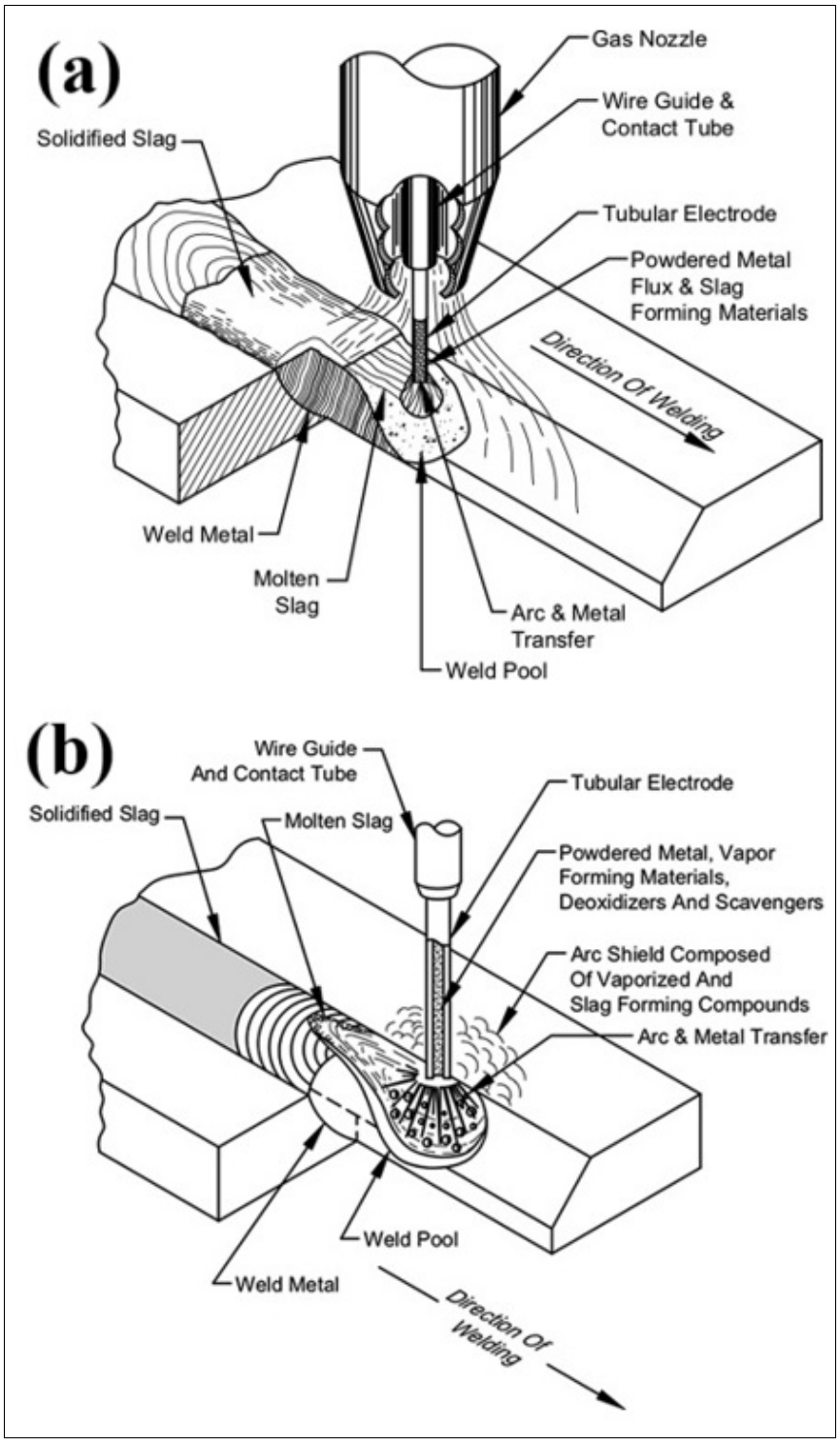

Figure 1.2 Schematic view of (a) FCAW-G, (b) FCAW-S
Taken from Stewart (2021, p. 215 and 216)

FCAW is widely used in structural welding, shipbuilding, and pipeline applications due to its efficiency and ability to produce strong welds in various positions. The flux in the electrode helps in deoxidizing and stabilizing the arc, allowing for better weld penetration and reduced porosity (Smith, 2005).

1.2.3 Different Zones in a Welded Joint

During welding, 316L stainless steel undergoes significant thermal cycles that create distinct zones with varying microstructural and mechanical properties, as shown in Figure 1.3.

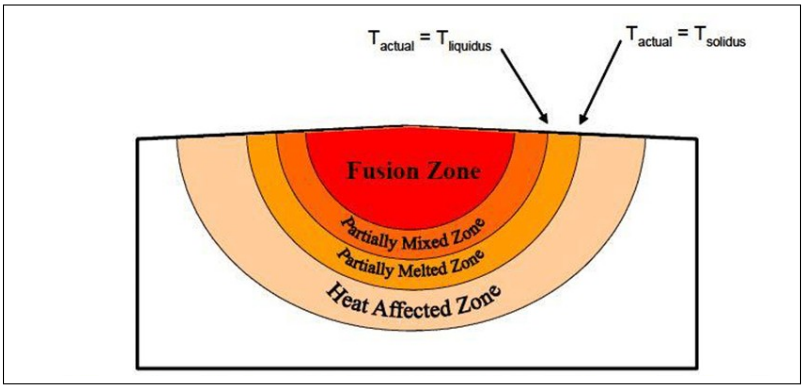

Figure 1.3 Schematic of different zones in welding
Taken from Mouginot & Hänninen (2013, p. 22)

- **Fusion Zone (FZ):** This is the region that experiences complete melting during welding. The material in this zone solidifies upon cooling, forming the weld bead. The fusion zone typically inherits a composition like the filler material used in welding. The cooling rate in this zone affects grain structure formation, with rapid cooling leading to fine dendritic grains, while slow cooling can cause coarse microstructures, which may influence mechanical strength and corrosion resistance. The fusion zone is also susceptible to solidification cracking if impurities or improper heat input parameters are present.
- **The partially mixed zone (PMZ) and the unmixed zone (UMZ):**they forms as a thin boundary layer between the fusion zone and the base metal. In this region, the base metal undergoes complete melting and re-solidification, but mixing with the filler metal

remains incomplete. This limited mixing results from the stagnant layer that develops at the interface, where friction between the liquid weld metal and the solid base metal restricts convection. A distinct composition gradient typically appears across the PMZ, bridging the fully mixed fusion zone and the unaffected base metal. This gradient plays a critical role in determining local microstructure and performance. Increasing weld-pool convection, for example through electromagnetic stirring, has been shown to reduce or even eliminate the UMZ in dissimilar metal welds Mouginot & Hänninen (2013, p. 22).

- **Heat-Affected Zone (HAZ):** The region is affected by the extent of the thermal cycle, leading to microstructure and mechanical property changes. The HAZ has a number of subzones depending on the temperatures reached during the welding process (Tsuei, 2000). Easterling illustrated the sub-zones of HAZ and their microstructure, as shown in Figure 1.4.

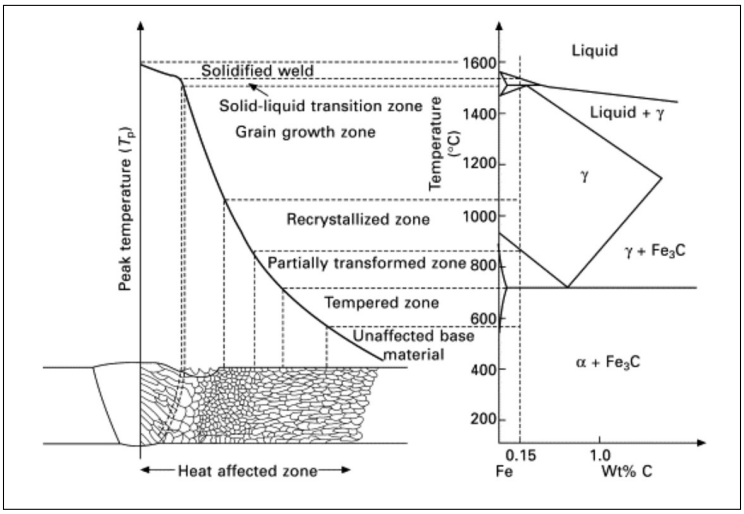

Figure 1.4 Schematic diagram of various sub-zones of HAZ approximately corresponding to alloy C0 (0.15 wt% C) on the Fe-Fe_3C equilibrium diagram
Taken from Martin (2006, p. 119)

- **Weld Interface:** The weld interface is the transition region between the fusion zone and the base metal, where diffusion and mixing of elements from both zones occur (Parsian, Akbari, Karimipour, Rafiei & Razzaghi, 2025). The chemical composition in this region is crucial, as variations can lead to incomplete fusion, lack of penetration, or hot cracking (Kadoi & Shinozaki, 2017).

1.2.4 Discoloration Zone

In the discoloration area of the weld zone, a range of colors from straw yellow to blue, purple, or even black is observed (Figure 1.5). The extent of these colors is influenced by oxidation and temperature changes during welding. One of the primary causes is the formation of oxide layers on the metal surface. The thickness and composition of the oxide layer can vary depending on the welding process, atmosphere, heat input, exposure time, and the specific metal (Kimbrel, 2011).

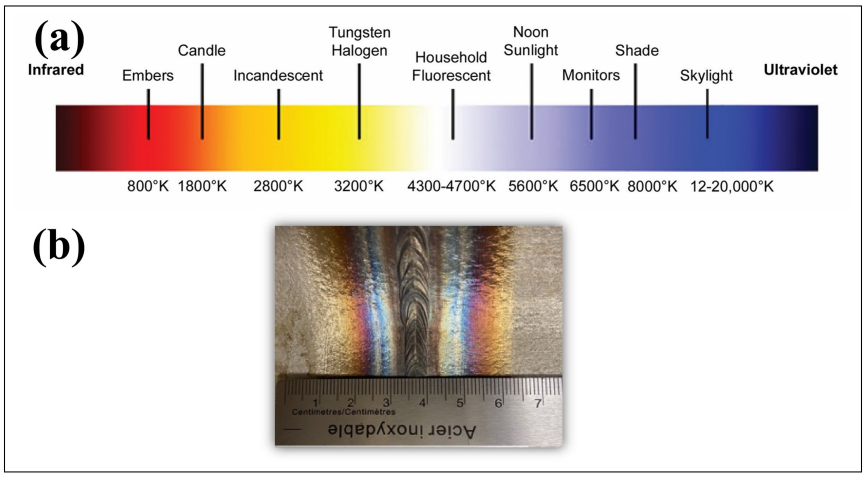

Figure 1.5 (a) Color temperature imaging of weld discoloration
Taken from Kimbrel (2011, p. 2),(b) Discoloration zone for 316L weld

These oxide layers interact with light, resulting in selective absorption, reflection, and scattering of different wavelengths. Thicker oxide layers result in a broader range of colors, including blues, purples, and black, while thinner ones appear as straw yellow or light shades (Macleod & Macleod, 2010; Pedrotti, 2008).

This phenomenon is governed by the optical path difference (OPD) between light rays reflected from the oxide layer surface and those that pass through and reflect back from the oxide/base interface. The OPD is described by:

$$\mathrm{OPD} = 2 \cdot n_2(\lambda) \cdot t \cdot \cos(\theta_2) \tag{1.1}$$

Where:

- $n_2(\lambda)$ is the wavelength-dependent refractive index,
- t is the oxide layer thickness,
- θ_2 is the refraction angle (from Snell's law),
- λ is the wavelength of light.

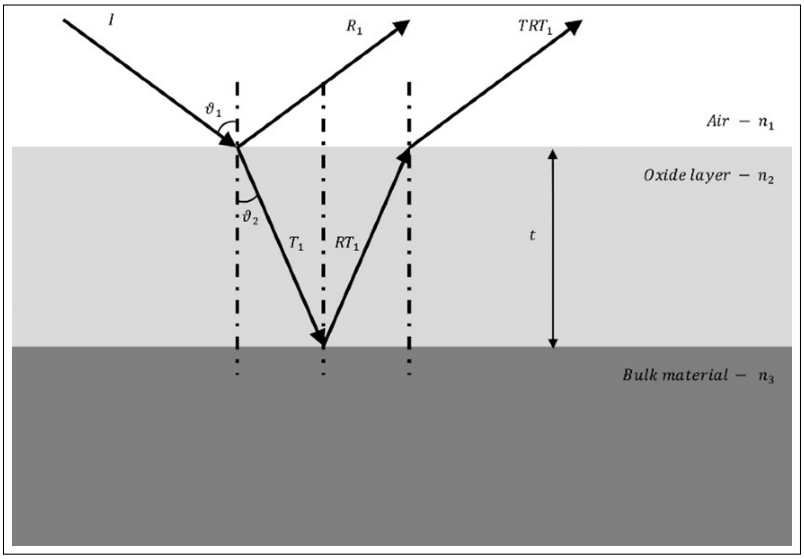

Figure 1.6 Schematic representation of light interference due to oxide layers
Taken from Khafaji *et al.* (2017, p. 157)

In cases where oxide films consist of multiple layers with different refractive indices, interference patterns become more complex, but the same principles apply (Pedrotti, 2008; Macleod & Macleod, 2010).

1.3 Oxidation of metals

1.3.1 Introduction

Oxidation is a fundamental process that occurs when a metal reacts with oxygen, leading to the formation of a metal oxide. This reaction plays a critical role in determining the longevity and performance of metals in various environments. The oxidation process is influenced by thermodynamics, kinetics, and environmental conditions, such as temperature, oxygen concentration, and humidity (Zhou *et al.*, 2023).

At a fundamental level, oxidation follows the reaction:

$$x\,\mathrm{M} + \frac{y}{2}\,\mathrm{O_2} \rightarrow \mathrm{M}_x\mathrm{O}_y \tag{1.2}$$

where M represents the metal, and $\mathrm{M}_x\mathrm{O}_y$ denotes the oxide product. The formation of an oxide layer can be either protective—preventing further reaction—or porous and non-protective, allowing continued oxidation (Li *et al.*, 2024). The characteristics of the oxide layer depend on the metal composition, temperature, and oxidizing environment.

A simple schematic of the oxidation process is shown in Figure 1.7, where a metal surface is exposed to oxygen, leading to the gradual formation of a metal oxide layer.

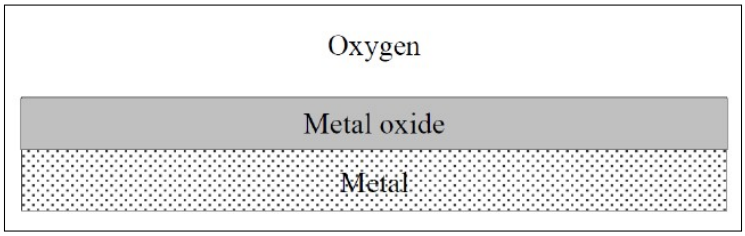

Figure 1.7 Schematic diagram showing a cross-section of a metal with an oxide scale
Taken from Birks (2006, p. 2)

1.3.2 Theory of oxidation

The absorption of oxygen on the clean metal surface is the first step of oxidation (Ropo *et al.*, 2021) (see Figure 1.8a). Physisorption and chemisorption are two pivotal processes governing the absorption of oxygen onto the metal surface (Ropo *et al.*, 2021). Physisorption occurs due to weak van der Waals forces, causing oxygen molecules to adhere to the surface without forming strong chemical bonds. In contrast, chemisorption involves a more significant energy exchange, where oxygen molecules react with the metal, forming a stable chemical bond (Kofstad, 1988; Ropo *et al.*, 2021).

During the chemical reaction, oxygen dissolves into the metal surface, leading to the nucleation and growth of oxides (Figure 1.8b and 1.8c) (Xiao *et al.*, 2025). As the oxidation progresses, the oxide film thickens; however, various defects such as porosity, cracks, and pits may develop due to internal stress accumulation (Figure 1.8d) (Xiao *et al.*, 2025). These defects can compromise the protective nature of the oxide layer, increasing the susceptibility to further oxidation and corrosion (Kofstad, 1988).

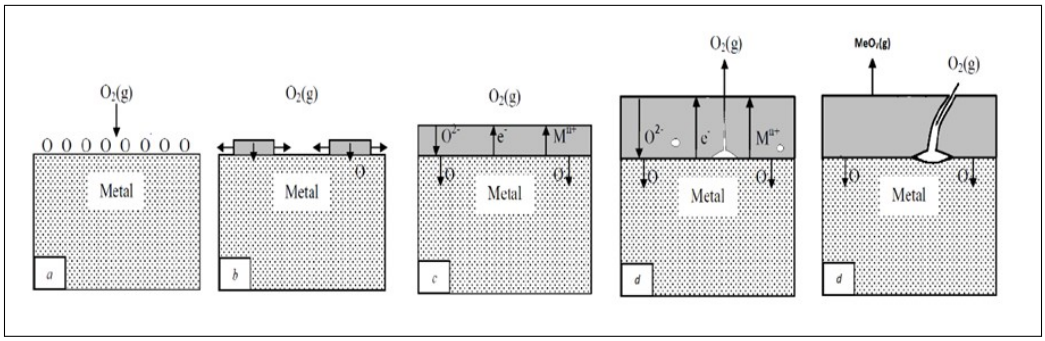

Figure 1.8 Schematic diagram showing the stages of oxidation: (a) initial oxidation, (b) nucleation, (c) scale growth, (d) cavities, porosities, microcracks, and (f) macrocrack, possible molten phases, and oxide evaporation
Taken from Kofstad (1988, p. 3)

1.3.2.1 Oxide transport mechanisms

Metals are generally considered ionic in oxidation reactions (Binninger *et al.*, 2015). Instead of the direct transport of metal and oxygen atoms, oxidation involves the movement of metal cations (M^{2+}) and oxygen anions (O^{2-}) through the oxide layer (Pratt *et al.*, 2014; Binninger *et al.*, 2015). The diffusion of these ions dictates the growth mechanism of the oxide film, influencing its protective nature and stability (Pratt *et al.*, 2014; Binninger *et al.*, 2015).

The transport of metal and non-metal ions can be classified into stoichiometric and non-stoichiometric mechanisms, which determine how oxidation progresses (Zhou *et al.*, 2023).

1.3.2.2 Crystal structures of oxides

The crystal structure of oxides plays an important role in defining their mechanical stability, ion transport properties, and oxidation resistance. These structures determine how oxygen and metal ions are arranged, influencing the oxide's ability to act as a protective barrier or contribute to further oxidation and degradation. The most common oxide structures include body-centered cubic (BCC), face-centered cubic (FCC), and hexagonal close-packed (HCP). Each of these structures affects the diffusion rate of cations and anions, the stability of the oxide layer, and its ability to protect the underlying metal. Different oxides form based on these structures, significantly impacting their performance in high-temperature applications.

1.3.2.2.1 Halite structure

The halite structure, also known as the rock salt structure, consists of a cubic close-packed (CCP) arrangement of oxygen anions with metal cations occupying the octahedral interstitial sites. This structure is found in simple oxides such as FeO (wüstite), MgO (magnesia), CaO (lime), and NiO (nickel oxide). The cation-to-anion ratio in this structure remains 1:1, ensuring charge neutrality. The stability of the halite structure depends on the ionic radii ratio between metal cations and oxygen anions, which influences packing efficiency and defect formation.

1.3.2.2.2 Corundum structure

The corundum structure is characterized by a hexagonal close-packed (HCP) arrangement of oxygen ions, with metal cations occupying two-thirds of the octahedral interstitial sites. This structure exhibits high thermal stability and low ion diffusivity, making it a fundamental component in protective oxide layers. Oxides such as Cr_2O_3 (chromia), Al_2O_3 (alumina), Ti_2O_3, and V_2O_3 exhibit this structure. The strong bonding environment created by the close-packing of oxygen atoms and the coordination of metal cations enhances the oxidation resistance of corundum-type oxides.

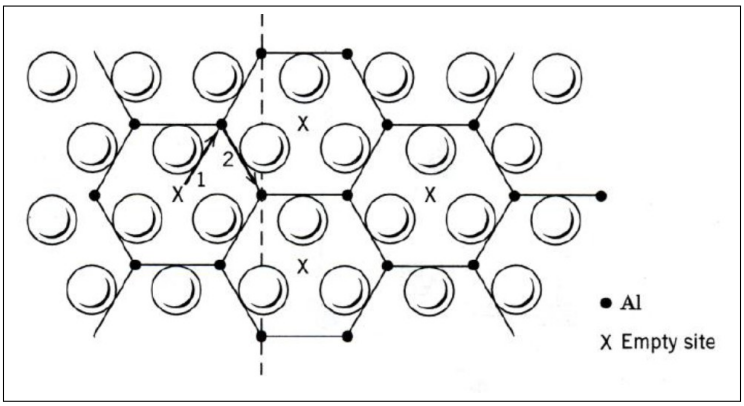

Figure 1.9 Corundum crystal structure
Taken from Chiang (1997, p. 32)

The high degree of atomic packing in these oxides results in a low rate of ion transport, which significantly improves their resistance to oxidation. Due to their stability and compact nature, oxides such as Al_2O_3 and Cr_2O_3 form some of the most protective layers in high-temperature environments. The effectiveness of these oxides as barriers is attributed to their low defect density, which prevents the rapid diffusion of oxygen and metal ions. Additionally, their anisotropic growth behavior leads to differences in oxide scale development depending on crystallographic orientation, influencing stress accumulation, crack formation, and eventual spallation in extreme conditions.

1.3.2.2.3 Spinel structure

The spinel structure is more complex than the halite and corundum structures, consisting of a three-dimensional FCC lattice where oxygen ions form a rigid framework. Within this structure, metal cations occupy both tetrahedral and octahedral interstitial sites, creating a unique balance of electronic and ionic transport properties. The general formula for spinel oxides is AB_2O_4, where A represents divalent cations in tetrahedral coordination, and B represents trivalent cations in octahedral coordination.

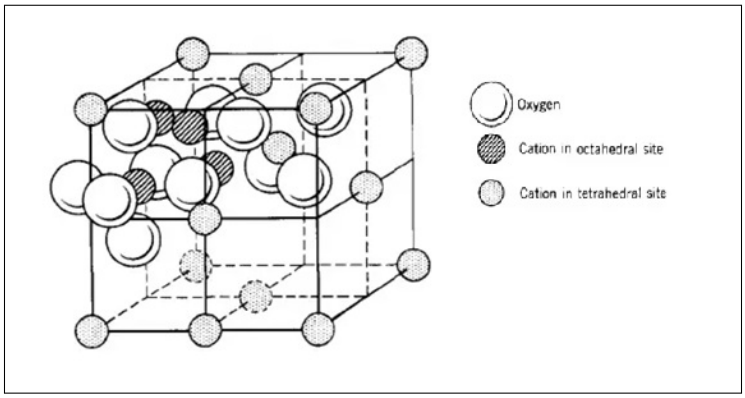

Figure 1.10 Spinel crystal structure
Taken from Chiang (1997, p. 50)

In the oxidation of austenitic stainless steels such as AISI 316L, spinel-type oxides play a critical role in determining the protective nature of the oxide scale. Among these, $(Fe,Cr)_3O_4$ spinels are commonly formed, where Fe and Cr cations occupy both tetrahedral and octahedral sites, depending on oxidation temperature and oxygen partial pressure. These spinel oxides exhibit relatively high electronic conductivity, which can influence the growth kinetics of the oxide layer. The spinel structure may adopt either a normal or inverse configuration, and in high-temperature oxidation of 316L, inverse spinel forms such as $Fe_2O_3{\cdot}FeO$ (Fe_3O_4) are often detected in the outer layers.Magnetite (Fe_3O_4) has the characteristic inverse-spinel cation distribution $Fe^{3+}(Fe^{2+}Fe^{3+})O_4$, where Fe^{3+} occupies the tetrahedral sites while the octahedral sites contain both Fe^{2+} and Fe^{3+}.

Spinel-type oxides play a crucial role in high-temperature oxidation, particularly in stainless steel, where mixed Fe-Cr-O spinel phases form. The formation of such oxides can alter the protective nature of the oxide scale by introducing pathways for ion transport, affecting long-term stability. This is particularly important in welding applications, where variations in oxygen content influence oxide composition. Additionally, the tendency of spinel oxides to intermix with other oxide phases can lead to the development of multi-layered oxide scales with varying protective properties.

1.3.3 Oxidation of iron and mild steel

The oxidation of iron and mild steel leads to the formation of a multi-layered oxide scale consisting of wüstite (FeO), magnetite (Fe_3O_4), and hematite (Fe_2O_3). These oxides develop in different layers depending on the temperature and oxygen partial pressure in the surrounding environment. Below 570°C, wüstite is thermodynamically unstable and does not persist, while magnetite and hematite dominate the oxide layer. Above this temperature, wüstite forms the innermost layer, directly in contact with the metal surface, whereas magnetite and hematite form progressively outward. The iron-oxygen phase diagram (Figure 1.11) illustrates the stability regions of these oxides under various temperature and oxygen partial pressure conditions (Jepson, 2008).

1.3.3.1 Formation of oxide scale

The oxidation process of iron begins with the surface reaction between iron and oxygen, leading to the formation of Fe^{2+} and Fe^{3+} ions. The oxidation mechanism can be described by the following reactions:

$$Fe \rightarrow Fe^{2+} + 2e^{-} \tag{1.3}$$

$$Fe^{2+} + 2e^{-} + Fe_2O_4 \rightarrow 4FeO \tag{1.4}$$

At temperatures above 570°C, the primary oxidation product is wüstite, which forms due to the reduction of magnetite. Wüstite requires a low partial pressure of oxygen, making it the first oxide to form adjacent to the metal substrate. However, as the oxygen potential increases toward the outer surface, magnetite (Fe_3O_4) and hematite (Fe_2O_3) develop as successive layers (Figure 1.12) (Us, 2016).

1.3.3.1.1 Stability of wüstite at room temperature

At room temperature, wüstite is thermodynamically unstable and tends to convert into hematite through oxidation. This transformation is typically driven by oxygen diffusion into the wüstite structure, promoting the reaction:

$$4FeO + O_2 \rightarrow 2Fe_2O_3 \tag{1.5}$$

However, when wüstite is porous, oxygen diffusion is significantly restricted, preventing complete conversion into hematite or magnetite. In such cases, a thin hematite layer forms on the outer surface due to localized oxidation, while wüstite remains underneath. This phenomenon is commonly observed in corroded iron and steel surfaces, where a residual FeO phase persists beneath a hematite-rich outer layer. The limited oxygen transport through porous wüstite slows down oxidation, resulting in incomplete phase transformation at ambient conditions (Balasko, Batic & Burja, 2025).

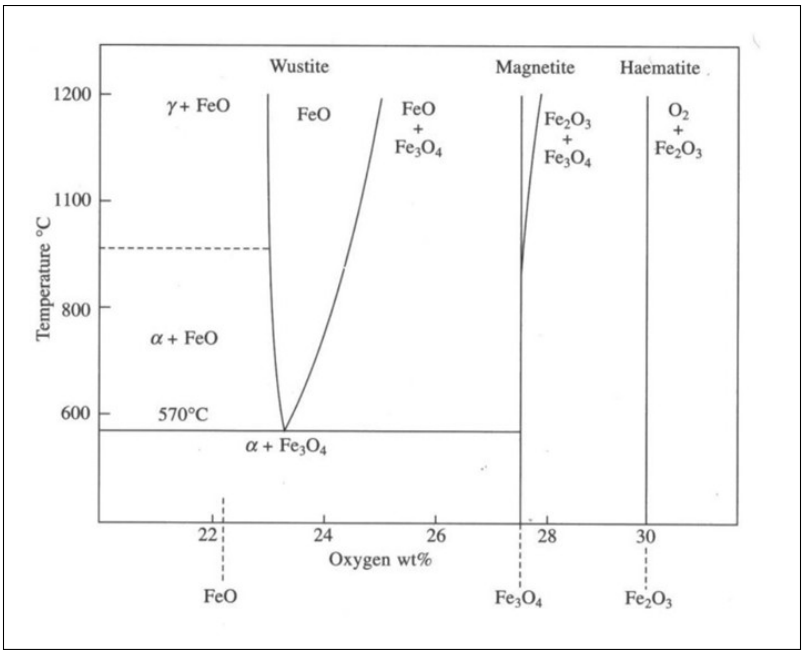

Figure 1.11 Iron-oxygen phase diagram
Taken from Khanna (2005, p. 85)

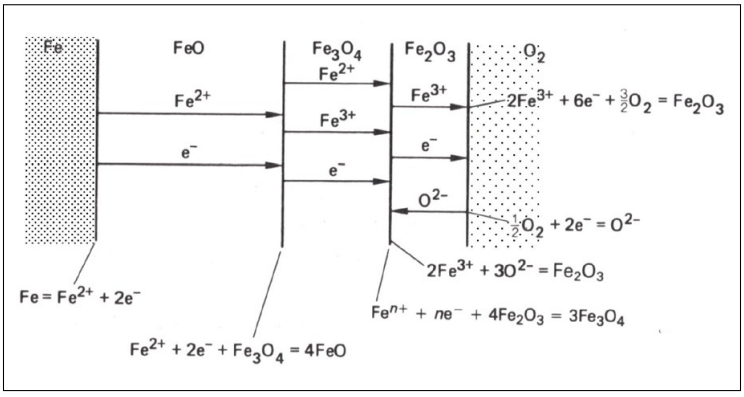

Figure 1.12 Oxidation mechanism of iron oxide above 570°C
Taken from Birks (2006, p. 84)

1.3.3.2 Oxidation of alloys

The oxidation behavior of iron-based alloys differs significantly from that of pure iron due to the presence of alloying elements such as chromium, silicon, and aluminum. These elements

influence the oxide scale structure by forming more stable and protective oxide layers, reducing oxidation rates. Chromium, in particular, plays a critical role in the oxidation resistance of stainless steels by forming a continuous Cr_2O_3 layer, which acts as a diffusion barrier (Jepson, 2008).

1.3.3.2.1 Oxidation of Fe-Cr Alloys

Iron-chromium alloys are widely used in industrial applications due to their superior oxidation resistance. In low-chromium alloys, both iron and chromium oxides form on the metal surface. As the chromium content increases, Fe^{2+} ions become trapped in $FeCr_2O_4$ spinel phases, leading to a thinner wüstite layer compared to magnetite. When the chromium concentration exceeds a critical level, the oxidation rate decreases significantly due to the formation of a stable Cr_2O_3 layer (Us, 2016).

Figure 1.13 illustrates the effect of chromium content on oxidation morphology and parabolic rate constants. In the early stages of oxidation, iron-based oxides dominate, but as chromium concentration increases beyond 20%, the oxidation rate drops sharply, and chromium oxide (Cr_2O_3) becomes the dominant protective layer (Us, 2016).

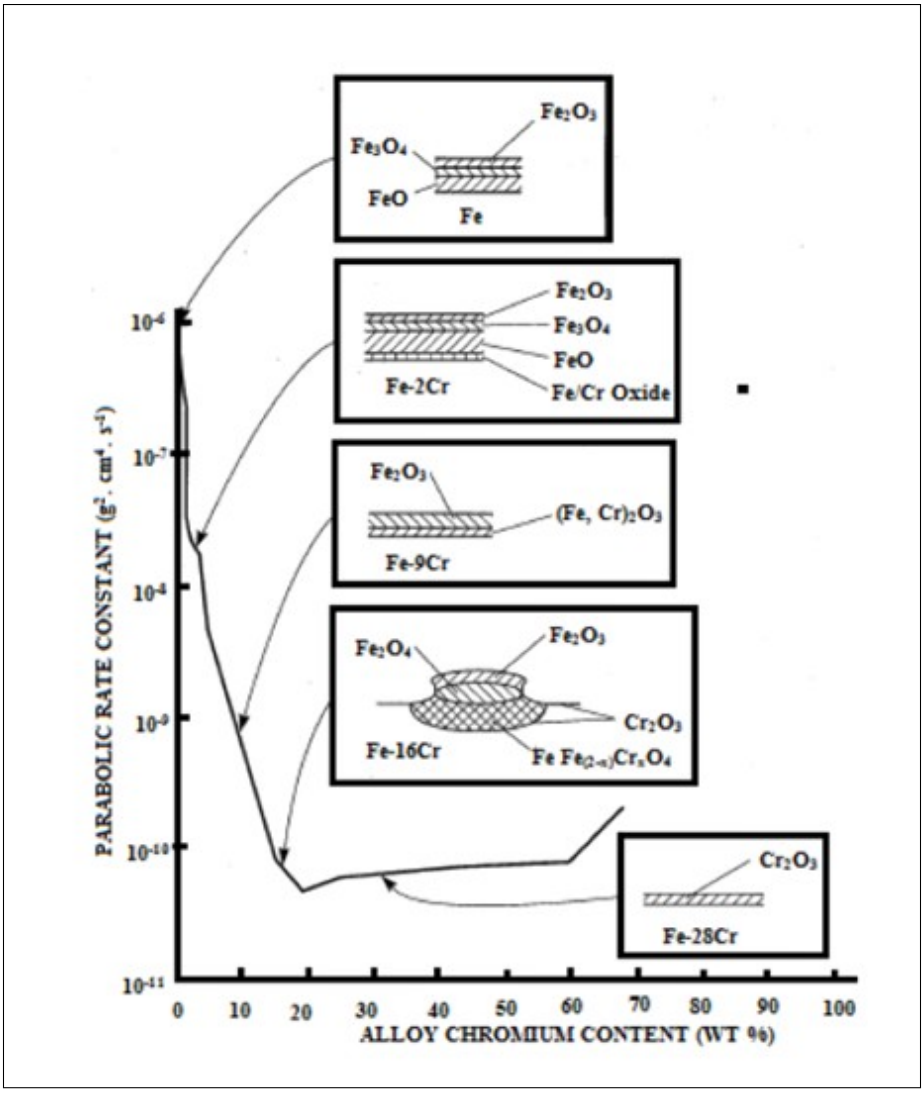

Figure 1.13 Effect of chromium content on oxide morphology and the rate at 1273 K
Taken fromUs (2016, p. 16)

1.3.3.3 Chromium evaporation and vaporization

At high temperatures, such as those encountered during welding (> 1000 °C), chromium-containing oxides become volatile, particularly in oxygen-rich or humid environments. Under these conditions, the protective chromia layer (Cr_2O_3) can partially convert into gaseous chromium speciesa, described by thereaction shown in Figure 1.14. In dry oxygen atmospheres, Cr_2O_3 is further oxidized to volatile CrO_3 according to:

$$Cr_2O_3(s) + \frac{3}{2}O_2(g) \longrightarrow 2\,CrO_3(g) \tag{1.6}$$

In atmospheres containing both oxygen and water vapor, chromium volatilizes primarily as chromium oxyhydroxide, $CrO_2(OH)_2$, through the reaction:

$$\frac{1}{2}Cr_2O_3(s) + \frac{3}{4}O_2(g) + H_2O(g) \longrightarrow CrO_2(OH)_2(g) \tag{1.7}$$

These reactions, reported by (Yamauchi, Kurokawa & Takahashi, 2003), demonstrate that water vapor significantly increases chromium volatility by promoting the formation of $CrO_2(OH)_2(g)$.

As chromium evaporates, the Cr_2O_3 scale becomes depleted, exposing iron-rich oxides such as Fe_2O_3 and Fe_3O_4. This transition reduces the protective capability of the oxide scale and can trigger breakaway oxidation, where oxidation rates accelerate once chromia is lost.

Asteman et al. (Asteman *et al.*, 2000) investigated the role of water vapor in promoting chromium oxide hydroxide formation in 304L stainless steel at **600 °C**. The study revealed that under humid conditions, chromium diffuses to the surface, forming a thin oxide layer. Over time, chromium is depleted from the upper oxide layer due to evaporation, creating a Cr-depleted zone. This depletion allows iron to migrate toward the surface, leading to hematite formation, which is less protective than chromia.

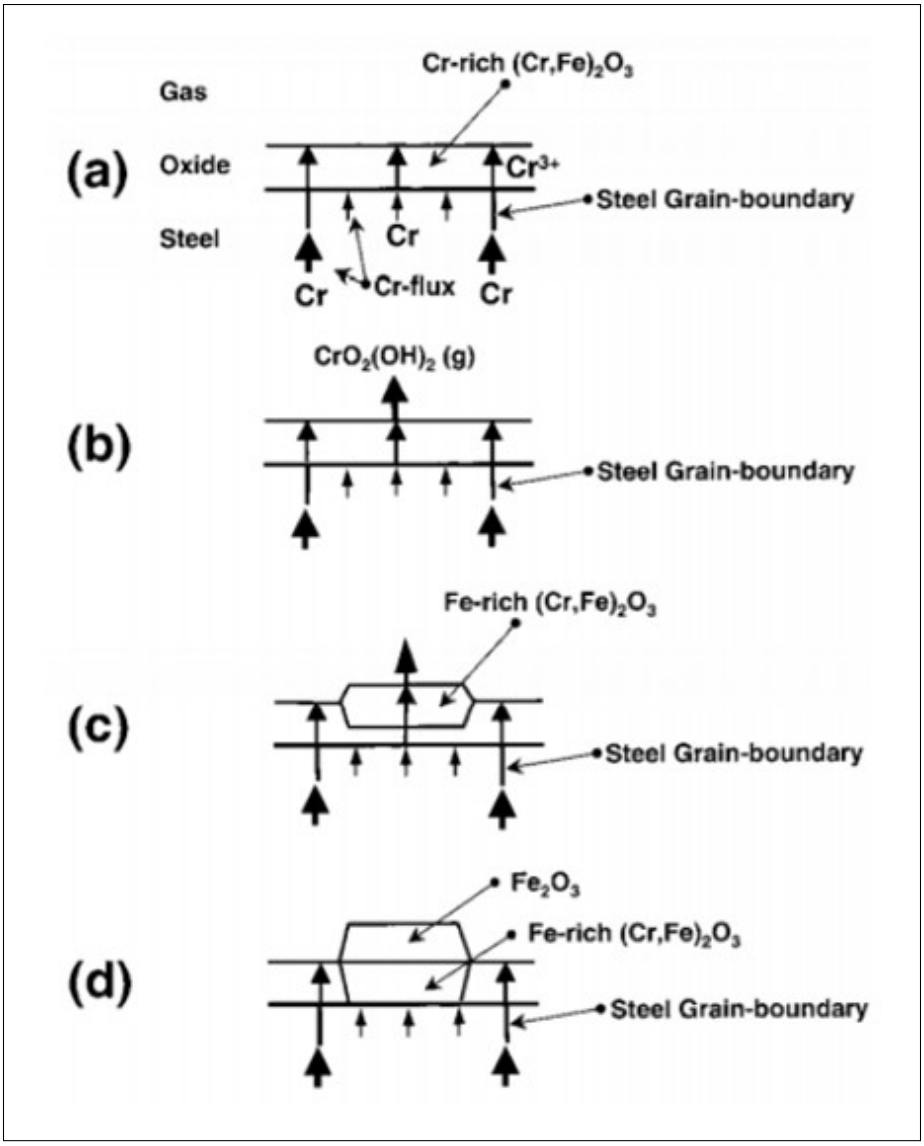

Figure 1.14 Mechanism of chromium evaporation and breakaway oxidation in stainless steel
Taken from Asteman *et al.* (2000, p. 24)

1.4 Oxidation Mechanisms in 316L Stainless Steel

316L stainless steel (SS) is a widely used austenitic stainless steel known for its high corrosion and oxidation resistance, particularly in high-temperature and aggressive environments. Its superior oxidation behavior is attributed to its high chromium (16–18 wt%), nickel (10–14 wt%),

and molybdenum (2–3 wt%) content, which enhances resistance to oxidation, pitting, and high-temperature degradation (Huang *et al.*, 2022).

The oxidation mechanisms of 316L SS depend on temperature, exposure time, and environmental conditions. At moderate temperatures, a thin and protective chromium oxide (Cr_2O_3) layer forms, acting as a diffusion barrier. However, at higher temperatures (>900°C) or in oxygen-rich and humid environments, additional oxidation phenomena occur, including the formation of spinel oxides ($FeCr_2O_4$, $NiCr_2O_4$) and volatilization of chromium species, which may compromise the material's oxidation resistance (Nezakat, Akhiani, Penttilä & Szpunar, 2016; Dudziak *et al.*, 2023).

1.4.1 Protective Oxide Layers in 316L SS

The oxidation resistance of 316L SS primarily relies on the formation of a dense, continuous Cr_2O_3 layer, which limits further oxidation. The oxidation reaction can be expressed as:

$$2Cr + \frac{3}{2}O_2 \rightarrow Cr_2O_3 \tag{1.8}$$

This chromium oxide layer is highly protective due to its low oxygen diffusivity. The presence of nickel enhances oxide stability by reducing the oxidation rate and improving adhesion. Molybdenum also helps to prevent localized oxidation and pitting, particularly in chloride-containing environments (Buscail *et al.*, 2008; Chen *et al.*, 2024).

1.4.1.1 High-Temperature Oxidation and Spinel Formation

At temperatures exceeding 900°C, spinel-type oxides form, including $FeCr_2O_4$ and $MnCr_2O_4$ (Dudziak *et al.*, 2023). Their formation can be represented by:

$$FeO + Cr_2O_3 \rightarrow FeCr_2O_4 \tag{1.9}$$

$$MnO + Cr_2O_3 \rightarrow Mn_2Cr_2O_4 \tag{1.10}$$

Spinel oxides serve as additional diffusion barriers, enhancing oxidation resistance. However, in oxygen-rich environments, Fe-rich oxides such as Fe_2O_3 and Fe_3O_4 may develop in outer layers, reducing protection. The Fe/Cr ratio in spinels plays a crucial role in determining long-term oxidation resistance (Dudziak *et al.*, 2023; Wang *et al.*, 2024b).

1.4.2 Thermodynamics of High-Temperature Oxidation

The oxidation behavior of 316L SS is governed by thermodynamics, especially Gibbs free energy (ΔG), which determines reaction spontaneity (Khanna, 2002):

$$\Delta G = \Delta H - T\Delta S \tag{1.11}$$

where ΔH is enthalpy, T is temperature, and ΔS is entropy. A negative ΔG indicates a spontaneous oxidation reaction.

The general oxidation reaction is:

$$\frac{2x}{y}M + O_2 \rightarrow \frac{2}{y}M_xO_y \tag{1.12}$$

For 316L SS, iron and nickel oxidation reactions are:

$$Fe + \frac{1}{2}O_2 \rightarrow FeO \tag{1.13}$$

$$Ni + \frac{1}{2}O_2 \rightarrow NiO \tag{1.14}$$

Assuming activity of pure solids is unity, the free energy change becomes:

$$\Delta G^{\circ}_{O_2/MO} = \Delta G^{\circ}_{O_2/MO} + RT \ln \left(\frac{a^{2/y}_{M_xO_y}}{a^{2x/y}_{M} \cdot a_{O_2,MO}} \right) \tag{1.15}$$

Since $a_M = a_{M_xO_y} = 1$, the equation simplifies to:

$$\Delta G^{\circ}_{O_2/MO} = RT \ln p_{O_2/MO} \tag{1.16}$$

At equilibrium ($\Delta G^{\circ} = 0$):

$$p_{O_2/MO} = a_{O_2/MO} \tag{1.17}$$

1.4.2.1 Ellingham-Richardson Diagram and Oxide Stability

The Ellingham-Richardson diagram is a valuable thermodynamic tool for predicting oxidation behavior by plotting ΔG° versus temperature (Birks, 2006):

- Metals with more negative ΔG° oxidize more readily.
- Cr_2O_3 becomes stable at $p_{O_2} \approx 10^{-22}$ atm at 1000°C.
- SiO_2 becomes stable at $p_{O_2} \approx 10^{-26}$ atm.

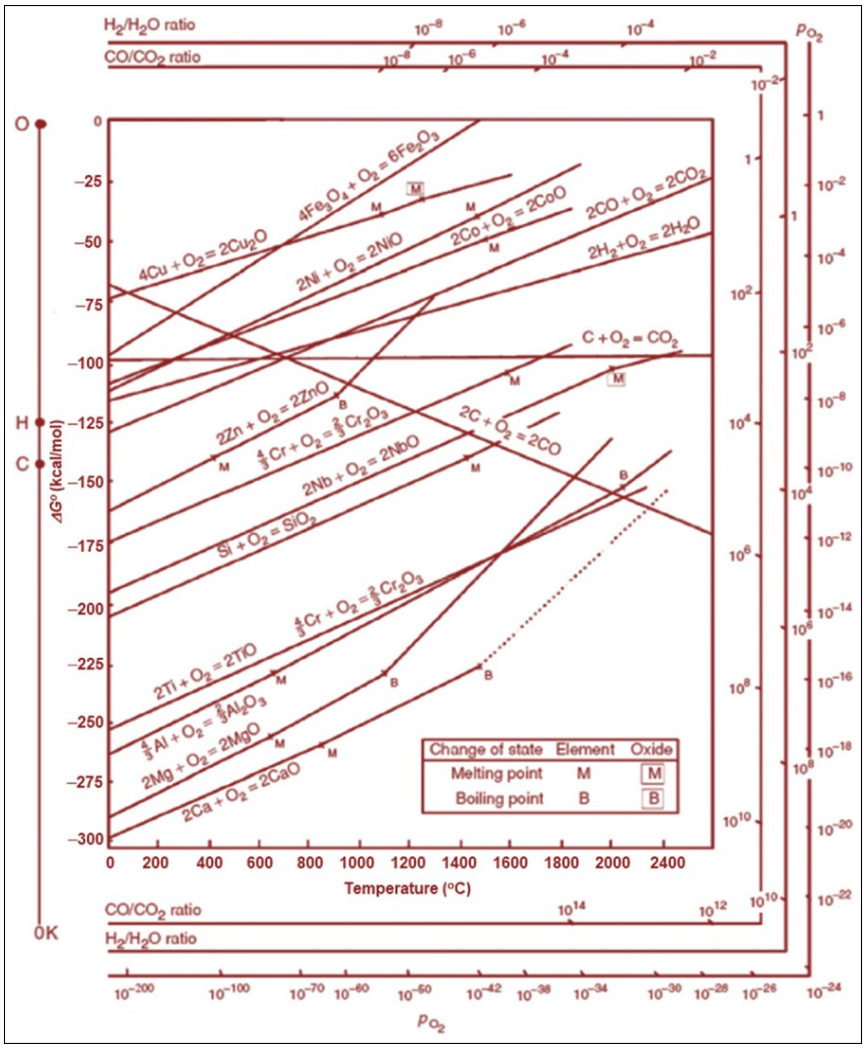

Figure 1.15 Ellingham diagram showing free energy vs. temperature for metal oxidation
Taken from Sahoo *et al.* (2023, p. 141)

At temperatures exceeding 1000°C, Cr_2O_3 can volatilize, weakening its protective effect. In humid environments, water vapor forms volatile chromium species, e.g., $CrO_2(OH)_2$, depleting chromium from the oxide scale.

To counteract this, alloying with Si and Al is common; they form SiO_2 and Al_2O_3, which are more resistant to high-temperature degradation.

1.5 Effect of Welding Parameters on the Oxidation of Stainless Steels

1.5.1 Effect of Surface Preparation

Surface preparation plays a key role in determining the corrosion resistance of stainless steels. The methods employed to finish and treat the surface can significantly influence the formation and stability of the passive oxide layer, thereby affecting the material's susceptibility to various forms of corrosion.

Surface roughness is a critical factor in corrosion behavior. Smoother surfaces generally promote the development of a more uniform and protective passive oxide layer, enhancing corrosion resistance. Nowak (Nowak, 2020) investigated the oxidation resistance of 316Ti stainless steel at high temperatures under different surface roughness conditions. The study examined three different surface preparations: a polished surface with $R_a = 0.009$ μm, a surface ground with 1000 grit sandpaper ($R_a = 0.042$ μm), and another ground with 80 grit sandpaper ($R_a = 1.128$ μm). The mass gain after 48 hours of exposure at 1000 °C was approximately 1.5 mg/cm^2 for the 80 and 1000 grit samples, while the polished sample exhibited a higher mass gain of 2.5 mg/cm^2. In the first 7 hours, the ground samples showed the highest increasing trend in mass gain, after which the mass change stabilized between 7 and 48 hours (Figure 1.16).

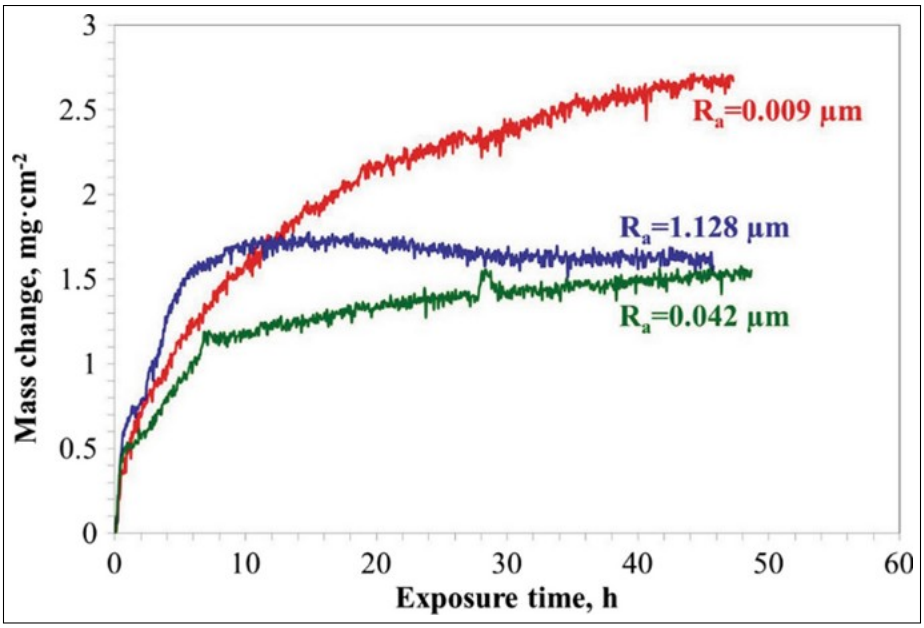

Figure 1.16 Mass change plot obtained during isothermal exposure of AISI 316Ti at 1000 °C in air for 48 h
Taken from Nowak (2020, p. 8062)

According to Figure 1.17, the outer oxidation layer consists of a mixture of chromium and iron oxides, with manganese also observed in the outer oxide layer. Manganese depletion increased with sputtering time, reaching up to 1300 seconds, and was more pronounced in the ground samples. The polished sample did not show significant iron enrichment in the outer oxide layer. The primary difference between the 80 and 1000 grit samples was the chromium content in the outer oxide layer, which was higher than iron in the 80 grit sample (Nowak, 2020).

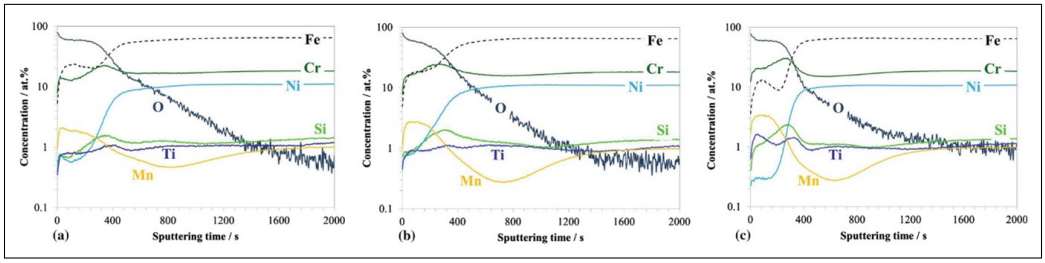

Figure 1.17 GD-OES depth profiles obtained on AISI 316Ti after isothermal exposure at 1000 °C in air: (a) 1 μm polished, (b) 1000 grit, and (c) 80 grit ground
Taken from Nowak (2020, p. 8062)

Jaffré et al. (Jaffré *et al.*, 2021b) observed that mechanical surface treatments, particularly dry grinding, significantly degrade the passive film stability and corrosion resistance of 304L stainless steel, especially in chloride environments, due to increased surface roughness and residual stresses.

Figure 1.18 provides a schematic representation of cross-sections of samples subjected to various mechanical surface treatments, illustrating the microstructural changes induced by each method. The ground surface (Figure 5a) exhibits an ultra-fine grain layer, followed by a plastic deformation zone and the presence of high residual compressive stresses. In contrast, polishing to 2400 grit SiC (Figure 5b) and 1 μm (Figure 5c) results in a more refined grain structure with significantly lower residual compressive stresses. Additionally, grinding leads to higher surface roughness, producing deeper scratches compared to polished specimens, which maintain a relatively smoother surface finish.

Since a passive film forms on all surfaces, the microstructural modifications induced by mechanical treatments influence corrosion-related processes, including charge transfer, adsorption, passive film formation, and stability. The differences in surface characteristics alter the electrochemical behavior of stainless steel, affecting passivation efficiency and corrosion current densities (Jaffré *et al.*, 2021b).

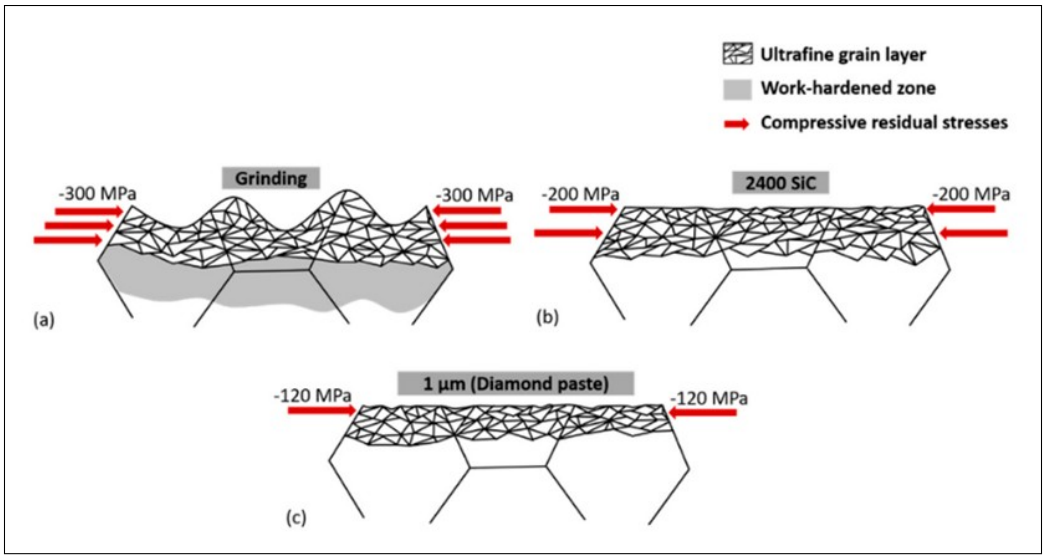

Figure 1.18 Schematic representation of surface alterations in 304L stainless steel specimens after mechanical surface treatment: (a) ground surface, (b) polished surface using 2400-grit SiC, and (c) polished surface refined to 1 μm with diamond paste
Taken from Jaffré *et al.* (2021b, p. 10)

Kim et al. (Kim *et al.*, 2015) investigated the role of grain boundaries in the initial oxidation behavior of austenitic stainless steel. As shown in Figure 1.19, during the first 2.5 hours of oxidation, specimens with smaller grain sizes exhibited a higher mass increase trend, indicating a more rapid oxidation rate compared to their larger-grain counterparts.

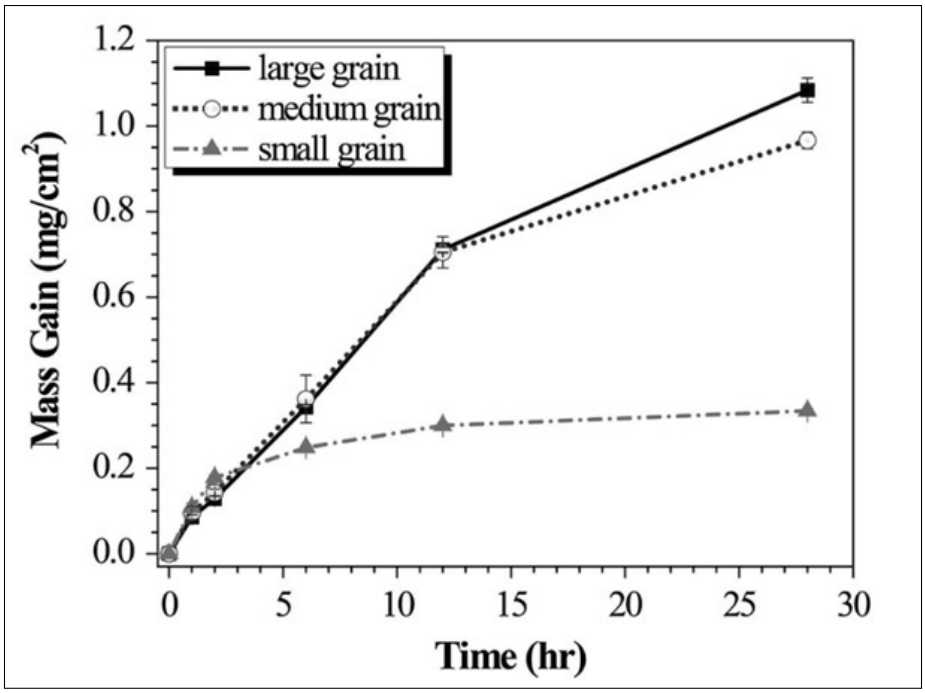

Figure 1.19 Mass gain vs. time curve for large grain (27μm), medium grain (17 μm), and small grain (8 μm) samples over 28 h of oxidation at 700 °C in air with 20% water vapor
Taken from Kim *et al.* (2015, p. 61)

1.5.2 Effect of Backing and Shielding Gas

Shielding and backing gases are critical factors in determining the oxidation behavior of stainless steel during welding. These gases influence the composition and stability of the passive oxide layer, affecting both corrosion resistance and mechanical properties of the welded joint. The selection of an appropriate shielding gas is essential to minimize oxidation, control weld bead appearance, and ensure optimal material performance.

Shielding gases, such as argon, helium, nitrogen, and carbon dioxide, are used to protect the molten weld pool from atmospheric contamination. Backing gases, which protect the root side of the weld, help prevent excessive oxidation and discoloration, ensuring uniform and controlled oxide formation. The presence of oxygen, nitrogen, or moisture in the shielding

gas can significantly affect oxidation kinetics, leading to changes in the microstructure and corrosion resistance of the welded region.

Trigwell et al. (Trigwell & Selvaduray, 2005) investigated the effect of varying oxygen concentrations leaking into the argon purge gas during welding. The study analyzed the chemical composition and oxide layer thickness of the heat-affected zone (HAZ) and a clean reference area using Auger electron spectroscopy. As shown in Figure 1.20, an increase in oxygen concentration in the purging gas leads to a corresponding increase in oxide thickness. This effect was observed across different electrode types, highlighting the significant influence of purging gas composition on oxidation behavior in welded stainless steel.

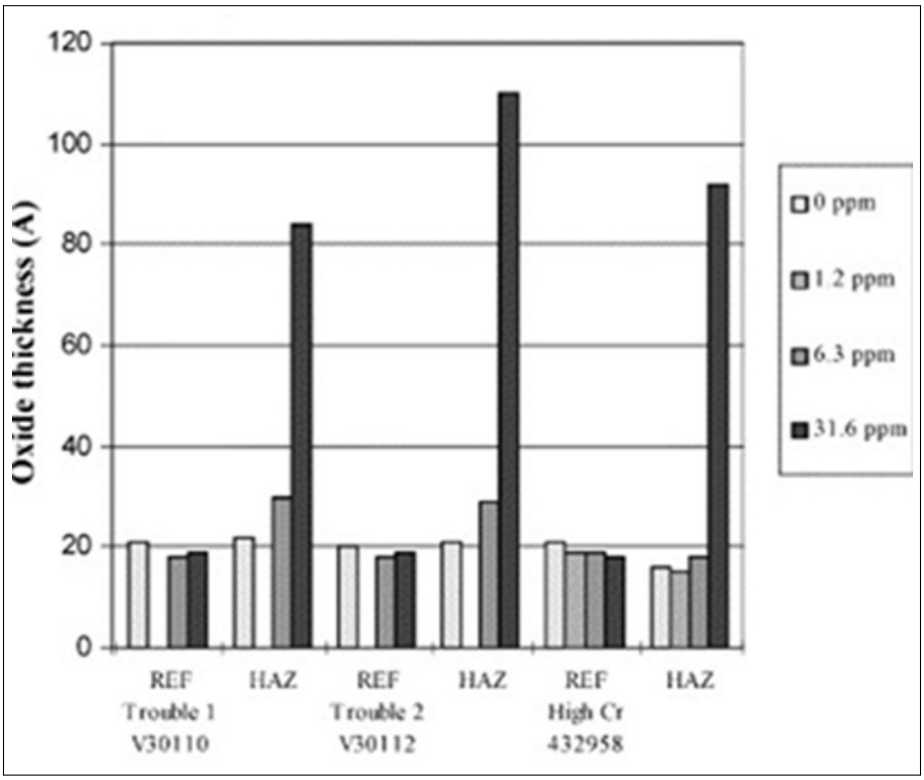

Figure 1.20 Oxide layer thickness for different levels of O_2 in weld purge gas in 316L SS
Taken from Trigwell & Selvaduray (2005, p. 40)

Somrerk et al. (Chandra-Ambhorn & Saranyachot, 2019) investigated the effect of hydrogen content in shielding gas on the microstructure and oxidation resistance of Fe–15.7 wt.% Cr–

8.5 wt.% Mn steel using GTAW. Figure 1.21 presents the mass gain as a function of oxidation cycles for welds produced at a welding speed of 3.3 mm·s^{-1} using two different shielding gas compositions: Ar–7 vol.% N_2 and Ar–7 vol.% N_2–5 vol.% H_2. The oxidation test was conducted in simulated air at 700 °C. The results indicate that the addition of hydrogen to the Ar–N_2 shielding gas effectively reduced the oxidation rate of the welds, demonstrating its role in improving oxidation resistance during high-temperature exposure.

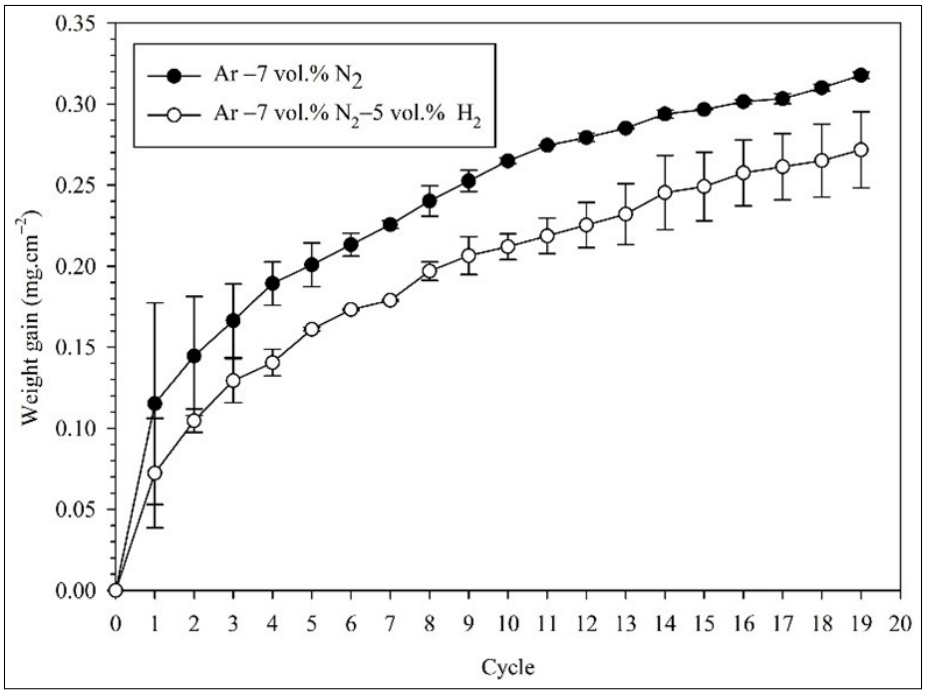

Figure 1.21 Weight gain as a function of time for welds produced using Ar–7 vol.% N_2 and Ar–7 vol.% N_2–5 vol.% H_2 shielding gas at a welding speed of 3.3 mm·s^{-1}
Taken from Chandra-Ambhorn & Saranyachot (2019, p. 22)

Somrerk et al. (Chandra-Ambhorn & Saranyachot, 2019) also studied the high-temperature oxidation behavior of Fe–15.7 wt.% Cr–8.5 wt.% Mn steel. Their results indicated that the mass gain increased with the addition of 9% water vapor, suggesting that water vapor accelerates oxidation kinetics and enhances oxide scale growth during high-temperature exposure (Figure 1.22).

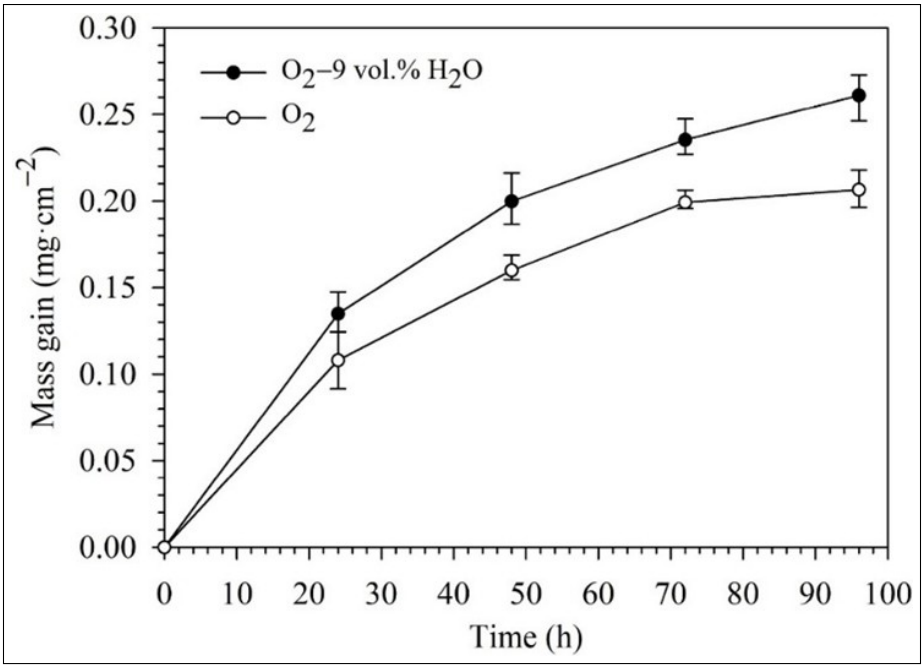

Figure 1.22 Mass gain as a function of time of Fe–15.7 wt.% Cr–8.5 wt.% Mn oxidized at 700 °C in oxygen with and without 9 vol.% water vapor
Taken from Chandra-Ambhorn *et al.* (2019, p. 40)

M.A. Bermejo et al. (Valiente Bermejo *et al.*, 2015) demonstrated that duplex and superduplex stainless steel samples shielded with gas mixtures containing 2% CO_2 (Ar + 2% CO_2, Ar + 30% He + 2% CO_2) exhibited higher depth-to-width (D/W) ratios compared to those shielded with gas mixtures containing only 0.5% CO_2 (Ar + 30% He + 0.5% CO_2, Ar + 30% He + 0.5% CO_2 + 1.8% N_2), as shown in Figure 1.23. This effect is likely attributed to the oxygen content in the weld pool resulting from CO_2 decomposition in the welding arc. The presence of oxygen influences Marangoni convection in the weld pool, leading to narrower and deeper weld profiles.

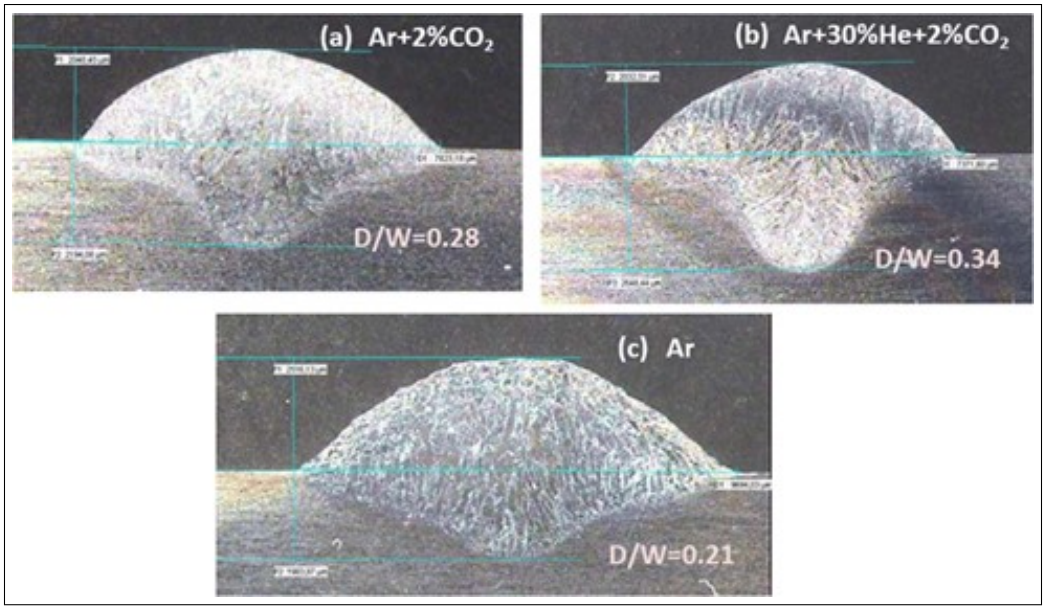

Figure 1.23 Effect of shielding gas on welding of duplex and superduplex stainless steel welds: (a) Ar + 2% CO_2, (b) Ar + 30% He + 2% CO_2, (c) Ar
Taken from Valiente Bermejo *et al.* (2015, p. 244)

1.6 Corrosion Mechanisms

Corrosion is a natural degradation process that occurs due to the interaction between materials and their environment. It affects a wide range of materials, including metals, polymers, concrete, and ceramics, but is most critical in metals due to their high susceptibility to oxidation and electrochemical reactions (Ahmad, 2006; Kazemipour, 2020). The thermodynamic driving force behind corrosion is the tendency of metals to return to their most stable state. In nature, most metals exist in the form of oxides, sulfides, or carbonates, and refining them into metallic form requires energy input. Over time, metals release this stored energy and revert to a lower-energy state through corrosion (West, 1986).

Corrosion can be categorized into two major types (Wallace, Hoeppner & Kandachar, 1985; Chilingar, Mourhatch & Al-Qahtani, 2013):

- **Dry Corrosion (Non-Aqueous Corrosion):** Occurs in the absence of a liquid (e.g., at high temperatures in oxidizing environments) and involves direct chemical reactions with gases like oxygen, sulfur, or carbon dioxide.
- **Wet Corrosion (Electrochemical Corrosion):** Occurs in the presence of an electrolyte, such as water or an aqueous solution, and involves electrochemical reactions, where metals act as anodes and corrode due to oxidation.

1.6.1 Principles of Electrochemical Corrosion

Corrosion is fundamentally an electrochemical process, which involves redox (oxidation-reduction) reactions at the metal surface in contact with an electrolyte. A typical wet corrosion cell consists of four essential components:

- **Anode** – The region where oxidation occurs, leading to metal dissolution.
- **Cathode** – The region where reduction reactions take place.
- **Electrolyte** – A conductive solution that facilitates the transport of ions.
- **Electrical connection** – A pathway for electron movement between the anode and cathode.

A schematic of a typical corrosion cell is shown in Figure 1.24, illustrating how corrosion occurs in the presence of an electrolyte and electrochemical potential differences between metal regions.

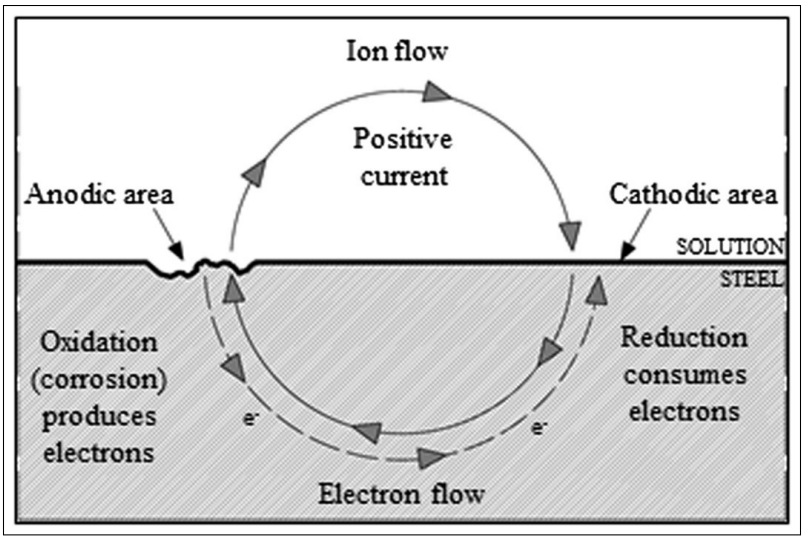

Figure 1.24 Schematic of a typical corrosion cell
Taken from Di Benedetti *et al.* (2013, p. 1023)

In a corrosion process, the anode (which is more electrochemically reactive) dissolves into the electrolyte, following the general oxidation reaction (anodic reaction):

$$\mathrm{M} \rightarrow \mathrm{M}^{z+} + ze^{-} \tag{1.18}$$

where M is the metal and z is the number of electrons lost per atom.

The cathodic (reduction) reaction is represented as:

$$\mathrm{Ox} + ze^{-} \rightarrow \mathrm{Red} \tag{1.19}$$

The overall corrosion reaction is:

$$\mathrm{M} + \mathrm{Ox} \rightarrow \mathrm{M}^{z+} + \mathrm{Red} \tag{1.20}$$

The thermodynamic spontaneity of corrosion is determined by the Gibbs free energy change (ΔG) of the reaction. If $\Delta G < 0$, the reaction is spontaneous, meaning that the metal will corrode. The relationship between Gibbs free energy and electrochemical potential is given by:

$$\Delta G = -zF(E_c - E_a) \tag{1.21}$$

where:

- F is the Faraday constant (96,585 C·mol^{-1}),
- E_c and E_a are the electrode potentials of the cathodic and anodic reactions.

For corrosion to occur, the potential difference ΔE must be positive:

$$\Delta E_{\text{eq}} = E_c - E_a > 0 \tag{1.22}$$

This electrochemical potential difference serves as the driving force of corrosion. However, while thermodynamics predicts whether corrosion can occur, it does not indicate the rate at which it happens (Trethewey, 1995).

1.6.2 Corrosion thermodynamics

Thermodynamics provides insight into the energy changes associated with electrochemical corrosion reactions. These energy transformations dictate the driving force and direction of a chemical reaction. However, thermodynamics alone does not predict the rate of corrosion; it merely determines whether corrosion is possible under given conditions (Sheir, Jarman & Burstein, 1994). A metal's tendency to corrode depends on its electrochemical potential in each environment. This potential is influenced by ionic strength, electrolyte composition, temperature, and the metal or alloy itself. The potential of a galvanic cell is determined by the sum of the anodic and cathodic half-cell potentials in the surrounding

environment. According to thermodynamics, the potential of an electrochemical reaction can be related to Gibbs free energy change (ΔG) using the following equation (Roberge, 2000):

$$\Delta G = -nFE \tag{1.22}$$

Where n is the number of electrons participating in the reaction, F is Faraday's constant (96,500 C/mol), and E is the electrode potential.

A negative ΔG ($\Delta G < 0$) signifies that the reaction is spontaneous, indicating a natural tendency for metal oxidation to occur. The change in electrode potential as a function of ion concentration follows the Nernst equation (Roberge, 2000):

$$E = E^0 + \frac{2.3RT}{nF} \log \left(\frac{\text{Oxidized species}}{\text{Reduced species}} \right) \tag{1.23}$$

Where E^0 is the standard electrode potential, R is the ideal gas constant (8.314 J/mol·K), T is the temperature (K), and n is the number of electrons involved.

The relationship between potential and pH is illustrated by Pourbaix diagrams, which show regions where a metal remains stable, undergoes dissolution, or forms an oxide layer.

A Pourbaix diagram (potential-pH diagram) is a powerful tool in corrosion science, showing the thermodynamic stability of a metal in different environments. The diagram has three key regions (Steigerwald, 1968):

- **Immunity (No Corrosion - Region A)**: The metal remains in its elemental form.
  Example: Iron is stable under very negative electrode potentials (E_p), corresponding to strongly reducing conditions
- **Active Corrosion (Region B)**: The metal dissolves as ions in solution.
  Example: $Fe \rightarrow Fe^{2+} + 2e^-$ occurs in acidic environments.

- **Passivation (Region C)**: The metal forms a protective oxide layer, preventing further corrosion.

  Example: Formation of Fe_2O_3 or Fe_3O_4 in neutral or slightly alkaline environments.

A simplified Pourbaix diagram for iron in an aqueous system at 25°C illustrates these regions. As seen in Figure 1.25, at low pH, Fe dissolves actively, while at neutral pH, a protective oxide layer forms.

$$Fe^{2+} + 2H_2O \rightarrow Fe_2O_3 + 4H^+ + 2e^- \tag{1.24}$$

This explains why stainless steels resist corrosion—they form a stable Cr_2O_3 passive layer.

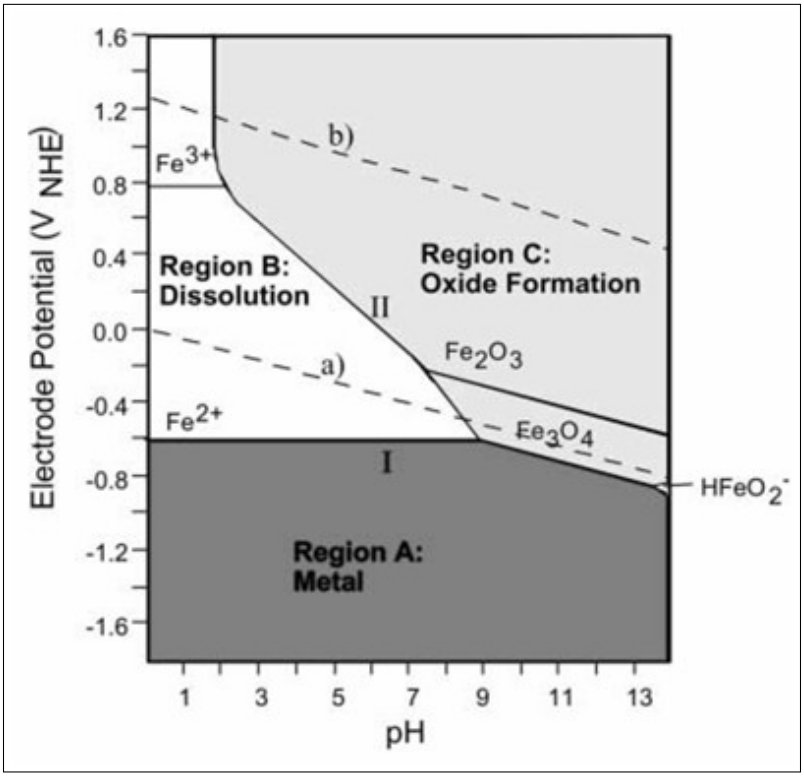

Figure 1.25 Pourbaix diagram for iron-water system at 25°C
Taken from Uhlig & Revie (1985, p. 46)

While thermodynamics determines the feasibility of corrosion, kinetics describes how fast the reaction proceeds. Corroding systems are typically out of equilibrium, meaning oxidation and reduction reactions occur at a potential displaced from equilibrium. This displacement is termed polarization (η_{pol}), which is given by (Roberge, 2000):

$$\eta_{\text{pol}} = |E - E_{eq}| \tag{1.25}$$

Where E_{eq} is the equilibrium potential.

There are three primary types of polarization (Fontana, Greene & Klerer, 1968):

- **Activation Polarization**: The electrochemical reaction rate is controlled by charge transfer across the metal-solution interface. The activation polarization equation follows the Tafel relationship:

  $$\eta_A = \beta_A \log\left(\frac{i_A}{i_0}\right)$$

  where i_A is the anodic current density, i_0 is the exchange current density, and β_A is the Tafel slope.
- **Concentration Polarization**: The reaction rate is limited by mass transport of reactants or products. The concentration polarization equation is:

  $$\eta_C = -\frac{2.3RT}{zF} \log\left(1 - \frac{i}{i_{\text{lim}}}\right)$$

  where i_{lim} is the limiting current density.
- **Resistance Polarization**: The potential drop across the electrolyte and corrosion product films contributes to resistance polarization:

  $$\eta_R = I(R_{\text{sol.}} + R_f)$$

  where $R_{\text{sol.}}$ is the solution resistance and R_f is the film resistance.

The total polarization in an electrochemical cell is the sum of all three (Fontana *et al.*, 1968):

$$\eta_{\text{total}} = \eta_A + \eta_C + \eta_R \tag{1.26}$$

The corrosion rate is determined by the magnitude of the electrochemical current, which can be described by Faraday's law (Sheir *et al.*, 1994):

$$I = \frac{nFK}{M} \tag{1.27}$$

Where I, K, and M are the corrosion current, the rate of corrosion (g/s), and the atomic weight of the metal, respectively.

Electrochemical corrosion is governed by mixed potential theory, where anodic and cathodic reactions occur simultaneously. The sum of anodic currents equals the sum of cathodic currents (Li, 2020):

$$\sum i_A = \sum |i_C| \tag{1.28}$$

This balance determines the corrosion potential, where the anodic and cathodic current densities are equal:

$$i = |i_c| = i_{\text{corr}} \tag{1.29}$$

The relationship between corrosion potential and current density is expressed by the Wagner-Traud equation:

$$i = i_{\text{corr}} \left(e^{\left(\frac{\alpha_A z F (E - E_{\text{corr}})}{RT} \right)} - e^{\left(\frac{-\alpha_C z F (E - E_{\text{corr}})}{RT} \right)} \right) \tag{1.30}$$

Where z represents the number of electrons transferred in the electrochemical reaction.

At small potential deviations, this reduces to a linear form:

$$i = 2.303\, i_{\text{corr}} \left(\frac{1}{b_A} + \frac{1}{b_C} \right) (E - E_{\text{corr}}) \tag{1.31}$$

Where b_A and b_C are the Tafel slopes of the anodic and cathodic reactions.

Electrochemical techniques are essential for evaluating the corrosion behavior of passive metals in aggressive environments. Among the most informative methods are cyclic polarization, which provides insight into the pitting resistance and repassivation behavior of materials, and electrochemical impedance spectroscopy (EIS), which offers detailed information about the interfacial properties and passive film stability through frequency-domain analysis. These methods are particularly effective in characterizing localized corrosion in stainless steels and other corrosion-resistant alloys.

1.6.2.1 1.5.3 Cyclic Polarization Technique for Evaluating Pitting Corrosion

Cyclic polarization is a widely utilized potentiodynamic technique that provides critical insight into the pitting corrosion behavior of metals and alloys, particularly those that form passive films such as stainless steels (Testing & Materials, 2009). This technique is employed to evaluate not only the susceptibility of a material to localized corrosion but also its capacity for repassivation once the protective oxide layer has broken down. The method yields quantitative electrochemical parameters, such as the pitting potential, repassivation potential, and corrosion potential, all of which are essential for assessing the stability of passive films under aggressive conditions (Testing & Materials, 2009).

1.6.2.2 Principle and Experimental Methodology

In a standard cyclic polarization experiment, the working electrode (i.e., the metal sample) is immersed in an electrolyte that simulates the target environment. The electrochemical cell consists of a three-electrode configuration, comprising the working electrode, a reference electrode (e.g., saturated calomel electrode (SCE) or Ag/AgCl), and a counter electrode (typically platinum mesh) (Bard, Faulkner & White, 2022).

The measurement begins by holding the electrode at its open circuit potential (OCP)—the natural equilibrium potential established in the absence of external current. The potential is then swept anodically (in the positive direction) at a fixed scan rate. As the potential increases, the electrochemical response of the metal is monitored as a function of current density. Upon reaching a predefined upper vertex potential (selected to be above the pitting or transpassive potential), the scan is reversed in the cathodic direction. This reverse scan provides information about the metal's ability to repassivate after pit initiation. The resulting plot of current density (i) versus applied potential (E) is the cyclic polarization curve (Szklarska-Smialowska, 1999; Jones, 1996; Frankel, 1998).

1.6.2.3 Interpretation of the Cyclic Polarization Curve

The cyclic polarization curve can be divided into distinct electrochemical regions, each of which corresponds to a specific mechanism occurring at the metal-electrolyte interface. Understanding these regions allows for the interpretation of both general and localized corrosion phenomena (Esmailzadeh, Aliofkhazraei & Sarlak, 2018).

At the outset, in the active region, the current density increases rapidly with potential, indicating active metal dissolution. This corresponds to the anodic oxidation reaction of the metal are provided in (Fontana, 1986):

$$\mathrm{M} \rightarrow \mathrm{M}^{z+} + ze^{-} \tag{1.32}$$

In this region, the surface is free of any protective oxide layer, and the electrochemical behavior obeys Tafel kinetics. The slope of the current response is directly related to the anodic Tafel slope and can provide information about activation-controlled dissolution processes (Jones, 1996).

As the potential increases further, the current reaches a peak and subsequently declines to a plateau region. This inflection marks the onset of the passive region, where a thin, adherent oxide film forms on the metal surface. This film acts as a kinetic barrier to further dissolution by impeding electron and ion transfer (Frankel, 1998).

Continued scanning leads to a point known as the pitting potential, at which the current density begins to rise sharply. This increase is not associated with uniform corrosion but rather with the localized breakdown of the passive film, typically initiated by aggressive anions such as chloride. At this point, pits nucleate and propagate autocatalytically. The onset of this current rise indicates a transition to the transpassive or pitting region and marks the potential above which the material becomes susceptible to localized corrosion.

The scan is then reversed after reaching a maximum potential (E_reverse), which is usually selected slightly above E_pit or in the transpassive range. During the reverse scan, the current density initially decreases but does not immediately follow the same path as the forward scan. Instead, a hysteresis loop is observed, which is indicative of the material's inability to immediately repassivate. The magnitude and width of this loop are direct indicators of the severity of pitting corrosion (Fontana, 1986; Frankel, 1998).

As the reverse scan proceeds, a sharp drop in current is observed at the repassivation potential. This is the potential at which pit growth ceases, and a stable passive film begins to re-establish. The difference between the pitting potential and the repassivation potential ($\Delta E = E_{\text{pit}} - E_{\text{rep}}$) is a critical parameter (Fontana, 1986; Frankel, 1998).

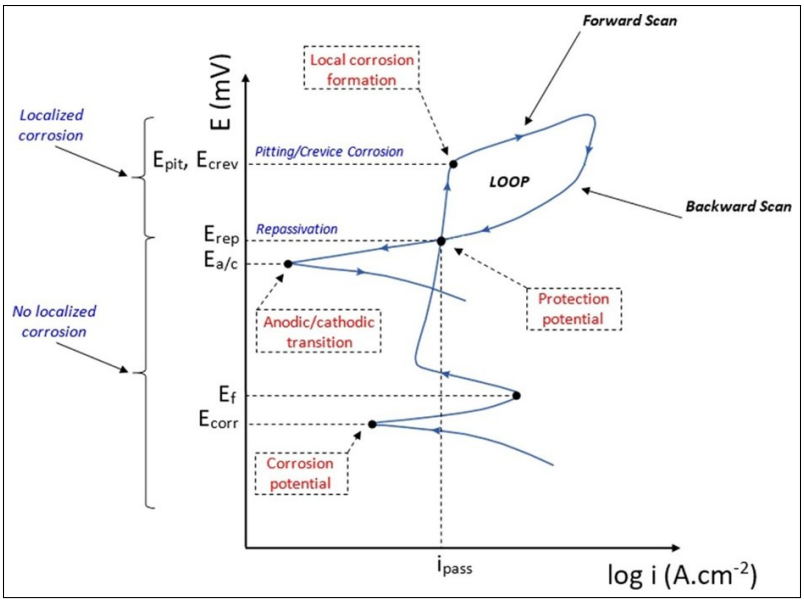

Figure 1.26 Representative cyclic polarization curve
Taken from Costa *et al.* (2023, p. 7)

1.6.2.4 Mechanistic Insights and Quantitative Parameters

The cyclic polarization curve offers not only qualitative insights into corrosion behavior but also quantitative parameters that are widely used to compare materials or treatment conditions. The corrosion potential is the potential at which the net current is zero, and it reflects the thermodynamic tendency of the metal to corrode in the test environment. The corrosion current density, which can be estimated using Tafel extrapolation near E_{corr}, is directly proportional to the rate of uniform corrosion via Faraday's law (Frankel, 1998; Esmailzadeh *et al.*, 2018).

The E_{pit} is a kinetic threshold for passive film breakdown. Materials with higher E_{pit} values are more resistant to pitting initiation. The repassivation potential E_{rep} is a practical indicator of how easily pits can be arrested. Materials with high E_{rep} values, close to E_{pit}, exhibit stable passivity. The hysteresis area between the forward and reverse scans can be integrated to provide an estimate of the energy barrier for repassivation (Xiuming, Yanliang, Yadav, Wenjuan & De Marco, 2015; Zakeri, Naghizadeh, Nakhaie & Moayed, 2016).

1.6.3 Electrochemical Impedance Spectroscopy (EIS)

Electrochemical Impedance Spectroscopy (EIS) is a sophisticated, non-destructive analytical technique used to probe the electrical response of an electrochemical system over a wide range of frequencies. Unlike DC techniques such as linear polarization or Tafel extrapolation, which offer point-specific information about corrosion potential or current, EIS provides a comprehensive frequency-dependent characterization of the metal–electrolyte interface. It is particularly valuable in corrosion science due to its ability to distinguish and quantify multiple overlapping processes—such as solution resistance, charge transfer, double-layer capacitance, and passive film properties—by analyzing their distinct time constants (Macdonald, 1992; Mansfeld, 1995; Orazem & Tribollet, 2008).

1.6.3.1 Experimental Conditions and System Setup

A typical EIS experiment is performed using a potentiostat in a three-electrode configuration: the working electrode, a reference electrode, and a counter electrode. The potentiostat maintains the working electrode at a constant DC potential—often the open circuit potential (OCP), which is the steady-state potential of the system without external current—and superimposes a small-amplitude AC voltage perturbation.

The perturbation is applied over a logarithmically spaced frequency range. High-frequency measurements capture fast processes such as electrolyte resistance and double-layer charging, while lower frequencies probe slower processes such as ionic diffusion, charge transfer at the interface, or long-term degradation of surface films. During the test, the potentiostat records the amplitude and phase of the current response relative to the applied voltage at each frequency point.

1.6.3.2 Impedance as a Complex Quantity

The fundamental measured quantity in EIS is the electrochemical impedance $Z(\omega)$, which is defined as the ratio of the sinusoidal voltage perturbation $V(\omega)$ to the resulting sinusoidal current $I(\omega)$ at a given angular frequency $\omega = 2\pi f$, where f is the frequency in hertz:

$$Z(\omega) = \frac{V(\omega)}{I(\omega)} = Z'(\omega) + jZ''(\omega) \tag{1.33}$$

Here, $Z'(\omega)$ is the real part of the impedance, representing resistive components (such as solution resistance and charge transfer resistance), while $Z''(\omega)$ is the imaginary part, which arises from reactive (energy-storing) components such as capacitors or inductors. The imaginary unit j is defined as $\sqrt{-1}$.

The phase shift ϕ between the voltage and current signals is a key parameter in EIS. If the current and voltage are in phase ($\phi = 0°$), the system behaves as a pure resistor. A negative phase shift indicates capacitive behavior (current leads voltage), while a positive phase shift indicates inductive behavior (current lags voltage). These phase shifts enable the separation of resistive and capacitive contributions at each frequency.

The magnitude and phase of the impedance are typically expressed as:

$$|Z| = \sqrt{Z'^2 + Z''^2} \tag{1.34}$$

$$\phi = \tan^{-1}\left(\frac{Z''}{Z'}\right) \tag{1.35}$$

This information is collected point-by-point across the selected frequency range, forming a dataset of complex impedance values that can be visualized using graphical tools such as Nyquist and Bode plots (Lasia, 2002; Macdonald *et al.*, 2018; Bard *et al.*, 2022).

1.6.4 Nyquist and Bode Plot Interpretation

The Nyquist plot is a widely used graphical representation in EIS, where the negative imaginary part of the impedance ($-Z''$) is plotted on the y-axis against the real part (Z') on the x-axis. Each point on this plot corresponds to a unique frequency, though frequency itself is not directly shown on the axes. Typically, the frequency decreases from left to right.

For simple electrochemical systems characterized by a single time constant, such as a bare metal electrode in an electrolyte undergoing charge transfer reactions, the Nyquist plot exhibits a semicircular arc. The high-frequency intercept of the semicircle with the real axis represents the solution resistance (R_s), which is primarily determined by the ionic conductivity of the electrolyte. The diameter of the semicircle corresponds to the charge transfer resistance (R_{ct}), which reflects the ease or difficulty with which electrons are transferred across the metal–electrolyte interface. The low-frequency intercept of the arc with the real axis gives the total resistance of the system ($R_s + R_{ct}$) (Lasia, 2002; Orazem & Tribollet, 2008).

In more complex systems, such as those involving passive films, porous layers, or diffusion-controlled processes, the Nyquist plot may exhibit multiple semicircles, depressed arcs, or Warburg tails. A depressed semicircle often indicates surface heterogeneity or distributed time constants and is typically modeled using a constant phase element (CPE) rather than an ideal capacitor (Macdonald *et al.*, 2018).

The Bode plot offers complementary information and consists of two parts. The first is the magnitude plot, where the logarithm of the absolute impedance $|Z|$ is plotted versus the logarithm of the frequency. This plot reveals how the total impedance of the system changes across different time scales. At high frequencies, the impedance is usually low and dominated by the solution resistance. At low frequencies, impedance increases as capacitive or resistive processes within passive films become significant.

The second part is the phase angle plot, where the phase angle ϕ is plotted versus the logarithm of the frequency. A large, broad peak in the phase angle suggests dominant capacitive behavior

and indicates the presence of a stable, compact passive film. The width and position of this peak correlate with the characteristic time constants of the electrochemical processes. In systems with multiple time constants, the Bode plot may display multiple peaks or inflection points, each associated with a distinct physical or chemical process (Lasia, 2002; Orazem & Tribollet, 2008).

Equivalent Circuit Modeling and Physical Interpretation

The true power of EIS lies in its ability to model the impedance response using an equivalent electrical circuit that simulates the electrochemical behavior of the interface. These models are composed of combinations of resistors, capacitors, inductors, and constant phase elements, and are fitted to the experimental data using non-linear least-squares regression (Lasia, 2002; Zhang *et al.*, 2024).

For a passive metal surface, a common equivalent circuit includes a solution resistance R_s in series with a parallel network consisting of a charge transfer resistance R_{ct} and a CPE to account for double-layer capacitance. In systems where a passive oxide film contributes significantly to impedance, an additional parallel resistance and capacitance pair—representing film resistance (R_f) and film capacitance (C)—is included (Lasia, 2002). The complete circuit may be expressed as (Lasia, 2002):

$$Z(\omega) = R_s + \frac{1}{\frac{1}{R_f} + j\omega C} + \frac{1}{\frac{1}{R_{ct}} + (j\omega)^n T} \tag{1.36}$$

In this model, the CPE is described by two parameters: the magnitude T (in Ω^{-1}) and the exponent n, which varies between 0 and 1. When $n = 1$, the CPE behaves as a pure capacitor; when $n = 0.5$, it approximates Warburg impedance; and when $n = 0$, it behaves as a resistor. The values of R_{ct} and T extracted from the model fitting can be correlated with corrosion resistance, passive film integrity, and the roughness or heterogeneity of the electrode surface (Lasia, 2002; Macdonald *et al.*, 2018; Zhang *et al.*, 2024).

Model selection must be based not only on statistical goodness-of-fit but also on physical realism. For example, an overly complex circuit may fit the data well numerically but fail to correspond meaningfully to actual electrochemical processes. Therefore, model development should be guided by prior knowledge of the system, experimental observations, and mechanistic hypotheses (Lasia, 2002; Zhang *et al.*, 2024). Figure 1.27 shows typical Nyquist and Bode plot from EIS results.

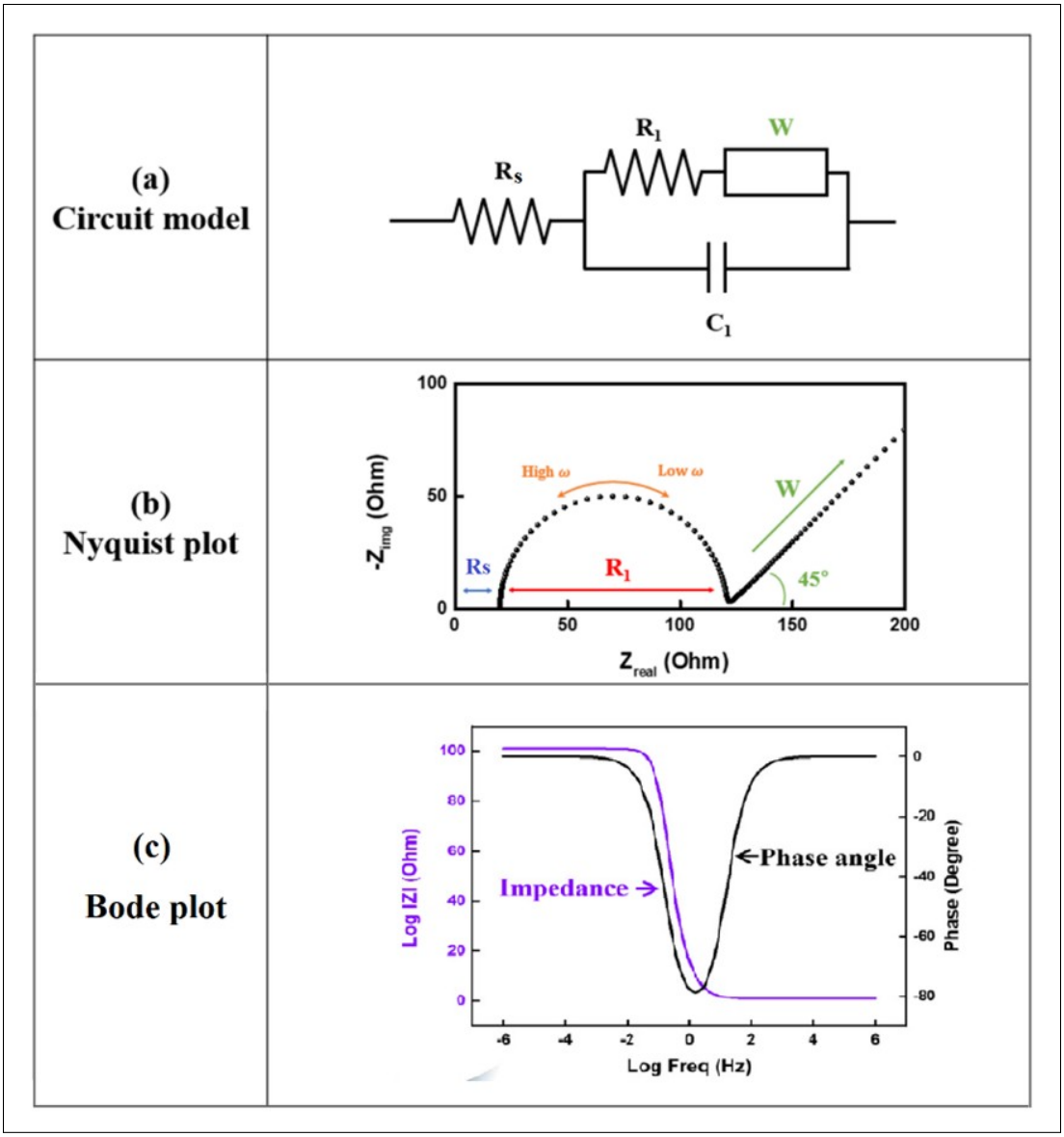

Figure 1.27 (a) Equivalent circuit used to fit EIS data for passivated metal surfaces and Typical (b) Nyquist and (c) Bode plots for a passive metal electrode in an electrolyte Taken from Choi *et al.* (2020, p. 3 and 5)

1.6.4.1 Passivity

Metals generally exhibit a high level of reactivity when exposed to common environmental conditions, such as humid air, elevated temperatures, or aqueous solutions containing salts,

acids, or bases. However, many metals form a protective oxide layer upon exposure to dry, clean air, preventing further corrosion. This naturally occurring thin film limits the passage of ions and slows down further degradation, a phenomenon known as *passivity* (Hoar, 1967).

Passivity is best understood by examining the anodic behavior of metals under electrochemical conditions. When a metal is exposed to an oxidizing environment, its dissolution follows an exponential rate increase, known as active corrosion. However, at a specific anodic potential, the dissolution rate drastically declines as a stable oxide layer forms. This transition from an active to a passive state results in a corrosion rate reduction by several orders of magnitude, typically between 10^3 to 10^6 times (Uhlig, 1978; Sheir *et al.*, 1994).

The passive behavior of metals is commonly analyzed using polarization studies. The critical anodic current density (i_c) indicates the highest dissolution rate before passivity begins, followed by a passive region where current density remains low and stable. However, at very high potentials, the passive film can deteriorate, leading to a renewed increase in metal dissolution in what is referred to as the *transpassive* region (Figure 1.28) (Uhlig, 1978).

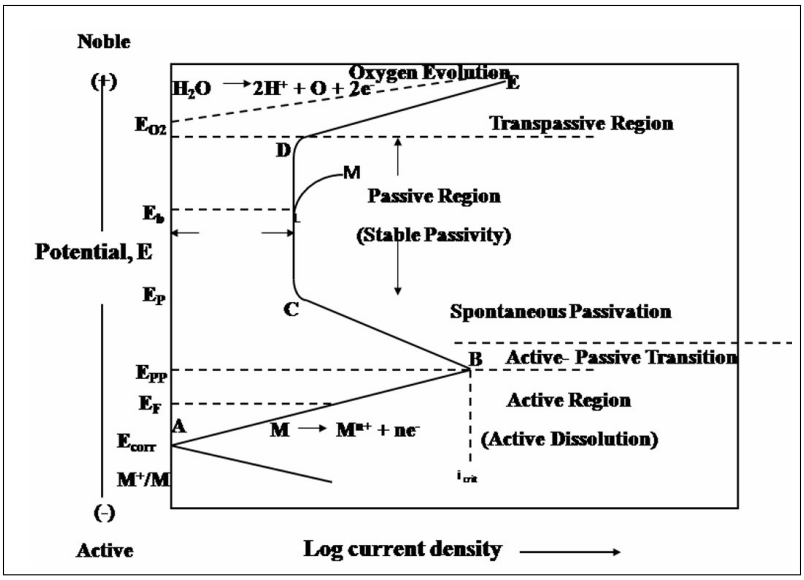

Figure 1.28 Typical anodic dissolution behavior of an active-passive metal
Taken from Dhawan *et al.* (2020, p. 22)

Two prevailing theories explain the mechanism of passivity (Uhlig, 1978):

1. **Oxide-Film Theory**: This perspective suggests that a passive metal is protected by an adherent, diffusion-resistant oxide layer. The oxide film acts as a barrier, restricting ionic and electronic transport between the metal and the environment, thus lowering the corrosion rate.
2. **Adsorption Theory**: This theory posits that passivity arises due to adsorbed oxygen or other species on the metal surface. This chemisorbed layer alters the electrochemical characteristics of the metal, preventing further dissolution. Even a monolayer of oxygen atoms has been observed to induce passivity.

1.6.5 1.5.6 Pitting Corrosion

Pitting corrosion is a highly localized form of corrosion that leads to the formation of cavities or pits on a metal surface. It primarily affects metals that rely on passivation for corrosion resistance, such as stainless steel and aluminum alloys. This degradation occurs when the passive film protecting the metal undergoes localized breakdown, exposing the underlying metal to aggressive environmental factors. The complexity of pitting corrosion stems from the variations in oxide film properties across different metals, including differences in electronic conduction, porosity, thickness, and hydration state (Frankel, 1998).

Many engineering materials are valued for their passive films, which significantly slow down corrosion rates. However, when these films fail, the localized attack accelerates the dissolution of the metal. If the attack occurs on an open surface, it is categorized as pitting corrosion, whereas in occluded sites, it is referred to as crevice corrosion (Frankel, 1998).

1.6.6 Mechanism of Pitting Corrosion

Pitting corrosion is an electrochemical process driven by localized anodic and cathodic reactions. Once a pit forms, the local conditions within it promote further pit growth, making the process autocatalytic (Szklarska-Smialowska, 1999).

The anodic reaction occurring within the pit is represented as:

$$\mathrm{M} \rightarrow \mathrm{M}^{n+} + ne^{-} \tag{1.37}$$

where metal (M) dissolves into the electrolyte, releasing metal cations.

Simultaneously, the cathodic reaction generally involves oxygen reduction:

$$\mathrm{O_2} + 2\mathrm{H_2O} + 4e^{-} \rightarrow 4\mathrm{OH}^{-} \tag{1.38}$$

As a result, the electrolyte inside the pit becomes more acidic due to hydrolysis:

$$\mathrm{M}^{n+} + \mathrm{H_2O} \rightarrow \mathrm{M(OH)}^{(n-1)+} + \mathrm{H}^{+} \tag{1.39}$$

This reduction in pH within the pit accelerates corrosion, while the surrounding metal surface acts as a cathode, sustaining the electrochemical reaction (Galvele, 1981).

The breakdown of the passive film is often attributed to one of the following mechanisms:

- **Film penetration model:** Chloride ions penetrate the passive film, disrupting its protective properties.
- **Film breaking model:** Local mechanical or chemical defects lead to the rupture of the passive layer.
- **Adsorption model:** Chloride ions adsorb onto the metal surface, destabilizing the passive film and initiating pit formation.

Once the pit forms, chloride ions migrate inward due to electromigration, sustaining high local acidity and preventing repassivation (Strehblow, 2002).

Pitting corrosion progresses through several distinct stages:

- **Passive Film Breakdown:** Local defects in the passive film initiate corrosion.

- **Metastable Pitting:** Small pits form and either repassivate or grow into stable pits.
- **Stable Pit Growth:** The pits develop in size, deepening into the metal.
- **Pit Stifling or Death:** Some pits may repassivate if local conditions become unfavorable for corrosion.

The resistance of an alloy to pitting is heavily dependent on its chemical composition. Chromium plays a crucial role in passivation, and an increase in chromium concentration above 13% enhances resistance to pitting (Figure 1.29). Additional alloying elements, such as molybdenum and nitrogen, further improve resistance.

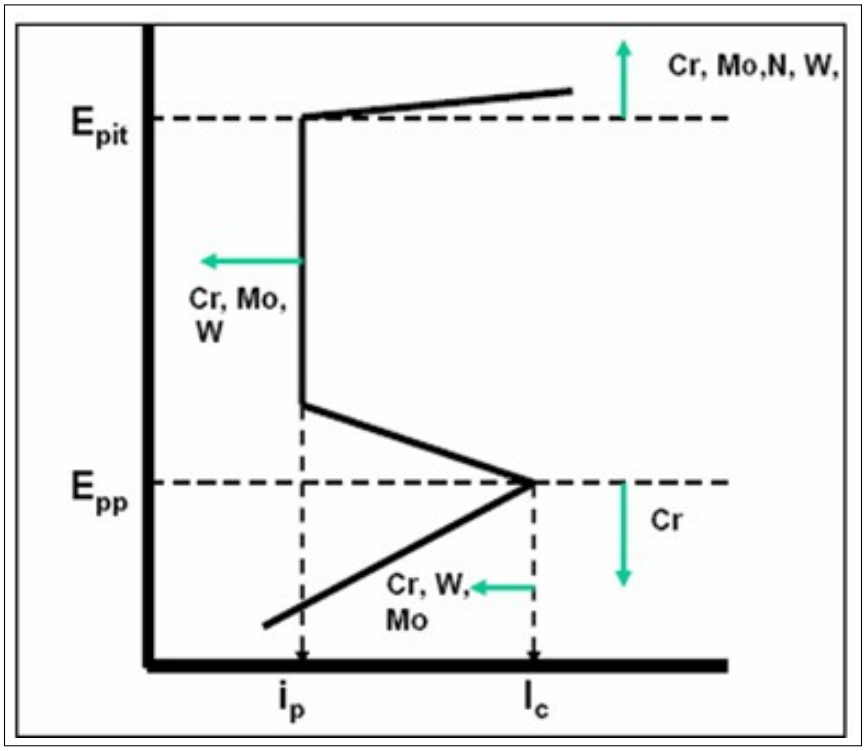

Figure 1.29 Effect of alloy chemical composition on pitting corrosion resistance
Taken from Abood (2008, p. 30)

Ha et al. (Ha *et al.*, 2018) concluded that the addition of Mo improves the alloy's resistance to pitting corrosion by enhancing the protectiveness of the passive film and reducing the pit propagation rate.

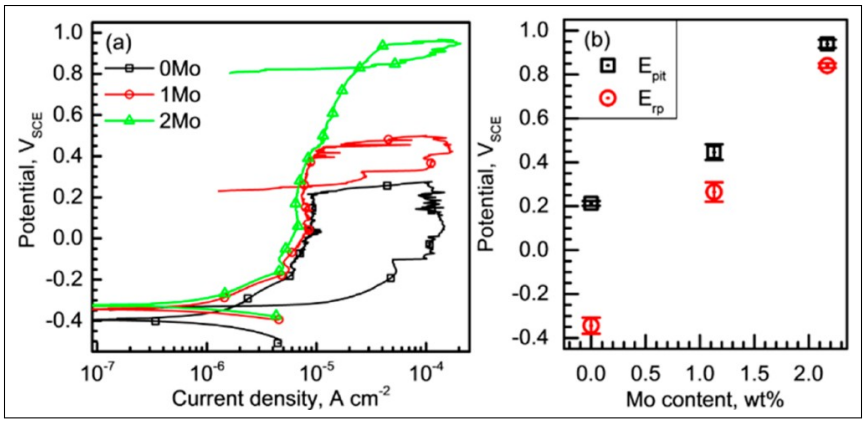

Figure 1.30 Effect of Mo on pitting corrosion resistance in 4 M NaCl solution for FeCrMnMoNC Austenitic Stainless Steels
Taken from Ha *et al.* (2018, p. 5)

Ha et al. (Ha *et al.*, 2022) found that the Fe–12Al–19Mn–1.5–5Cr alloy exhibited the highest pitting corrosion resistance, surpassing Fe–11Cr stainless steel, with Cr additions up to 5 wt% enhancing resistance, while higher Cr content and secondary phase formation reduced it by acting as pit initiation sites.

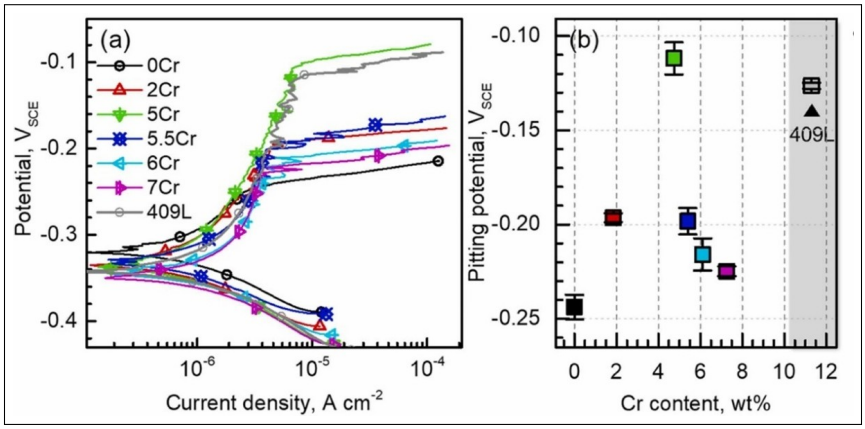

Figure 1.31 Effect of %Cr on pitting corrosion in austenitic Fe–19Mn–12Al–1.5C lightweight steel
Taken from Ha *et al.* (2022, p. 5)

The external environment significantly impacts pitting corrosion:

Temperature: Higher temperatures increase the likelihood of passive film breakdown, leading to accelerated pitting. Klapper et al. (Klapper *et al.*, 2013) studied the pitting corrosion resistance of CrMn austenitic stainless steel under simulated drilling conditions, focusing on the effects of pH, temperature, and chloride concentration. As shown in figure 1.32 , an increase in temperature led to a decrease in both the pitting potential and the repassivation potential, indicating a higher susceptibility to pitting corrosion at elevated temperatures.

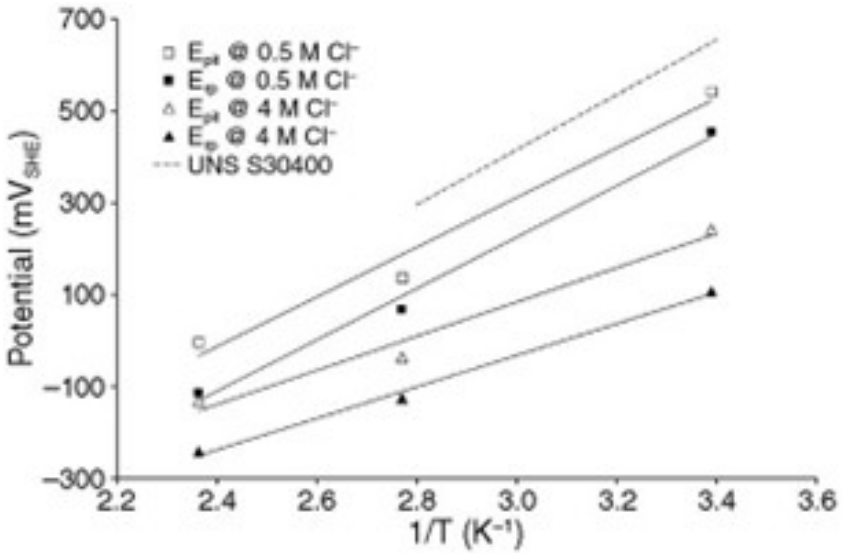

Figure 1.32 Effect of temperature on pitting corrosion of CrMn stainless steel
Taken from Klapper *et al.* (2013, p. 1101)

Ezuber et al. (Ezuber *et al.*, 2017) investigated the role of thiosulfate in the pitting corrosion susceptibility of AISI 316L stainless steel in a 3.5% NaCl solution. Their study revealed that AISI 316L SS experienced pitting corrosion in a 0.6 M NaCl solution, with pitting intensity increasing as the electrolyte temperature rose from 25°C to 80°C.

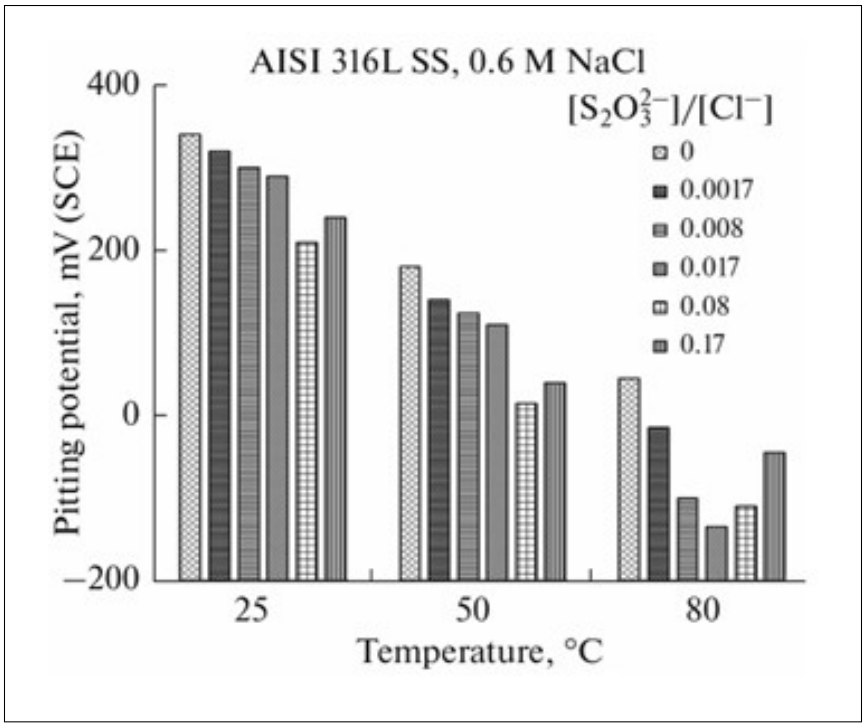

Figure 1.33 Effect of temperature on pitting corrosion of AISI 316L SS in $S_2O_3^{2-}/Cl^-$ solution
Taken from Ezuber *et al.* (2017, p. 497)

Surface Condition: Wang et al. (Wang *et al.*, 2024b) studied the effect of surface roughness on the corrosion of HP-13Cr stainless steel in a dynamic oilfield environment, revealing that pitting profiles resemble peaks and troughs with high aspect ratios, where turbulent vortices influence pit expansion along the flow direction; as pit depth increases, reduced vortex velocity inhibits Fe^{2+} diffusion, leading to localized acidification at the pit bottom and promoting vertical over horizontal pit growth, ultimately forming a shallow-disk morphology.

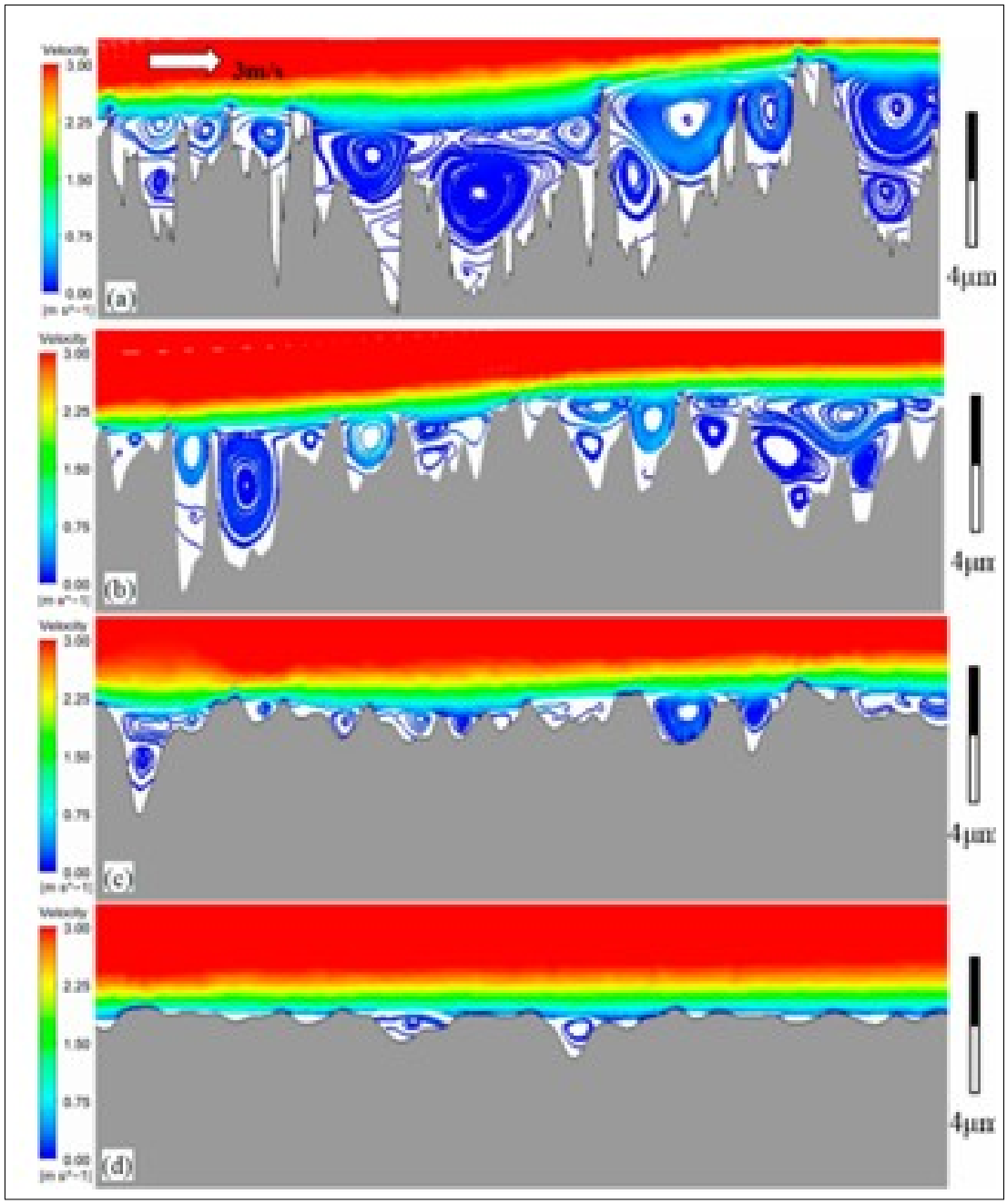

Figure 1.34 Velocity distribution cloud map at 3 m/s and 150°C/3.6 MPa in HP-13Cr stainless steel with varying surface roughness: (a) 120 grit, (b) 240 grit, (c) 600 grit, (d) 1000 grit
Taken from Wang *et al.* (2024b, p. 15)

Grain Size: Zhao et al. (Zhao *et al.*, 2022) Investigated the influence of grain size on the mechanical properties and corrosion behavior of metastable austenitic stainless steel. The study revealed that reducing the austenite grain size from 3.6 μm to 360 nm significantly enhanced the steel's corrosion resistance in a 3.5 wt% NaCl solution. As the grain size decreased, the pitting corrosion resistance improved, with the ultrafine-grained (UFG) steel exhibiting the highest resistance. This was attributed to its higher pitting potential (−64.4 mV vs. SCE) and greater overall polarization resistance (117.66 k$\Omega \cdot cm^2$)(figures 1.35 and 1.36).

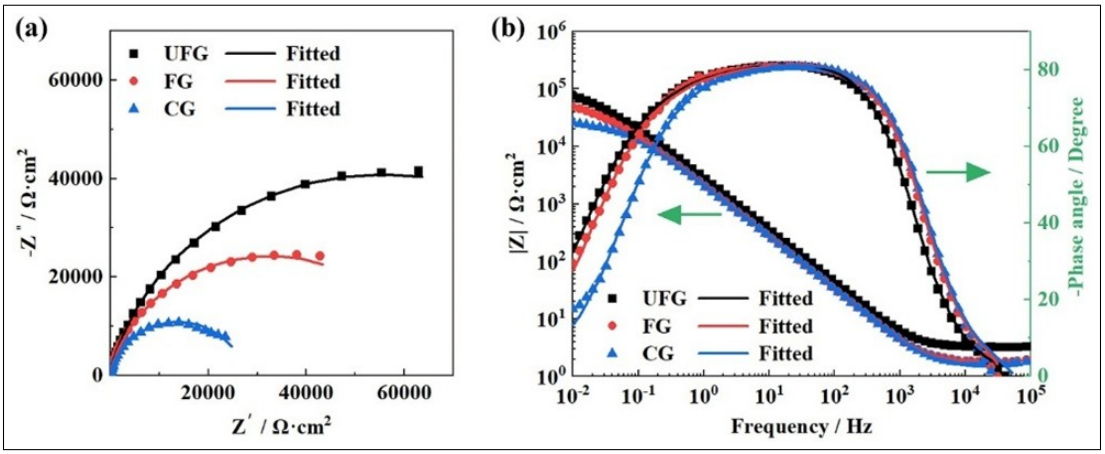

Figure 1.35 (a) Nyquist and (b) Bode plots for different grain sizes in 3.5 wt% NaCl solution
Taken from Zhao *et al.* (2022, p. 6)

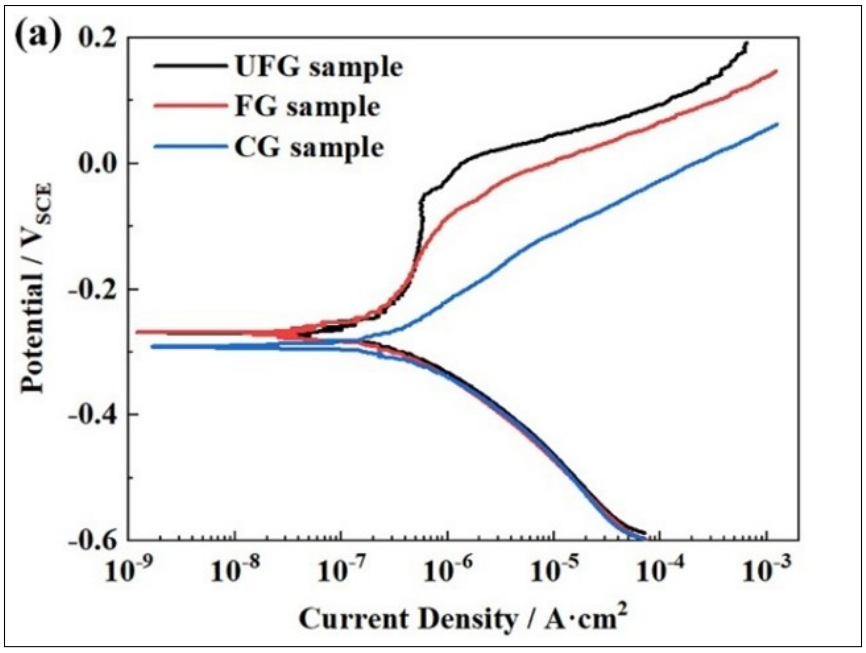

Figure 1.36 Potentiodynamic polarization curves for different grain sizes in 3.5 wt% NaCl solution
Taken from Zhao *et al.* (2022, p. 5)

1.7 Computational and Experimental Studies on Temperature Distribution During Welding 316L SS

Experimental testing is often time-consuming and costly for industries; therefore, simulation is recommended as an alternative. Modeling is utilized to analyze temperature distribution and residual stress in the weld zone and heat-affected zone (HAZ) during and after various welding processes, including GMAW, FCAW, and GTAW. The thermo-mechanical behavior of thin-walled pipelines can be examined using finite element (FE) analysis. To ensure accuracy, FE analysis of welding must account for temperature-dependent material properties, stress and strain behavior, structural deformations, phase transformations, and creep phenomena, which are inherent complexities of the arc welding process (Malik, Qureshi, Dar & Khan, 2008).

In recent decades, FE simulation has emerged as a powerful tool for analyzing temperature distribution in welding processes. Numerous simulation and experimental studies have been

conducted, particularly on circumferential welding, to examine temperature variations. Due to the highly concentrated heat source, regions near the weld zone are subjected to a wide range of temperatures, leading to discoloration in the weld metal (Malik *et al.*, 2008).

Ravisankar et al. (Ravisankar *et al.*, 2014) have evaluated residual stress and thermal gradients during gas tungsten arc welding by means of the FE method using SYSWELD. The temperature decreases with measurement locations longitudinally away from the weld center. It is observed that the temperature increases with increasing weld speed and power at the same heat input across all locations (Figure 1.37).

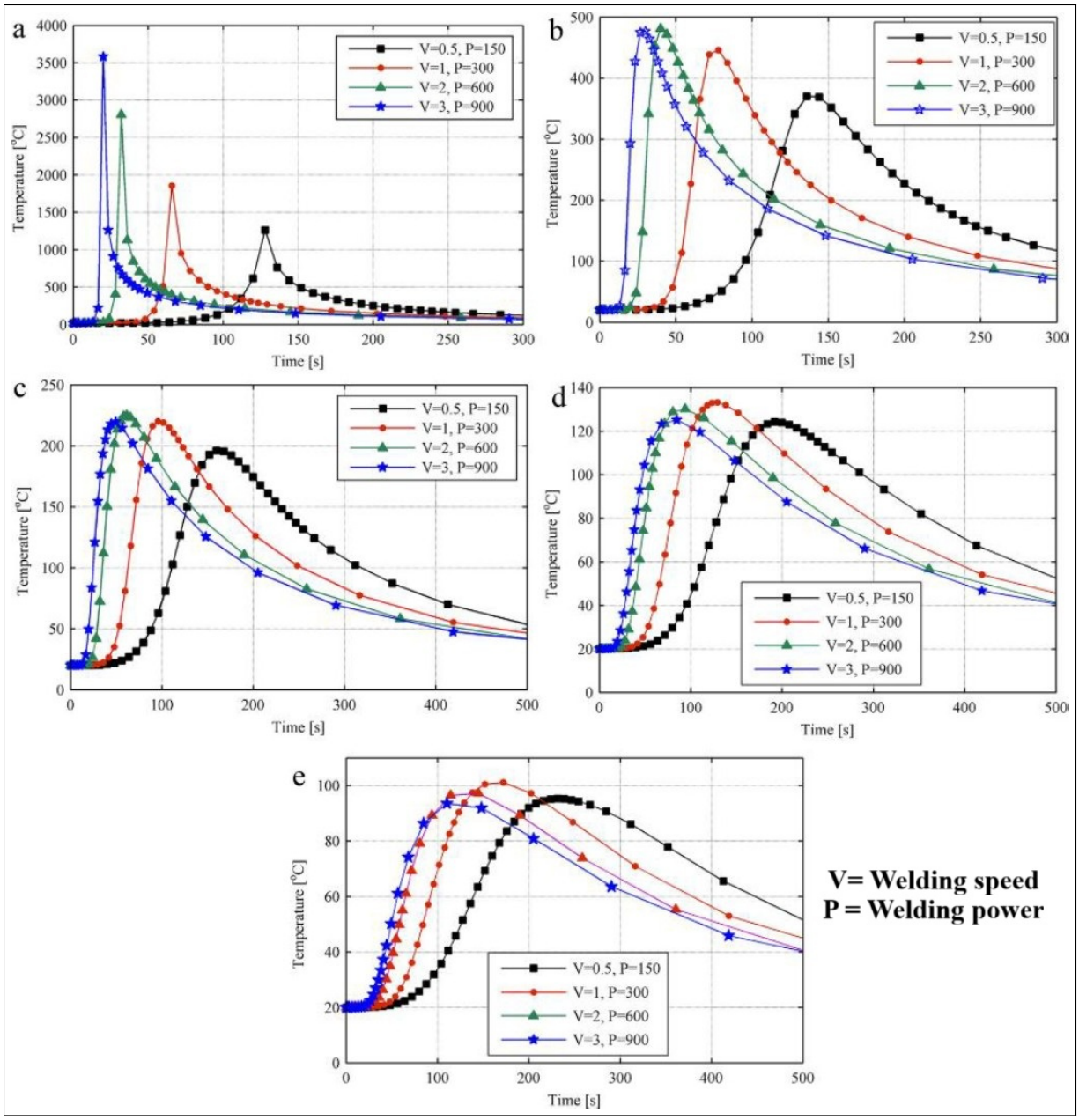

Figure 1.37 Comparison between simulated transient thermal cycles for four different cases at different locations longitudinally away from weld center: (a) weld center, (b) 10 mm, (c) 20 mm, (d) 30 mm, and (e) 40 mm
Taken from Ravisankar *et al.* (2014, p. 205)

Tarak (Tarak, 2013) studied residual stresses and thermal distribution in GTAW of austenitic stainless steel pipes using SYSWELD. The temperature profile and distribution, illustrated in

Figure 1.38 and Figure 1.39, show that the peak temperature reaches approximately 2150°C at the weld center one second after welding, with the HAZ extending up to 12 mm. The HAZ reaches its maximum width of 24 mm from the weld center at 7.5 seconds after welding.

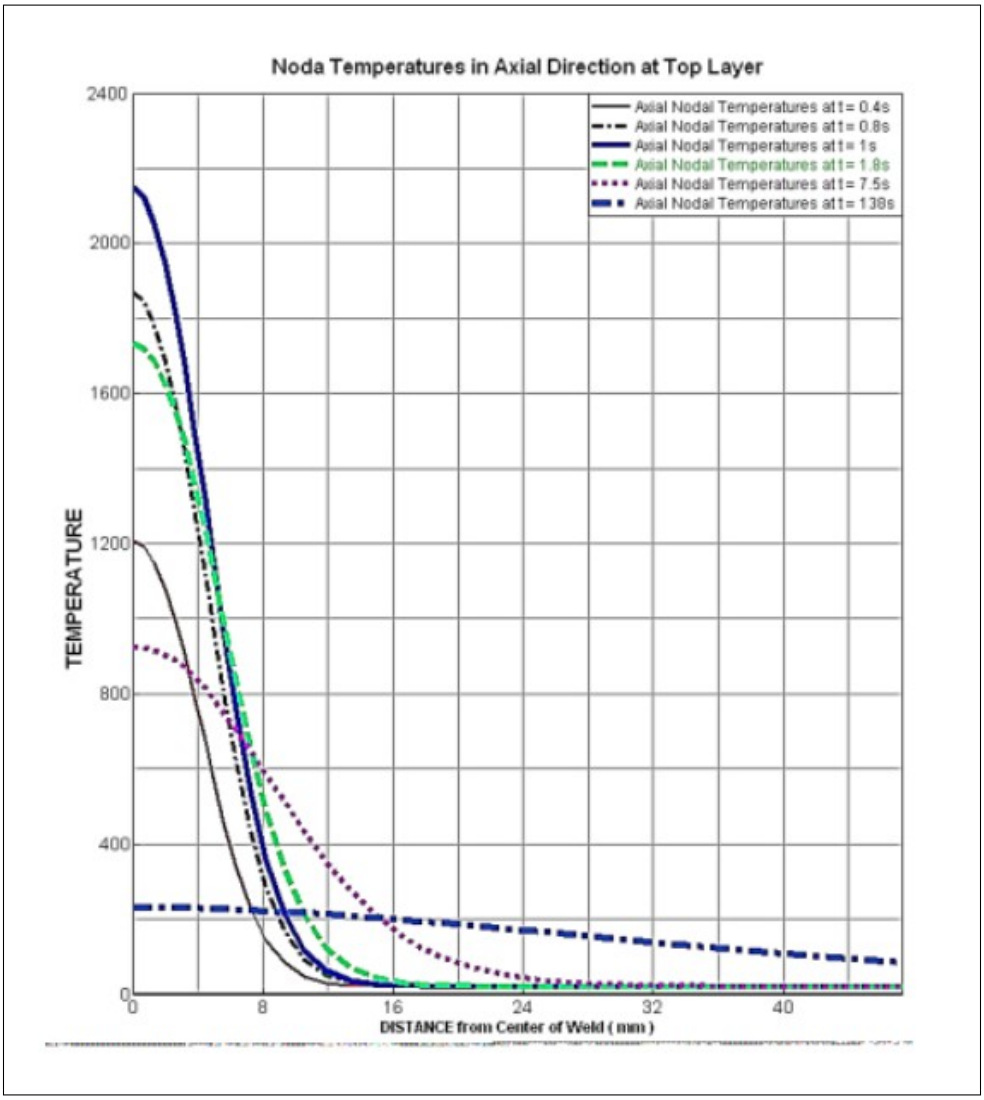

Figure 1.38 Nodal temperature (°C) in the axial direction at the outside surface of the pipe
Taken from Tarak (2013, p. 39)

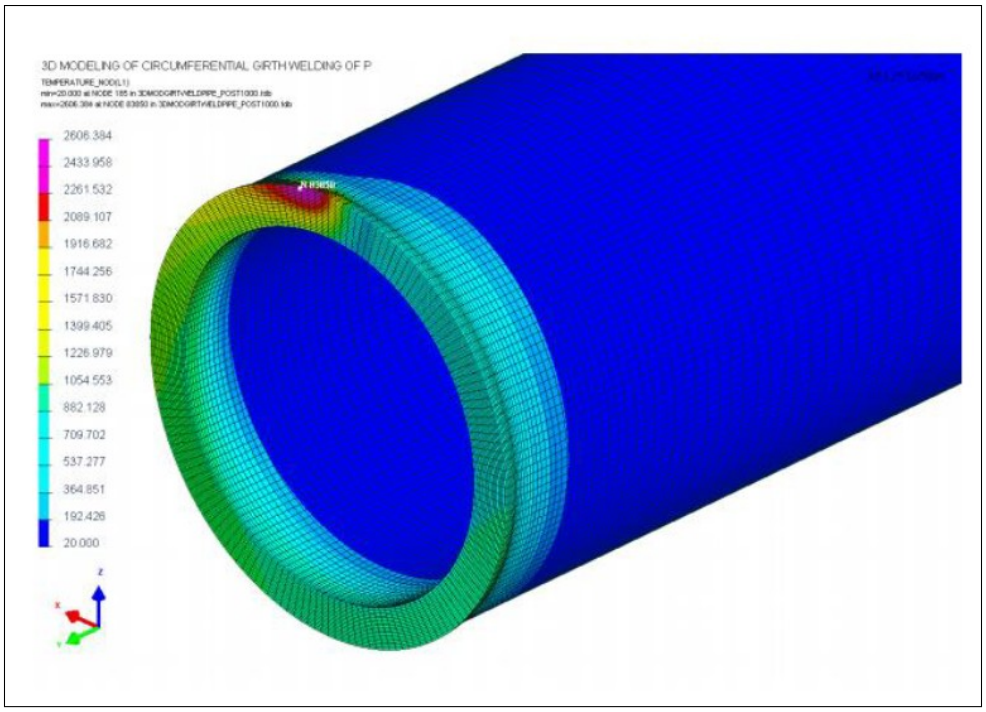

Figure 1.39 Temperature distribution (°C) during welding at time t = 25.5 seconds
Taken from Tarak (2013, p. 49)

1.8 Research Gap and Contribution of This Work

A review of the existing literature on AISI 316L stainless steel reveals substantial insights into high-temperature oxidation, welding thermal effects, and pitting corrosion. However, several critical gaps remain unaddressed, which this thesis directly confronts:

1. **No comprehensive study on the combined effect of oxygen content in backing gas and surface roughness on corrosion resistance:** Previous works have independently studied oxygen concentration (Trigwell & Selvaduray, 2005) and surface roughness (Nowak, 2020; Jaffré *et al.*, 2021a) on oxidation or corrosion. However, their combined influence, especially on pitting corrosion behavior in welded stainless steel, remains unexplored.
   → This study is the first to systematically assess the combined effect of oxygen content (50 to 5000 ppm) and surface roughness (40 vs. 60 grit) on corrosion resistance, filling this significant gap.

2. **Lack of corrosion studies on the discoloration zone with oxide layer intact under real environmental conditions:** Most previous investigations polish or remove the oxide layer before testing corrosion properties, thereby losing the real effect of welding-induced oxide scales.

   → This work uniquely evaluates corrosion behavior of the as-formed discoloration zone without oxide removal, better representing field conditions and industrial reality.

3. **No detailed investigation of GTAW discoloration and oxidation in multipass pipeline welding conditions:** Existing GTAW oxidation studies often focus on single-pass welds or small-scale samples. The influence of repeated thermal cycling on oxide structure and corrosion behavior in pipeline-grade multipass GTAW welds is poorly understood.

   → This thesis explores oxidation and corrosion response of multipass-welded 316L pipeline specimens, addressing the thermal complexities found in real fabrication.

4. **Absence of integrated simulation linking oxygen and temperature distributions to oxide growth in discoloration zones:** Finite element studies (Tarak, 2013; Ravisankar *et al.*, 2014) simulate temperature fields during welding but omit oxygen transport and oxide thickness prediction.

   → This study introduces a coupled simulation framework modeling temperature and oxygen distribution in the backing gas to predict oxide layer thickness on the back side of welds.

5. **No kinetic studies using isoconversional model-free methods for oxidation of 316L discoloration layers:** While oxidation kinetics are well-characterized using parabolic laws, few studies quantify activation energy in the discoloration zone using rigorous techniques such as k_p.

   → This thesis calculates oxidation activation energy using isoconversional and model-free methods, establishing a quantitative basis for oxide layer growth.

6. **Scarcity of electrochemical testing directly applied to discolored weld zones in 316L:** EIS and cyclic polarization have been extensively used in corrosion studies, but not specifically for evaluating passive film stability and pit resistance in the discolored GTAW regions.

→ This study performs EIS and cyclic polarization on the back side of GTAW welds, revealing the electrochemical behavior of as-formed oxides under real exposure conditions.

7. **No integrated comparison across oxide morphology, roughness, activation energy, electrochemical behavior, and welding parameters in discolored zones:**
   → This research presents a complete framework linking oxide microstructure, roughness, oxide thickness (via simulation), and electrochemical corrosion performance, thus offering a holistic understanding of discoloration-driven degradation mechanisms in GTAW-welded 316L.

CHAPTER 2

MATERIAL AND METHODS

2.1 Materials

The specimens utilized in this study were fabricated from AISI 316L stainless steel (SS) and were provided by PCL Construction in Edmonton, Alberta, Canada. The material received was in the form of a 154.4 mm (6-inches) pipeline with a base metal thickness of 7 mm and as-weld material.

The chemical composition of the alloy was determined using a SPECTROMAXx LMF08 (Ametec, Kleve, Germany) (Figure 2.1, Figure 2.2). Each measurement was conducted five times to validate the results, ensuring high accuracy and repeatability. The detailed chemical composition is presented in Table 2.1.

Figure 2.1 SPECTROMAXx LMF08 (Ametec, Kleve, Germany)

Figure 2.2 Spectrometer sample

Table 2.1 Chemical composition of 316L SS (wt%)

Element	C	Mn	Si	P	S	Mo	Cr
Amount	0.02	0.97	0.43	0.28	0.001	2.05	16.47
Element	Ni	Al	Co	Cu	W	N	Other
Amount	11.37	0.0162	0.22	0.25	0.073	0.093	0.13

To provide a visual reference of the received material, Figure 2.3 presents images of the half-pipe section used in this study.

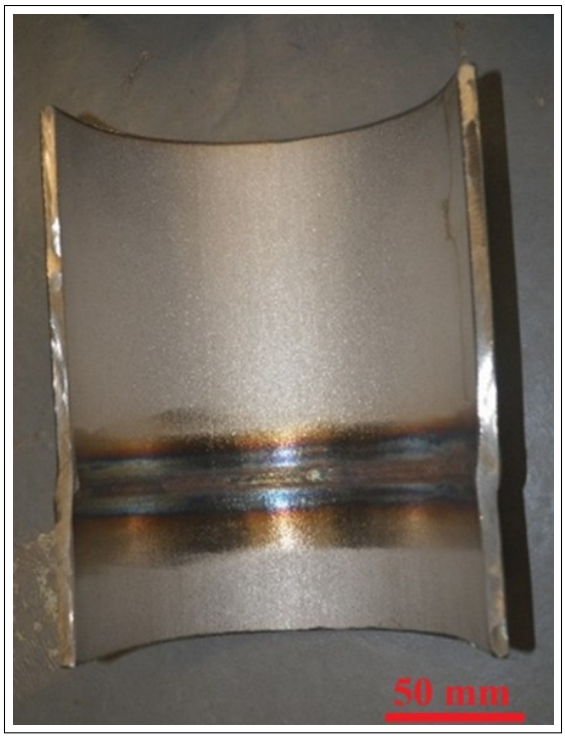

Figure 2.3 As weld samples

2.1.1 Specimen Preparation Before Welding

The specimens were mechanically prepared using two different grinding discs, specifically 40-grit and 60-grit (as shown in Figure 2.4). Following the buffing process, surface roughness measurements were conducted using a Keyence VR2500 3D scanner (KEYENCE CANADA INC, Mississauga, ON, Canada) (Figure 2.5). The Ra (average roughness) values were obtained from 120 measurements per grit size. The roughness measurements recorded were 2.29 ± 0.14 μm for the 60-grit samples (B2) and 2.80 ± 0.32 μm for the 40-grit samples (B1). Representative 3D and line-profile surface roughness images are illustrated in Figure 2.6.

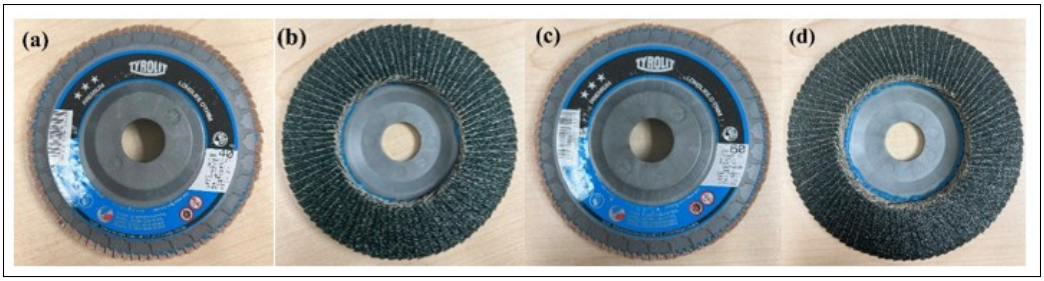

Figure 2.4 Grinding disc for buffing before welding: (a, b) 40-grit, (c, d) 60-grit

Figure 2.5 Keyence VR2500 3D scanner

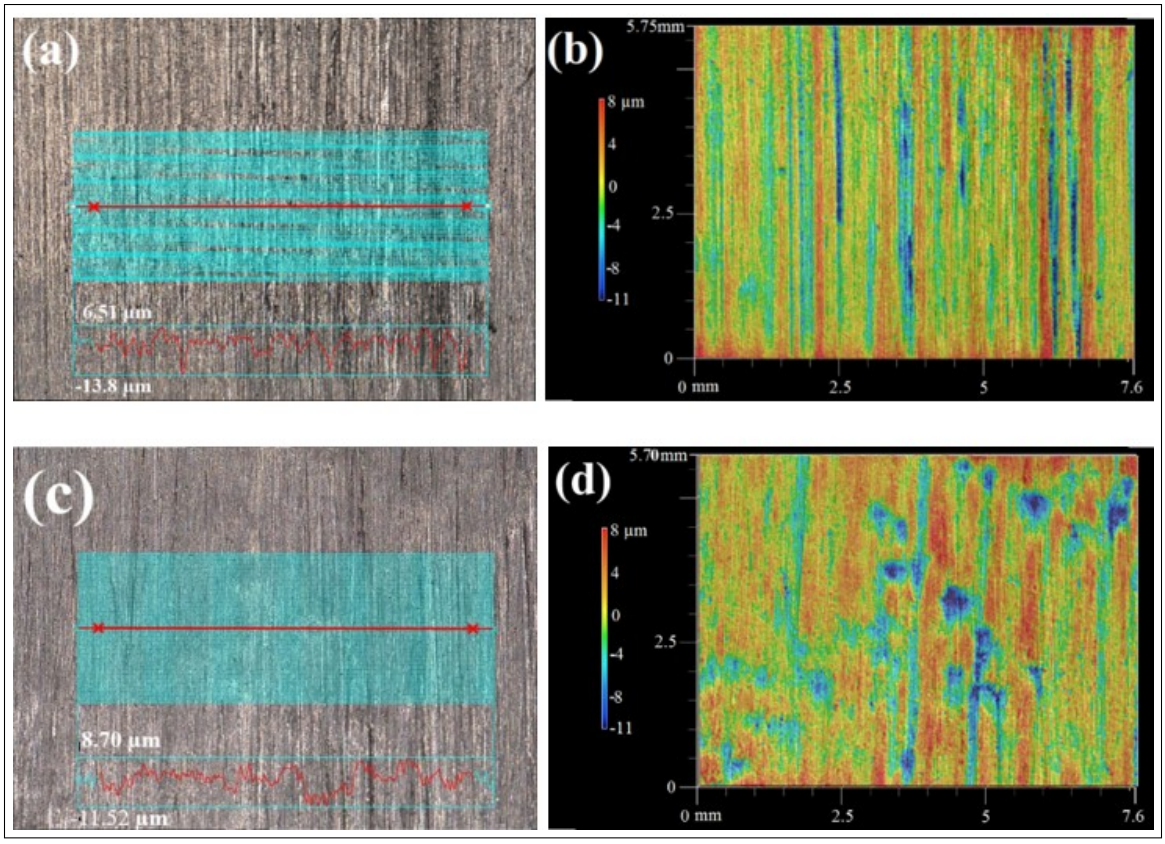

Figure 2.6 Multi-line surface roughness profile of a buffed sample: (a) 60-grit, (c) 40-grit. 3D surface roughness map of a buffed sample, showing the anisotropic texture and grooves formed during the abrasive process: (b) 60-grit, (d) 40-grit

2.2 Experimental Methods

2.2.1 Welding Process

The welding of 316L SS specimens was conducted using two different methods: GTAW and FCAW. To simulate actual industrial conditions, two distinct welding procedures were applied.The welding was performed in the 1G position, with the welding torch fixed in place and the pipe rotated during deposition, corresponding to an automated/mechanized welding setup.

In the first method, a multi-pass GTAW process was applied, involving four passes to replicate industrial welding conditions. The joint geometry is depicted in Figure 2.7, and the detailed welding parameters for each pass are listed in Table 2.2.

In the second method, GTAW was used for the root pass, followed by two FCAW passes for filling, making a total of three welding passes per specimen. The joint geometry is shown in Figure 2.8, and the detailed welding parameters for each pass are presented in Table 2.3.

Before welding, the interior (back side) of the pipe was purged with argon gas containing 50, 200, 500, and 5000 ppm oxygen. The oxygen gas was obtained from commercially available sources with varying degrees of argon purity, analyzed by Air Liquide. The purging process was carefully controlled and maintained until the target oxygen level was achieved, ensuring uniform conditions across all specimens. The purging gas composition is detailed in Table 2.4. Oxygen concentration was continuously monitored using the PurgEye 300 instrument (Huntingdon Fusion Techniques, HFT, Carms, Wales) to maintain precise gas levels. In both methods, the pipe was sealed at both ends, with inert gas introduced from one side and oxygen concentration measured at the opposite end to maintain a controlled welding environment. Welding equipment condition is shown in Figure 2.9.

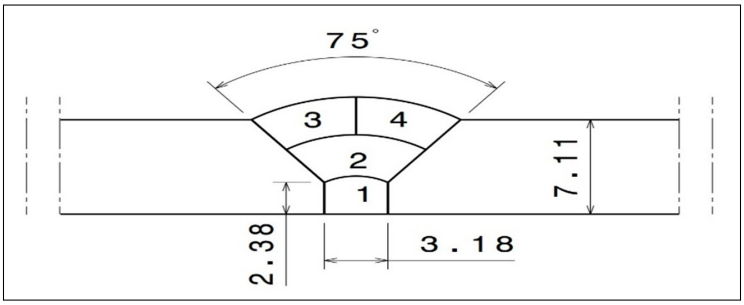

Figure 2.7 Weld zone geometry: 4 passes of GTAW (dimensions in mm)

Table 2.2 Welding parameters for 316L SS samples (4 passes of GTAW)

Process	**GTAW**	**GTAW**	**GTAW**	**GTAW**
Pass	1	2	3	4
Shielding gas	Ar	Ar	Ar	Ar
Purge gas flow rate (CFH)	40	40	40	40
Current (A)	125–202	166–215	200–223	208–243
Voltage (V)	10.6–14	11.8–15.7	12.8–16.4	13.8–16.4
Tube to work distance (mm)	9.52	9.52	9.52	9.52
Heat Input (kJ/mm)	1.31	1.17	1.28	1.44
Filler material	ER316L (Exocor)	ER316L (Exocor)	ER316L (Exocor)	ER316L (Exocor)

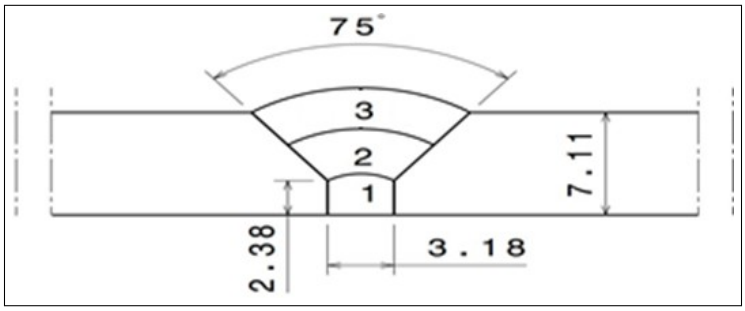

Figure 2.8 Weld zone geometry for FCAW + GTAW (dimensions in mm)

Table 2.3 Welding parameters for 316L SS samples (FCAW + GTAW)

Process	**GTAW**	**FCAW**	**FCAW**
Pass	1	2	3
Shielding gas	Ar	Ar	Ar
Purge gas flow rate (CFH)	30	40	40
Current (A)	170 ± 20	236 ± 20	262 ± 20
Voltage (V)	12.6 ± 1	29.5 ± 1	29.5 ± 0.2
Tube to work distance (mm)	9.52	9.52	9.52
Heat Input (kJ/mm)	1.24	0.87	1.18

Table 2.4 Purging gas concentrations

Oxygen content (ppm)	**Component**
50	Ar + 0.005% O_2
200	Ar + 0.02% O_2
500	Ar + 0.05% O_2
5000	Ar + 0.5% O_2

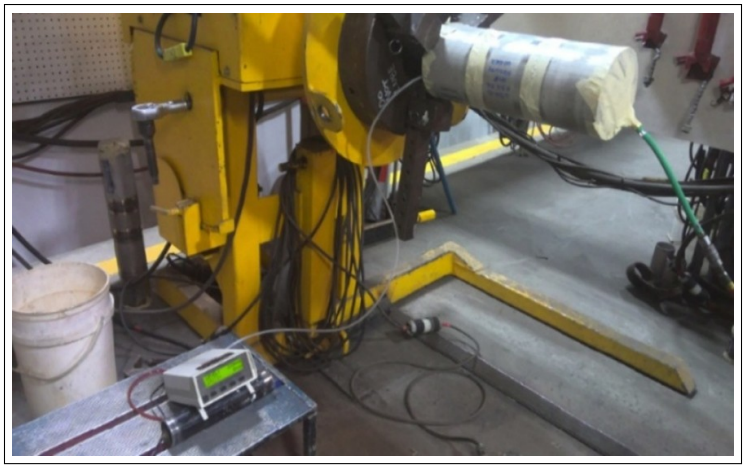

Figure 2.9 Welding process setup

Figure 2.10 presents as-welded pipe samples received from PCL. Images (a–d) depict samples welded with four passes of GTAW, while images (e–h) correspond to samples welded with two passes of FCAW plus a root pass of GTAW. Additionally, (a, e), (b, f), (c, g), and (d, h) represent samples exposed to backing gas with oxygen contents of 50, 200, 500, and 500 ppm, respectively.

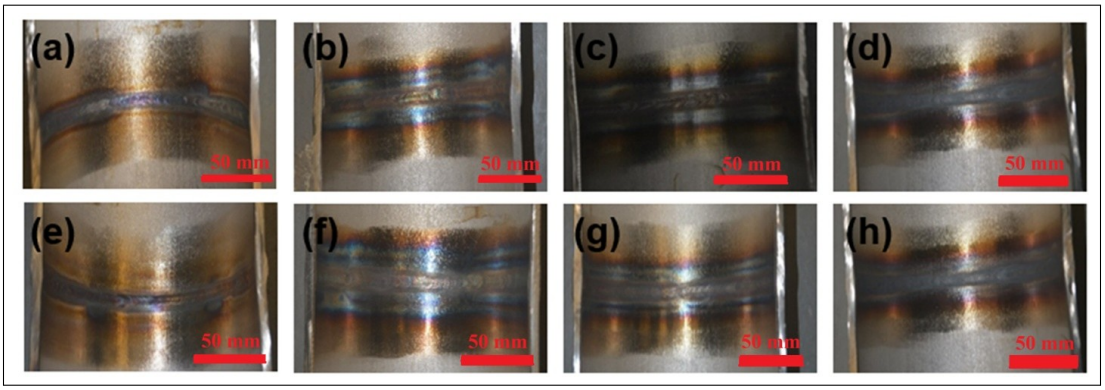

Figure 2.10 As-weld samples from PCL: (a–d) 4 passes of GTAW, (e–h) 2 passes of FCAW + root pass of GTAW, at different oxygen levels (50–5000 ppm)

2.2.2 Microstructural characterization

Discoloration images were acquired using a Keyence VR2500 3D scanner to examine the oxide layer formed during welding. To analyze the oxide layer morphology, Scanning Electron Microscopy (SEM) was conducted using two high-resolution instruments: the Hitachi TM3000 SEM and the Hitachi SU8230 FE-SEM (Hitachi High-Tech Canada, Toronto, ON, Canada). Additionally, Electron Backscatter Diffraction (EBSD) was employed to analyze the grain structure of the welded specimens, providing insights into the crystallographic orientation and grain boundary evolution post-welding.

To preserve the oxide layers for analysis, samples were prepared using a combination of hot mounting resin and ion milling techniques. The sample preparation methodology followed an optimized procedure to maintain the structural integrity of the oxide layers in both cross-sectional and surface views. For the cross-section part, ion milling was conducted for 2 h at 6 kV with a speed of 60 reciprocations per minute and a swing of ±15 degrees. This was followed by 1 h of ion milling at 5 kV with a speed of 30 reciprocations per minute and a swing of ±30 degrees. For the surface ion milling, a 3 min process was carried out at 5 kV with 15 reciprocations per minute and a swing of ±60 degrees. In order to prepare the sample surface for analysis, the IM4000 Plus ion milling Hitachi machine was utilized, allowing for precise surface preparation and optimal imaging quality. Figure 2.11 provides a schematic representation of the ion milling process used for precise oxide thickness determination and also samples for ion milling.

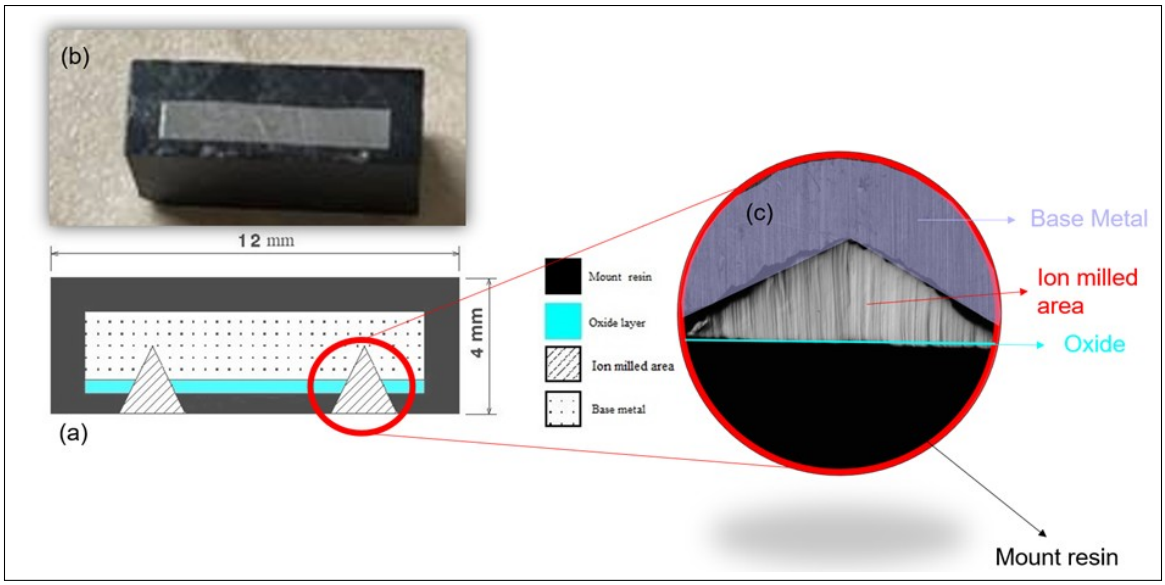

Figure 2.11 (a) Schematic showing the ion mill regions of the samples, (b) Ion milled sample, (c) Ion milled area

To find the composition of each distinct zone within the discoloration, XRD measurements were conducted. This method enables to discern the constituent phases in various locations across the discoloration zones. The PANalytical X'pert Pro X-ray diffractometer was used, equipped with Co (Kα) radiation (wavelength: 1.78896 Å) at operating conditions of 40 mA and 45 kV. The diffraction patterns were recorded over a 20° to 80° range with a 0.016° step size, ensuring detailed structural characterization. Each scan lasted 1 hour and 37 minutes to acquire high-resolution data.

To gain insights into the thermal behavior of the materials, hot-stage video microscopy analysis was conducted using a Mettler FP84HT hot stage with a Nikon Eclipse LV150N optical microscope. The samples were placed in a 7-mm quartz crucible and subjected to a controlled heating rate of 100°C per minute. During analysis, argon gas containing 5000 ppm oxygen was purged to simulate welding conditions. Data from this analysis was imported for further processing and interpretation, providing essential information on high-temperature transformations in the welded specimens. Figure 2.12 shows all equipment used for the characterization.

Figure 2.12 Characterization equipment: (a) Scanning electron microscopy TM3000, (b) Scanning electron microscopy SU8230, (c) X'Pert3 MRD PANalytical, (d) Mettler FP84HT hot stage with Nikon Eclipse LV150N, (e) IM4000 Plus ion milling machine (Hitachi)

2.2.3 Thermogravimetric Analysis (TGA)

TGA was performed using a Pyris Diamond TGA instrument (Figure 2.13) to analyze oxidation kinetics. Samples were heated up to 1200°C at a rate of 30°C/min in air and argon containing 5000 ppm oxygen. The mass gain was plotted as a function of temperature, and oxidation kinetics were determined using iso-convectional and model-free methods for calculating activation energy (E_a).

Figure 2.13 Pyris Diamond TGA instrument

2.3 Corrosion Testing

2.3.1 Solution

Each sample was placed in a flask containing the test solution, 0.5 M NaCl and 0.5 M H_2SO_4.

2.3.2 Potentiodynamic Anodic Polarization (PAP)

Potentiodynamic anodic polarization (PAP) tests were conducted to determine the pitting potential (E_{pit}) of the discoloration zone. The testing followed the ASTM G5-13 standard,

ensuring accuracy and reproducibility. The test specimens were prepared with dimensions of 15 × 15 mm, with an exposed surface area of 1 cm^2 to the electrolyte solution.

Before polarization, the open circuit potential (OCP), also referred to as the corrosion potential, was recorded after a stabilization period of 300 seconds. The polarization scan started 50 mV below the OCP and increased up to 2000 mV (vs. Ag/AgCl) at a scan rate of 0.0016 V/s, following the literature recommendations (Kumar, Shahi, Sharma & Malhotra, 2021). Each test was performed at 23 ± 2°C, and three repetitions were conducted to ensure consistency in determining the average pitting potential (E_{pit}) for each condition.

The cell configuration was connected to an Autolab PGSTAT302N potentiostat/galvanostat (Metrohm, FL, USA) (Figure 2.14), controlled using ANOVA software v2.1.6 (Metrohm Autolab B.V, Utrecht, The Netherlands). The sample holder for the 316L SS specimen was sourced from Redox Company (Norrköping, Sweden), while the electrochemical cell, CE, and RE were obtained from Pine Research Inc.

Figure 2.14 Autolab PGSTAT302N potentiostat/galvanostat

2.3.3 Electrochemical Impedance Spectroscopy (EIS)

The EIS measurements were performed at open circuit potential (OCP) using an Autolab PGSTAT302N potentiostat/galvanostat (Metrohm, FL, USA), controlled via ANOVA software

v2.1.6. The data were collected across a frequency range of 0.1 Hz to 100 kHz, with an AC amplitude of 10 mV applied at the OCP.

2.4 Finite Element Modeling (FEM) of Temperature Distribution

A FEM simulation was conducted using ABAQUS to model the temperature distribution during the welding process. A Gaussian heat source model was applied, and temperature-dependent material properties were used to simulate heat transfer. All simulations related to oxygen distribution were performed by Fatemeh Jafari. Details regarding the FEM setup, including boundary conditions and meshing parameters, are provided in Section 6.3.1.

CHAPTER 3

INFLUENCE OF OXYGEN CONTENT IN THE PROTECTIVE GAS ON PITTING CORROSION RESISTANCE OF A 316L STAINLESS STEEL WELD JOINT

Mohammad Maroufkhani[a,*] , Soroosh Hakimian[b] , Alireza Khodabandeh[c] , Iulian Radu[d] , Lucas A. Hof[e] , Mohammad Jahazi[f,*]

[a,b,c,e,f] Department of Mechanical Engineering, École de Technologie Supérieure (ÉTS), 1100 Notre-Dame Street West, Montreal, QC, Canada H3C 1K3
[d] PCL Industrial Management Inc.,2107 4 St, Nisku, AB, Canada,T9E 7W6

Paper published in the journal "Materials" (MDPI), August 31, 2023
https://doi.org/10.3390/ma16175968

3.1 Abstract

Gas tungsten arc welding (GTAW) is commonly used for joining pipelines; however, it often leads to discoloration in the heat-affected zone (HAZ). In this study, 316L pipes were welded with different concentrations of oxygen present in the argon purge gas during welding. The objective of this study was to investigate the effect of oxygen concentration in the protective gas on the pitting corrosion resistance of the welded pipes.Experimental results showed that the thickness of the oxide layer formed in the HAZ depends on the concentration of oxygen in the protective gas. Increasing the oxygen concentration in the protective gas resulted in an increase in pitting corrosion resistance until a critical value, beyond which the resistance decreased. This decrease was attributed to the formation of iron oxide.

This study provides valuable insights for improving the corrosion resistance of welded pipes in the oil and gas industry.

Keywords: 316L SS; Pitting corrosion; Oil and gas pipeline; Discoloration; Oxygen concentration

3.2 Introduction

Although stainless steels (SS) are known for their good corrosion resistance, some industrial welded joints made of SS are prone to pitting corrosion. The presence of chloride ions can break down the passive film, leading to the formation of pits in both welded and non-welded SS. Pitting corrosion is considered one of the most dangerous types of corrosion due to its ability to cause localized damage and lead to sudden failures in equipment or structures (Revie, 2011; Dai *et al.*, 2020).

The welding process is a complex and intricate process that requires careful attention to various parameters. These parameters have a significant impact on the quality and performance of welded joints. Among the critical parameters that need to be monitored and controlled are voltage, current, welding speed, shielding and backing gas, as well as pre-and post-weld heat treatments (Yang *et al.*, 2012; Paulraj & Garg, 2016). Therefore, these parameters must be carefully monitored and adjusted to ensure the production of high-quality welded joints that meet the required performance standards (Chuaiphan & Srijaroenpramong, 2014; Mohammed, Ishak, Aqida & Abdulhadi, 2017).To this end, during welding, particularly for the root pass, it is necessary to remove air from the fusion zone by employing an inert purging gas on the back side of the weld (i.e., from the inside of the tube). It has been reported that the presence of oxygen at atmospheric concentration levels, i.e., about 210,000 ppm, can lead to the formation of an oxide layer on the surface of the weld root (Bergquist, Huhtala & Karlsson, 2011). Some authors reported that this oxide layer can lead to contamination that results in reduced mechanical properties and lower corrosion resistance in the weldments. Specifically, the occurrence of pitting corrosion in the HAZ of welded austenitic SS joints has been reported by many authors (Shirwaikar & GP, 1975; Bergquist *et al.*, 2011; TABAN, KALUC & AYKAN, 2014). To reduce and alleviate the susceptibility to pitting corrosion, Argon (Ar) has been used as a purging gas in GTAW of various austenitic SS. Although pure Ar would be the ideal option, the rising cost provides a strong incentive to switch to a lower purity option (Trigwell & Selvaduray, 2005).

The typically studied corrosion parameters include the passive current density (i_{passive}), passive potential (E_{passive}), pitting current density (i_{pit}), and pitting potential (E_{pit}) . The passive current density is defined as the current density required to maintain a passive film on the metal surface, the Epassive value indicates the passive potential for a given metal, which is the potential at which the metal surface becomes passive hence a protective oxide film forms, while the ipit and Epit values indicate the current density required to initiate localized corrosion in the form of pits on the metal surface and the potential at which the metal surface begins to undergo localized corrosion in the form of pits, respectively (Perez, 2016).

Ling et al. (Ling, Liu, Lu & Guo, 2019) studied the oxidation behavior of 304L during GTAW and found that without inert gas shielding, the surface near the weld oxidized at a higher rate.Specifically, they observed that the extent of oxidation increased as the distance to the fusion line decreased, leading to the growth of oxide film and cracks on the oxide film. The HAZ region mainly consisted of the Fe-Cr oxides and the oxidation extent and severity increased with the welding temperature (Ling *et al.*, 2019). Huang et al. (Huang *et al.*, 2020) found an outer layer of Cr_2O_3/Fe_2O_3 and an inner layer of $FeCr_2O_4$ in samples exposed at 400 °C, while at 600 °C , an oxide film with a Fe-rich outer layer and Cr-rich inner layer in 316L SS was observed. According to Xie et al. (Xie *et al.*, 2019)Fe and Cr oxide were detected in the oxide scale of 316L SS , while the high vacuum-generated initial oxide layer consisted of a Fe_3O_4 outer layer and an inner layer enriched with both Fe and Cr .

In the discoloration area of the weld zone, a range of colors from straw yellow to blue, purple, or even black is observed. The extent of colors is influenced by a combination of factors, including oxidation and temperature changes during welding (Kimbrel, 2011). One of the primary factors contributing to the colors observed in the HAZ is the formation of oxide layers on the metal surface (Kimbrel, 2011). The thickness and composition of the oxide layer can vary depending on factors such as the welding process, atmosphere, heat input, exposure time, and the specific metal being welded (Kimbrel, 2011). These oxide layers interact with light, resulting in selective absorption, reflection, and scattering of different wavelengths, leading to the observed colors (Macleod & Macleod, 2010).

Furthermore, the thickness of the oxide layer also influences the observed color. For example, it has been reported that thicker oxide layers can result in a broader range of colors, including blues, purples, and even black while thinner oxide layers appear as straw yellow or light shades (Pedrotti, 2008).

Equation 3.1 illustrates the Ray optic concept, where an incident light ray (I) interacts with the surface of an oxide layer. The incident ray splits into a reflected ray (R_1) and a transmitted ray (T_1) that passes through the oxide layer. Upon reaching the oxide layer/bulk material interface, the transmitted ray is reflected (RT_1) and travels back through the oxide layer before exiting into the air. The color observed depends on the optical path difference (OPD) between the reflected ray (R_1) and the transmitted-reflected ray (TRT_1). This path difference is determined by the refraction angle, which follows Snell's law (θ_2), the thickness of the oxide layer (t), the refractive index of the oxide layer (n_2), and the wavelength of light (λ). The refractive index (n_2) is wavelength-dependent, influencing the interference pattern (Pedrotti, 2008; Macleod & Macleod, 2010; Khafaji *et al.*, 2017).

$$\text{OPD} = 2 \cdot n_2(\lambda) \cdot t \cdot \cos(\theta_2) \tag{3.1}$$

In the case of oxide films, which could be composed by different layers of materials with different refractive indices, interference effects can occur, as the thickness of the thin film influences the optical path difference (Pedrotti, 2008; Macleod & Macleod, 2010). The optical path difference determines the phase relationship between the interfering waves, which, in turn, affects the resulting observed color. Depending on the film's thickness and the wavelength of the incident light, different colors will be determined (Pedrotti, 2008).

The current study aims to fill existing gaps in the literature by investigating the impact of oxygen content in the purging gas during GTAW on the discoloration levels of the root joint area and the pitting corrosion resistance of AISI 316L SS. Specifically, this research focuses on evaluating the pitting corrosion resistance of the steel without removing the discoloration.

The present study aims to investigate the critical value of oxygen impurity in argon backing gas, with a specific focus on its influence on pitting corrosion resistance. By identifying the optimum oxygen content for enhanced corrosion resistance, this research contributes to the development of practical solutions for industries seeking both effective welding outcomes and cost efficiency. The principal objective of this research is to quantify the impact of variations in oxygen content on the pitting corrosion resistance of the welded joint. Therefore, four different oxygen content levels in the backing gas were selected for the analysis. A combination of microscopic and chemical analysis methods, as well as thermodynamic modeling, were used to characterize the discoloration, then pitting corrosion tests were carried out and the oxide layers' nature and compositions were analyzed and the operating mechanisms are discussed. Finally, recommendations on operational conditions are proposed.

3.3 Materials and Methods

The specimens used in this work were made of 316L SS with a chemical composition (wt.%) as indicated in Table 3.1. The chemical composition was determined through the utilization of spectrometry, a technique well-regarded for its precision in analyzing material composition. The analysis process involved taking multiple measurements to ensure accuracy and repeatability. In fact, measurements were carried out five times to establish the reliability of the results. To perform the chemical composition determination, the SPECTROMAXx LMF08 (Ametec, Kleve, Germany) was employed. In this study, 316L SS specimens were welded using GTAW with varying concentrations of oxygen in the purging gas. The effect of oxygen content on the discoloration levels and pitting corrosion resistance of the root welded joints was investigated. The interior of the pipe was purged with argon gas containing specific oxygen concentrations, ranging from 50 to 5000 ppm. The thermodynamic software FactSage was used to predict the formation of possible phases based on oxygen content and temperature. Potentiodynamic anodic polarization tests were conducted to determine the pitting potential. Discoloration images were acquired using a 3D scanner, and the oxide layer was analyzed using scanning electron microscopy (SEM) with the help of mounting techniques and ion

milling methods. The detailed methodology and analysis procedures will be described in the subsequent paragraphs.

Table 3.1 Chemical composition of 316L SS (wt %)

Element	C	Mn	Si	P	S	Mo	Cr
Amount	0.02	0.97	0.43	0.28	0.001	2.05	16.47
Element	Ni	Al	Co	Cu	W	N	Other
Amount	11.37	0.0162	0.22	0.25	0.073	0.093	0.13

The pipe diameter was 154.4 mm (6 in) and the thickness of the base metal was 7.11 mm (0.285 in). GTAW was used for welding the 316L SS pipe. A total of four (4) passes were applied for welding to be as close as possible to the actual industrial conditions. The joint geometry is shown in Figure 3.1. The welding parameters of each four welding passes shown in Figure 3.1 are presented in Table 3.2. Before welding, the interior of the pipe (i.e., the back of the weld) was purged with Ar gas containing a specific oxygen content. Four different oxygen concentrations, namely 50, 200, 500, and 5000 ppm, were used for the purging, as indicated in Table 3.3. The oxygen gas used for welding was obtained from commercially available sources offering varying degrees of argon purity. To ensure its suitability, the gas underwent meticulous analysis conducted by Airliquid, a distinguished company specializing in precise gas assessments. Throughout the welding procedure, continuous monitoring of oxygen concentration was undertaken using the PurgEye 300 instrument. The initiation and maintenance of gas purging was meticulously executed until the desired and predetermined oxygen level was successfully attained. To create an environment conducive to accurate measurements, the pipe was effectively sealed from both ends. One end of the pipe was subjected to inert gas introduction, while at the opposite end, the oxygen concentration was carefully gauged. The formation of possible phases as a function of the oxygen content and temperature was predicted using the thermodynamic software FactSage (Bale *et al.*, 2002).

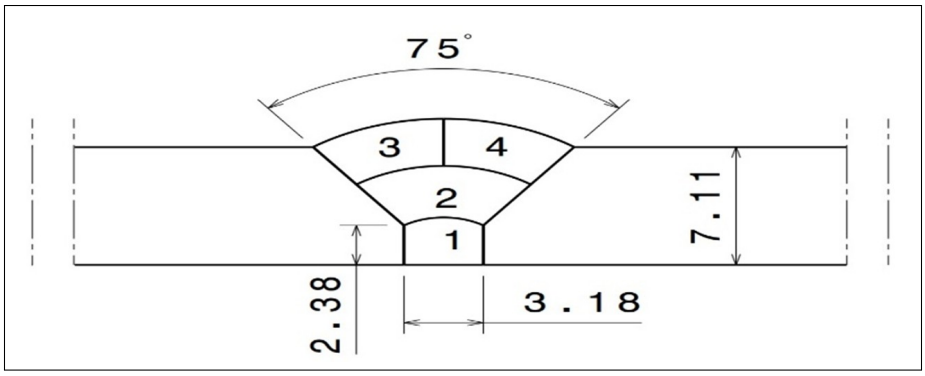

Figure 3.1 Weld zone geometry (dimensions in mm)

Table 3.2 Welding condition parameters of 316L SS samples

Parameter	**Pass 1**	**Pass 2**	**Pass 3**	**Pass 4**
Process	GTAW	GTAW	GTAW	GTAW
Shielding gas	Ar	Ar	Ar	Ar
Purge gas flow rate (CFH)	40	40	40	40
Current (A)	125–202	166–215	200–223	208–243
Voltage (V)	10.6–14	11.8–15.7	12.8–16.4	13.8–16.4
Tube to work distance (mm)	9.52	9.52	9.52	9.52
Heat Input ($kJ.mm^{-1}$)	1.31	1.17	1.28	1.44
Filler material	ER316L (Exocor)	ER316L (Exocor)	ER316L (Exocor)	ER316L (Exocor)

Table 3.3 Purging gas concentrations used during welding

Oxygen content (ppm)	Component
50	Ar + 0.005% O
200	Ar + 0.02% O
500	Ar + 0.05% O
5000	Ar + 0.5% O

FactSage is a comprehensive software package widely used in the field of computational thermochemistry. Originally designed for pyrometallurgical processing, FactSage has evolved to encompass a wide range of applications. The Equilib module within FactSage performs Gibbs energy minimization calculations, enabling the determination of chemical species concentrations in systems reaching a state of chemical equilibrium. Additionally, the phase diagram module offers the capability to calculate various types of phase diagram sections, providing insights into phase transformations, stability ranges, and boundaries of different phases. In this study, the Equilib and Phase Diagram modules of FactSage were utilized to analyze the thermodynamic behavior of the steel (Bale *et al.*, 2002).

Potentiodynamic anodic polarization (PAP) was used for determining the pitting potential of the HAZ. The tests were performed based on the ASTM G5-13 standard (ASTM, 2014). The size of the test specimens was 15 × 15 mm, with an exposed area to the solution and examined of 1 cm^2. Each sample was placed in a flask containing the test solution, 0.5 M NaCl and 0.5 M H_2SO_4, for the pitting corrosion tests. The open circuit potential (OCP) values, also referred to as the corrosion potential, for each experiment was measured with a delay of 300 s. The polarization curve was plotted from 50 mV below OCP to 2000 mV (vs. Ag/AgCl) at a potential rate of 0.0016 V/s, as suggested by the literature (Kumar *et al.*, 2021). Potentiodynamic polarization tests were repeated three times to determine the average pitting potential (E_{pitt}) for each condition. The tests were performed at 23 ± 2 °C according to the ASTM G5-13 standard test method.

For the electrochemical polarization tests, an electrochemical cell, consisting of three electrodes, was deployed. The 316L sample (working electrode (WE)) and the platinum counter electrode (CE) were immersed in the electrolyte and connected to a saturated Ag/AgCl reference electrode (RE) by a salt bridge. The sample holder used for holding the 316L sample (WE) was provided by Redox Company and the electrochemical cell, CE, and RE were obtained from Pine Research Inc. The electrodes were connected to an Autolab potential/galvanostat PGSTAT302N potentiostat, which was controlled by a computer using Nova software.

In order to determine the pitting parameters (E_{pit}, I_{pit}, I_{passive}, E_{passive}) in this study, the inflection point method was employed, as suggested by literature (Finšgar & Milošev, 2010; Comotti, Trueba & Trasatti, 2013; Bellezze, Giuliani & Roventi, 2018). The method suggested by researchers involves identifying the point on the polarization curve where a change in slope occurs. It is characterized by the intersection of two tangent lines that represent the transition from activity to passivity (E_{passive}, i_{passive}) and from passivity to pitting (E_{pit}, i_{pit}).

Discoloration images were acquired using a Keyence VR2500 3D scanner to examine the oxide layer. Subsequently, the oxide layer was carefully analyzed using scanning electron microscopy (SEM). Two high-resolution SEM instruments, the Hitachi SEM TM3000 and the Hitachi SU8230 FE-SEM, were employed for the analysis. To ensure the preservation of the delicate oxide layers, a combination of mounting techniques and cross-section and face ion milling methods were employed. Figure 3.2 illustrates the specific technique that was developed and employed in this investigation. This developed method involved the use of hot mounting resin and cross-section and surface ion milling, effectively protecting the integrity of the oxide layers. For the cross-section part, ion milling was conducted for 2 h at 6 kV with a speed of 60 reciprocations per minute and a swing of ±15 degrees. This was followed by 1 h of ion milling at 5 kV with a speed of 30 reciprocations per minute and a swing of ±30 degrees. For the surface ion milling, a 3 min process was carried out at 5 kV with 15 reciprocations per minute and a swing of ±60 degrees. In order to prepare the sample surface for analysis, the IM4000 Plus ion milling Hitachi machine was utilized, allowing for precise surface preparation and optimal imaging quality.

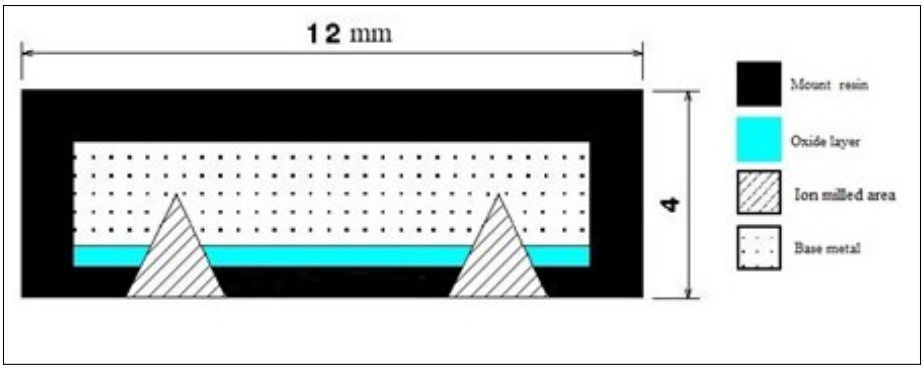

Figure 3.2 Schematic showing the ion mill regions of the samples for accurate determination of the thickness of the oxide layers and its composition

3.4 Results

3.4.1 Influence of oxygen content on discoloration

Figure 3.3 provides illustrative examples of the extent of discoloration observed in the HAZ of the tested samples with different oxygen concentrations. The results indicate that the highest discoloration width occurs for 5000 ppm oxygen, whereas the differences in width diminish as the oxygen content rises. Elevated oxygen levels can lead to higher oxidation rates, particularly at elevated temperatures. This means that the rate at which the metal reacts with oxygen to form oxides increases. Consequently, the discoloration width expands as more metal reacts and forms an oxide layer (ASTM, 2020). This finding suggests that the presence of oxygen plays a crucial role in the formation and extent of discoloration in the HAZ. These findings, which indicate variations in discoloration width based on different oxygen content, will be utilized in the subsequent sections of the paper to deepen our understanding of the relationship between oxygen content, discoloration, and its impact on pitting corrosion. As discussed in section 3.2, the colors of the oxide layers correspond to different oxide thicknesses, and each welding condition exhibits a specific discoloration pattern. Therefore, it is crucial to determine the width of discoloration for each welding condition to gain comprehensive insights into corrosion behavior.

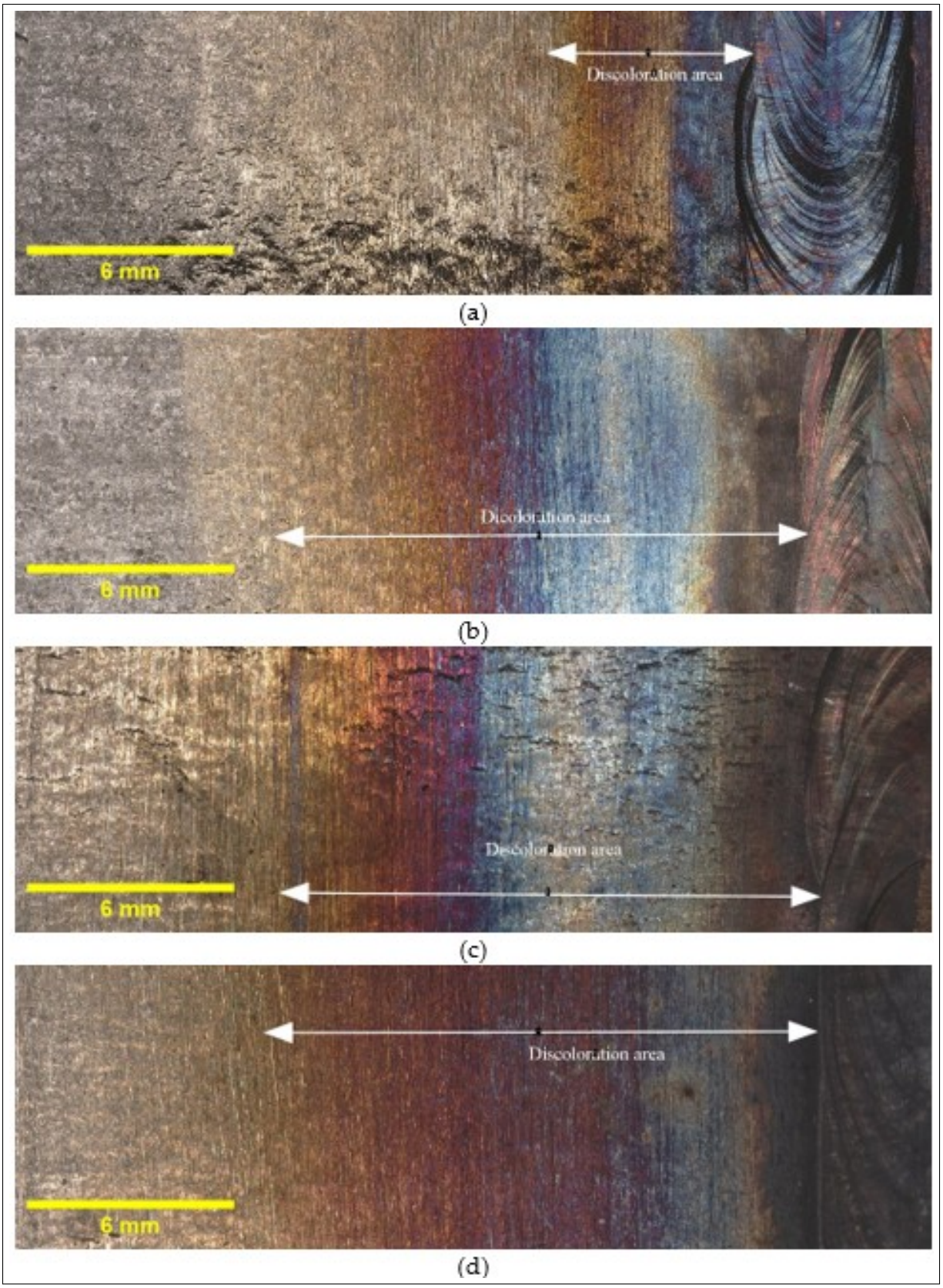

Figure 3.3 Discoloration zone with different oxygen concentrations in purging gas: (a) 50, (b) 200, (c) 500, and (d) 5000 ppm

3.4.2 Thermodynamic calculation

Figure 3.4 presents the oxide scale formation at different temperatures in 316L SS, calculated using FactSage, and represents the different zones of the HAZ, ranging from the weld pool to the base metal. The type and structure at various temperatures and different partial pressures of oxygen indicates the amount of oxygen present from air to the base material.

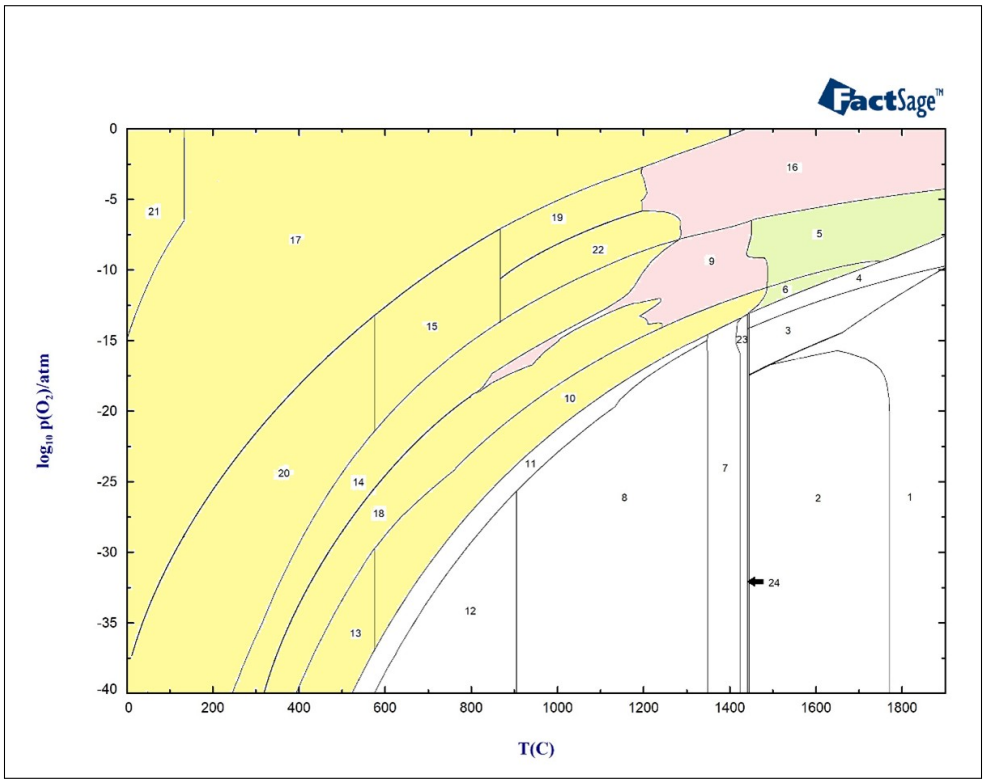

Figure 3.4 Oxide scale formation at different temperatures in 316L SS

The graph indicates that the oxide layer contains Spinel, Olivine, and Corundum with different concentrations until around 1300 °C when delta ferrite begins to form (yellow zone). At around 1300 °C, the formation of oxide liquid begins to increase with the higher partial pressure of oxygen as shown in pink zones. Between 1423 °C and 1445 °C, the material experiences a mushy zone consisting of delta ferrite, austenite, and liquid metal, after which the base metal starts to melt at temperatures above 1445 °C.

Table 3.4 Components in different zones

Zone	**Phase**
1	Liquid
2	Liquid + MeS
3	Liquid + α Ca_2SiO_4
4	Liquid + Oxide Liquid
5	Liquid + Oxide Liquid + Spinel
6	Liquid + Oxide Liquid + Corundum + SiO_2 + TSpinel
7	Delta ferrite + Austenite + MeS
8	Austenite + MeS
9	Oxide Liquid + Austenite + Spinel + TSpinel
10	Austenite + MeS + Corundum + SiO_2 + TSpinel + $Ca_3Cr_2Si_3O_{12}$
11	Austenite + MeS + Wollastonite
12	Austenite + MeS
13	Austenite + MeS + Corundum + SiO_2 + TSpinel + Wollastonite
14	Spinel + Austenite + Olivine + β Ni_3S_2
15	Spinel + Olivine + Rhodonite + Pyrrhotite
16	Oxide Liquid + Spinel
17	Spinel + Corundum + SiO_2 + $MnSO_4$ + $CaSO_4$
18	Austenite + MeS + Spinel + Rhodonite + TSpinel + Wollastonite
19	Spinel + Olivine + Rhodonite + $MnSO_4$ + $CaSO_4$
20	Spinel + Corundum + Olivine + $CaSO_4$ + $MnSO_4$
21	Spinel + Corundum + SiO_2 + $MnSO_4$ + $CaSO_4$ + MnO_2 + CrO_3
22	Spinel + Olivine
23	Delta ferrite + Austenite + MeS + Liquid
24	Delta ferrite + MeS + Liquid

In Figure 3.5, the mass fraction of different phases at 800 °C under different partial pressures of oxygen is shown using the Equilib module of FactSage software. The figure indicates the presence of the Corundum phase for two different ranges of partial pressures of oxygen. The first layer of Corundum, which contains chromium, nickel, and oxygen, is present between 10^{-31} and 10^{-27} atm, while the second layer, which is the outer layer of the oxide and begins at 10^{-9} atm, contains Cr, Fe, Ni, and oxygen (Figure 3.5c). The other phase observed after 10^{-25} atm is the spinel phase consisting of Ni, Fe, Cr, and oxygen. In the spinel phase, chromium is found to be more stable until around 10^{-12} atm partial pressure of oxygen, followed by iron becoming more stable. Nickel is formed at 10^{-15} atm and becomes more stable than chromium after 10^{-9} atm (Figure 3.5b).

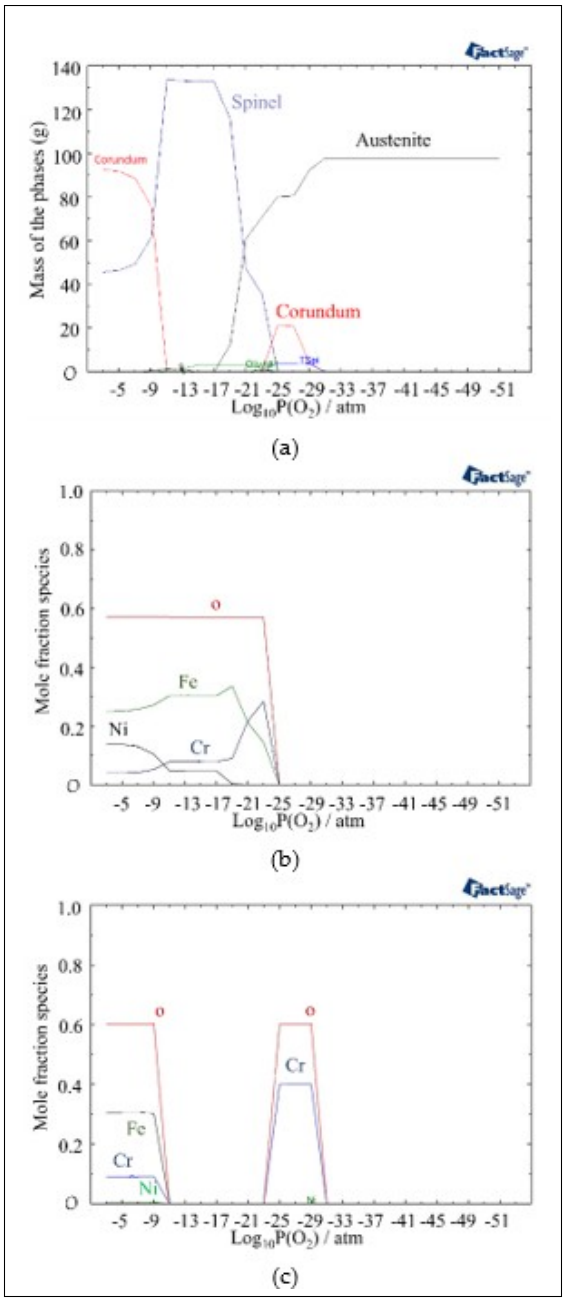

Figure 3.5 (a) Mass fraction of different phases at 800 °C as a function of partial pressure of oxygen, (b) Mole fraction of elements in the Spinel phase, (c) Mole fraction of elements in the Corundum phase

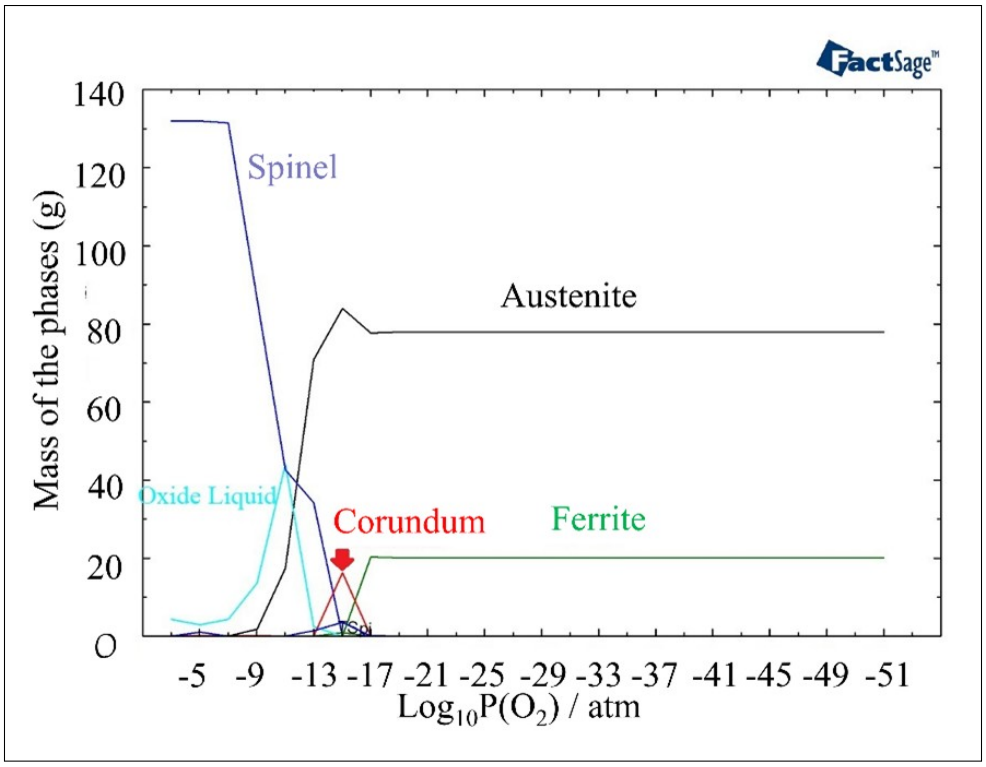

Figure 3.6 The structure of oxide formation at 1400 °C in 316L SS for various partial pressures of oxygen

Oxide formation initiates at a higher partial pressure of oxygen, specifically at a level of 10^{-17} atm, when the temperature reaches 1400 °C (Figure 3.6). This indicates that the oxide formation process is more favorable at higher temperatures compared to 800 °C. The amount of the Corundum phase becomes less and appears between 10^{-17} atm and 10^{-13} atm. Oxide liquid starts to form after a partial pressure of oxygen of 10^{-16} atm in the outer layer of oxide, but it is less stable than the spinel phase.

In Figure 3.7a, the phases present at 1440 °C and different partial pressures of oxygen are displayed. Compared to 1400 °C, the outer layer contains a higher amount of oxide liquid. Figure 3.7b provides information on the phases present in the oxide liquid at different partial pressures of oxygen. The most stable phase between 10^{-21} atm to 10^{-9} atm is FeO. The inner and outer layers of the oxide liquid phase contain SiO_2, a stable phase at these pressures. In addition, there are small amounts of Fe_2O_3 and NiO present in the outer layer and CrO

in the inner layer. These analyses of the oxide composition and phase transitions provide valuable insights into the behavior of the material under different temperature and oxygen partial pressure conditions. Indeed, the presence of Spinel, Olivine, and Corundum phases, with varying proportions, indicates the complex nature of the oxide layer formed at the surface of the material. The identification of specific phases and their stability under different conditions allows for a better understanding of the structure of the phases in different discolored zones. The following sections delve into the impact of specific phases on the corrosion resistance of the material.

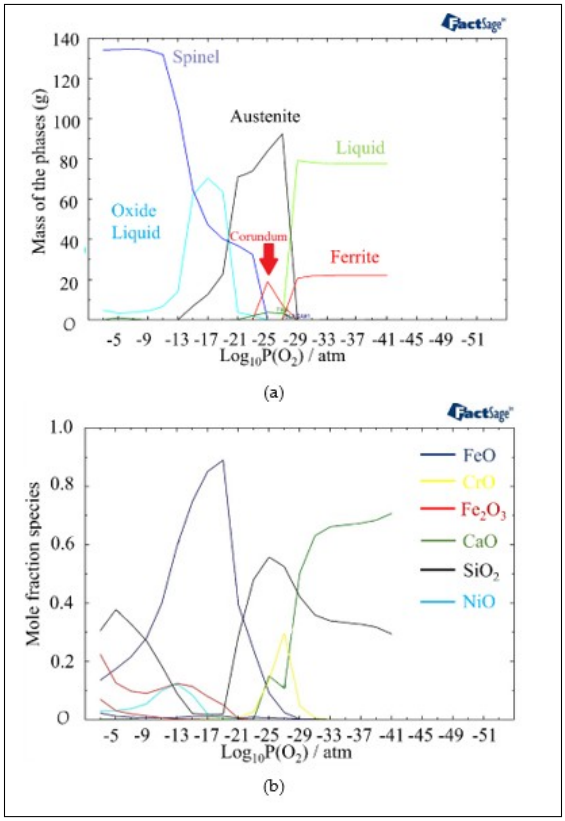

Figure 3.7 (a) Mass fraction of different phases at 1440 °C as a function of partial pressure of oxygen (b) Component distribution in the oxide liquid phase

3.4.2.1 Oxide geometrical characteristics

By increasing the oxygen content in the backing gas, the growth of the oxide layer was observed. Figure 3.8 illustrates such variation of the oxide layer thickness with the oxygen content for a given use case. The image was taken at a distance of 1.5 ± 0.3 mm from the fusion line, where the thickness of the oxide layer increases from 700 ± 300 nm for 50 ppm oxygen to 2.7 ± 0.3 µm, 2.8 ± 0.3 µm, and 3 ± 0.3 µm for 200, 500, and 5000 ppm oxygen, respectively. It must be noted that other images were taken at distances from the weld line and they all showed the same trend.

In order to comprehensively analyze the kinetics of oxide growth in the weld zone of 316L SS, it is essential to consider the combined effects of oxygen content in the atmosphere and temperature. To incorporate the impact of the oxygen content, we can introduce a term representing the partial pressure of oxygen (P_{O_2}). Assuming a power-law relationship between the rate constant and the partial pressure of oxygen, the equation becomes (Geffroy *et al.*, 2019):

$$K = A \cdot (P_{O_2})^n \tag{3.2}$$

In this equation, A is a constant and n denotes the power-law exponent that describes the dependence of the rate constant on the oxygen partial pressure.

Next, we can consider the Arrhenius equation, which relates the rate constant to temperature (Laidler, 1984):

$$K = A' \cdot e^{-E_a/RT} \tag{3.3}$$

Using the two equations, we get:

$$K \propto (P_{O_2})^n \cdot e^{-E_a/RT} \tag{3.4}$$

In this equation, assuming a linear relationship between the oxide thickness and time (Wagner equation), $X = Kt$:

$$X \propto (P_{O_2})^n \cdot e^{-E_a/RT} \tag{3.5}$$

Where t is time and X is oxide thickness. This equation shows that the oxide thickness also increases with the oxygen content and temperature.

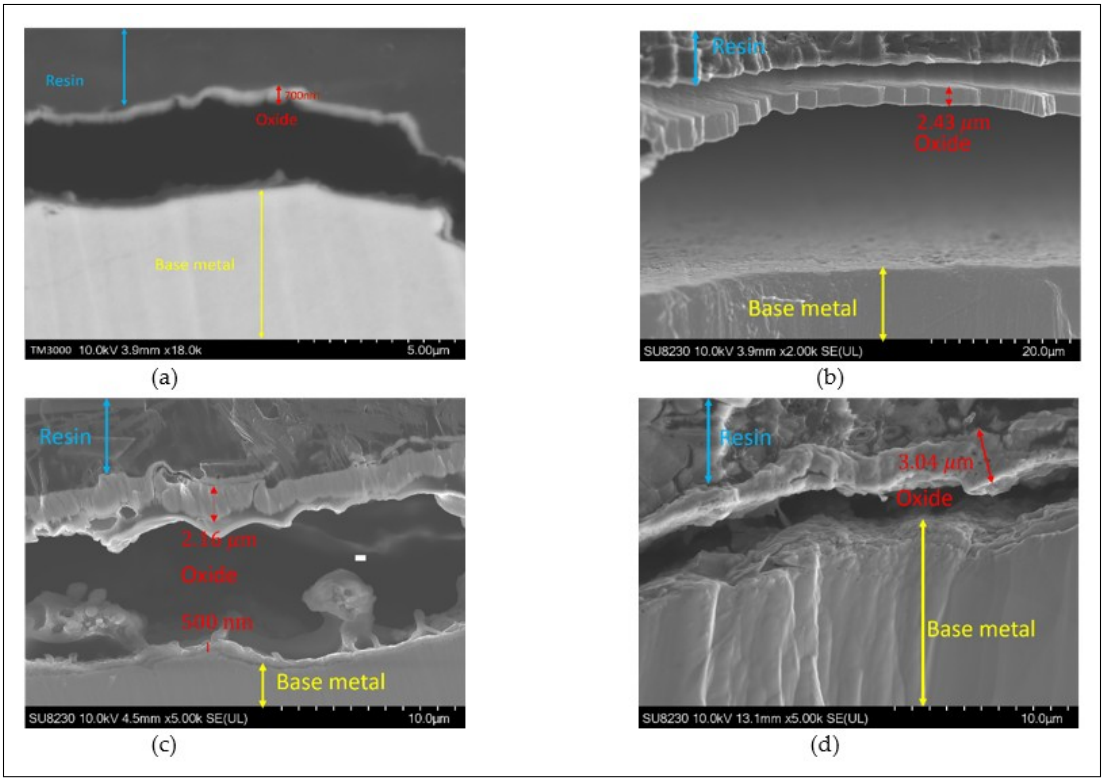

Figure 3.8 Oxide layer at a distance of 1.5 mm from the fusion line: a) 50, b) 200, c) 500, and d) 5000 ppm.

Figure 3.9 shows the elemental map of the oxide layer at a distance of 1.7 mm from the fusion zone in the sample with 5000 ppm oxygen content. The image reveals that the inner layer contains iron, Cr, and Mn, which are spinel and Corundum phases based on Figure 3.5, Figure 3.6 and Figure 3.7. The outer layer consists of iron oxide, which is a mixture of the outer spinel with an iron-rich area, and the second layer of corundum. Moreover, there is a porous structure that appears in the 5000 ppm sample near the fusion line, possibly an oxide liquid with an iron oxide structure (Habib, Damra, Saura, Cervera & Bellés, 2011; Li *et al.*, 2020). These porous structures are shown in Figure 3.10.

The findings presented in this section highlight the influence of oxygen content on the oxide layer's thickness, composition, and morphology. This knowledge is crucial for understanding pitting corrosion behavior. The quantitative data and visual evidence provided in the figures serve as a foundation for further analysis and discussions in the subsequent section of the paper.

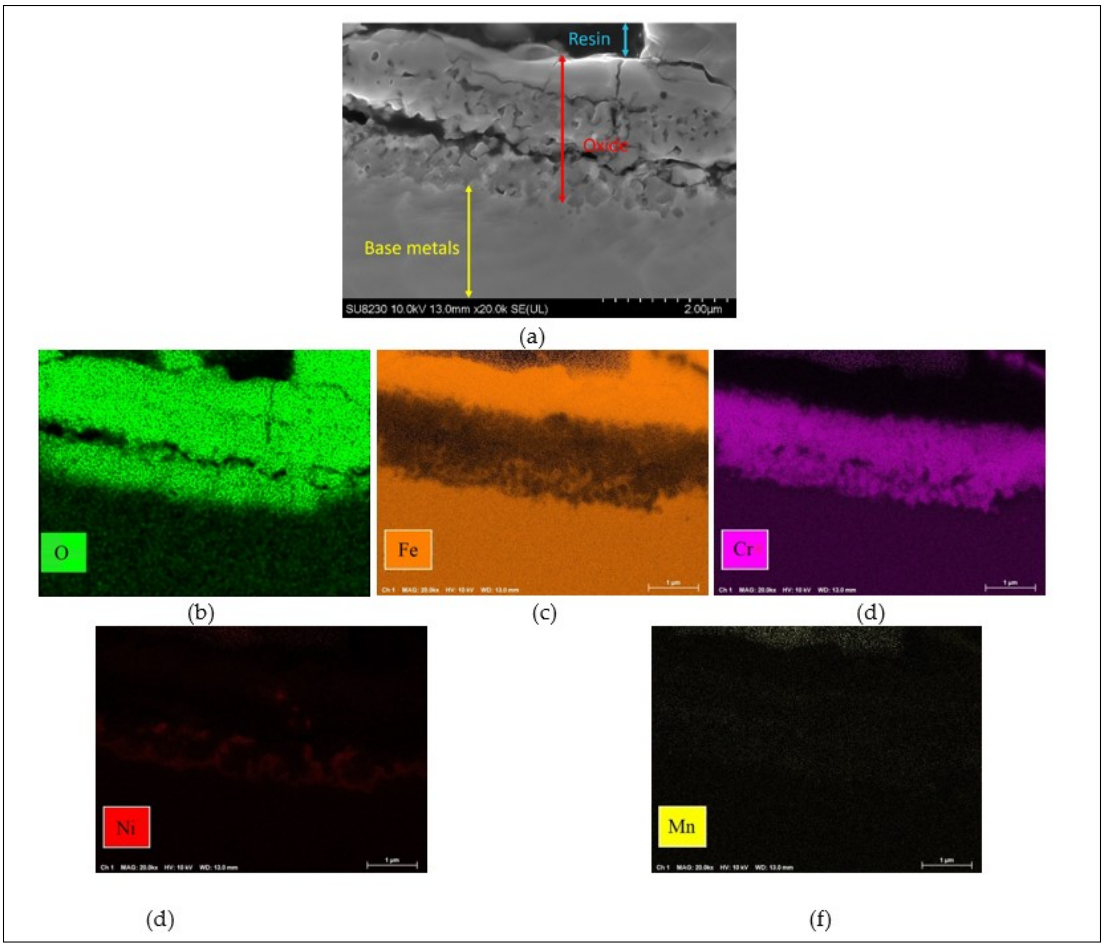

Figure 3.9 Oxide scale at 1.7 mm distance from fusion line of 5000 ppm oxygen content and elemental map: b) O, c) Fe, d) Cr, e) Ni, f) Mn

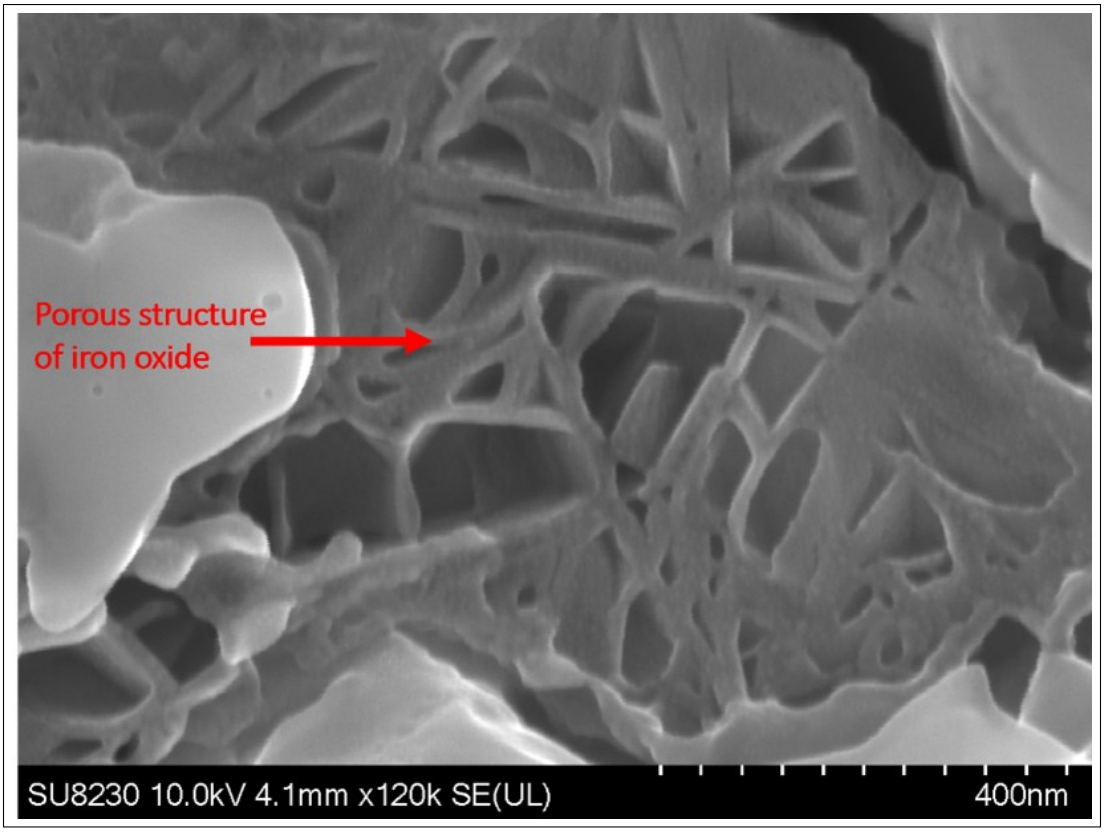

Figure 3.10 Oxide scale at 1.7 mm distance from fusion line of 5000 ppm oxygen content and porous structure

3.4.3 Pitting corrosion tests

The polarization curves and corrosion parameters for the samples with different oxygen contents are presented in Table 3.5 and Figure 3.11. As shown in Table 3.5, the passive current densities for all samples initially increased with the increase in oxygen content up to 500 ppm, followed by a decrease in the sample with 5000 ppm. This can be attributed to the porous structure observed in the oxide layer near the fusion line of the sample with 5000 ppm, which may have led to the formation of more active sites for corrosion. For the sample with 50 ppm of oxygen, the passive current was determined to be 463 ± 10 μA. This value indicates the rate of spontaneous oxidation processes occurring on the surface, suggesting a moderate level of corrosion resistance. As the oxygen content increased to 200 ppm, the passive current decreased to 210 ± 10 μA. This

reduction in passive current density suggests an improvement in the corrosion resistance of the material, as a more protective passive film is forming on the surface. Further increasing the oxygen content to 500 ppm led to a slightly higher passive current of 230 ± 20 μA. Although the passive current density increased slightly, it still indicates a relatively good corrosion resistance compared to the sample with 50 ppm. However, in the sample with 5000 ppm of oxygen, the passive current exhibited a further increase to 290 ± 30 μA. This unexpected rise in the passive current density suggests a slight decrease in the corrosion resistance compared to the samples with lower oxygen contents. The presence of a porous oxide structure near the fusion line, as observed in the composition analysis, has contributed to this phenomenon by creating more active sites for corrosion (Prado, Anastasiou et al. 2021).

In terms of the pit current densities, as shown in Figure 3.11, the pit current was measured to be 463 ± 10 μA. This can be attributed to the limited availability of oxygen, which impedes the formation of a fully protective passive film. The lower oxygen content restricts the extent of passivation, rendering the material more susceptible to localized corrosion. As the oxygen content increased to 200 ppm, the pit current decreased to 200 ± 10 μA. Further increasing the oxygen content to 500 ppm resulted in a slightly higher pit current of 210 ± 30 μA. This can be attributed to the formation of a more stable and protective passive film on the material surface. The presence of oxygen promotes the development of this film, enhancing the resistance to localized corrosion. Interestingly, for samples with 5000 ppm of oxygen, the pit current density did not decrease as anticipated but remained slightly elevated. This behavior can be attributed to the presence of a porous oxide structure near the fusion line. The porous nature of the oxide layer creates preferential sites for localized corrosion initiation, contributing to the higher pit current density.

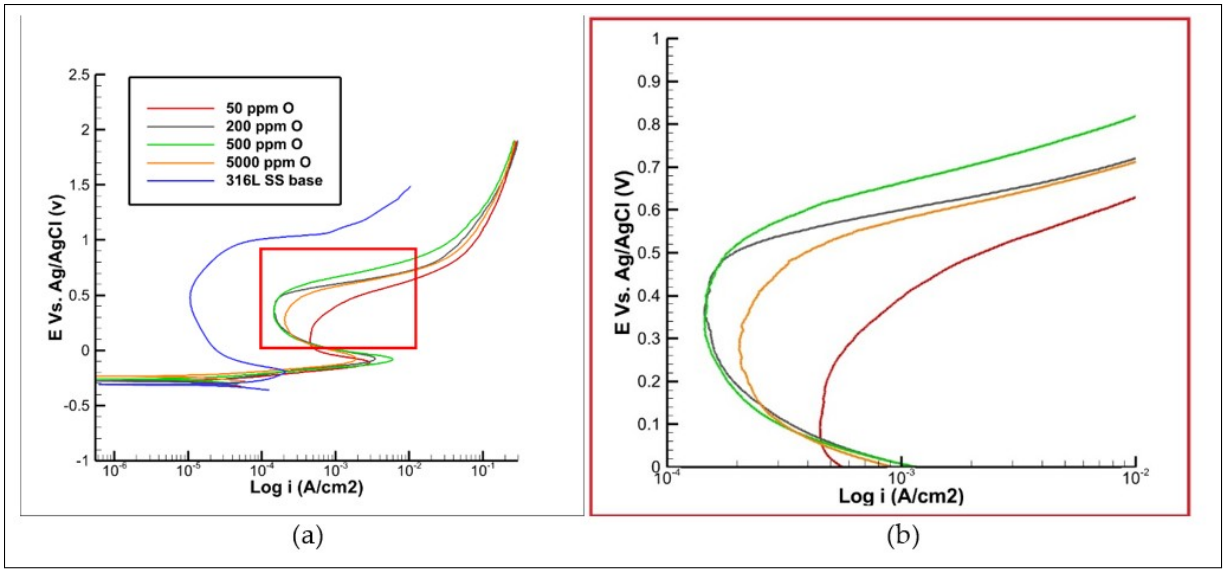

Figure 3.11 (a) Polarization curve of 316L SS with varying oxygen content, (b) High magnification of the red area in the plot (a)

Table 3.5 Corrosion parameters of 316L SS with varying oxygen content

Oxygen content (PPM)	**50**	**200**	**500**	**5000**	**316L SS base**
$i_{passive}$ **(µA)**	463 ± 10	210 ± 10	230 ± 20	290 ± 30	198 ± 30
i_{pit} **(µA)**	463 ± 10	200 ± 10	210 ± 10	260 ± 20	297 ± 30
$E_{passive}$ **(V)**	0 ± 0.01	0.05 ± 0.03	0.07 ± 0.03	0.09 ± 0.01	-0.04 ± 0.01
E_{pit} **(V)**	0.42 ± 0.06	0.53 ± 0.01	0.54 ± 0.01	0.49 ± 0.02	0.96 ± 0.01

The passive potential values are reported in Table 3.5, showing zero for the sample with 50 ppm oxygen indicating the absence of a stable passive film. In contrast, the passive potential value increases to 0.05 V for the sample with 200 ppm oxygen and then by 0.07 V and 0.09 V for the two other samples with 500 and 5000 ppm oxygen, respectively. The obtained results indicate that by increasing the oxygen content the formation of the passive film is accelerated. In the base metal, where there are no oxides present, the passive potential is lower when compared

to the samples with discoloration. At 50 ppm of oxygen, the pitting potential was found to be 0.42 V. This relatively higher pit potential suggests a greater susceptibility to localized corrosion. The pitting potential of the base metal is significantly higher compared to the sample with discoloration, which measures at 0.96 V. This disparity can be attributed to the heat and temperature experience during welding in the heat-affected zone. The limited availability of oxygen at this concentration may hinder the formation of a robust passive film, making the material more vulnerable to localized attack. As the oxygen concentration increased to 200 and 500 ppm, the pit potential increased to 0.53 and 0.54 V, respectively. This indicates a slight improvement in the resistance to localized corrosion. The higher pit potentials suggest the formation of a more stable and protective passive film, which provides better defense against localized corrosion initiation and propagation. In samples with 5000 ppm of oxygen, the pitting potential decreased to 0.49 V. This decrease in pit potential can be attributed to the presence of a porous iron oxide structure near the fusion line, as observed in previous analyses. The porous nature of the oxide layer promotes the formation of localized corrosion sites, resulting in a reduction in the pit potential. This implies a higher susceptibility to localized corrosion, potentially compromising the integrity of the material.

3.4.4 Conclusion

This research study presents an investigation into the corrosion behavior and the influence of oxygen content on the properties of a welded 316L SS pipeline in the root joint area. By exploring the microstructural characteristics, polarization curves, and corrosion parameters, valuable insights are gained into the material's corrosion resistance. The investigation presented in this work yields the following results:

1. The width of discoloration increased with increasing oxygen content, and notable differences in color were observed between the samples with 5000 ppm and 500 ppm/200 ppm of oxygen. In particular, the 5000 ppm sample exhibited an opaque zone located behind the welding line, indicating distinct characteristics in the oxide formation process at high oxygen concentrations.

2. The results indicate that the oxide thickness increases with an increase in the oxygen content of the purging gas, ranging from 50 to 5000 ppm. This suggests that a higher concentration of oxygen promotes the formation of a thicker oxide layer on the surface of the material. The observed trend in oxide thickness provides valuable insights into the influence of oxygen content on the oxide formation process and its subsequent impact on the corrosion resistance of the material.
3. The oxide structure was found to be a mixture of spinel and corundum phases, with the presence of an oxide liquid phase at high temperatures. The oxide liquid phase exhibited a higher concentration of FeO, which resulted in a porous structure.
4. The pitting corrosion resistance showed an increasing trend up to 500 ppm oxygen content, followed by a decrease at 5000 ppm. The sample with 500 ppm exhibited the highest pit potential, suggesting the formation of a more stable passive film that is less susceptible to localized corrosion. The presence of a porous oxide structure near the fusion line in the 5000 ppm sample may have contributed to its lower pitting corrosion resistance.

Author Contributions: Conceptualization, M.M., I.R., L.A.H., M.J. and S.H.; methodology, M.M., S.H., A.K. and M.J.; software, M.M.; formal analysis, M.J.; investigation, M.M., S.H. and L.A.H.; resources, M.M. and I.R.; data curation, S.H.; writing—original draft preparation, M.M.; writing—review and editing, M.M., A.K., L.A.H. and M.J.; visualization, M.M.; supervision, A.K., I.R. and M.J. All authors have read and agreed to the published version of the manuscript.

Funding: The research project presented in this article was conducted in collaboration with PCL Construction in Edmonton, who provided the materials for the study, and was funded by The Natural Sciences and Engineering Research Council of Canada (NSERC-Grant number RDC 542299-19).

Institutional Review Board Statement: Not applicable.

Informed Consent Statement: Not applicable.

Acknowledgments: The author would like to express gratitude to PCL Construction for their support and contribution to this project. Special thanks to Mohammad Saadati for his invaluable assistance for electron microscopy examinations.

Conflicts of Interest: The authors declare no conflict of interest.

CHAPTER 4

HYBRID GTAW–FCAW OF 316L STAINLESS STEEL PIPES: INFLUENCE OF OXYGEN CONTENT IN BAKING GAS AND SURFACE PREPARATION ON OXIDE CHARACTERISTICS AND CORROSION BEHAVIOR

Mohammad Maroufkhani[a], Alireza Khodabandeh[b], Iulian Radu[c], Mohammad Jahazi[d]

[a,b,d] Department of Mechanical Engineering, École de Technologie Supérieure (ÉTS),
1100 Notre-Dame Street West, Montreal, QC, Canada H3C 1K3
[c] PCL Industrial Management Inc.,2107 4 St, Nisku, AB, Canada,T9E 7W6

Paper Submitted for publication in Metals and Materials International, Springer , July 2025

4.1 Abstract

This study investigates the combined effects of oxygen content in the purging gas and pre-weld surface finish on the discoloration and corrosion resistance of AISI 316L pipe joints, with relevance to pipe welding where internal cleaning is constrained. The hybrid GTAW–FCAW process was used. Welds were produced at two oxygen levels (500 and 5000 ppm) and two finishes (40- vs. 60-grit). Discoloration and oxide morphology were examined by SEM/EDS, and corrosion behavior was evaluated without oxide removal using cyclic polarization and electrochemical impedance spectroscopy. The results reveal that higher oxygen levels in the purging gas produced more porous, less protective oxide layers, along with intensified oxidation around surface defects such as micro-holes. Surface roughness was also found to influence corrosion behavior: rougher surfaces exhibited higher resistance to pit initiation, whereas smoother surfaces were more susceptible to initiation but offered greater resistance to pit propagation. The corresponding governing mechanisms were identified and discussed in terms of how surface preparation affects crystallographic texture, heterogeneities and recrystallization. Taken together, the results link oxide morphology and near-surface microstructure to electrochemical response and offer practical guidance for pipe welding when internal cleaning is constrained, balancing purging control with surface preparation to preserve corrosion performance. The findings further highlight the critical roles of both purging-gas

composition and surface preparation in the corrosion performance of stainless steel welded pipes.

Keywords: Discoloration, Pitting corrosion, 316L SS, GTAW

4.2 Introduction

The durability and performance of stainless steels are crucial in industrial environments where resistance to pitting corrosion determines the longevity and reliability of components. Among them, austenitic stainless steel AISI 316L is widely used for pipelines and structural parts exposed to corrosive media because of its excellent corrosion resistance and mechanical strength (Gao, Wang, Li, Xu & Qiao, 2022; Bedoya-Zapata, Franco-Rendon, Leon-Henao, Santa & Barrada, 2021; Maroufkhani, Khodabandeh, Radu, Moosavi-Khoonsari & Jahazi, 2025). During welding, surface discoloration inevitably occurs and can degrade the material's behavior in aggressive conditions (Aumpiem & Prateepasen, 2017; Garcia, Santos, Esteves, Campos & Rabelo, 2019; Maroufkhani *et al.*, 2023). The oxide film that develops on the weld surface may strongly influence the alloy's resistance to localized corrosion, particularly pitting, a common failure mode in chloride-containing environments (Gao *et al.*, 2022).Several welding parameters affect the corrosion resistance of AISI 316L (Ezuber, Alshater, Nisar, Gonsalvez & Aslam, 2018; Zhang *et al.*, 2019; Li, Zou, Li & Tong, 2023; Liu *et al.*, 2024). ; among these, the oxygen content of the purging gas and the surface roughness of the weld are especially significant (Liu *et al.*, 2024).

The oxygen concentration in the backing gas has a direct impact on the oxide formation at the weld root surface, leading to discoloration and altering the chemical composition of the oxide layer (Kim, Lee, Kim & Lee, 2024). This discoloration, caused by oxygen impurities during purging, is especially critical in industries such as oil and gas, where pitting corrosion resistance is vital (Kimbrel, 2011). Several studies have examined the influence of oxygen content in purging gases on both discoloration and corrosion behavior of stainless steels (Ling *et al.*, 2019; Maroufkhani *et al.*, 2023). To ensure optimal corrosion performance, the atmospheric air must

be effectively displaced from the fusion zone during welding—particularly for the root pass—by supplying an inert purging gas on the backside of the weld. Bergquist et al. (Bergquist *et al.*, 2011) reported that atmospheric oxygen levels of about 210,000 ppm can produce a thick oxide film on the weld root surface. Picha et al. (Panmongkol & Phung-on, 2021) dobserved that adding nitrogen (N2) to argon as a purging gas enhanced the pitting corrosion resistance of 304 stainless steel welds made by Gas Tungsten Arc Welding (GTAW). Similarly, Trigwell et al. (Trigwell & Selvaduray, 2005) attributed oxidation-induced discoloration in the heat-affected zone of electropolished stainless steel to oxygen contamination in the argon backing gas, noting that the discoloration intensity increases with oxygen content due to the formation of an iron-rich oxide layer. Studies have shown that excessive oxygen content can lead to the formation of porous oxide layers and chromium-depleted zones, which compromise the material's ability to resist pitting corrosion (Aumpiem & Prateepasen, 2017).

Thermal heterogeneity across the heat-affected zone (HAZ) plays a crucial role in determining oxide formation, thickness, and corrosion resistance. Our recent thermodynamic analysis using FactSage (Maroufkhani *et al.*, 2023) revealed that around 800 °C, stable phases such as corundum and spinel are favored, while at higher temperatures approaching 1300 °C, δ-ferrite and liquid oxide phases begin to appear; partial melting occurs beyond 1445 °C. These variations in phase stability explain why low-temperature regions typically form thin, chromium-rich protective oxides, whereas high-temperature areas develop thicker, iron-rich and liquid-like oxides that are porous and less protective (Maroufkhani *et al.*, 2023). The resulting oxide thickness directly influences the interference colors visible on the weld surface. According to optical principles, these colors arise from the path difference of light reflected at the air/oxide and oxide/metal interfaces. Consequently, the straw-yellow, blue, purple, and black discolorations are not merely aesthetic effects but correspond to specific oxide thickness ranges associated with the thermal cycles during welding (Macleod & Macleod, 2010; Pedrotti, 2008; Khafaji *et al.*, 2017).

The American Welding Society (AWS) standards, including AWS D18.1 and AWS D18.2, establish strict limits for discoloration in stainless steels used in sanitary and food-processing

applications, where only light blue or lighter shades are considered acceptable (Avery, 2000). However, these specifications do not extend to the oil and gas sector, leaving a knowledge gap for this field. Previous studies have shown that using a purging gas with an oxygen concentration of about 500 ppm during GTAW produces optimal results in multi-pass welds by improving pitting corrosion resistance, whereas increasing the oxygen level to 5000 ppm significantly reduces it (Maroufkhani *et al.*, 2023). Despite these findings, the combined effect of oxygen content and surface roughness on pitting corrosion resistance during hybrid GTAW/Flux-Cored Arc Welding (FCAW), a process widely employed in industrial pipe fabrication, has not yet been investigated.

Surface roughness is another key factor that strongly affects the corrosion behavior of stainless steel. In general, smoother surfaces enhance corrosion resistance by promoting the formation of a uniform and stable passive oxide film (Hong & Nagumo, 1997; Nowak, 2020). Nowak (Nowak, 2020) reported that increasing the surface roughness of AISI 316Ti improved oxidation resistance by facilitating the development of a stable Cr–Mn mixed oxide layer. Wang et al. (Wang *et al.*, 2024b) found that increasing surface roughness intensified pit depth growth in HP-13Cr Stainless Steel. They explained their findings in terms of the influence of surface roughness in reducing the stagnant layer thickness and accelerating cation diffusion while forming multistage vortices in surface troughs, which inhibited Fe^{2+} diffusion, promoting local acidification and therefore accelerating pitting corrosion. Jaffré et al. (Jaffré *et al.*, 2021a) found that mechanical surface treatments, particularly dry grinding, significantly impair the passive film stability and corrosion resistance of 304L stainless steel in chloride environments, mainly due to increased roughness and residual stresses. Similarly, Zhang et al. (Zhang *et al.*, 2024) demonstrated that electropolishing improves the corrosion resistance of 304L stainless steel by removing surface deformation, whereas sandpaper grinding introduces residual stress that reduces passive film stability. Guo et al. (Guo *et al.*, 2025) further showed that in ENiCrFe-7 welds tested without oxide removal, decreasing surface roughness led to lower passive current density and higher corrosion potential—confirming that smoother surfaces provide superior corrosion protection.

Although it is well established that reducing surface roughness generally improves resistance to pitting corrosion, most of these findings are based on experiments where the oxide layers were removed before testing (Liu *et al.*, 2024; Guo *et al.*, 2025; Messinese *et al.*, 2022; Tang, Dai, Wu, Jiang & Li, 2019a; Salah-Rousset, Chaouachi & Chellouf, 1996; Tang, Dai, Wu, Jiang & Li, 2019b). In real industrial environments, however, the oxide layer on the inner surface of welded pipes is often retained, and its influence on corrosion performance has been rarely examined. In this study, the oxide layer formed during high-temperature exposure was deliberately preserved to reflect realistic service conditions. As reported by several researchers (Zhao *et al.*, 2022; Balusamy, Kumar & Narayanan, 2010; Wang, Sun, Xu, Long & Zhang, 2018; Hao, Deng, Zhong, Jiang & Li, 2009; Wang, Feng, Zhang, Zhang & Sun, 2021; Aghuy, Zakeri, Moayed & Mazinani, 2015), rougher surfaces tend to develop thicker oxide layers, whereas smoother surfaces produce thinner and less porous oxides. These contrasting morphologies are expected to affect the corrosion behavior of welded joints in service. Accordingly, this work offers new insights into the combined influence of surface roughness and intact oxide layers on the corrosion resistance of 316L stainless steel pipe welds used in the oil and gas industry.

Although numerous studies have examined the influence of oxygen content in the purging gas on surface discoloration and corrosion resistance of stainless steels, the combined effects of oxygen concentration and surface roughness remain insufficiently understood—particularly under industrial conditions where the discolored oxide layer is left intact. Moreover, the specific role of surface roughness in governing corrosion resistance in discolored welds has not been systematically investigated. This study addresses these knowledge gaps by evaluating whether an oxygen concentration of 500 ppm remains optimal for hybrid GTAW/FCAW and by assessing how surface roughness affects the corrosion resistance of AISI 316L stainless steel welds. The results aim to provide practical guidance for optimizing welding parameters in the oil and gas industry, balancing performance and cost efficiency without the need for post-weld surface treatments. To achieve these objectives, the effects of two oxygen contents in the purging gas (500 ppm and 5000 ppm) and two surface roughness levels (buffed with 40- and 60-grit abrasives) on discoloration and corrosion resistance of AISI 316L stainless steel

were investigated. The discoloration level was characterized by microscopic and chemical analyses, while electrochemical testing was conducted to evaluate the welded joints' resistance to localized corrosion. The composition and morphology of the oxide layers were also examined to elucidate the underlying mechanisms. Finally, the results were integrated to propose practical recommendations for optimizing welding parameters and ensuring reliable performance in industrial applications. This study addresses key gaps in current knowledge by examining how oxygen contents in the backing gas and surface finish influence pitting corrosion resistance in GTAW/FCAW-welded AISI 316L joints. The novelty lies in assessing the effect of surface roughness on corrosion behavior within the discoloration zone, while preserving the internal oxide layer to realistically represent pipe interiors where post-weld cleaning is impractical. This zone, exposed to distinct thermal conditions during welding, plays a critical role in corrosion performance yet remains insufficiently investigated, particularly for hybrid GTAW/FCAW processes applied to 316L stainless steel pipelines. Electrochemical Impedance Spectroscopy (EIS) and cyclic polarization tests were employed to clarify how surface roughness influences the underlying corrosion mechanisms.

4.3 Methodology

4.3.1 Materials and Sample Preparation

The AISI 316L stainless steel samples used in this study were supplied by PCL (Edmonton,Alberta Canada). The alloy's chemical composition was determined using a SPECTROMAXx LMF08 optical emission spectrometer (Ametek, Kleve, Germany). To ensure measurement of accuracy and reproducibility, five independent readings were performed, and their average values were used for analysis (Table 1). The pipe employed in this study had an external diameter of 154.4 mm and a wall thickness of 7.11 mm for the base metal section.

Table 4.1 Elemental composition of the 316L stainless steel used in this study (wt.%)

Element	C	Mn	Si	P	S
wt.%	0.0212 ± 0.0004	1.70 ± 0.0070	0.439 ± 0.0020	0.0333 ± 0.0004	0.0290 ± 0.0023
Element	Ni	Al	Co	Cu	N
wt.%	10.13 ± 0.0327	0.0061 ± 0	0.209 ± 0.00055	0.55 ± 0.0016	0.0601 ± 0.0003

4.3.2 Surface Preparation and Roughness

To evaluate the effect of surface roughness on pitting corrosion resistance, the samples were mechanically polished using 40- and 60-grit abrasive papers to produce two distinct surface finishes. These surface conditions replicate the industrial partner's standard pre-weld preparation for curved pipe sections. Surface roughness was measured using a Keyence VR-2500 3D surface profiler (Keyence Canada Inc., Mississauga, ON, Canada). For each grit size, 120 individual measurements were taken to ensure statistical reliability, and the average roughness (Ra) values were calculated accordingly. The measured Ra for the 60-grit samples (B2) was 2.29 ± 0.14 µm, , while for the 40-grit samples (B1), it was 2.80 ± 0.32 µm.The base metal outside the weld zone exhibited a higher roughness of 6.64 ± 0.89 µm. Representative 3D and line-profile images of the 60-grit surface topography are presented in 4.1.

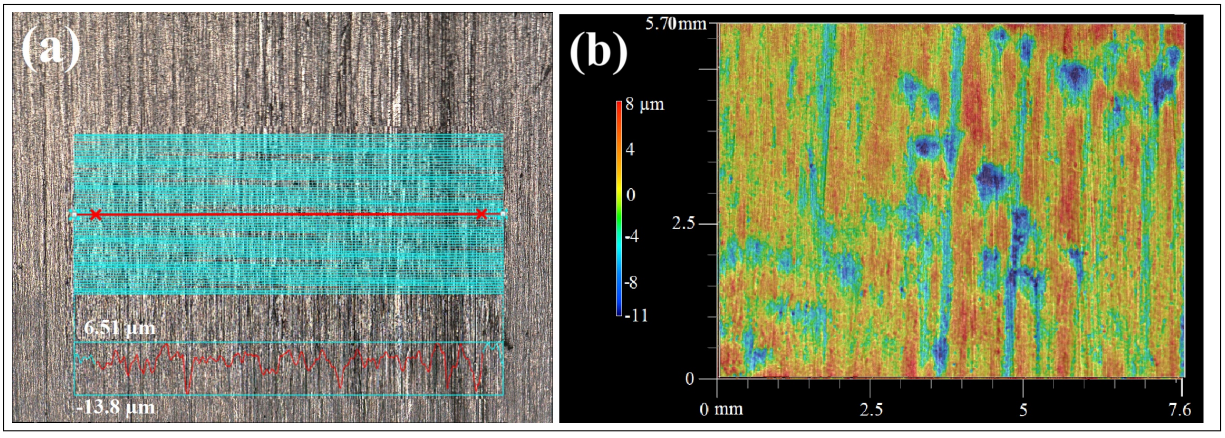

Figure 4.1 (a)Multi-line roughness profile ; (b) 3D surface map showing anisotropic grooves

4.3.3 Welding Procedures

The 316L stainless steel specimens were welded using a hybrid process combining GTAW and FCAW. Argon gas containing controlled oxygen contents (500 or 5000 ppm) was employed to purge the interior of each pipe. The root pass was deposited by GTAW, followed by two FCAW passes for filling, resulting in a total of three welding passes per specimen. The geometry of the welded joint is illustrated in Figure 4.2.

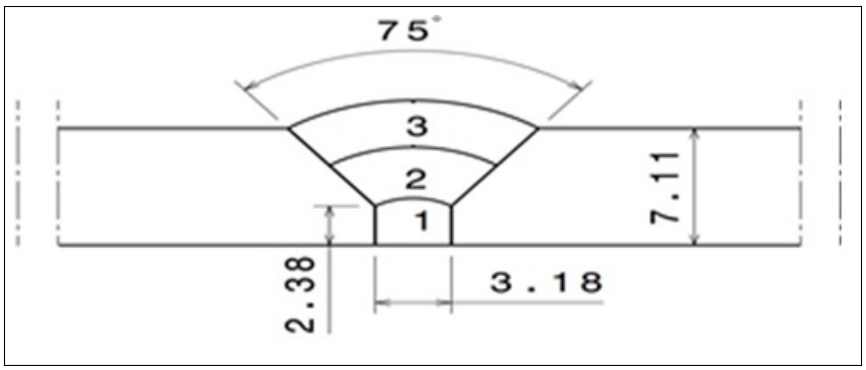

Figure 4.2 Weld zone geometry (dimensions in mm)

The detailed welding parameters for each pass are summarized in Table 4.2, while the purging gas compositions are listed in Table 4.3. Before welding, argon gas with precisely adjusted oxygen contents (500 and 5000 ppm) was introduced to purge the inner surface of the pipe. Commercial-grade oxygen was mixed with argon of different purity levels to obtain the desired concentrations. All tests were conducted in the as-welded condition to replicate actual pipeline interiors, where post-weld cleaning is generally not feasible. The oxygen levels of 500 ppm and 5000 ppm were selected based on prior GTAW work (Ling *et al.*, 2019; Maroufkhani *et al.*, 2023),which identified distinct discoloration characteristics, particularly a marked transition to opaque black and porous oxide formation at 5000 ppm.

Table 4.2 Welding parameters of 316L SS samples

Process	GTAW	FCAW	FCAW
Pass	1	2	3
Shielding gas	Ar	Ar	Ar
Purge gas flow rate (CFH)	30	40	40
Current (A)	170 ± 20	236 ± 20	262 ± 20
Voltage (V)	12.6 ± 1	29.5 ± 1	29.5 ± 0.2
Tube to work distance (mm)	9.52	9.52	9.52
Heat input (KJ/mm)	1.24	0.87	1.18

Table 4.3 Purging gas concentrations

Oxygen content (ppm)	500	5000
Component	Ar + 0.05% O	Ar + 0.5% O

To ensure precise control of oxygen concentration during welding, the oxygen level was continuously monitored using a PurgEye 300 instrument (Huntingdon Fusion Techniques, Burry Port, Wales). The purging process was carefully initiated and maintained until the target oxygen content was reached. Both pipe ends were sealed to ensure a controlled atmosphere, with inert gas introduced from one side and oxygen content continuously measured at the opposite end to maintain the specified environment.

4.3.4 Oxide Layer Analysis

The surface discoloration and oxide layer morphology were initially examined using a Keyence VR-2500 3D optical profilometer (Keyence Canada, Mississauga, ON, Canada). Detailed characterization of the oxide layers was then carried out by scanning electron microscopy (SEM) with two high-resolution instruments: Hitachi TM3000 (Hitachi High-Tech, Tokyo, Japan) and SU8230 FE-SEM (Hitachi High-Tech, Tokyo, Japan).

A specialized sample preparation technique—previously described in detail by the authors (Maroufkhani *et al.*, 2023), was employed to preserve the oxide layers during examination. This method combines hot mounting with advanced ion milling to maintain the structural integrity of the oxide in both cross-sectional and surface observations. For cross-sectional analysis, ion milling was performed in two stages: the first at 6 kV for 2 h with a reciprocation speed of 60 strokes/min and a ±15 ° swing angle, followed by a second stage at 5 kV for 1 h with 30 strokes/min and a ±30 ° swing angle. For surface preparation, ion milling was conducted at 5 kV for 3 min, using a reciprocation speed of 15 strokes/min and a ±60 ° swing angle. The IM4000 Plus ion mill (Hitachi) was used for all operations, ensuring precise surface conditioning suitable for high-resolution SEM imaging.

In addition to SEM, Electron Backscatter Diffraction (EBSD) was performed to analyze the grain structure of samples after buffing and welding. The chemical composition of the discoloration zone was determined using X-ray diffraction (XRD) analysis with a PANalytical X'Pert Pro diffractometer (Malvern Panalytical, Malvern, Worcestershire, United Kingdom) operating with Co Kα radiation (λ = 1.78896 Å) at 40 mA and 45 kV. Diffraction patterns were collected over a 2θ range of 20–80 °, with a step size of 0.016 ° and a total scan duration of 1 h and 37 min, yielding high-resolution data. Following the detailed morphological and compositional analysis of the oxide layer, electrochemical tests were conducted to evaluate the pitting corrosion behavior within HAZ.

4.3.5 Corrosion Testing

The pitting corrosion behavior within the HAZ was evaluated through cyclic polarization and EIS, following the ASTM G5-13 standard. The specimens were prepared to dimension of 15 × 15 mm, with an exposed surface area of 1 cm^2 in contact with the test solution (Figure 4.3). For each test, the sample was immersed in a solution prepared in an electrolyte composed of 0.5 M sodium chloride and 0.5 M sulfuric acid, which served as the electrolyte for simulating a corrosive environment (Aramaki, 2001; hai XIA *et al.*, 2012; Cardoso, Silva Nunes Cavalcante, Araujo Vieira, de Lima-Neto & Gomes da Silva, 2016; Fattah-Alhosseini & Vafaeian, 2016;

Osório, Rosa & Garcia, 2012). Experiments were carried out under a maintained temperature of 23 ± 2 °C, adhering to ASTM standards, and was repeated three times to ensure reproducibility.

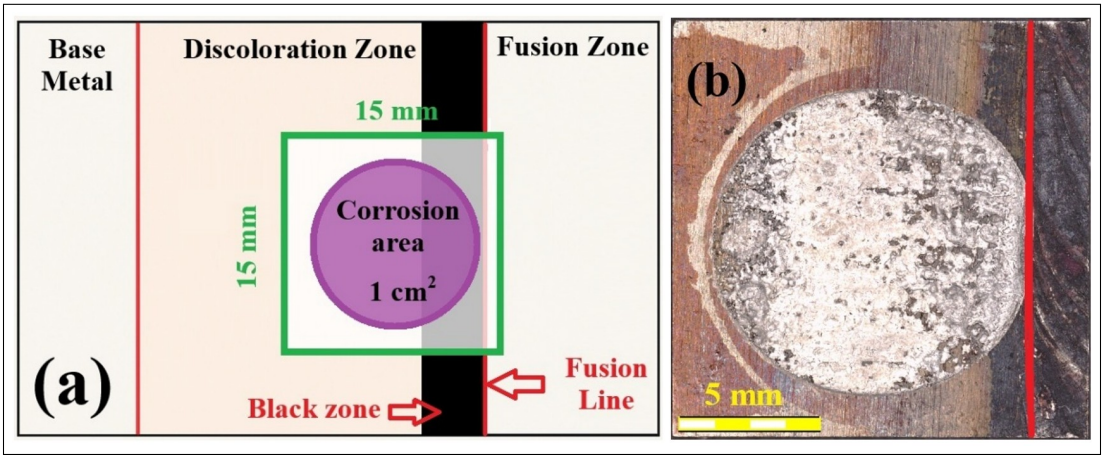

Figure 4.3 (a) Schematic representation of the location of the corrosion test sample, (b) Sample after corrosion test

The open-circuit potential (OCP), or corrosion potential, was recorded for 300 s to allow stabilization before polarization. Cyclic polarization scans began 50 mV below the OCP and extended up to 2000 mV (vs. Ag/AgCl), with a scan rate of 0.0016 V/s, as suggested by previous studies (Azuma, Kudo, Miyuki, Yamashita & Uchida, 2004; Loto, 2017; Sanni & Popoola, 2021). EIS measurements were performed over a frequency range of 0.1 Hz to 100 kHz, using a 10 mV AC perturbation at the OCP. The electrochemical setup comprised the 316L stainless steel specimen as the working electrode (WE), a platinum counter electrode (CE), and a saturated Ag/AgCl reference electrode (RE). All measurements were carried out using an Autolab PGSTAT302N potentiostat/galvanostat (Metrohm, Riverview, FL, USA) operated with NOVA 2.1.6 software (Metrohm, Riverview, FL, USA). The specimen holder was supplied by Redox Company (Redox, Norrköping, Sweden), and the electrochemical accessories—including the reference and counter electrodes—were obtained from Pine Research Inc. In this study, corrosion testing was conducted without removing the oxide layer, as the focus was on evaluating the pitting corrosion behavior under conditions simulating actual industrial operating conditions. However, this approach made it difficult to observe individual

pit propagation and distinguish corrosion features from surface imperfections and therefore, this aspect could not be investigated in the present work. Consequently, direct imaging of pit propagation under the intact oxide was not undertaken; propagation was assessed indirectly via cyclic polarization curve.

MATLAB R2022a (MathWorks, Natick, MA, USA) was utilized to plot the cyclic polarization and EIS data, allowing for detailed visualization and analysis of key electrochemical parameters. Pitting and passivation parameters, including pitting potential (E_{pit}), repassivation potential, and passive current density, were determined using the inflection point method (Bellezze *et al.*, 2018), which identifies slope changes along the polarization curve corresponding to transitions between active, passive, and pitting regimes (Bellezze *et al.*, 2018).

4.4 Results and Discussion

4.4.1 Oxide Layer Discoloration Analysis

Figure 4.4 presents the discoloration patterns observed on the inner welded surfaces (the red lines indicate the fusion line) under the different oxygen and surface roughness conditions. Since this study focuses on the pipe-relevant as-welded (heat-tinted) condition, no oxide-free control samples were included. The selected factor levels—oxygen content (500 vs. 5000 ppm) and surface roughness (40- vs. 60-grit)—represent the industrial extremes defined by the partner, allowing evaluation of both main effects and their interaction.

amples welded under 500 ppm oxygen exhibited a uniform discoloration gradient, transitioning gradually from lighter to darker shades for both roughness levels. At 5000 ppm, however, a distinct blackened region appeared near the weld interface for both surface finishes 4.4(d and c). This dark zone, consistent across all roughness types, indicates excessive oxidation (Maroufkhani *et al.*, 2023). This phenomenon will be further explained in subsequent sections, where the microstructural and corrosion properties of these zones are analyzed.

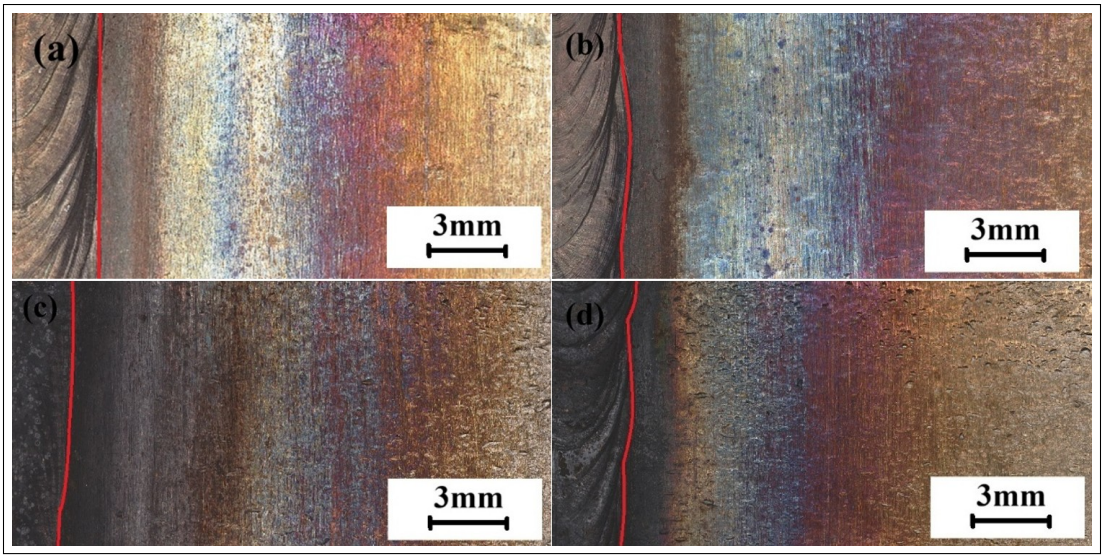

Figure 4.4 Discoloration of oxide layers (the red lines indicate the fusion line): (a) 500 ppm, B1; (b) 500 ppm, B2; (c) 5000 ppm, B1; (d) 5000 ppm, B2

n AISI 316L stainless steel, the weld pool solidifies in the ferrite–austenite mode, producing a predominantly austenitic weld metal. As shown in Figure 4.5 (d) , the fusion zone exhibits dendritic austenite, while Figure 4.5 (b) provides a closer view of the weld line and fusion boundary (highlighted by the blue box in panel a). Figure 4.5 (c) (red box in b) depicts the adjacent heat-affected zone (HAZ) and base metal region, where thermal exposure caused recrystallization and grain coarsening without melting or dendrite formation (Miranda-Pérez, Rodríguez-Vargas, Calliari & Pezzato, 2023).Our work evaluates only the inner surface of the HAZ (discoloration layer); the fusion-zone image is included solely to orient the reader and mark boundaries, and subsurface features inside the material do not affect our results and are not investigated in this paper.

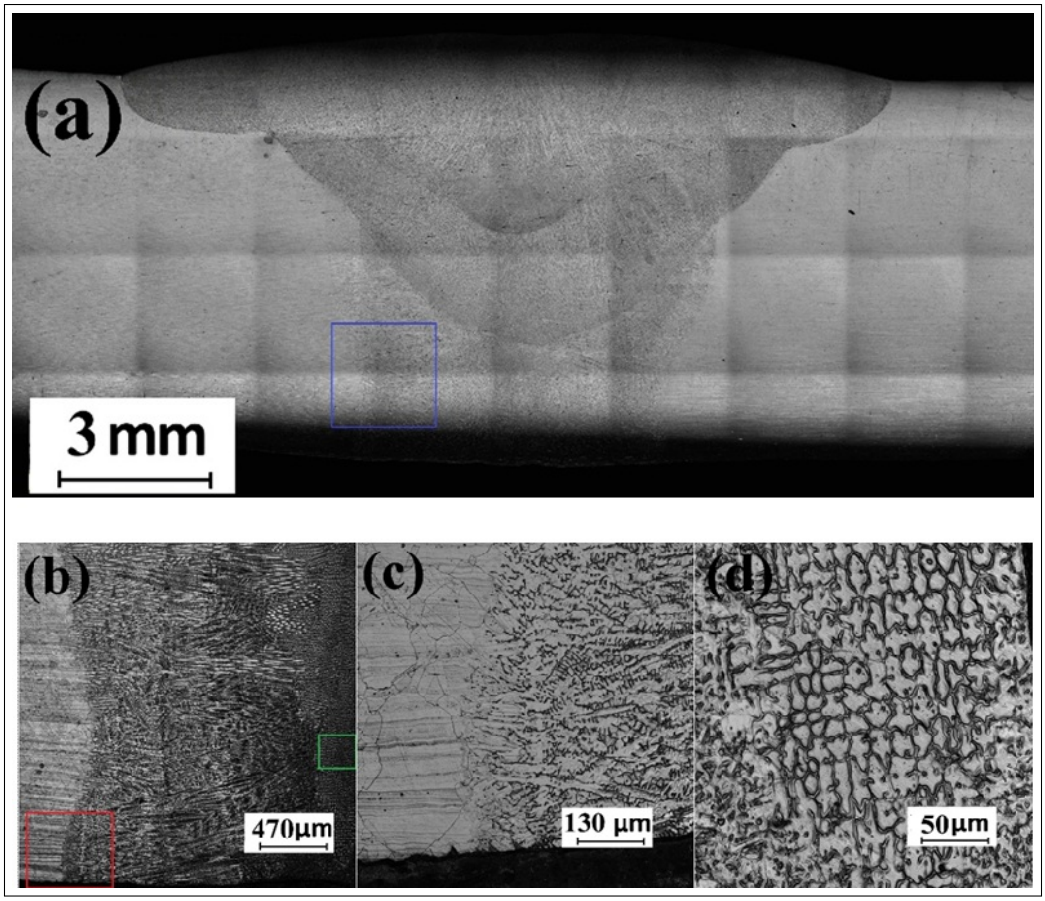

Figure 4.5 Microstructural analysis of the AISI 316L welded joint. (a) Cross-sectional image of the weld zone. (b) The blue square in (a) highlights the weld line. (c) The red square in (b) and (d) The green square in (b)

Figure 4.6 shows a cross-sectional SEM image and corresponding elemental maps (Fe, Cr, Mn) taken 1.5 mm from the fusion boundary of a weld produced under 5000 ppm oxygen with the rougher surface (B2). The inner oxide layer consists mainly of Fe, Cr, and Mn, consistent with the formation of spinel and corundum phases, in agreement with previous studies (Xie *et al.*, 2019; Huang *et al.*, 2020). TThe outermost oxide is dominated by iron oxides, featuring spinel-type structures enriched in Fe and an overlying corundum layer. A porous morphology, characteristic of excessive oxidation, was observed near the fusion line only under the 5000 ppm oxygen condition (Figure 4.7).

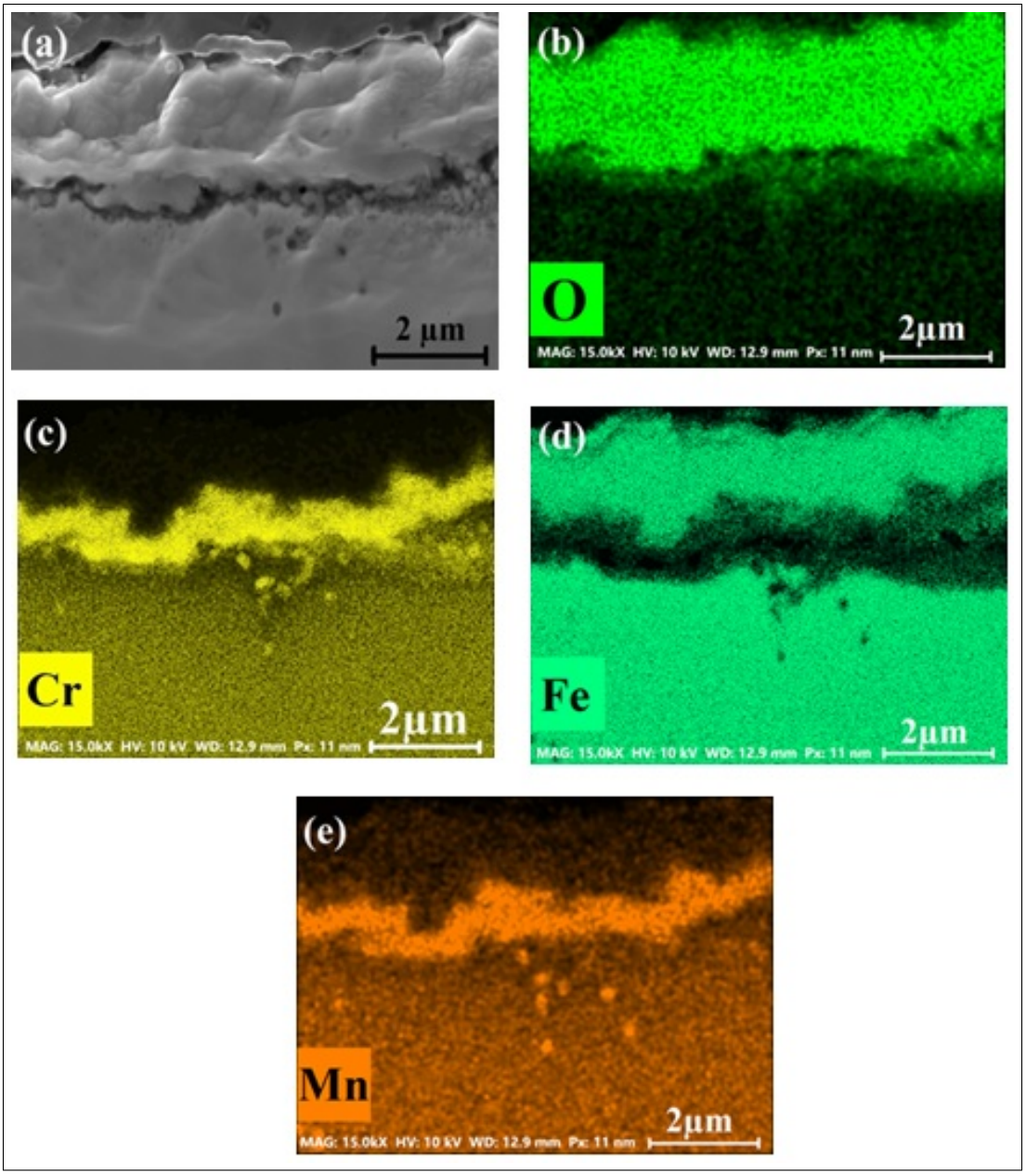

Figure 4.6 (a) Oxide cross-section 1.5 mm from fusion line (5000 ppm Oxygen, B2); elemental maps: (b) O, (c) Cr, (d) Fe, (e) Mn

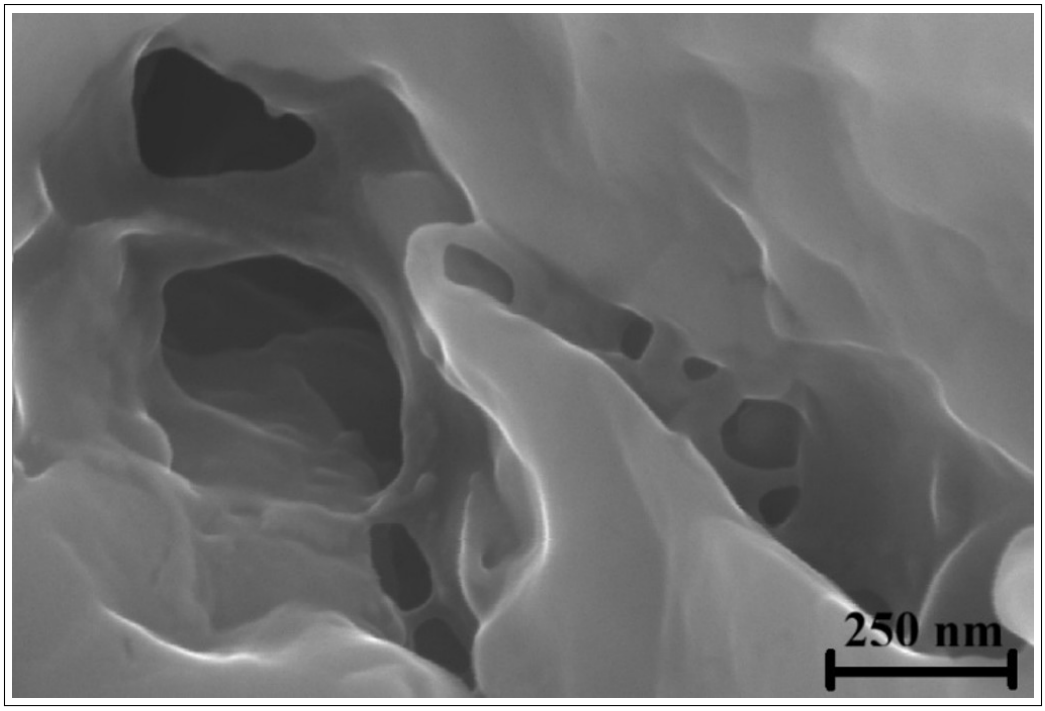

Figure 4.7 High-magnification SEM image of the porous oxide layer near the fusion line

The XRD pattern of the sample taken 1.5 mm from the fusion line under 5000 ppm oxygen shows peaks corresponding to spinel ($Fe(Mn, Cr)_2O_4$), corundum (hematite, Fe_2O_3), magnetite (Fe_3O_4), and wustite (FeO) (Figure 4.8). , confirming that the oxide layer is multi-phase. The presence of spinel indicates a mixed Fe–Cr–Mn oxide, while the corundum peaks reflect enrichment in Fe and Cr. The detection of wüstite, recognized by its distinct peak, suggests formation in the outermost oxide or within porous regions (Habib *et al.*, 2011). A magnetite peak at 53 ° and a strong wüstite peak in the FeO spectrum further support this interpretation. At room temperature, wüstite is thermodynamically unstable and tends to convert into magnetite through oxidation. This transformation is driven by oxygen diffusion into the wüstite structure, promoting the reaction:

$$3FeO + \frac{1}{2}O_2 \rightarrow Fe_3O_4 \tag{4.1}$$

When wüstite is porous, however, oxygen diffusion is restricted, preventing complete conversion to magnetite or hematite. A thin magnetite layer then forms on the surface, while wüstite persists beneath it—a phenomenon previously observed on corroded steel surfaces (Balasko *et al.*, 2025). The limited oxygen transport through porous wüstite thus slows oxidation and leaves residual FeO even at ambient conditions. Notably, FeO and Fe2O3 peaks are visible at 1.5 mm from the fusion line, with FeO identified near 48°, but these peaks disappear at 3 mm, as shown in 4.8.

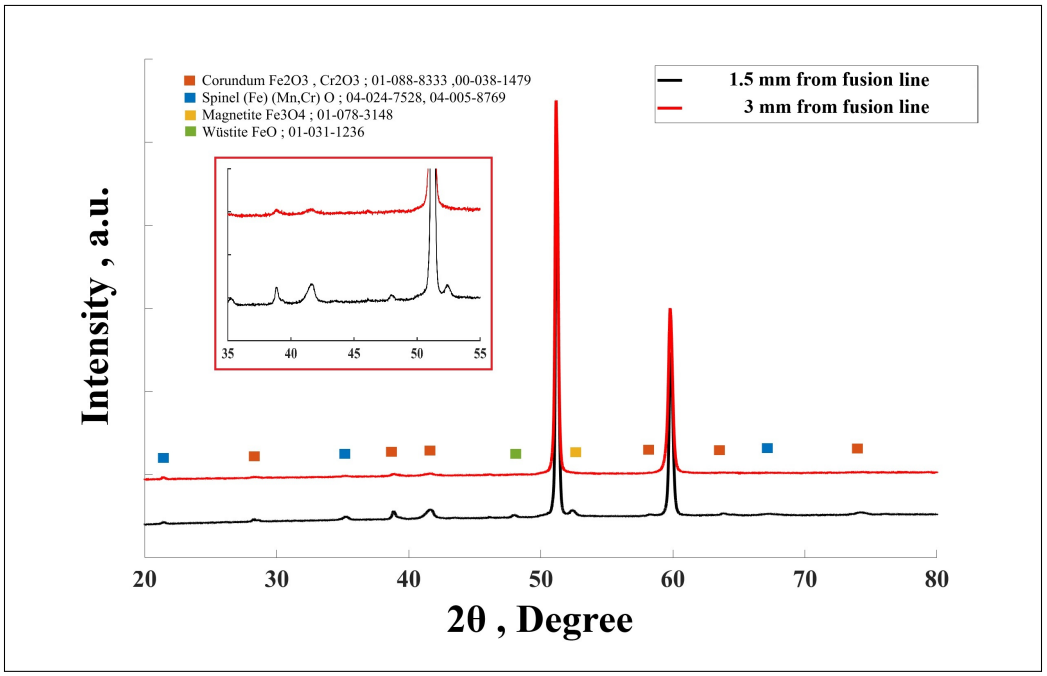

Figure 4.8 XRD pattern under 5000 ppm oxygen condition

Figure 4.9illustrates surface oxidation features likely associated with pre-existing surface imperfections from machining or forming. These features acted as preferential oxidation sites during welding, and their evolution differed significantly between the 500 ppm and 5000 ppm conditions. At the lower oxygen level, oxidation remained localized within surface cavities, producing a thin oxide with limited lateral growth (Figure 4.9a and b). At 5000 ppm oxygen content, oxidation is significantly more pronounced, with greater propagation beyond the original surface features. This is evident from the thicker oxide layers and more extensive coverage of the material surface. As shown in 4.9c, oxidation within surface features

propagates to a depth of approximately 7 micrometers. This oxidation leads to detachment or delamination of the oxide layer from the underlying metal.

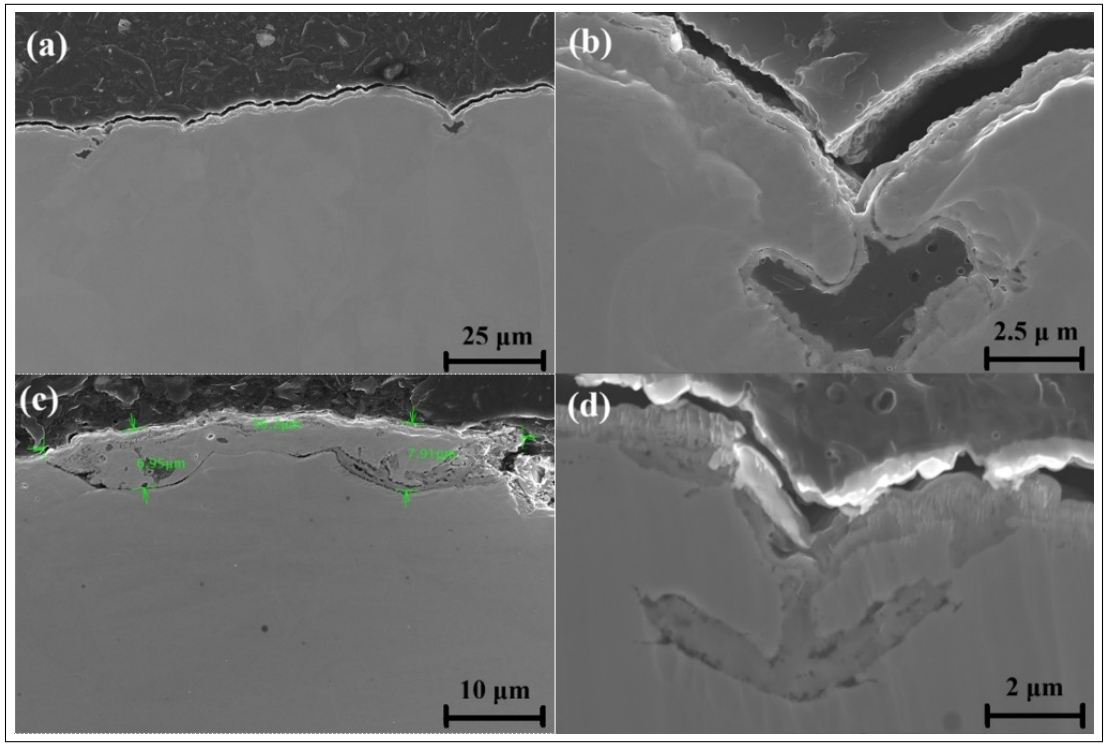

Figure 4.9 SEM of surface oxidation: (a,b) 500 ppm Oxygen, 3 mm from fusion line; (c,d) 5000 ppm Oxygen, 3 mm from fusion line

4.4.2 Surface Grain Size Before and After Welding

The EBSD maps in 4.10 show the cross-sectional microstructure of the AISI 316L stainless steel base metal. A variety of crystallographic orientations are observed, yet the grains appear uniform, with smooth boundaries and limited deformation. The average grain size is approximately 5 µm, establishing a baseline for assessing the effects of surface preparation and welding.

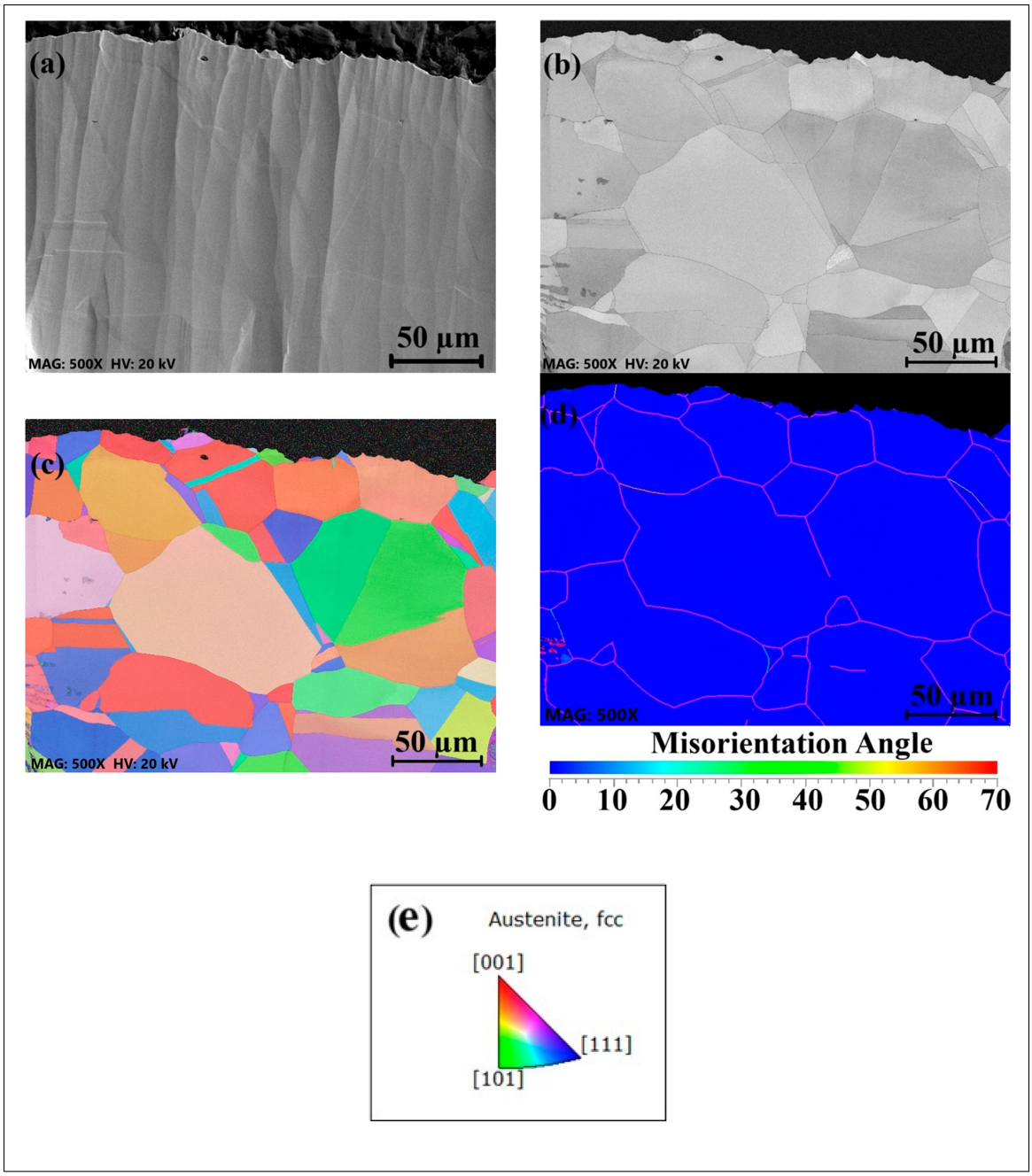

Figure 4.10 (a) SEM cross-section before welding/buffing; (b) band-contrast map (grain boundaries); (c) IPF-Z map used in simulations; (d) EBSD orientation map; (e) IPF color legend

The EBSD analysis of sample B2 (Figure 4.11) reveals localized misorientation near the surface, reaching up to 50.91°. This misorientation, visible in both the angular misorientation graph and

the color-coded EBSD map, reflects strain introduced by the buffing process. The affected zone extends roughly 5 μm beneath the surface, beyond which the grains return to their original orientation and size. Slip bands observed in Figure 4.11(c) confirm plastic deformation in the near-surface region.

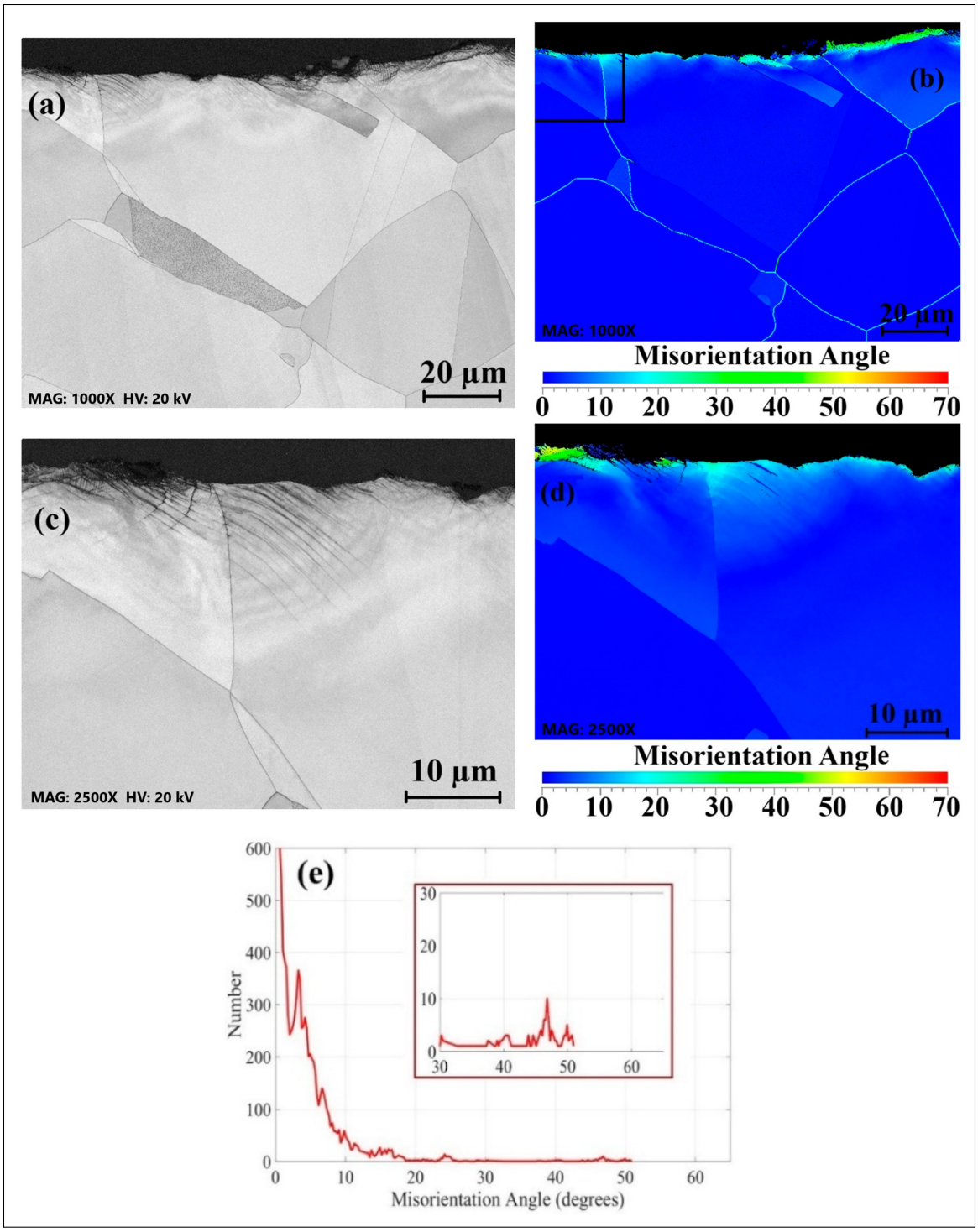

Figure 4.11 EBSD of 316L (B2): (a) band-contrast map; (b) orientation map; (c) higher-magnification view of the black zone in (b); (d) orientation map for (c); (e) average misorientation vs. depth for B2

In contrast, sample B1 exhibits greater surface deformation, with misorientation angles up to 61.11° and a deformation depth of about 7 μm. The misorientation is continuous across the surface, indicating a more uniform strain distribution. These findings highlight that higher roughness introduces more pronounced surface deformation, both in terms of misorientation angle and depth (Figure 4.12). The observed differences suggest that the surface preparation technique significantly influences the subsurface strain and deformation characteristics. Figure 4.12(c) shows a higher density of slip bands compared to B2, indicating more pronounced plastic deformation near the surface. The increased slip band density suggests a greater degree of localized strain.

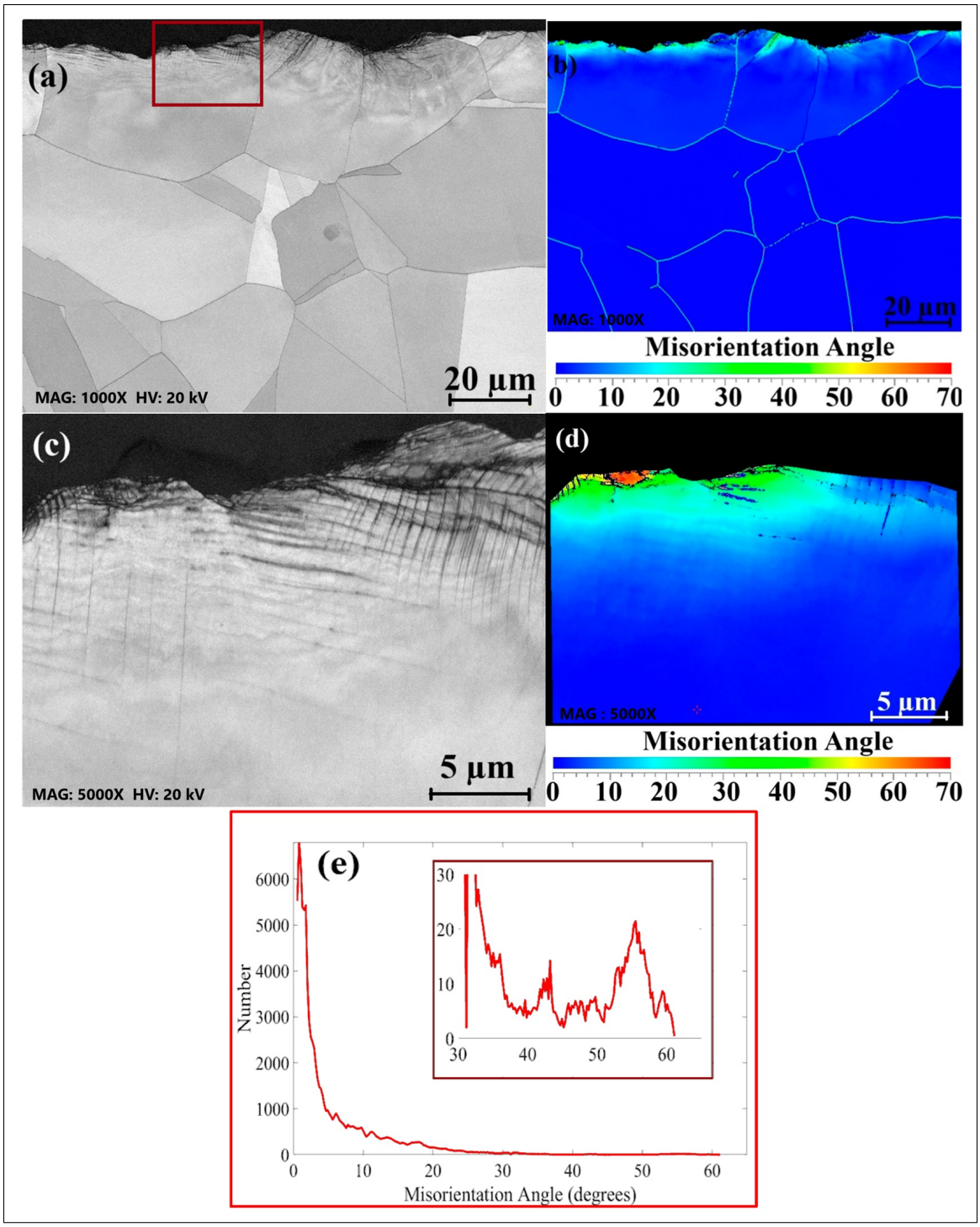

Figure 4.12 EBSD of 316L (B1): (a) band-contrast map; (b) orientation map; (c) higher-magnification view of the red zone in (a); (d) orientation map of the grain in (c); (e) average misorientation vs. depth for B1

Figure 4.13 compares the kernel average misorientation (KAM) maps for B1 (40-grit) and B2 (60-grit). The blue-to-red color gradient represents increasing misorientation. The B1 specimen shows higher concentrations of localized strain near the surface, corroborated by the normalized misorientation distribution(Figure 4.13(c)). This trend confirms that rougher surface preparation promotes more deformation-induced strain energy.

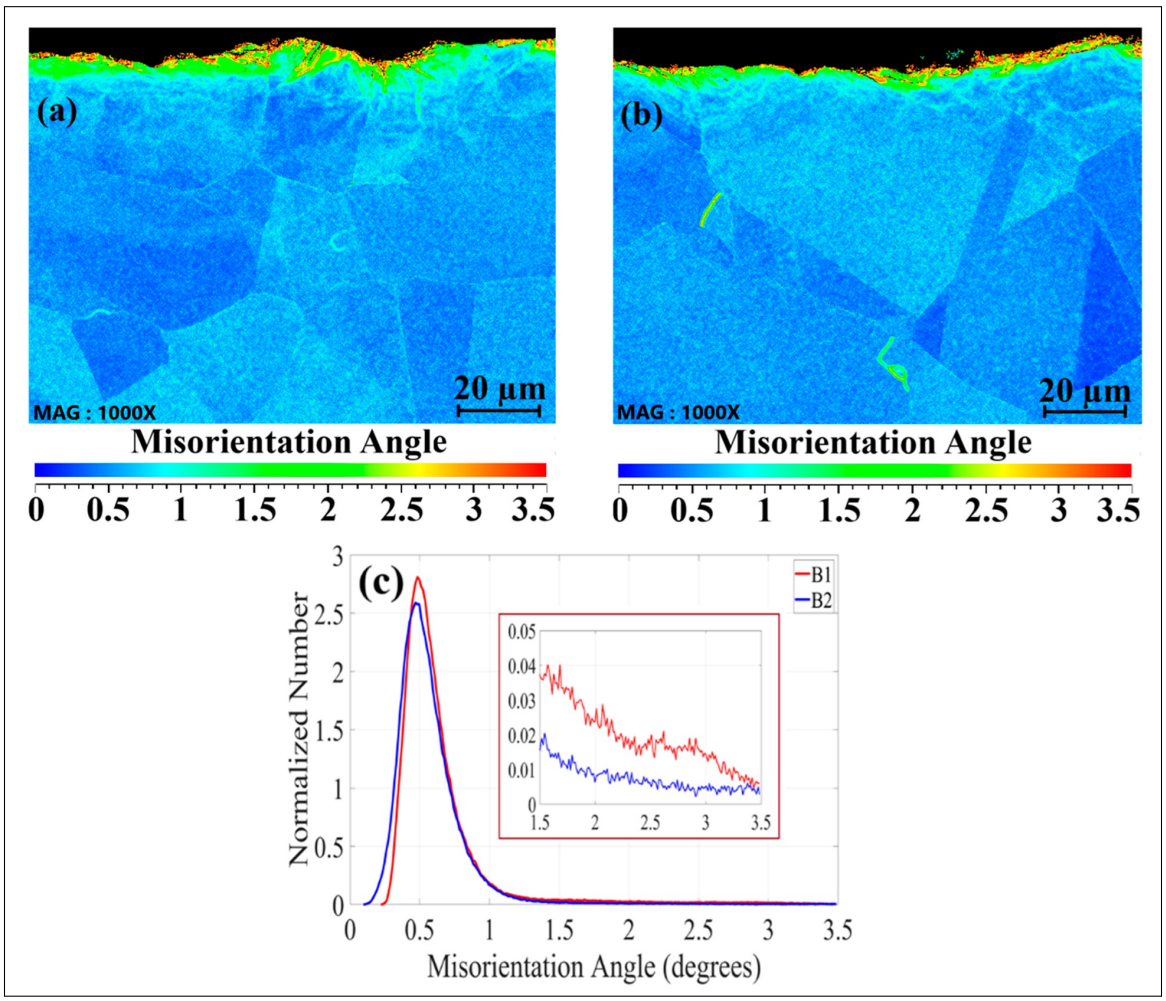

Figure 4.13 Kernel average misorientation analysis: (a) KAM map of B1, (b) KAM map of B2, (c) normalized misorientation distribution

As illustrated in Figure 4.13, , the misorientation introduced by buffing is largely relieved after welding due to the thermal cycle, which promotes recovery and recrystallization in the surface layer (Celik & Ersozlu, 2020; Pinto, Aota, Souza Filho, Raabe & Sandim,

2022; Zhao *et al.*, 2024). During recovery, stored strain energy is partially released, reducing misorientation and residual stress (Xiao *et al.*, 2024). ecrystallization subsequently replaces the deformed grains with new, strain-free grains (Gao *et al.*, 2020). In austenitic stainless steels, these microstructural transformations correlate closely with the observed discoloration: thicker oxides formed under higher thermal exposure correspond to recrystallized regions, whereas lighter discoloration zones reflect thinner Cr-rich oxides and limited recrystallization (Humphreys & Hatherly, 2012).

After welding, the near-surface microstructure consists of fine, equiaxed grains (Figure 4.14), markedly smaller than those in the pre-weld condition. The heat input during welding—particularly within the HAZ—drives this grain refinement. The prior deformation induced by buffing acts as a catalyst for recrystallization, providing nucleation sites for the formation of smaller grains during thermal exposure.

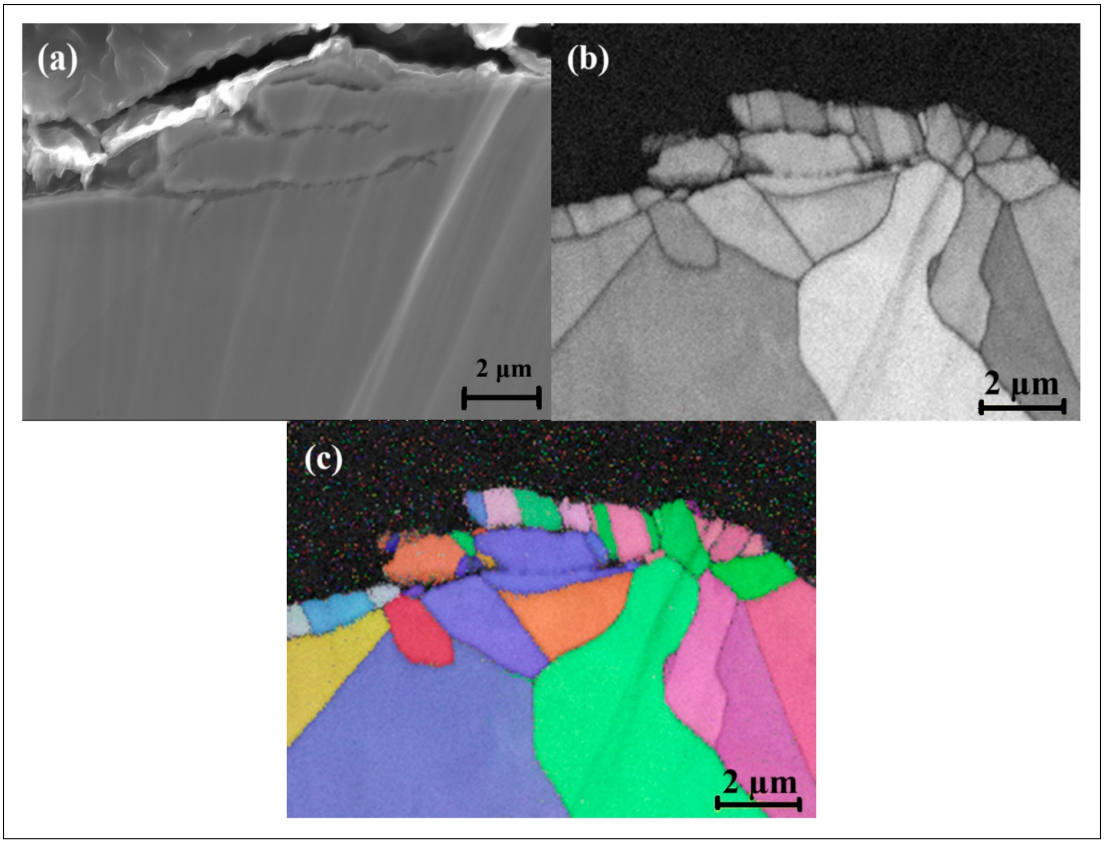

Figure 4.14 Post-weld EBSD, 316L (B2), 2.5 mm from fusion line: (a) SEM of HAZ; (b) grain boundary map (recrystallization/grain refinement); (c) orientation map

Overall, EBSD analysis revealed that the rougher 40-grit (B1) surface condition produced higher misorientation and greater strain energy near the surface than the 60-grit (B2) condition. This increased density of grain boundaries and local deformation directly influences corrosion behavior in the HAZ—regions most susceptible to pitting. Enhanced misorientation and grain boundary density in B1 likely accelerate the diffusion of alloying elements such as Cr and Mn along grain boundaries, linking surface roughness to both microstructural evolution and corrosion resistance.

4.4.3 Oxidation Analysis

Figure 4.15 shows elemental maps revealing Cr- and Mn-depleted zones along grain boundaries after welding. These depleted areas form due to preferential oxidation of Cr and Mn during high-temperature exposure.

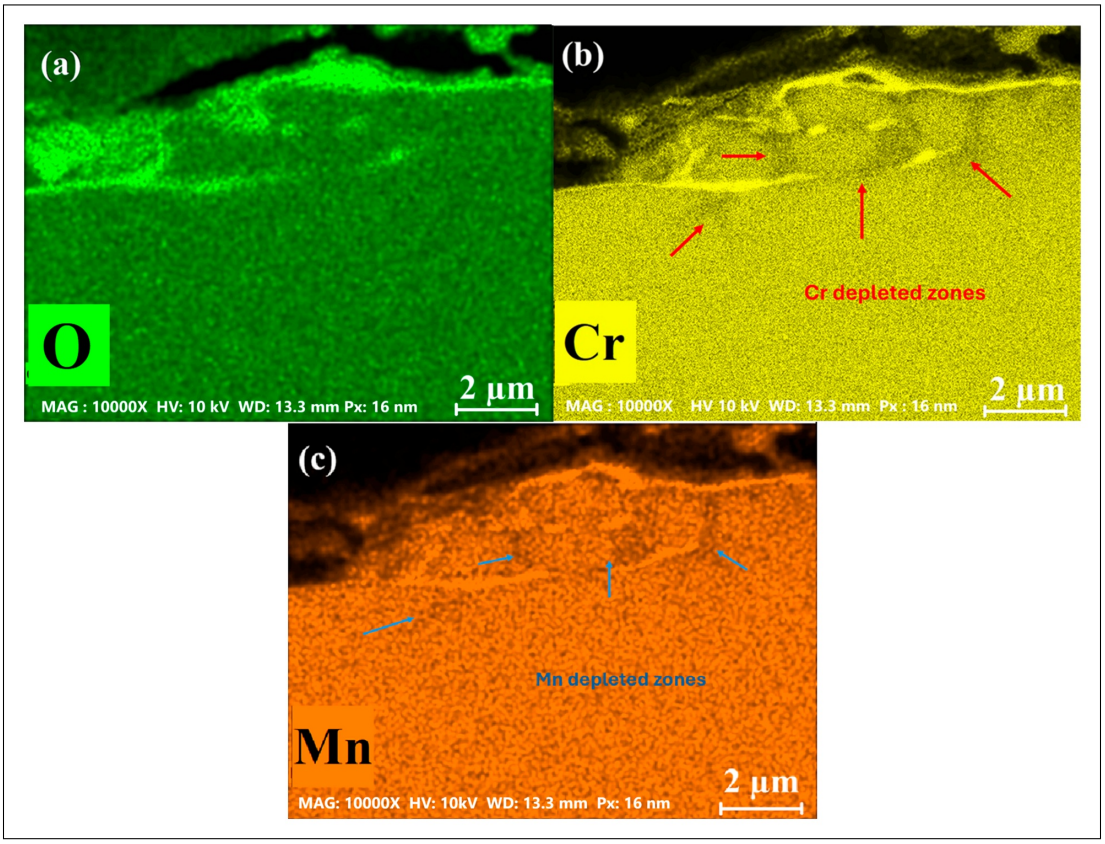

Figure 4.15 Elemental maps of the welded sample B2 (Figure 4.14): (a) O, (b) Cr, and (c) Mn.

The formation and stability of the oxide layer in welded AISI 316L stainless steel are governed by the diffusion of Cr and manganese (Mn) from the bulk material to the surface and grain boundaries (Wei, Wang, Misra & Chen, 2024). The diffusion process is strongly influenced by the grain boundary density, surface roughness, and the oxygen content in the purging gas during welding. Since grain boundaries act as fast diffusion pathways, the effective diffusivity (D_{eff}) can be estimated using a modified version of Hart's equation (Hart, 1957):

$$D_{\text{eff}} = (1 - f)D_L + fD_{GB} \tag{4.2}$$

Where D_{GB} and D_L are the grain boundary and lattice diffusion coefficients, respectively. f is the grain boundary volume fraction:

$$f = \frac{2\delta}{d} \tag{4.3}$$

Here, δ is the grain boundary width and d is the grain size. Since the grain boundary diffusion coefficient is significantly higher than the lattice diffusion coefficient ($D_{GB} \gg D_L$) (Sabioni *et al.*, 2012), the effective diffusivity can be approximated as (Wang *et al.*, 2024b):

$$D_{\text{eff}} \approx D_L + \frac{2\delta}{d} D_{GB} \tag{4.4}$$

This equation demonstrates that as grain size decreases, the contribution of grain boundary diffusion to D_{eff} increases. In the present study, samples buffed with 40-grit abrasive (B1) exhibit a higher density of grain boundaries compared to 60-grit (B2), resulting in enhanced diffusion rates for Cr and Mn.

The presence of oxygen in the backing gas accelerates oxidation kinetics by increasing the driving force for Cr diffusion towards the surface (Kim *et al.*, 2015). The flux of chromium (Cr) along grain boundaries can be estimated using the flux ratio equation where J_{GB}/J_L is the flux ratio (Lobb & Evans, 1981):

$$\frac{J_{GB}}{J_L} = \frac{2\delta_{GB}}{d_L} \left(\frac{D_{GB}}{D_L} \right)^{0.5} \tag{4.5}$$

According to Kim et al. (Kim *et al.*, 2015), the flux ratio in stainless steel is approximately 4% for coarse-grained (27 μm) structures. However, for finer grains, this ratio increases by

approximately 8% to 12%, meaning that the effective diffusion through grain boundaries becomes more dominant. The calculated values for different grain sizes indicate that as grain size decreases, Cr flux increases, which promotes the formation of Cr-rich oxides in the oxidation layer.

The preferential oxidation of Cr and Mn over other alloying elements, such as Fe or Ni, occurs because they exhibit a stronger affinity for oxygen and form oxides with lower Gibbs free energy, making them thermodynamically more favorable for oxidation (Lobb & Evans, 1981).

The depletion of Cr and Mn adjacent to grain boundaries reflects their thermodynamic preference for oxidation, forming (Cr_2O_3) and manganese oxide (MnO), both characterized by low Gibbs free energies of formation. These elements segregate toward boundaries during thermal exposure, where accelerated boundary diffusion at elevated temperatures produces localized depletion zones in the matrix (Zhao *et al.*, 2023).

As shown in Figure 4.16 , this setup enabled observation of early-stage oxidation while preserving thin oxides and grain boundary contrast. The maps reveal oxygen enrichment behind the grain boundaries and Cr accumulation along them, with corresponding oxygen depletion at the boundaries.

The localized build-up of chromium at grain boundaries is attributed to the rapid diffusion that occurs along grain boundaries, far exceeding the rate of lattice diffusion at high temperatures (Yamamoto *et al.*, 2023). Cr, being a highly reactive element, migrates towards the grain boundaries where it interacts with oxygen to form chromium oxide, a stable and protective oxide layer (Feng, Zhang, Liu & Kuang, 2023; Zhao *et al.*, 2023). This enrichment of chromium at the grain boundaries results in oxygen consumption for oxide formation, thereby leading to a notable reduction of oxygen concentration in those regions (Kim *et al.*, 2015).

Behind the grain boundaries, the elemental maps show a notable enrichment of oxygen. This was attributed to the diffusion of oxygen into the material's bulk during the high-temperature exposure. However, in these regions, the availability of Cr is limited due to its preferential

segregation to the grain boundaries, as seen in the microstructural analysis of the subsurface layers, reported in Figure 4.15. The Cr-depleted zones beneath the surface observed in Figure 4.15 further contribute to the inability of oxygen to form Cr oxide in these regions. Consequently, oxygen enrichment occurs in areas behind the grain boundaries where no protective oxide formation can occur, leading to potential vulnerability to localized oxidation or corrosion.

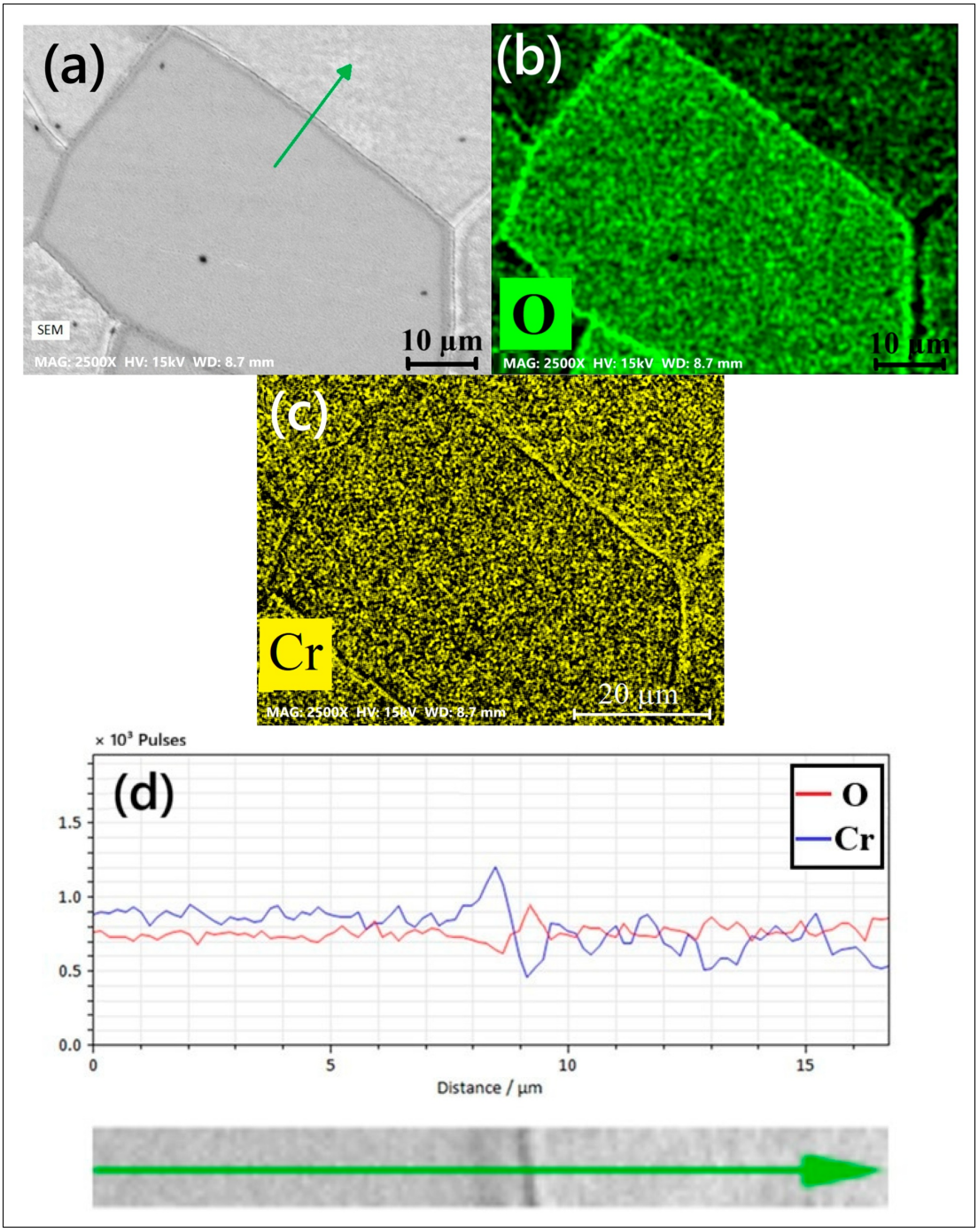

Figure 4.16 Hot-stage (800 °C) surface maps: (a) SEM (grain boundaries); (b) O; (c) Cr; (d) line profile across a grain boundary

Figure 4.17 compares surface oxidation 1 mm from the fusion line under 5000 ppm O2 for the two buffing conditions. The 40-grit (B1) sample exhibits a significantly thicker oxide (4.19 ± 0.40 μm), consistent with its rougher surface and higher density of high-energy sites that promote oxidation. Conversely, the 60-grit (B2) sample develops a thinner oxide (2.43 ± 0.23 μm), reflecting a more uniform element distribution and fewer preferential oxidation sites. Lower misorientation and reduced grain boundary density in B2 restricted oxidation, producing a thinner, more homogeneous oxide (Wang, Xue, Zhao, Zhang & Wang, 2024c).Ji et al. (Ji, Hao, Wang & Ke, 2025) similarly reported that higher roughness in 304 SS promotes thicker, porous oxides, whereas polished surfaces yield thinner, compact films.

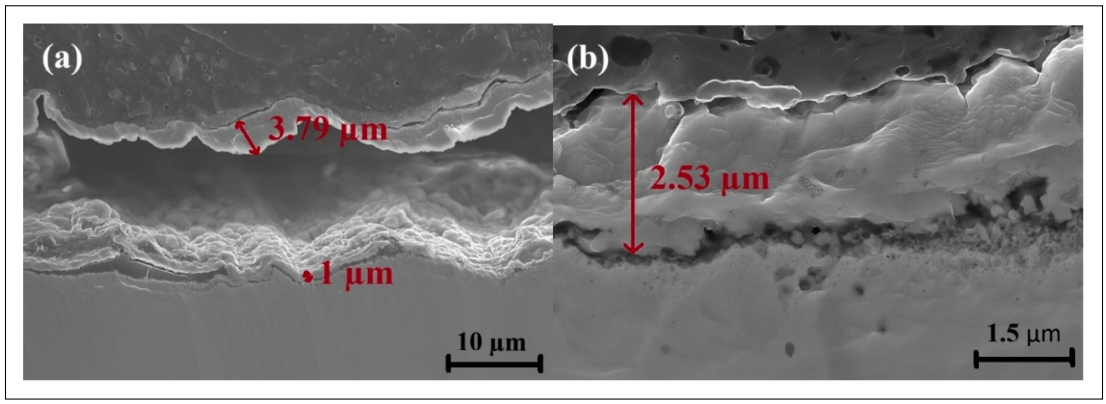

Figure 4.17 SEM images of surface oxidation at 1 mm from the fusion line under 5000 ppm oxygen condition with different buffing conditions: (a) B1, (b) B2

Previous studies have further clarified how grain size influences corrosion behavior. Zhao et al. (Zhao *et al.*, 2022) found that reducing austenite grain size in metastable stainless steel enhances corrosion resistance by lowering corrosion current density and increasing polarization resistance. Similarly, Fattah-alhosseini et al. (Fattah-Alhosseini, 2016) ffound that finer-grained AISI 430 stainless steel exhibited lower polarization resistance due to higher point defect density in the passive film, affecting its passivation stability. Additionally, studies by Balusamy et al. (Balusamy *et al.*, 2010) and Wang et al. (Wang *et al.*, 2018) highlighted that surface nano-crystallization can either enhance or deteriorate corrosion resistance, depending on the microstructural changes induced by grain refinement. In 316L, surface mechanical

attrition treatment (SMAT) initially reduces corrosion resistance due to defect introduction but improves stability after annealing (Hao *et al.*, 2009). Moreover, Wang et al. (Wang *et al.*, 2021) rreviewed the general influence of grain refinement on pitting corrosion and found that increasing grain boundary density can facilitate passive film formation, thereby improving resistance to localized attack. However, in certain cases, grain refinement increases the number of active sites for localized dissolution, making the material more susceptible to pitting corrosion under aggressive conditions (Aghuy *et al.*, 2015). These findings highlight the complex interplay between grain structure, passive film stability, and localized corrosion resistance.

4.4.4 EIS Analysis

The EIS results, represented in Nyquist (Figure 4.18a), Bode (Figure 4.18c), and phase angle (Figure 4.18d) plots, combined with the equivalent circuit fitting parameters, offer important insights into how surface roughness and oxygen concentration influence the corrosion resistance of welded AISI 316L stainless steel (Figure 4.18, Table 4.4). The equivalent circuit used for fitting the EIS data is based on similar models reported previously in the literature (Hernández *et al.*, 2020) and includes the following parameters, as shown in Figure 4.18b: R_s (solution resistance) represents the resistance of the electrolyte solution. R_{ct1} and R_{ct2} (Charge Transfer Resistance) represent the resistance to charge transfer at the electrode/electrolyte interface. In the present study, R_{ct1} corresponds to the initial oxidation process, while R_{ct2} is linked to the behavior after the oxide layer has formed. The CPE (Constant Phase Element) models non-ideal capacitance behavior resulting from surface roughness, heterogeneity, or defects in the oxide layer and α is the exponent in CPE. This configuration allows for a more accurate representation of the complex oxide film and the electrochemical processes occurring at both the outer oxide/electrolyte interface (CPE1, R_{ct1}) and the inner oxide/metal interface (CPE2, R_{ct2}).

The Nyquist plots indicate that 40-grit (B1) samples display larger semicircles compared to 60-grit (B2) samples at both oxygen levels. This suggests that the rougher surface (B1) offers

higher R_{ct2} compared to the smoother surface (B2). At 500 ppm, the R_{ct1} value for 500B1 is 1195.47 ± 318.18 Ω, while it decreases to 534.51 ± 150.97 Ω for 500B2. Similarly, at 5000 ppm oxygen, the R_{ct1} value for 5000B1 is 999.49 ± 98.55 Ω, whereas it is 344.81 ± 34.25 Ω for 5000B2. These results indicate that the rougher surface (B1) develops a more resistive and thicker oxide layer, thereby confirming the microstructural results reported in Figure 4.17.

The Bode impedance magnitude plots and phase angle plots further support the Nyquist plot observations. The impedance magnitude for 40-grit (B1) is consistently higher than that for 60-grit (B2) across the frequency range, especially at 500 ppm. The higher impedance reflects better barrier properties in B1 samples. The phase angle plots reveal that B1 samples maintain a higher phase angle at intermediate frequencies compared to B2. At 5000 ppm oxygen, the impedance magnitude and phase angle drop for both B1 and B2 samples, but B1 still exhibits better performance. This reduction in performance at higher oxygen levels was attributed to the formation of porous and less protective oxide layers, which are less effective at preventing corrosion.

As shown in Table 4.4, CPE1 values increase with both increasing oxygen content and decreasing surface roughness. For instance, CPE1 for 500B1 is 236.35 ± 38.84 $\mu s^{\circ}/\Omega$ and increases to 563.2 ± 151.25 $\mu s^{\circ}/\Omega$ in 500B2, and to 692.58 ± 136.83 $\mu s^{\circ}/\Omega$ in 5000B2. The corresponding α values slightly decrease, from 0.86 ± 0.01 in 500B1 to 0.83 ± 0.06 in 5000B2, indicating more non-ideal capacitive behavior and higher surface heterogeneity in smoother or more oxidized samples. CPE2 also increases significantly with oxygen content, particularly in B1 samples—from 2962.53 ± 479.05 $\mu s^{\circ}/\Omega$ at 500 ppm to 7427.93 ± 56.7 $\mu s^{\circ}/\Omega$ at 5000 ppm—confirming that the oxide layers formed at higher oxygen levels are more porous and less protective. This is consistent with the reduction in both R_{ct1} and R_{ct2} values under these conditions.

An effective way to assess corrosion resistance is through the analysis of polarization resistance. This parameter, which is the sum of charge transfer resistances ($R_{total} = R_{ct1} + R_{ct2}$), serves as an indicator of a material's ability to withstand corrosive environments — with higher values

reflecting enhanced resistance to corrosion (Li *et al.*, 2024). Among the samples, 500B1 (1202.04 Ω) exhibits the highest total resistance (R_{total}), while 5000B2 (348.12 Ω) shows the lowest.

As shown in Figure 4.18c and d, higher oxygen content (5000 ppm) reduces corrosion resistance for both buffing conditions. This is evident in the reduced R_{ct2} values, lower impedance magnitudes, and lower phase angles. This behavior could be related to the formation of more porous oxide layers with increasing oxygen levels, as reported in the literature (Habib *et al.*, 2011; Maroufkhani *et al.*, 2023). The porous layer reduces the protective properties of the surface, leading to increased susceptibility to corrosion.

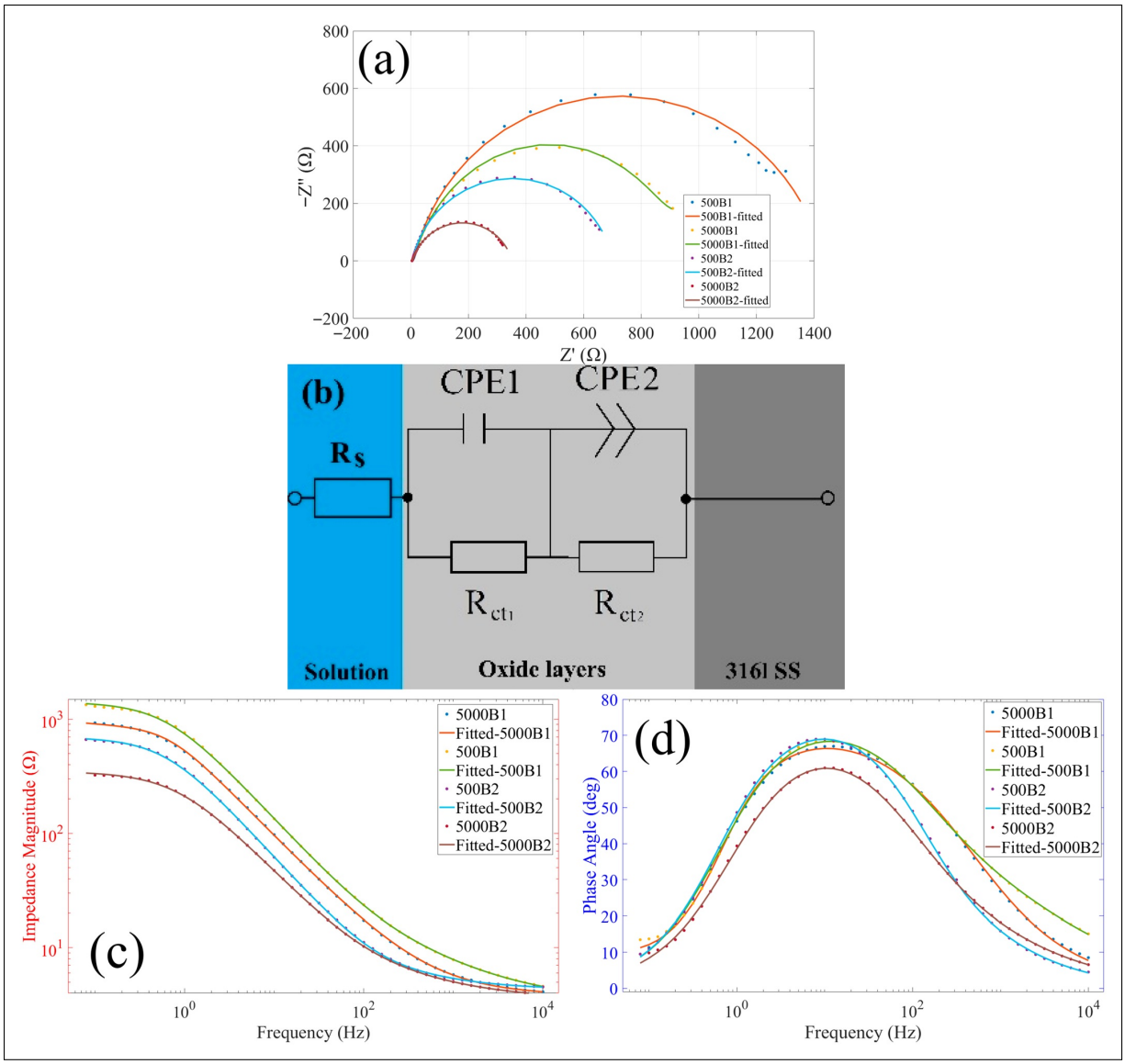

Figure 4.18 (a) Nyquist plots (B1 and B2); (b) equivalent circuit used for fits; (c) Bode magnitude; (d) phase angle vs. frequency

Table 4.4 Fitted EIS parameters for (B1) and (B2) samples at 500 ppm and 5000 ppm oxygen concentrations

Parameter	**CPE1** ($\mu s^{\circ}/\Omega$)	α	**CPE2** ($\mu s^{\circ}/\Omega$)	α	**Rs** (Ω)	**Rct1** (Ω)	**Rct2** (Ω)	**X2**
500B1	236.35 ± 38.84	0.86± 0.01	2962.53± 479.05	0.5 ± 0.01	3.30± 0.01	1195.47± 318.18	6.57± 3.2	0.049± 0.042
5000B1	310.67 ± 0	0.84± 0.06	7427.93± 56.7	0.5 ± 0.03	3.60± 1.12	999.49± 98.55	4.55± 2.06	0.0039± 0.003
500B2	563.2 ± 151.25	0.85± 0.03	3443.84± 56.66	0.62± 0.01	3.83± 0.43	534.51± 150.97	1.34± 0.2	0.0077± 0.003
5000B2	692.58 ± 136.83	0.83± 0.06	7039.1 ± 44.66	0.5 ± 0.01	3.47± 0.95	344.81± 34.25	3.31± 10.40	0.0054± 0.002

4.4.5 Analysis of the pitting corrosion

Figure 4.19 and Table 4.5 present the cyclic polarization curves and key parameters for samples prepared with 40-grit (B1) and 60-grit (B2) buffing at oxygen concentrations of 500 ppm and 5000 ppm. These results are analyzed in conjunction with the EIS data to provide a more comprehensive understanding of how pitting corrosion resistance varies with surface roughness and oxygen level.

At 500 ppm oxygen, the pitting current density for B1 is 234±16 μA, which is slightly lower than 253 ± 55 μA for B2 with same pitting potential (0.48 V). This suggests that B1 samples, with a rougher surface, exhibit better initial resistance to pit initiation. However, when considering repassivation behavior, the 60-grit B2 samples show superior performance. The repassivation current density for B2 is 429 ± 11 μA, significantly higher than 379 ± 1 μA for B1, indicating better recovery from localized corrosion events in B2. The hysteresis loop area for B2 (1.15

A. V) is also smaller than that of B1 (1.26 A. V), indicating lower energy loss during pit repassivation and more stable pit recovery.

At 5000 ppm oxygen, the B1 samples exhibit ipitt 251 μA, which is lower than 409 ± 37 μA for B2 while B2 has 0.53± 0.02 V pitting potential which is higher than 0.50 V for B1, indicating better resistance to pit initiation for B1. However, the repassivation behavior remains superior for B2. The repassivation current density for B2 is 748 ± 71 μA , higher than that for B1 (483 μA). The hysteresis loop area for B2 (1.12 A. V) is smaller than that of B1 (1.33 A. V) indicating better pit recovery and overall stability for B2.

These results highlight a contrast between the initiation and propagation stages of pitting corrosion. While B1 samples exhibit better resistance to pit initiation (lower ipitt) due to their higher density of grain boundaries and thicker oxide layer acting as initial barriers to pit formation, they are more susceptible to pit propagation and have poorer repassivation behavior. This is because the grain boundaries in B1 are sites of Cr and Mn depletion, which weaken the passive film, as confirmed by EBSD and elemental mapping results. This phenomenon occurs because grain boundaries are high-energy sites with greater atomic diffusivity, making them more reactive and prone to oxidation. Cr and Mn, which have a high affinity for oxygen, migrate to these grain boundaries during high-temperature processes, such as welding or heat exposure, to form oxides like Cr_2O_3 and MnO (Hernández *et al.*, 2020). Consequently, the adjacent regions are left deficient in Cr and Mn, creating weak points. These weak points lead to an increased likelihood of pit propagation. B2 samples have fewer grain boundaries near the surface due to lower initial misorientation. This depletion makes the pits more likely to propagate once they are initiated.

On the other hand, B2 samples, with smoother surfaces, have fewer grain boundaries near the surface. This results in a more stable passive film and better repassivation capabilities, as reflected in the smaller hysteresis loop area and lower irepassive. The smoother surface of B2 facilitates more effective repassivation, reducing the likelihood of pit growth.

The superior pitting corrosion resistance of the 500 ppm samples compared to the 5000 ppm samples can be clearly observed from the polarization curves. The 500 ppm samples exhibit a lower pitting current density and a more positive pitting potential, indicating that higher energy is required for pit initiation and propagation. These features are indicative of a more stable passive layer, providing better protection against localized corrosion. Conversely, the 5000 ppm samples exhibit elevated pitting current density, which is linked to the formation of a porous oxide layer. This porous structure facilitates the ingress of chloride ions into the substrate, thereby increasing susceptibility to localized corrosion. The porous nature of the oxide layer disrupts the uniformity and stability of the passive film, leading to easier pit initiation and faster propagation of localized corrosion. The correlation with EIS results further supports these interpretations. The higher overall impedance measured for B1 reflects its thicker, more resistive oxide layer formed on the rougher surface. However, the cyclic polarization data show that despite higher impedance, localized corrosion resistance is superior in B2, which repassivates more efficiently once pits form. Therefore, while rougher surfaces (B1) provide stronger initial resistance to pit initiation, smoother surfaces (B2) demonstrate better repassivation and long-term stability against localized corrosion. Finally, since the oxide layer was intentionally preserved during corrosion testing, the exact pit locations and propagation features could not be directly observed. The discoloration layer served as a protective oxide, preventing direct visualization of pit initiation and growth, and thus the corrosion behavior was evaluated indirectly through electrochemical analysis.

Following the comprehensive EIS analysis in Section 4.4.4, which revealed clear differences across roughness and oxygen content, Section 4.4.5 examines corrosion behavior via cyclic polarization. With the oxide left intact, surface finish affects corrosion differently at initiation versus growth: EIS shows the smoother surface B2 (60-grit) has lower Rct and thus lower resistance to pit initiation, while the rougher B1 (40-grit) exhibits higher barrier properties. In contrast, the polarization data confirms that the smoother B2 limits pit growth and more readily repassivates smaller hysteresis, whereas the rougher B1 permits deeper propagation once initiation occurs.

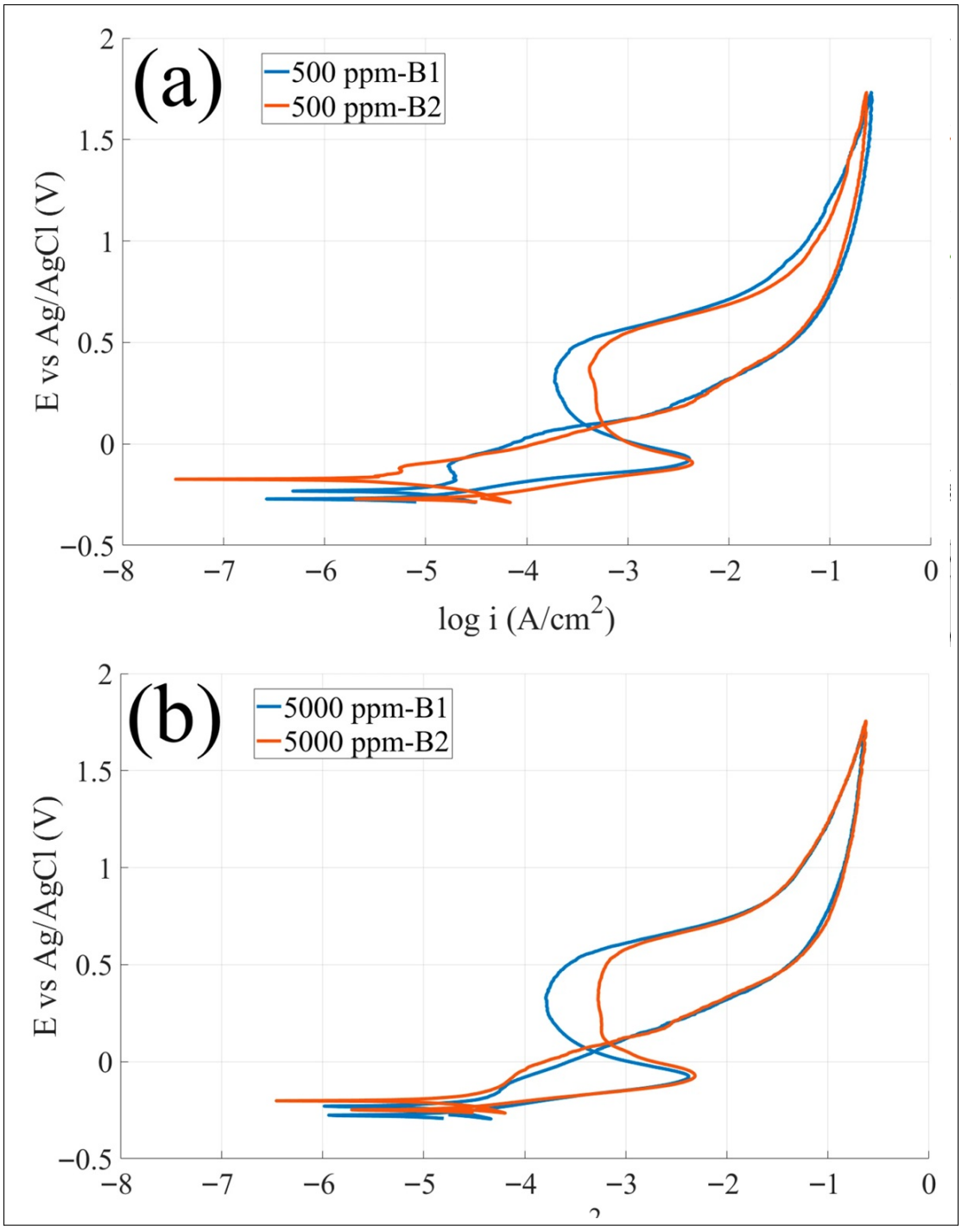

Figure 4.19 Cyclic polarization curves for different surface roughness levels with two oxygen contents in the backing gas: (a) 500 ppm, (b) 5000 ppm

Table 4.5 Corrosion parameters from cyclic polarization curve of 316L SS with varying oxygen content and surface roughness

Sample	$i_{\mathbf{pitt}}$ (μA)	$E_{\mathbf{pitt}}$ (V)	$i_{\mathbf{passive}}$ (μA)	$E_{\mathbf{passive}}$ (V)	$i_{\mathbf{repassive}}$ (μA)	$E_{\mathbf{repassive}}$ (V)	**Hysteresis area (W)**
500B1	234 ± 16	0.48 ± 0.02	271 ± 24	0.07 ± 0.01	379 ± 1	0.07 ± 0.01	1.26 ± 0.00
5000B1	251 ± 14	0.50 ± 0.01	251 ± 19	0.08 ± 0.01	483 ± 3	0.05 ± 0.01	1.33 ± 0.05
500B2	253 ± 55	0.48 ± 0.00	257 ± 27	0.03 ± 0.01	429 ± 11	0.06 ± 0.02	1.15 ± 0.11
5000B2	409 ± 37	0.53 ± 0.02	461 ± 89	0.13 ± 0.02	748 ± 71	0.10 ± 0.01	1.12 ± 0.01

4.5 Conclusions

In the present work, an investigation was conducted on the combined effects of surface roughness and oxygen content in the purging gas on the pitting corrosion resistance of AISI 316L stainless steel welds without removing the oxides. The results provide important insights into the role of oxide layer characteristics and surface morphology in influencing the material's corrosion behavior. The key findings are summarized as follows:

1. Surface buffing significantly affected the misorientation of grains and recrystallization after welding. Higher misorientation levels were observed for the rougher surface, while the smoother surface exhibited a more uniform misorientation with lower values.

2. Chromium (Cr) and manganese (Mn) depleted zones were revealed along the grain boundaries. The Cr-Mn oxide layer was thicker on the rougher surface. This thicker oxide layer offers initial resistance to corrosion.
3. Surface roughness significantly affects corrosion resistance, with smoother surfaces exhibiting lower pitting corrosion resistance compared to rougher surfaces. However, smoother surfaces demonstrated better pitting propagation resistance. The findings are explained in terms of the rogher surface's higher grain boundary density, which helps prevent initiation of localized corrosion, though it does not prevent the development of deeper pits once they have formed.
4. The oxygen content in the purging gas strongly influences the oxide layer properties and corrosion resistance. Samples welded with 500 ppm oxygen demonstrated superior pitting resistance compared to those welded with 5000 ppm oxygen. In samples welded with 5000 ppm oxygen, reduced pitting corrosion resistance was observed due to the porous oxide structure and increased oxidation in surface defects, such as micro-holes formed during metal forming. These defects act as pathways for aggressive ions, promoting localized corrosion and pit propagation.

The findings of the present work suggest that optimizing oxygen content and surface preparation techniques are essential for improving the discoloration severity and corrosion resistance of welded joints in industrial applications. Future work will map intermediate purge-gas oxygen content between 500 and 5000 ppm. Industrial perspective: For inner-surface welds where discoloration remains, keep purge oxygen ≤ 500 ppm to limit porous oxides and preserve pitting resistance. Smoother preparation where repassivation matters is preferred—a rougher surface can raise initiation resistance but tends to favor faster pit growth.

Author Contributions

Conceptualization, M.M., I.R. and M.J.; methodology, M.M., A.K. and M.J.; software, M.M.; formal analysis, M.J.; investigation, M.M. and A.K.; resources, M.M. and I.R.; writing—original draft preparation, M.M.; writing—review and editing, M.M., A.K. and M.J.;

visualization, M.M.; supervision, A.K., I.R. and M.J. All authors have read and agreed to the published version of the manuscript.

Funding

This research was funded by the Natural Sciences and Engineering Research Council of Canada (NSERC) under Grant Number CRD 542299-19.

Data Availability Statement

All data supporting the findings of this study are included within the article.

Acknowledgments

The authors sincerely thank PCL Construction for their significant support and material provision, which greatly facilitated the success of this study. Appreciation is extended to Mohammad Saadati for his expert guidance and assistance with electron microscopy analyses. The authors also extend their gratitude to Alireza Tirehkar for his valuable assistance in generating the MATLAB code used in this study and to Hamza Sofiane for his support with the Hotstage microscope experiments. This research was made possible through the collaboration with PCL Construction, based in Edmonton, Alberta, Canada, and financial support from the Natural Sciences and Engineering Research Council of Canada (NSERC) under Grant Number CRD 542299-19.

Conflicts of Interest

Author Iulian Radu is employed by PCL Industrial Constructor Inc. The remaining authors declare that the research was conducted in the absence of any commercial or financial relationships that could be construed as a potential conflict of interest.

CHAPTER 5

THERMODYNAMIC AND KINETIC ANALYSES OF HIGH TEMPERATURE OXIDATION OF 316L STAINLESS STEEL

[a,b,d,e] Department of Mechanical Engineering, École de Technologie Supérieure (ÉTS), 1100 Notre-Dame Street West, Montreal, QC, Canada,H3C 1K3

[c] PCL Industrial Management Inc.,2107 4 St, Nisku, AB, Canada,T9E 7W6

Paper Submitted for publication in Results in Materials, Elsevier , February 2025

Abstract

This study investigates the thermodynamic behavior and non-isothermal oxidation kinetics of 316L stainless steel in the temperature range of 1100–1373 K, with relevance to the heat-affected zone during welding in oil and gas pipeline applications. Thermogravimetric analysis was performed at heating rates of 5, 10, 15, 20, and 25 K/min to study the high-temperature oxidation kinetics of AISI 316L stainless steel welds. Kinetic analysis was conducted using Kennedy-Clark and Coats-Redfern methods as well as Friedman, Starink, Kissinger-Akahira-Sunose, and Flynn-Wall-Ozawa model-free isoconversional methods. Activation energies determined using isoconversional models ranged from 224.79 to 233.81 kJ/mol. The second-order (F2) and third-order (F3) reaction models provided the best fit to the experimental data, as confirmed by Criado master plot analysis. Thermodynamic properties ($\Delta H^{\neq}$, $\Delta S^{\neq}$, $\Delta G^{\neq}$) were also calculated for isoconversional models. FactSage thermochemical simulations revealed the formation of a dual-layer protective oxide scale primarily composed of spinel and corundum phases. These oxide layers enhance oxidation resistance at high temperatures. The findings contribute to a mechanistic and kinetic understanding of high-temperature oxidation in 316L stainless steel, supporting its reliable application in demanding oil and gas environments.

Keywords: 316L Stainless steel, Activation energy, Isoconversional methods, Kinetics, Reaction mechanism, Solid state oxidation, Thermodynamics.

Nomenclature

Table 5.1 List of symbols and abbreviations

Symbol	Definition	Symbol	Definition
TGA	Thermogravimetric analysis	CR	Coats-Redfern
K_p	Parabolic rate constant	t	Time (s)
E_a	Activation energy (kJ/mol)	A	Pre-exponential factor
DTA	Differential Thermal Analysis	MFR	Modified Friedman
FWO	Flynn-Wall-Ozawa	R	Gas constant 8.314 (J/mol·K)
T_p	Peak temperature (K)	KAS	Kissinger-Akahira-Sunose
α	Degree of conversion	Wt	Weight percentage (%)
KC	Kennedy-Clark	DTG	Differential thermogravimetric
β	Heating rate (K/min)	T	Temperature (K)
$g(\alpha)$	Integral form of the reaction model	R2	Correlation coefficient
$\Delta H^{\neq}$	Enthalpy of activation	$\Delta S^{\neq}$	Entropy of activation
$\Delta G^{\neq}$	Gibbs energy of activation	h	Planck's constant (6.626×10^{-34} J·s)
k_B	Boltzmann's constant (1.381×10^{-23} J/K)	.	

5.1 Introduction

316L stainless steel belongs to the austenitic alloy family and is widely recognized for its superior resistance to corrosion as well as its robust mechanical properties (Hakimian, Pourrahimi, Bouzid & Hof, 2023). Stainless steels, particularly 316L, are widely utilized in industries such as chemical processing, pipeline, and aerospace due to their ability to form a protective oxide layer that impedes further oxidation and corrosion (Dudziak *et al.*, 2023; Hakimian *et al.*, 2023). The protective nature of the oxide layer is primarily attributed to the formation of Cr_2O_3, which acts as a barrier to oxygen diffusion and helps in improving their resistance to corrosion (Sedriks, 1996). However, the stability of this protective layer can be compromised under certain service conditions, particularly during welding processes. In welding applications, especially on the root side of the weld, the presence of residual oxygen in the backing gas (ranging from 50 to 5000 ppm) can lead to high-temperature oxidation and discoloration (Maroufkhani *et al.*, 2023). This discoloration is not merely aesthetic; it indicates a change in surface chemistry and oxide structure, which can reduce corrosion resistance and lead to weld rejection in accordance with standards such as AWS D18.1 and AWS D18.2 (Avery, 2000; Maroufkhani *et al.*, 2023). These standards impose strict limits on allowable oxidation levels for welds in corrosive service environments (Avery, 2000). Therefore, understanding oxidation kinetics and the influence of trace oxygen levels is essential for predicting long-term performance and ensuring weld quality. Accurately assessing the oxidation kinetics of 316L at elevated temperatures is critical to mitigating such effects and preserving the integrity of welded structures.

Thermogravimetric analysis (TGA) is a powerful technique for studying the oxidation kinetics of metals and alloys. By measuring weight changes as a function of temperature, TGA provides insights into the oxidation rates and the formation of different oxide phases (Vyazovkin & Wight, 2000; De Blasio, Noreña & Gil, 2019; Cheng, Zhang, Zhou, Zhang & Wang, 2021; Fatahi Amirdehi, Gholipour, Pourazadi, Dadkhah & Jafari, 2024). The data obtained from TGA can be further analyzed using isoconversional methods and model-fitting approaches to determine the activation energies and reaction mechanisms involved in the oxidation process

(Starink, 2003). Isoconversional methods offer a model-free approach to evaluating the kinetic parameters by examining the temperature dependence of the reaction rate at different degrees of conversion (Kissinger, 1957; Friedman, 1964; Flynn & Wall, 1966). These methods are advantageous as they do not require a predefined reaction model, thus providing a more accurate representation of the complex oxidation processes. The Friedman method, being a differential isoconversional technique, offers detailed kinetic information at each conversion level but is sensitive to experimental noise (Friedman, 1964). In contrast, FWO and KAS are integral methods that offer robustness against noise and are widely accepted for non-isothermal kinetic studies (Kissinger, 1957; Flynn & Wall, 1966). The Starink method was selected for its improved accuracy in calculating activation energy by correcting systematic errors associated with the temperature integral approximation used in KAS and FWO (Starink, 2003). Various studies have successfully applied these methods to calculate the activation energy (E_a) for stainless steels and other high-temperature materials (Brown *et al.*, 2000; Alhulaybi *et al.*, 2022; Demirci, Kıran Yıldırım, Tünçay, Kaya & Dikici, 2024). Model-fitting methods, including the Coats-Redfern and Kennedy-Clark methods, involve fitting experimental data to specific reaction models to extract kinetic parameters such as activation energies (Coats & Redfern, 1964). These methods can offer detailed insights into the reaction mechanisms by assuming a specific functional form for the reaction rate. Both methods were used to enhance the robustness of the kinetic analysis. The CR method provides a reliable estimation for ideal reaction behaviors, and the KC method improves the fit for complex, multi-step reactions due to its refined approximation (Coats & Redfern, 1964, 1965; Kennedy & Clark, 1997). Using both allows cross-validation of the activation energy and better identification of the most representative solid-state reaction model. In Section 5.2.2, we provide more detail about all methods and related equations.

Thermogravimetric analysis (TGA) serves as an effective method for investigating the oxidation kinetics (De Blasio *et al.*, 2019; Cheng *et al.*, 2021). Cheng et al. (Cheng *et al.*, 2021) employed TGA to examine the oxidation behavior of Fe–10Cr steel in the temperature range of 1073–1273 K and determine the oxidation kinetics. The data obtained from TGA

can be further analyzed using different methods, including isoconversional and model-fitting approaches to determine activation energy (E_a) and reaction models involved in the oxidation process (Starink, 2003). Isoconversional methods provide a model-free strategy for assessing kinetic parameters by analyzing the temperature dependence of reaction rates at varying degrees of conversion (α) (Kissinger, 1957; Friedman, 1964; Flynn & Wall, 1966). Each method has a distinct approach to determining E_a. The Friedman method, for instance, is a differential technique that determines the conversion rate at each point, making it highly sensitive to fluctuations in data or noise while offering detailed insights into reaction kinetics at specific conversion levels (Friedman, 1964). Conversely, the Flynn-Wall-Ozawa (FWO) as well as Kissinger-Akahira-Sunose (KAS) methods employ an integral approach, averaging reaction data over a wider range, improving stability against noise and yielding a more reliable estimate of activation energy (Kissinger, 1957; Flynn & Wall, 1966; Akahira, 1971; Huang *et al.*, 2022). The Starink method modifies the KAS approach to further minimize experimental errors (Starink, 2003). Furthermore, research by Vázquez et al. identified the KAS method as the most effective for Cu_2S–FeS mixtures in an oxidative setting. This method demonstrated that activation energy varies significantly with conversion, validating a thermodynamic computational model that accurately replicates TGA curves (Vázquez *et al.*, 2024). While isoconversional methods offer a model-free approach to calculating E_a at various stages of the reaction, they do not provide detailed insights into specific reaction pathways. Therefore, the addition of non-isoconversional methods complements the analysis by offering more precise insights into the reaction models. The CR and KC methods, while both based on model-fitting techniques, differ in their assumptions and mathematical treatments. Both methods use a linearized form of the Arrhenius equation, where the natural log of the conversion function is represented in relation to the inverse of temperature. One limitation, however, is that it assumes a single dominant reaction mechanism, which may not always be applicable for complex reactions involving multiple stages (Coats & Redfern, 1964, 1965; Gao *et al.*, 2020). KC employs a slightly different mathematical simplification than the CR method, allowing for more flexibility in fitting various types of kinetic data. This method is particularly useful when analyzing reactions with complex mechanisms, as it can account for multiple stages

of the reaction process (Kennedy & Clark, 1997; Gao *et al.*, 2020; Alhulaybi *et al.*, 2022; Sugumaran, Kamalakkannan & Subramanian, 2023). Various studies have successfully applied these methods to calculate the E_a (Brown *et al.*, 2000; Alhulaybi *et al.*, 2022; Demirci *et al.*, 2024). Alhulaybi et al. (Alhulaybi *et al.*, 2022) utilized TGA for investigating the pyrolysis kinetics of polylactic acid (PLA) at different heating rates, calculating activation energies through different model-free techniques (Friedman, FWO, KAS, and Starink) as well as model-fitting approaches (Coats-Redfern and Criado). Fernández et al. calculated the activation energy and pre-exponential factor (A) during the pyrolysis of walnut and almond shells using thermogravimetric analysis (Fernandez *et al.*, 2024). Demirci et al. explored the oxidation characteristics of AM Ti-6Al-4V alloy in non-isothermal conditions using TGA-Differential Thermal Analysis (DTA) and examined kinetic parameters through both model-free and model-fitting techniques. Their findings indicated that oxidation mechanisms predominantly follow bidimensional diffusion (D2) and tridimensional diffusion (D3) models at lower heating rates, while F2 and F1 mechanisms take precedence at elevated heating rates (Demirci *et al.*, 2024). Model-fitting methods involve fitting experimental data to specific reaction models to extract kinetic parameters such as E_a (Coats & Redfern, 1964). These methods can offer detailed insights into the reaction models by assuming a specific functional form for the reaction rate.

Additionally, some studies have calculated the E_a of 316L stainless steel after determining the parabolic rate constant (K_p) using TGA (Buscail, El Messki, Riffard, Perrier & Issartel, 2011; Siri, Popa, Vion, Langlade & Chevalier, 2020; Ayvaz, Aydın. & Bahçepınar, 2023). For instance, calculating the E_a for 316L stainless steel or similar alloys has been reported in the literature, providing valuable benchmarks for comparison. Studies have reported E_a values of 206 kJ/mol for 316LN stainless steels (Ayvaz *et al.*, 2023). For 316L stainless steel plates, E_a values around 240 ± 20 kJ/mol have been observed within the temperature range of 973 to 1273 K (Siri *et al.*, 2020). The E_a in the 1073 to 1273 K temperature range has been calculated as 220 ± 30 kJ/mol (Buscail *et al.*, 2011). In addition to kinetic modeling, the use of thermochemical software like FactSage allows for the simulation of high-temperature

oxidation reactions and the prediction of stable phases and compounds (Maroufkhani *et al.*, 2023). Understanding these values and their variation across different temperature ranges is key to establishing a framework for oxidation kinetics.

Despite extensive research into the oxidation kinetics of 316L stainless steel, several gaps remain—particularly concerning the comprehensive application of advanced kinetic methodologies to understand high-temperature oxidation behavior. Most previous studies have relied on evaluating the parabolic rate constant (K_p) and deriving activation energy (E_a) indirectly, which may overlook the intricacies of multi-stage oxidation mechanisms and fail to accurately predict the associated solid-state reaction models (Buscail *et al.*, 2011; Siri *et al.*, 2020; Ayvaz *et al.*, 2023). Furthermore, while isoconversional and model-fitting methods have mostly been applied to polymers and non-metallic materials, their systematic integration for analyzing the oxidation kinetics of stainless steels remains limited.

To address these gaps, this study presents a novel and integrated kinetic–thermodynamic framework for evaluating the oxidation behavior of 316L stainless steel. Model-free isoconversional methods (FWO, KAS, Starink, and Friedman) were applied to calculate activation energies without assuming predefined reaction models, allowing for a precise assessment of oxidation behavior across varying degrees of conversion. Complementarily, model-fitting approaches such as Coats–Redfern (CR) and Kennedy–Clark (KC) were employed to identify reaction models and extract kinetic triplets (E_a, A, and $f(\alpha)$). By applying both methods (isoconversional and model-fitting), we aimed to cross-validate the activation energies and gain a deeper understanding of the reaction mechanisms. To further refine the analysis, the Criado master plot method was used to identify the most suitable reaction mechanisms by comparing theoretical and experimental reaction curves. By coupling kinetic modeling with thermochemical simulations via FactSage, this work presents a novel and comprehensive framework for understanding the high-temperature oxidation phenomena of 316L stainless steel in welding-related applications.

To the best of our knowledge, this is the first study to simultaneously apply multiple isoconversional and model-fitting methods to extract both kinetic and thermodynamic properties (E_a, A, enthalpy of activation $\Delta H^{\neq}$, entropy of activation $\Delta S^{\neq}$, and Gibbs energy of activation $\Delta G^{\neq}$) to identify oxidation reaction models for 316L stainless steel. The originality of this work lies in its comprehensive approach, combining kinetic modeling, thermodynamic analysis, and reaction model prediction using both experimental TGA data and thermochemical simulations. This multi-faceted methodology offers a robust framework for understanding the high-temperature oxidation behavior of stainless steels (in the range of 1100–1373 K), with direct relevance to the complex oxidation phenomena induced by welding and other high-temperature industrial applications.

5.2 Materials and Methods

5.2.1 Preparation

The samples utilized for this study were supplied by PCL, Alberta Canada, with the chemical composition reported in Table 5.2. Prior to TGA experiments, the samples were polished and cleaned using ultrasonic cleaning in ethanol to eliminate surface contaminants and ensure consistency in the analysis.

Table 5.2 316L stainless steel chemical composition

Element	C	Mo	Ni	Cu	S	P	Cr
wt.%	0.02	2.05	11.37	0.25	0.001	0.28	16.47
Element	Mn	Al	Co	Si	W	N	Others
wt.%	0.97	0.0162	0.22	0.43	0.073	0.093	0.13

TGA was conducted using a PerkinElmer STA 8000, United States. The instrument was calibrated for temperature according to the ASTM 967-18 standard using reference materials

Bi_2O_3 and MgF_2, as detailed in Table 5.3. Each condition was repeated twice to determine two calibration points. Based on the standard, the Root Mean Square Error (RMSE) for our experiment was calculated as 4.65 K, ensuring the accuracy and reliability of the temperature measurements. Calibration before testing helps to minimize systematic errors and ensures high reliability of the measurements, even with a limited number of experimental runs (Xu, Li, Whitely & Pan, 2005; Siddiqi, Siddiqui & Atakan, 2007; Saadatkhah *et al.*, 2020; Almaghrabi *et al.*, 2023; Fazlioglu-Yalcin, Hilse & Engel-Herbert, 2024).

Table 5.3 Calibration details for the TGA machine

Material	**Sample mass (mg)**	**Expected melting point (K)**	**Experimental average melting point (K)**	β **(K/min)**	**Ar gas flow (ml/min)**
Bi_2O_3	80.6	1098	1095	10	50
MgF_2	46.2	1536	1527	10	50

Approximately 100 mg of material was used for each TGA run. The samples were placed in Alumina sample pans to ensure uniform heat distribution and avoid any reaction between the sample and the container. The TGA experiments were conducted under a continuous flow of high-purity argon gas (99.95%) containing approximately 500 ppm (5×10^{-4} atm) of oxygen, at a flow rate of 50 ml/min. This condition was deliberately chosen to simulate the oxygen content typically present in industrial welding backing gas. Although argon is generally inert, this trace oxygen level induces high-temperature oxidation representative of the discoloration phenomenon observed in the HAZ during welding (Maroufkhani *et al.*, 2023).

Heating rates of 25, 20, 15, 10, and 5 K/min were used covering one distinct temperature range (1100 K to 1561 K) were used for the TGA experiments. These specific heating rates were chosen to explore the kinetics of oxidation across a broad spectrum of thermal conditions, allowing for a detailed analysis of the reaction models at both lower and higher heating rates. This range enables the application of isoconversional methods, which require multiple heating rates to determine reliable activation energies without assuming a specific reaction model (Rajabi, Mashreghi & Hasani, 2020). Moreover, the use of lower heating rates allows

the oxidation mechanisms to evolve more completely. The temperature ranges were chosen based on the DTG plot, that indicates different oxide formations occurring above 1100 K. The temperature-dependent weight loss of each sample was recorded.

5.2.2 Kinetic Analysis

The activation energy was determined using several methods, as summarized in Table 5.4. In this paper, the Modified Friedman (MFR) method was employed for minimizing noise sensitivity inherent to the conventional Friedman approach (Huidobro *et al.*, 2016). Linear regression analysis was performed to determine the E_a from the slope of the plots. R^2 was used to assess the quality of the fit for each method. The results for isoconvertional methods with R^2 values under 0.82 were excluded to maintain data reliability by eliminating poorly fitting models.

Table 5.4 Summary of methods for E_a calculation (Huidobro *et al.*, 2016; Sharma *et al.*, 2019; Agnihotri & Mondal, 2023; Gajera *et al.*, 2023)

Method	**Type**	**Equation**	**Plot**	**Data analysis**
Isoconversional				
Friedman	Differential	$\ln\left(\frac{d\alpha}{dt}\right) = \ln(A) - \frac{E_a}{RT}$	$\ln(d\alpha/dt)$ vs. $1/T$	Slope gives E_a/R
M-Friedman	Differential	$\ln\left(\frac{d\alpha_{T_{k,i}}}{dt}\right) = \ln(A) - \frac{E_a}{RT_{k,i}}$	$\ln(d\alpha_{T_{k,i}}/dt)$ vs. $1/T_{k,i}$	Slope gives E_a/R
FWO	Integral	$\ln(\beta) = \ln\left(\frac{AE_a}{Rg(\alpha)}\right) - 5.331 - \frac{1.052E_a}{RT}$	$\ln(\beta)$ vs. $1/T$	Slope gives $1.052\,E_a/R$
KAS	Integral	$\ln\left(\frac{\beta}{T^2}\right) = \ln\left(\frac{AR}{E_a g(\alpha)}\right) - \frac{E_a}{RT}$	$\ln(\beta/T^2)$ vs. $1/T$	Slope gives E_a/R
Starink	Integral	$\ln\left(\frac{\beta}{T^{1.92}}\right) = \ln\left(\frac{AR}{E_a^{0.92} g(\alpha)}\right) - \frac{1.0008E_a}{RT}$	$\ln(\beta/T^{1.92})$ vs. $1/T$	Slope gives $1.0008\,E_a/R$
Non-Isoconversional (Model-Fitting)				
KC	Differential	$\ln\left(\frac{\beta g(\alpha)}{T-T_0}\right) = \ln\left(\frac{A}{R}\right) - \frac{E_a}{RT}$	$\ln(\beta g(\alpha)/(T - T_0))$ vs. $1/T$	Slope gives E_a/R
CR	Integral	$\ln\left(\frac{g(\alpha)}{T^2}\right) = \ln\left(\frac{AR}{\beta E_a}\right) - \frac{E_a}{RT}$	$\ln(g(\alpha)/T^2)$ vs. $1/T$	Slope gives E_a/R

Based on the E_a and pre-exponential factor (A) obtained from both isoconversional and model-fitting methods, the thermodynamic properties of the oxidation process were calculated. The enthalpy of activation ($\Delta H^{\neq}$) was determined using the relation:

$$\Delta H^{\neq} = E_a - RT \tag{5.1}$$

The entropy of activation ($\Delta S^{\neq}$) was calculated using the Eyring equation (He *et al.*, 2018; Chong *et al.*, 2019; Vyazovkin, 2024):

$$\Delta S^{\neq} = R \ln\left(\frac{Ah}{k_B T}\right) \tag{5.2}$$

where R is the universal gas constant, h is Planck's constant (6.626×10^{-34} J·s), k_B is Boltzmann's constant (1.381×10^{-23} J/K), and T is the absolute temperature.

The Gibbs energy of activation ($\Delta G^{\neq}$) was then calculated using (Vyazovkin, 2024):

$$\Delta G^{\neq} = \Delta H^{\neq} - T\Delta S^{\neq} \tag{5.3}$$

Following the application of the CR and KC methods, the Criado method was employed to determine the solid-state reaction models (Alhulaybi *et al.*, 2022). The Criado plot involves plotting the reduced reaction rate against the extent of conversion to identify the most appropriate reaction model. In addition, to the Criado method, the methods reported by Alhulaybi et al. (Buscail *et al.*, 2011) and Agnihotri et al. (Agnihotri & Mondal, 2023) also conducted an investigation into reaction models at different conversion levels.

The models included in the analysis are presented in Table 5.5. Using Equation 5.4, a conversion range of 0.1 to 0.7 was used for plotting experimental curves (Sharma *et al.*, 2019; Alhulaybi *et al.*, 2022; Agnihotri & Mondal, 2023):

$$\frac{Z(\alpha)}{Z(0.5)} = \left(\frac{T_\alpha}{T_{0.5}}\right)^2 \frac{(d\alpha/dt)_\alpha}{(d\alpha/dt)_{0.5}} \tag{5.4}$$

Table 5.5 Solid-state reaction models (Yang *et al.*, 2021; Agnihotri & Mondal, 2023; Khattar *et al.*, 2023)

Model Type	**Integral Form** $g(\alpha) = kt$	**Differential Form** $f(\alpha)$
Nucleation Models		
Avrami-Erofeev (A4)	$[-\ln(1-\alpha)]^{1/4}$	$4(1-\alpha)[-\ln(1-\alpha)]^{3/4}$
Avrami-Erofeev (A3)	$[-\ln(1-\alpha)]^{1/3}$	$3(1-\alpha)[-\ln(1-\alpha)]^{2/3}$
Avrami-Erofeev (A2)	$[-\ln(1-\alpha)]^{1/2}$	$2(1-\alpha)[-\ln(1-\alpha)]^{1/2}$
Power Law (P4)	$\alpha^{1/4}$	$4\alpha^{3/4}$
Power Law (P3)	$\alpha^{1/3}$	$3\alpha^{2/3}$
Power Law (P2)	$\alpha^{1/2}$	$2\alpha^{1/2}$
Geometrical Contraction Models		
Contracting Volume (R3)	$1-(1-\alpha)^{1/3}$	$3(1-\alpha)^{2/3}$
Contracting Area (R2)	$1-(1-\alpha)^{1/2}$	$2(1-\alpha)^{1/2}$
Diffusion Models		
Ginstling-Brounshtein (D4)	$1-2\alpha/3-(1-\alpha)^{2/3}$	$3[(1-\alpha)^{-1/3}-1]^{-1}$
3D Diffusion (D3)	$[1-(1-\alpha)^{1/3}]^2$	$\frac{3}{2}[(1-\alpha)^{-1/3}-1]$
2D Diffusion (D2)	$(1-\alpha)\ln(1-\alpha)+\alpha$	$[-\ln(1-\alpha)]^{-1}$
1D Diffusion (D1)	α^2	$\frac{1}{2\alpha}$
Reaction Order Models		
Third Order (F3)	$\frac{1}{2(1-\alpha)^2}-\frac{1}{2}$	$(1-\alpha)^3$
Second Order (F2)	$\frac{1}{1-\alpha}-1$	$(1-\alpha)^2$
First Order (F1)	$-\ln(1-\alpha)$	$1-\alpha$
Zero Order (F0)	α	1

After determining the solid-state reaction model using the Criado method, FactSage thermochemical software (version 8.2, Ftstel and Ftoxid Database) was used to simulate the high-temperature reactions and identify the possible phases and compounds formed. The simulation inputs included the chemical composition of the investigated 316L stainless steel and examined temperature ranges. The FactSage analysis results were compared with experimental data to validate the reaction models and identify the predominant reactions occurring during the oxidation process. All data analyses and plots were generated using MATLAB R2022a.

5.3 Results and Discussion

5.3.1 Mass Gain

The percentage weight gain in relation to temperature at various heating rates is depicted in Figure 5.1. As the temperature increases, the sample begins to gain weight due to the formation of oxides. At 5 and 10 K/min (lower heating rates), the weight gain occurs gradually, with a more pronounced increase. This is because the slower heating rate allows more time for the oxidation reactions to occur uniformly across the sample's surface.

At higher heating rates (15, 20, and 25 K/min), the weight gain is more rapid, and the curves are steeper. This indicates that the oxidation reactions are more vigorous, leading to a faster formation of oxides. However, the higher heating rate may result in less uniform oxidation, as the reactions are limited by the rapid temperature increase.

The onset of weight gain typically starts around 1100 K, which aligns with the temperature range where significant oxidation reactions are expected based on DTG analysis, as reported in Figure 5.2.

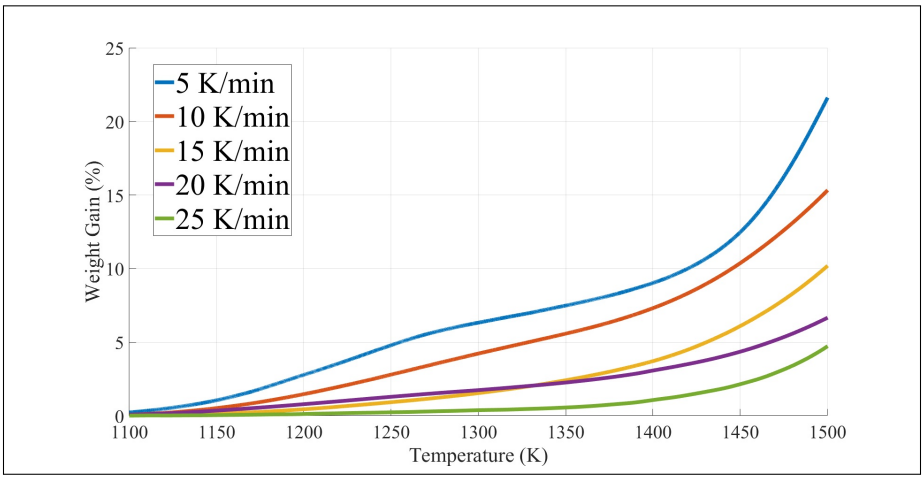

Figure 5.1 The percentage weight gain of 316L stainless steel during heating at different rates

DTG and Degree of Conversion

The results of the DTG curves are presented in figure 5.2. As shown, the DTG curves reveal two distinct behaviors at two different temperature ranges (1100–1373 K and 1400–1500 K). The peaks appear more pronounced at lower heating rates due to the extended time for oxidation reactions to occur, allowing for better resolution of different oxidation events.

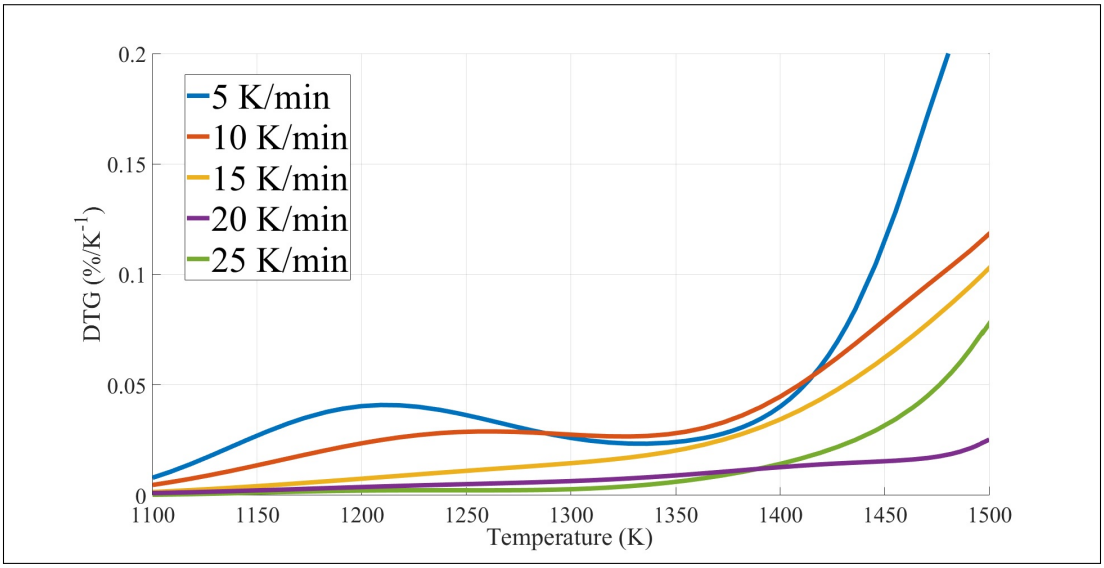

Figure 5.2 DTG curves for different heating rates

Figure 5.3 displays the progression of oxidation in 316L stainless steel as a function of temperature, from 5 to 25 K/min heating rates by utilizing degree of conversion versus temperature. The curves demonstrate that the degree of conversion increases more steeply as the temperature approaches higher values. This behavior indicates that the oxidation process accelerates at higher temperatures, with faster heating rates leading to quicker attainment of similar degrees of conversion.

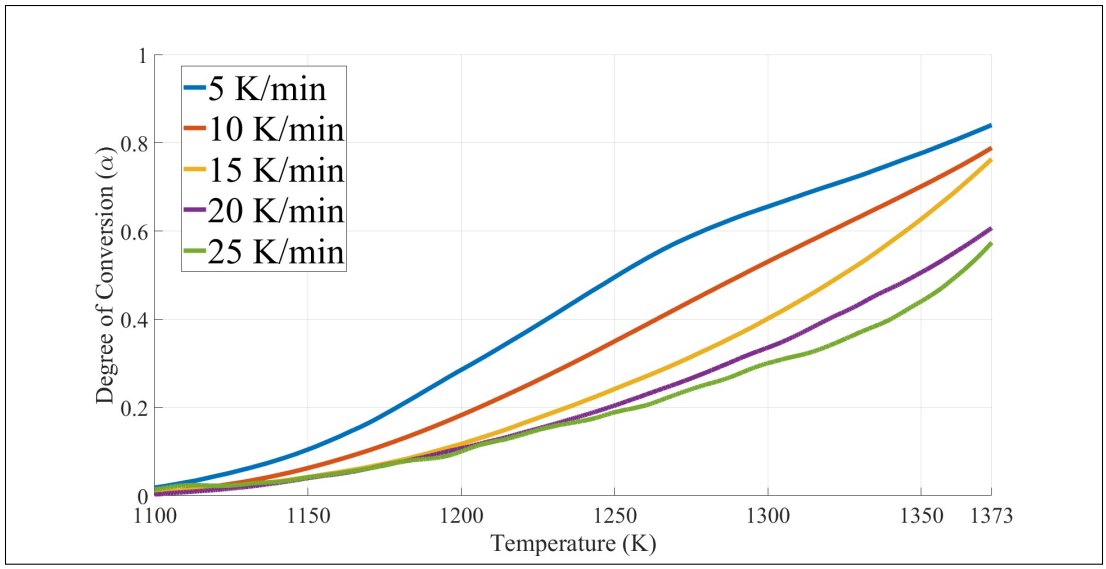

Figure 5.3 Variation in the relationship between the degree of conversion and temperature at various heating rates

5.4.3 Isoconversional Kinetic Models

As reported in Table 5.4, several isoconversional methods, including M-Friedman, FWO, KAS and Starink were employed in the present work.

On the basis of the data reported in Figure 5.4, the activation energy values were calculated and are reported in Table 5.6, along with the corresponding R^2 coefficients. While slight variations in E_a could be observed between the methods, the consistency across them validates the reliability of the kinetic parameters. For instance, at a α of 0.5, the Ea values for FWO, KAS, Starink and Friedman methods are 190.49 kJ/mol, 178.7 kJ/mol, 179.42 kJ/mol, and 226.71 kJ/mol, respectively, with R^2 values indicating a good fit for all methods. The higher activation energy value estimated when using M-Friedman method could be related to the differential nature, i.e., derivative based equations, of this method. As reported in Table 5.6, E_a values for the M-Friedman method oscillate between 104.13 and 825.7 kJ/mol with R^2 values between 0.31 and 0.99, demonstrating the sensitivity of the method to changes in the conversion

value. Therefore, the value obtained using the M-Friedman method will not be considered in the following sections.

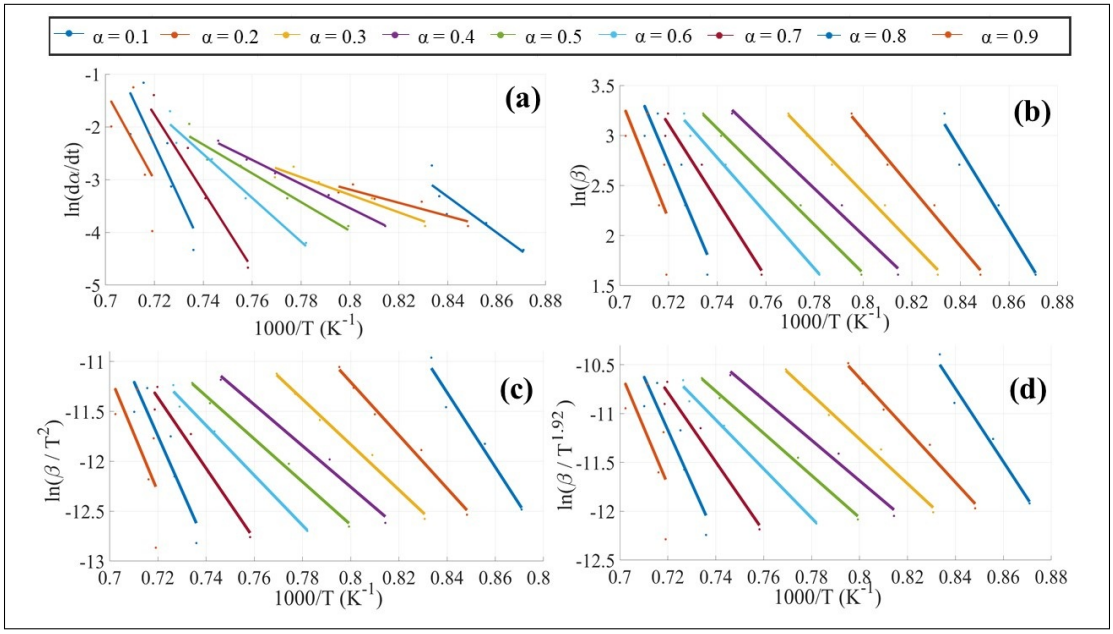

Figure 5.4 Isoconversional plots for Ea determination ; a) M-Friedman, b) FWO, c) KAS, and d) Starink

Table 5.6 Ea (kJ/mol), Ln(A) (1/s), and R^2 values determined using various isoconversional methods for different α values

α	FWO			KAS			Starink			M-Friedman		
	E_a	Ln(A)	R^2	E_a	Ln(A)	R^2	E_a	Ln(A)	R^2	E_a	Ln(A)	R^2
0.1	313.88	36.95	0.97	310.68	35.27	0.97	311.21	35.35	0.97	282.43	32.49	0.81
0.2	229.40	28.28	0.99	221.08	25.74	0.99	221.72	25.82	0.99	104.13	15.01	0.84
0.3	199.23	25.20	0.99	188.80	22.28	0.99	189.48	22.35	0.99	138.56	17.79	0.91
0.4	183.21	23.58	0.99	171.43	20.37	0.99	172.14	20.45	0.99	189.91	21.99	0.99
0.5	190.49	24.32	1.00	178.70	20.73	1.00	179.42	20.80	1.00	226.71	24.88	0.94
0.6	218.78	27.19	0.99	208.09	22.97	0.99	208.80	23.04	0.99	345.08	34.77	0.96
0.7	301.68	35.70	0.97	294.81	29.98	0.96	290.00	30.06	0.96	606.06	56.74	0.91
0.8	454.70	51.60	0.82	455.34	43.13	0.82	455.90	43.21	0.82	825.70	74.73	0.71
0.9	482.24	54.47	0.44	483.92	45.04	0.41	484.46	45.12	0.41	700.87	63.29	0.31

The thermodynamic properties calculated from different isoconversional methods offer crucial insights into the oxidation mechanism of 316L stainless steel. As shown in Table 5.7, $\Delta H^{\neq}$ values obtained from the FWO, KAS, Starink, and Friedman methods averaged 224.42, 214.14, 214.99, and 259.75 kJ/mol, respectively, indicating consistency across integral and differential approaches. The corresponding $\Delta G^{\neq}$ values were also closely aligned, averaging 252.97, 285.38, 285.43, and 286.19 kJ/mol. This agreement validates the robustness of the calculated kinetic parameters. Notably, the entropy of activation showed negative values for most methods suggesting a transition state with reduced disorder compared to the reactants, which is typical in solid-state diffusion-controlled processes. The positive $\Delta S^{\neq}$ values at low α and high α reflect the increasing complexity and possible multistep nature of the oxidation reaction at those conversion levels. These thermodynamic trends further confirm the progressive formation of protective oxide scales and the complex nature of the oxidation mechanism, as supported by the kinetic model fitting and phase transformation analysis.

Table 5.7 $\Delta H^{\neq}$ (kJ/mol), $\Delta S^{\neq}$ (J/mol·K), and $\Delta G^{\neq}$ (kJ/mol) values determined using various isoconversional methods for different α values

α	FWO			KAS			Starink			M-Friedman		
	$\Delta H^{\neq}$	$\Delta S^{\neq}$	$\Delta G^{\neq}$	$\Delta H^{\neq}$	$\Delta S^{\neq}$	$\Delta G^{\neq}$	$\Delta H^{\neq}$	$\Delta S^{\neq}$	$\Delta G^{\neq}$	$\Delta H^{\neq}$	$\Delta S^{\neq}$	$\Delta G^{\neq}$
0.1	304.49	43.03	255.93	300.87	28.56	267.14	301.65	29.20	267.17	272.61	5.43	266.21
0.2	220.01	-29.21	252.98	210.90	-50.96	273.33	211.71	-50.33	273.37	93.94	-140.18	265.66
0.3	189.85	-54.76	251.66	178.33	-80.00	279.08	179.16	-79.37	279.13	128.09	-117.31	275.84
0.4	173.83	-68.26	250.87	160.70	-96.05	284.63	161.55	-95.43	284.68	179.18	-82.57	285.73
0.5	181.10	-62.13	251.24	167.76	-93.24	290.41	168.63	-92.62	290.46	215.78	-58.71	293.01
0.6	209.40	-38.22	252.54	196.96	-74.75	297.01	197.84	-74.13	297.06	333.95	23.39	302.64
0.7	292.29	32.55	255.55	283.49	-16.58	306.07	284.39	-15.94	306.11	594.73	205.87	314.24
Average	224.42	-25.29	252.97	214.14	-54.72	285.38	214.99	-54.09	285.43	259.75	-23.44	286.19

Figure 5.5 shows the average E_a value from different Isoconversional methods examined in the present work, as reported in Table 5.6 . It is important to note that values for 0.8, 0.9 for all methods and 0.1 degrees of conversion for M-Friedman were excluded due to their low R^2, which indicated a poor fit. The M-Friedman method, being a differential approach, exhibits

higher sensitivity to experimental noise, leading to slight variations in activation energy values (Huidobro *et al.*, 2016).

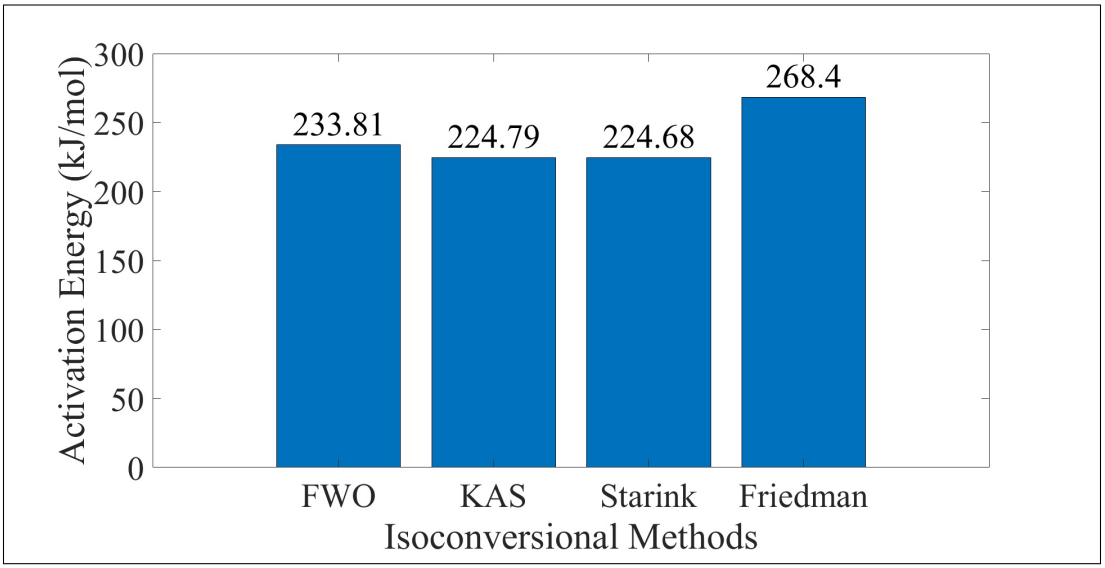

Figure 5.5 Average E_a from Isoconversional Methods

E_a in relation to α for various isoconversional methods is illustrated in Figure 5.6. In the initial phase of the oxidation process (α = 0.1 to 0.4), it is observed that there is a slight decrease in the Ea value in FWO, KAS and Starink. This trend is likely due to the initial development of oxide layers forming on the sample's surface. During this phase, the reaction is likely dominated by the nucleation and initial growth of oxide nuclei, which require relatively higher energies (Brylewski, Miruszewski, Kaczmarek & Moskal, 2004). As these nuclei grow and coalesce, the energy barrier decreases slightly, facilitating further oxidation (Brylewski *et al.*, 2004). From α = 0.4 to 0.7, a steady increase is observed in the Ea value, with a similar slope across all methods. This phase corresponds to the thickening and densification of the oxide layer (Fehlner, 1970; Young, 2008; Chen, Wang, Chen & Zhang, 2014). As the oxide layer grows, diffusion of oxygen and metal ions through the oxide becomes the rate-limiting factor. This diffusion-controlled process requires higher E_a, which accounts for the observed increase (Young, 2008).

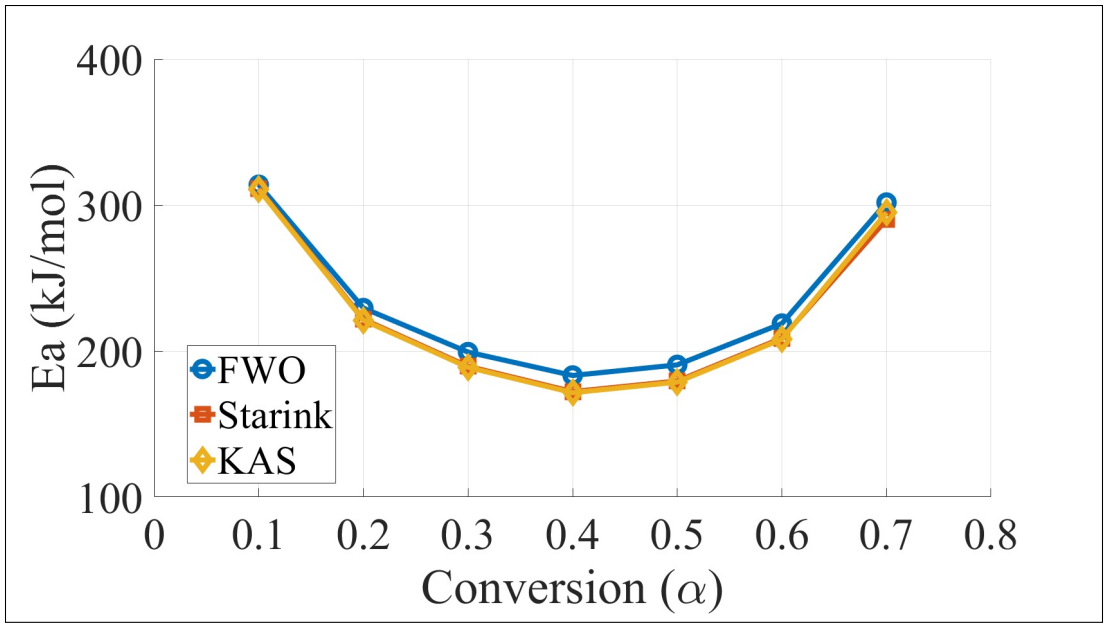

Figure 5.6 E_a as a function of α using various isoconversional methods

5.3.2 Model-Fitting Kinetics Methods

The CR method, reported by Demirci et al. (Demirci *et al.*, 2024) has been utilized to examine the oxidation behavior of the Ti-6Al-4V alloy and was applied to determine the activation energy for oxidation across different reaction models, as outlined in Table 5.4. Table 5.8 presents the E_a values obtained by this method for 15 different reaction models for the heating rates used in the present work.

Table 5.8 Activation energy (E_a) values obtained using the CR model

Reaction Model	Heating rate (K/min)										Average	
	5		10		15		20		25			
	E_a	R^2	E_a	R^2	E_a	R^2	E_a	R^2	E_a	R^2	E_a	R^2
D1	316.4	0.926	372.4	0.943	377.1	0.976	311.6	0.976	317.0	0.981	338.9	0.961
D2	336.7	0.939	387.7	0.951	387.5	0.980	322.8	0.980	323.9	0.983	351.7	0.967
D3	359.6	0.951	404.1	0.959	399.1	0.983	334.3	0.984	331.2	0.985	365.7	0.973
D4	-70.5	0.992	-59.8	0.979	-47.7	0.969	-48.8	0.977	-40.6	0.984	-53.5	0.980
F0	148.1	0.916	176.3	0.936	178.5	0.973	145.5	0.973	148.6	0.978	159.4	0.955
F1	181.6	0.957	200.5	0.963	195.1	0.985	163.0	0.985	158.9	0.985	179.8	0.975
F2	221.6	0.983	228.2	0.981	213.5	0.993	182.3	0.993	170.2	0.990	203.2	0.988
F3	268.0	0.996	259.3	0.992	233.7	0.997	203.8	0.997	182.2	0.994	229.4	0.995
P2	63.99	0.889	78.09	0.919	79.15	0.965	62.59	0.962	64.25	0.970	69.62	0.941
P3	35.94	0.847	45.34	0.894	46.05	0.953	34.87	0.944	36.14	0.957	39.67	0.919
P4	21.94	0.782	28.96	0.857	29.50	0.935	21.01	0.913	22.08	0.935	24.70	0.885
A2	80.73	0.944	90.18	0.953	87.49	0.980	71.20	0.980	69.43	0.980	79.80	0.968
A3	47.12	0.927	53.40	0.940	51.61	0.974	40.61	0.972	39.70	0.972	46.49	0.957
A4	30.30	0.901	35.01	0.921	33.66	0.965	25.31	0.958	24.75	0.958	29.81	0.941
R2	164.1	0.938	188.0	0.950	186.6	0.979	154.1	0.979	153.7	0.982	169.3	0.966
R3	169.7	0.945	191.9	0.955	189.5	0.981	156.9	0.982	155.6	0.983	172.7	0.969

After plotting the experimental data, they were fitted to a linear model using MATLAB. The high R^2 values (ranging from 0.961 and 0.989) demonstrate a strong correlation between the model and experimental data, supporting the validity of using a linear model to determine E_a.

Table 5.9 Activation energy (E_a) values obtained using the KC model

Reaction Model	Heating rate (K/min)										Average	
	5		10		15		20		25			
	E_a	R^2	E_a	R^2	E_a	R^2	E_a	R^2	E_a	R^2	E_a	R^2
D1	326.5	0.931	382.5	0.946	387.2	0.978	321.9	0.978	327.1	0.983	349.0	0.963
D2	346.8	0.942	397.8	0.954	397.6	0.981	333.1	0.982	333.9	0.985	361.8	0.969
D3	369.7	0.954	414.1	0.961	409.2	0.984	344.6	0.985	341.0	0.986	375.7	0.974
D4	-60.4	0.990	-49.8	0.972	-37.6	0.954	-38.6	0.966	-30.6	0.974	-43.4	0.971
F0	158.2	0.926	186.2	0.943	188.5	0.976	155.8	0.976	158.5	0.981	169.5	0.961
F1	191.7	0.961	210.6	0.966	205.2	0.986	173.3	0.987	169.0	0.987	190.0	0.978
F2	231.7	0.984	238.1	0.983	223.6	0.994	192.6	0.994	180.2	0.992	213.3	0.989
F3	278.1	0.996	269.4	0.993	243.8	0.998	214.2	0.997	192.2	0.995	239.5	0.996
P2	74.07	0.916	88.17	0.936	89.23	0.973	72.76	0.973	74.3	0.978	79.71	0.955
P3	46.02	0.904	55.42	0.928	56.13	0.969	45.08	0.968	46.18	0.975	49.77	0.949
P4	31.99	0.889	39.04	0.919	39.58	0.965	31.3	0.962	32.13	0.970	34.81	0.941
A2	90.81	0.957	100.3	0.963	97.57	0.985	81.49	0.985	79.47	0.985	89.92	0.975
A3	57.18	0.951	63.48	0.958	61.69	0.983	50.89	0.983	49.63	0.983	56.58	0.972
A4	40.36	0.944	45.09	0.953	43.75	0.980	35.6	0.980	34.71	0.980	39.90	0.968
R2	174.2	0.945	197.9	0.956	196.7	0.982	164.4	0.982	163.8	0.984	179.4	0.970
R3	179.8	0.951	202.0	0.959	199.5	0.983	167.2	0.984	165.6	0.985	182.8	0.973

By comparing the obtained E_a values with those from the isoconversional methods, the most plausible reaction models were identified. When comparing the E_a values from the CR and KC methods with those obtained through isoconversional methods, as presented in Table 5.8 ,5.9 and Figure 5.6, it is evident that the F2 (second-order) and F3 (third-order) reaction models, with E_a values ranging between 203.2 kJ/mol and 239.5 kJ/mol, present a good agreement with the isoconversional averages, which range between 224.79 kJ/mol and 268.41 kJ/mol. This finding indicates that these reaction models effectively represent the oxidation kinetics of 316L stainless steel. The close alignment with the isoconversional methods suggests that both the F2 and F3 models are appropriate for describing the formation and growth of oxide layers during oxidation, particularly in capturing the complex mechanisms of spinel and corundum formation at different stages of the process.

5.3.3 Criado Method Analysis

The Criado master plots shown in Figure 5.7 help identify the most appropriate reaction models that closely align with the experimental data. As shown, the normalized reaction rates ($Z(\alpha)/Z(0.5)$) are plotted against the extent of α for various heating rates used in this study.

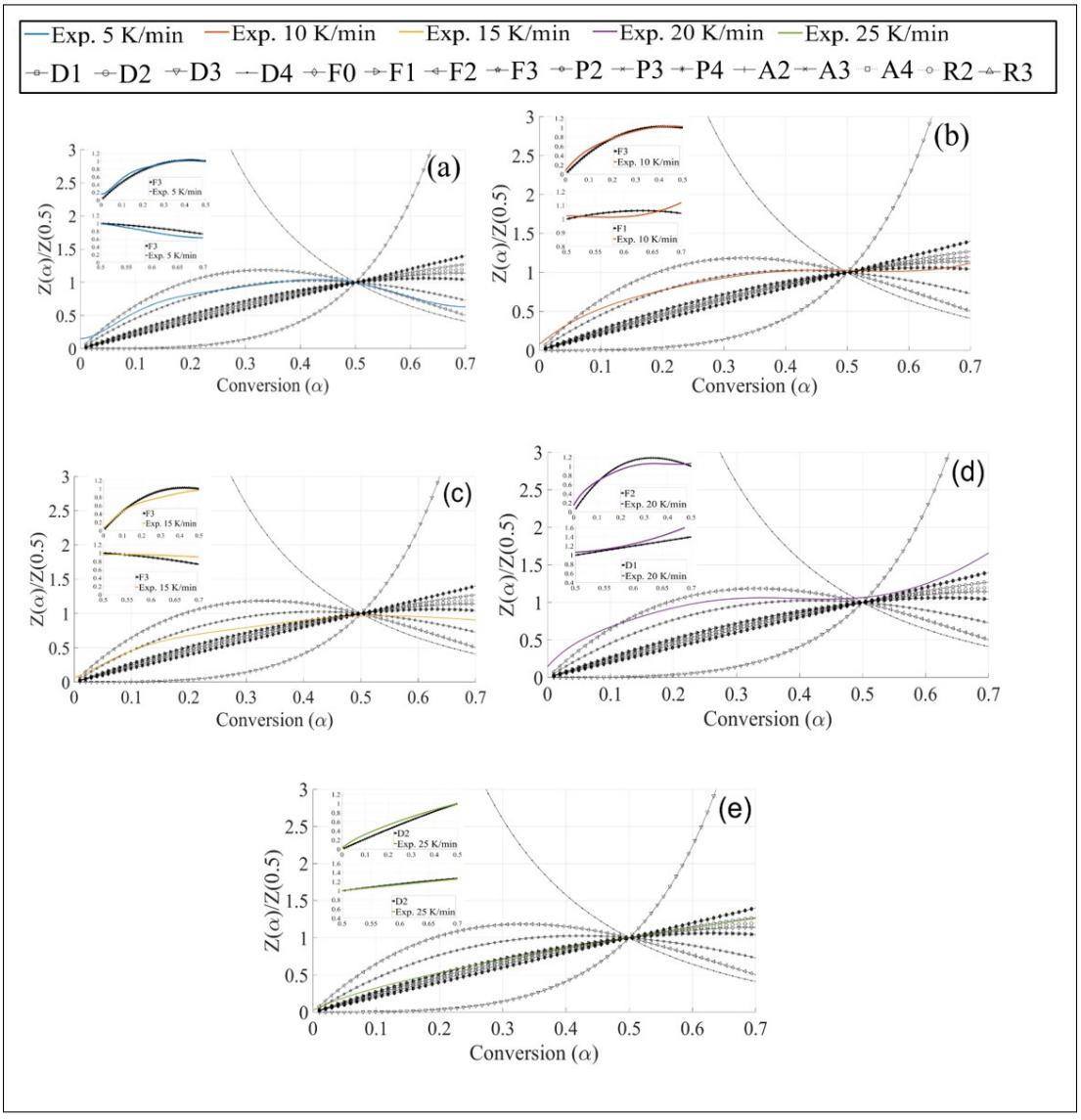

Figure 5.7 Criado master plots for low temperature tests with different β: a) 5, b) 10, c) 15, d) 20, e) 25 K/min

As shown in Figure 5.7, at higher heating rates, the oxidation kinetics of 316L stainless steel transition from being reaction-controlled to diffusion-controlled due to the interplay of reaction rates and diffusion limitations. While lower heating rates allow for the formation of thicker and more uniform oxide layers, the slower reaction rate ensures that diffusion does not become the rate-limiting step, leading to reaction-order kinetics dominated by models such as F1, F2, and F3. In contrast, higher heating rates (e.g., 20 and 25 K/min) lead to rapid temperature increases, causing the oxide layer to form more quickly but less uniformly. This rapid growth creates a scenario where the supply of oxygen or metal ions through the oxide layer cannot keep pace with the reaction at the metal-oxide interface, resulting in diffusion-controlled kinetics. Specifically, D1 dominates at 20 K/min, while at 25 K/min, the oxide morphology becomes more complex, favoring two-dimensional diffusion D2 through lateral pathways such as grain boundaries or pores.

5.3.4 Oxidation of 316L Stainless Steel below 1373 K

Thermochemical results obtained using FactSage showed that at 1073 K, the primary oxides formed include spinel and corundum, as shown in Equations (5.5) and (5.6), respectively. Spinel in this context likely contains chromium and iron oxides and corundum includes chromium and iron oxides in this alloy (Maroufkhani *et al.*, 2023).

$$\text{Spinel Formation: } Fe_3O_4 + Cr_2O_3 \rightarrow (Fe, Cr)_3O_4 \tag{5.5}$$

$$\text{Corundum Formation: } Fe_2O_3 + Cr_2O_3 \rightarrow (Fe, Cr)_2O_3 \tag{5.6}$$

The oxidation of 316L stainless steel begins with the formation of iron oxides and chromium oxides on the surface (Hou, Chen, Liu & Song, 2010).

$$\text{Formation of Iron Oxide: } \mathrm{Fe} + \frac{1}{2}\mathrm{O_2} \rightarrow \mathrm{FeO} \tag{5.7}$$

$$2\mathrm{FeO} + \frac{1}{2}\mathrm{O_2} \rightarrow \mathrm{Fe_2O_3} \tag{5.8}$$

$$\text{Formation of Chromium Oxide: } \mathrm{Cr} + \frac{3}{2}\mathrm{O_2} \rightarrow \mathrm{Cr_2O_3} \tag{5.9}$$

These simulations modeled oxide formation in 316L stainless steel under various oxygen partial pressures and temperature ranges representative of welding conditions. The predictions revealed a duplex oxide scale composed of an inner corundum layer $(\mathrm{Fe,Cr})_2\mathrm{O_3}$ and an outer spinel phase $(\mathrm{Fe,Cr})_3\mathrm{O_4}$, consistent with the elemental mapping and kinetic behavior observed in the present study. These thermochemical predictions align with the experimental observations of Maroufkhani et al. (Maroufkhani *et al.*, 2023), who reported a duplex oxide structure with an inner Cr-rich layer and an outer Fe-rich oxide layer near the fusion zone of welded 316L stainless steel, validating the progressive oxidation mechanism.

The presence of spinel and corundum phases in both the FactSage results and experimental EDS mapping supports the stepwise oxidation kinetics observed in this study, further justifying the reaction models (F2, F3) derived from kinetic analysis. These previously validated results are briefly incorporated in the current manuscript to reinforce the correlation between calculated phase stability and the experimental oxidation pathways under TGA conditions.

The composition and structure of the protective oxide layer are critical in determining the oxidation resistance of 316L stainless steel. Typically, a duplex oxide scale forms, consisting of an inner chromium-rich corundum phase ($\mathrm{Cr_2O_3}$ or $(\mathrm{Fe,Cr})_2\mathrm{O_3}$) and an outer iron-rich spinel phase ($(\mathrm{Fe,Cr})_3\mathrm{O_4}$). The inner corundum layer acts as a dense barrier, effectively limiting the diffusion of oxygen and metal ions, thereby enhancing corrosion resistance (van der Geest, Visser, de Keijzer & van Eekelen, 2013). In contrast, the outer spinel layer, while less dense,

accommodates defects and aids in stress relaxation, improving the adhesion of the oxide scale during thermal cycling (Huang *et al.*, 2020). This synergistic combination of corundum and spinel phases contributes to the overall protective nature of the oxide layer (Park, Park & Kim, 2007). These findings are consistent with the observations reported by Maroufkhani et al. (Maroufkhani *et al.*, 2023), who identified a duplex oxide structure with an inner Cr-rich layer and an outer Fe-rich oxide layer near the fusion zone of welded 316L stainless steel.

Reactions for F2 and F3 Models

The F2 model suggests that the oxidation rate is directly proportional to the square of the remaining unreacted material. The F3 model, also fitting well with experimental data, indicates that the oxidation rate is proportional to the cube of the amount of unreacted material. This suggests an even more complex mechanism involving rapid nucleation and growth of multiple oxide layers. By following both F2 and F3 models, this study offers a detailed understanding of the oxidation mechanisms in 316L stainless steel. There is a possibility that both models correspond to the formation of spinel and corundum.

Further investigation into the microstructural evolution beneath the oxide scale, including grain boundary effects and oxidation-induced transformations, is planned as a future extension of this research.

5.4 Conclusions

This study examined the oxidation kinetics of 316L stainless steel using both isoconversional and non-isoconversional methods. The main findings and their implications are summarized below:

1. The E_a from the CR and KC methods were compared with isoconversional methods. The second and third order (F2 and F3) reaction models were identified as the most accurate ones representing the oxidation process of 316L stainless steel at temperatures below

1373 K, and Criado plot analysis confirmed that the F2 and F3 models align closely with experimental data across different heating rates.

2. The FWO, KAS and Starink isoconversional methods provided average E_a values of 233.81 kJ/mol, 224.79 kJ/mol and 224.68 kJ/mol, respectively, which are consistent with those obtained from the CR and KC methods, ranging between 203.2 kJ/mol and 239.5 kJ/mol.
3. The thermodynamic properties were calculated using FWO, KAS, Starink, and Friedman methods. The average $\Delta H^{\neq}$ values ranged from 214.14 to 224.42 kJ/mol, average $\Delta S^{\neq}$ values ranged from −54.72 to −23.44 J/mol·K, and average $\Delta G^{\neq}$ values ranged from 252.97 to 286.19 kJ/mol. The negative $\Delta S^{\neq}$ values reflect a more ordered transition state, which is typical for solid-state oxidation reactions.
4. FactSage simulations and experimental data confirmed the formation of spinel (containing Fe-Cr oxides) and corundum (Fe_2O_3-Cr_2O_3 structures) as the primary oxides at temperatures below 1100 K.

Acknowledgment

This research was conducted in partnership with PCL Construction in Edmonton, which provided the study materials, and was supported by funding from the Natural Sciences and Engineering Research Council of Canada (NSERC) under Grant No. RDC 542299-19. Special thanks to Saleh Rasouli for his assistance with the calibration process.

CHAPTER 6

NUMERICAL SIMULATION OF 316L STAINLESS STEEL PIPE WELDS UNDER VARYING OXYGEN CONTENT IN BACKING GAS

Mohammad Maroufkhani[a], Fatemeh Jafari[b], Alireza Khodabandeh[c], Iulian Radu[d], and Mohammad Jahazi[e]

[a,b,c,e] Department of Mechanical Engineering, École de Technologie Supérieure (ÉTS), 1100 Notre-Dame Street West, Montreal, QC, Canada H3C 1K3
[d] PCL Industrial Management Inc.,2107 4 St, Nisku, AB, Canada,T9E 7W6

6.1 Abstract

The integrity and corrosion resistance of 316L stainless steel weldments are critically influenced by the presence of oxygen in the backing gas during gas tungsten arc welding (GTAW). In this study, the effect of varying oxygen concentrations (50, 200, 500, and 5000 ppm) in the purging gas on weld root oxidation was systematically investigated through a combination of experimental and numerical approaches. Computational fluid dynamics (CFD) simulations were conducted to determine the spatial distribution of oxygen in the weld region, revealing localized zones of oxygen accumulation at specific angular positions along the weld line. Additionally, a finite element model (FEM) was developed to calculate the temperature gradients in the heat-affected zone (HAZ) and weld region. Macroscopic discoloration, composition and thickness of oxide layers across various zones of discoloration were examined using scanning electron microscopy. Thermodynamic analysis was also employed to identify the dominant oxide phases. By integrating experimental findings with simulation results it was possible to quantitatively predict oxide thickness evolution as a function of oxygen content in the backing gas providing.

Keywords: 316L stainless steel, GTAW, Weld root discoloration, Oxide layer characterization, CFD, Backing gas purity, Oxygen distribution simulation.

6.2 Introduction

Austenitic stainless steels, particularly grade 316L, are extensively employed in industries such as petrochemical processing, food handling, and nuclear energy due to their excellent corrosion resistance, high ductility, and reliable weldability (Bitharas *et al.*, 2018; Li *et al.*, 2021; Pandey, Singh, Rathi & Verma, 2024). However, their corrosion performance can be significantly degraded during welding, especially on the root side of welded joints, where exposure to oxygen in the backing gas may result in oxide formation and discoloration (Li *et al.*, 2021).

In sanitary welding applications, discoloration is strictly limited by standards such as AWS D18.1 and D18.2, where anything beyond light straw or light blue hues is rejected (Avery, 2000). However, the visual appearance of the oxide scale is not a definitive indicator of its protectiveness. For instance, while they look very similar in visual inspection and appearance, oxides rich in corundum (Cr_2O_3) and spinel ($(Fe,Cr)_3O_4$) structures are typically more protective, whereas oxides dominated by FeO are more susceptible to localized corrosion (Huang *et al.*, 2020; Maroufkhani *et al.*, 2023).

Oxidation inside the pipe during welding is strongly influenced by both temperature and oxygen content, which together govern the formation, thickness, and composition of oxide layers. Oxides form primarily on the inner surface of the pipe, particularly in the heat-affected zones, and their growth is exacerbated by inadequate shielding or backing gas coverage. To minimize internal oxidation and discoloration, it is therefore critical to tightly control the oxygen content of the backing gas. Even slight increases can lead to changing oxide phases and affect corrosion resistance. Additionally, due to the pipe's curved geometry and the dynamic nature of orbital welding, local oxygen distribution and thermal profiles are highly nonuniform and cannot be fully predicted through experiments alone. As a result, numerical simulations are essential to model gas flow, oxygen mass fraction, and temperature fields, enabling a more comprehensive understanding of oxidation mechanisms.

Understanding the relationship between oxygen content, temperature, and oxide characteristics,such as thickness and composition, is thus crucial for optimizing welding procedures and preventing undesirable oxidation during pipe welding.

FEM simulations are widely used to characterize the thermal behavior and temperature gradients in welding (Arora, Singh & Brar, 2020). Hitesh Arora et al. investigated transient thermal cycles in SS-304 thin-walled welded pipes, revealing that the peak temperature occurs precisely at the weld centerline (0 mm), while temperatures at 5 and 10 mm from the weld line decay exponentially, confirming the steep thermal gradient away from the fusion zone (Arora *et al.*, 2020). Similarly, Sh. Zangeneh et al. conducted a fitness-for-service and failure analysis of AISI 304 weldments used in demineralized water pipelines, where FEM simulations demonstrated distinct thermal profiles at various distances from the weld centerline, with the maximum temperature reaching above 2500 °C and rapidly decreasing toward the heat-affected zone (Zangeneh, Lashgari & Sharifi, 2020). In addition, Obeid et al. performed FEM-based thermal and residual stress analysis for lined pipe welding using ABAQUS, showing that the thermal histories and peak temperatures at different circumferential angles (90 °, 180 °, and 270 °) remained nearly identical. This finding suggests that circumferential position exerts negligible influence on the temperature evolution, thereby simplifying thermal modeling for axisymmetric weld geometries (Obeid, Alfano, Bahai & Jouhara, 2018).

Understanding the spatial distribution and dynamics of oxygen in the shielding or backing gas during arc welding is equally critical for predicting localized oxidation and ensuring weld integrity. Bitharas et al. (Bitharas *et al.*, 2018) used schlieren imaging in conjunction with a magnetohydrodynamic (MHD) finite element model to simulate argon shielding gas flow during welding. They examined how variables such as gas flow rate, nozzle angle, and nozzle-to-surface distance influence the development and stability of the shielding gas region around the weld pool.

Their integrated experimental–numerical approach enabled the identification of critical oxygen concentration thresholds and demonstrated the effectiveness of combining flow visualization

with computational modeling to improve shielding performance and reduce oxidation (Bitharas *et al.*, 2018). Yang et al. conducted a CFD analysis to examine how shielding gas flow rate affects oxidation during Laser Hybrid Arc Welding (LHAW) and Metal Inert Gas (MIG) welding. Their study concluded that although increasing the gas flow rate improves arc stability and expands high-argon-concentration zones—thus reducing oxidation on the weld surface, it does not significantly alter the shielding gas flow pattern near the weld zone. However, their work was limited to surface oxidation and did not address oxidation inside the pipe or the influence of local oxygen accumulation due to pipe geometry. Schwedersky et al. investigated the feasibility of using Schlieren imaging to analyze shielding gas flow in arc welding, revealing key limitations when pure argon is used. Although theoretical predictions suggested observable flow patterns, the actual Schlieren lines for argon were too faint to yield detailed information. Interestingly, visible flow lines were only observed near the arc due to localized gas heating, and a gas mixture like Ar-25% CO_2 provided sufficient refractive index contrast for visualizing shielding gas turbulence. While their findings underscore the potential of optical diagnostics to complement flow modeling, their study focused solely on external shielding gas behavior and surface-level visualization.

However, their work did not address internal oxidation mechanisms, particularly within the weld root of stainless-steel pipe welding, where both shielding and backing gases interact in a confined geometry. Furthermore, they did not couple Schlieren observations with thermal field analysis or simulate oxygen distribution in the backing gas zone. In contrast, the present study integrates CFD and FEM simulations to map local oxygen content and temperature profiles, enabling prediction of oxide composition and thickness inside the pipe. This approach fills a key gap by offering a more comprehensive understanding of discoloration zones, beyond surface shielding, under varying welding conditions and oxygen levels.

In this work, we examine the influence of oxygen content in the backing gas on the oxidation behavior of 316L stainless steel weldments. Welds were performed under controlled oxygen levels of 50, 200, 500, and 5000 ppm. The phase composition of oxide layers was analyzed through thermodynamic modeling. CFD simulations were carried out to visualize the spatial

distribution and accumulation of oxygen near the root side of the weld, identifying regions susceptible to oxygen entrapment. FEM was employed to calculate temperature gradients in the HAZ and weld metal and correlate them to oxide formation behavior, including thickness and phase composition, under varying oxygen concentrations in the backing gas. By combining numerical simulations with experimental data, we were able to estimate both the local oxygen content and temperature in each region of discoloration, thereby predicting the resulting oxide phase and thickness. For this purpose, models developed to calculate activation energy and reaction kinetics were utilized in our previous study, and FactSage software was employed to determine the equilibrium oxide composition at various temperatures. By integrating numerical and experimental analyses, this study provides deeper insight into the threshold levels of oxygen and temperature that lead to deleterious oxide formation and proposes guidelines for optimizing purging strategies to ensure both structural integrity and corrosion resistance of stainless-steel piping systems in critical applications.

6.3 Material and Methods

6.3.1 Material and experimental setup

The specimens used in this study were machined from 316L stainless steel (SS) pipes with a diameter of 204 mm (8 inches) and a wall thickness of 7.11 mm (0.285 inches). The chemical composition of the base material was determined using a SPECTROMAXx LMF08 Optical Emission Spectrometer (Ametek, Kleve, Germany), with each analysis repeated five times to ensure measurement reliability. The composition is summarized in Table 6.1.

Two welding techniques were employed: Gas Tungsten Arc Welding (GTAW) for the root pass and Flux-Cored Arc Welding (FCAW) for the fill and cap passes. The detailed parameters used for each weld pass are presented in Table 6.2.

To study the influence of oxygen content in the backing gas on discoloration and oxide formation in the root area, purging was performed using argon gas with controlled oxygen

concentrations of 50, 200, 500, and 5000 ppm (see Table 6.3). The argon gas mixtures were sourced from certified commercial suppliers and verified by Air Liquide to meet the required oxygen specifications.

During welding, the interior of the pipe was sealed at both ends. Argon gas was introduced from one end, and the oxygen concentration at the opposite end was continuously monitored using a PurgEye 300 instrument. Gas flow and monitoring were maintained until the target oxygen concentration was stabilized before welding was initiated. This purging setup ensured a uniform and controlled backing environment during the welding process.

Thermodynamic predictions of phase stability and oxide formation as a function of temperature and oxygen content were carried out using the FactSage software. This simulation provided insight into the likely oxides forming in the discoloration zone, depending on the welding conditions and local atmosphere (Maroufkhani *et al.*, 2023).

Table 6.1 Chemical composition of 316L stainless steel (wt.%)

Element	C	Mn	Si	P	S	Mo	Cr
wt.%	0.02	0.97	0.43	0.28	0.001	2.05	16.47
Element	Ni	Al	Co	Cu	W	N	Others
wt.%	11.37	0.0162	0.22	0.25	0.073	0.093	0.13

Table 6.2 Welding condition parameters of 316L SS samples

Process	GTAW	FCAW	FCAW
Pass	1	2	3
Purge gas flow rate (CFH)	40	40	40
Current (A)	176.5 ± 22.5	246 ± 24.5	257 ± 15
Voltage (V)	12.2 ± 1.3	29.7 ± 0.4	29.65 ± 0.15
Tube to work distance (mm)	9.52	9.52	9.52
Heat Input (kJ/mm)	1.31	1.17	1.28

Table 6.3 Purging gas concentrations

Oxygen content (ppm)	50	200	500	5000
Component	Ar + 0.005% O_2	Ar + 0.02% O_2	Ar + 0.05% O_2	Ar + 0.5% O_2

X-ray diffraction (XRD) analysis was conducted to identify the oxide phases present in the different regions of discoloration resulting from varying purging gas compositions. The measurements were performed on a PANalytical X'Pert Pro diffractometer equipped with a cobalt (Co-Kα) radiation source ($\lambda = 1.78896$ Å), operated at 45 kV and 40 mA. Diffraction patterns were collected over a 2θ range of 20 ° to 80 °, with a step size of 0.016 °. The total acquisition time per sample was 1 hour and 37 minutes, and all scans were carried out at room temperature. The measurements were taken directly from the surface of the discolored regions to ensure representative analysis of the oxide layers formed during welding.

6.3.2 Model of welding process

6.3.2.1 Finite Element (FE) weld simulation

FEM was performed using ABAQUS to predict the temperature distribution during welding. The heat transfer in the FEM model is governed by the principle of energy conservation, expressed as:

$$\int_V \rho u \, dV = \int_S q \, dS + \int_V r \, dV \tag{6.1}$$

Here, (V) represents the volume of the material under consideration, (S) indicates the surface area through which heat flux occurs, (ρ) stands for material density, (U) is the rate of change of internal energy, (q) is the surface heat flux, and (r) signifies the volumetric rate of internal heat generation.

To capture the spatial and temporal evolution of the thermal field, the heat conduction equation is employed, characterizing the diffusion of heat within the material:

$$\frac{\partial}{\partial x}(k(t)\frac{\partial}{\partial x}) + \frac{\partial}{\partial y}(k(t)\frac{\partial}{\partial y}) + \frac{\partial}{\partial z}(k(t)\frac{\partial}{\partial z}) + Q_v = \rho(T)C_p(T)\frac{\partial T}{\partial t} \tag{6.2}$$

In the above expression, (k(T)) denotes the thermal conductivity, which, along with the density ($\rho(T)$) and specific heat capacity ($C_p(T)$), varies with temperature (T). The term (Q_v) represents the volumetric heat source attributable to the welding process.

The 3D FEM comprises 256480 nodes, intricately connected through 226710 elements. Within this structure, 3,500 elements specifically cater to the welding passes, while the remaining elements delineate the pipe (6.1). To accommodate the anticipated higher temperature and flux gradients in and around FZ and HAZ, a finely detailed mesh is employed within a 10 mm distance of the Weld Centerline (CL). Beyond the HAZ, element size increases proportionally with distance from the CL. For thermal analyses, Linear 8-node brick elements have been strategically chosen to ensure computational efficiency and accuracy.

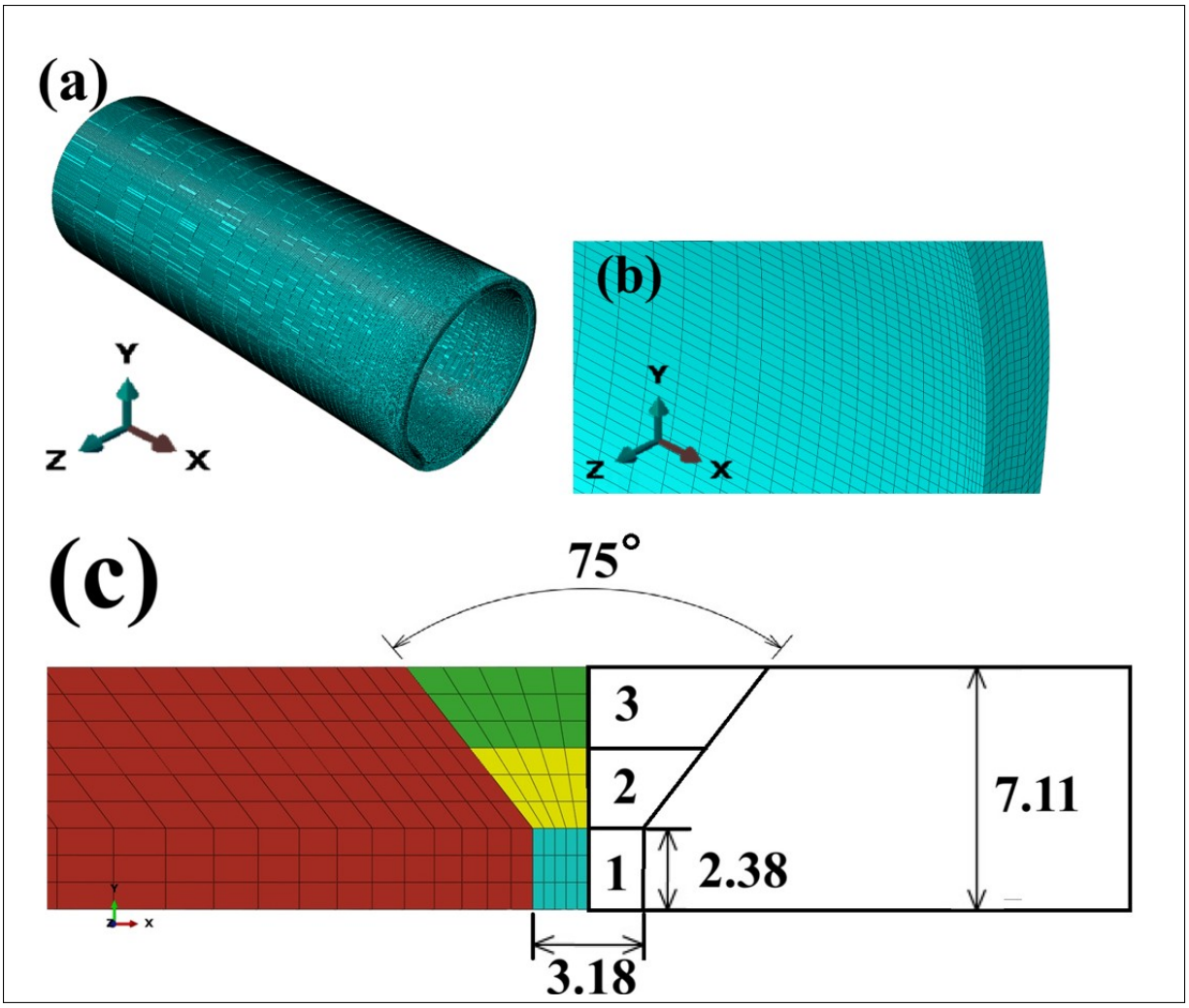

Figure 6.1 The setup used for simulating thermal distribution during the welding of 316L stainless steel pipe: (a) Three-dimensional meshed geometry of the pipe, (b) A zoomed-in view of the mesh near the weld zone, (c) Cross-sectional schematic of the welded joint (all in mm)

A user-defined subroutine, developed in FORTRAN, was integrated into the ABAQUS simulation framework to model the heat input from the welding arc and accurately control the moving heat source during the welding process. The heat from the arc was applied as a volumetric heat source using the double ellipsoidal distribution proposed by Goldak and Akhlaghi(Goldak and Akhlaghi 2005). The distribution is mathematically expressed by the following equations:

For the front heat source center z>0:

$$q_f = \frac{6\sqrt{3f_fQ}}{abc_f\sqrt{\pi}} e^{\left(-\frac{x^2}{a^2}\right)} e^{\left(-\frac{3y^2}{b^2}\right)} e^{\left(-\frac{3z^2}{c^2}\right)} \tag{6.3}$$

For the rear heat source center z<0:

$$q_r = \frac{6\sqrt{3f_rQ}}{abc_r\sqrt{\pi}} e^{\left(-\frac{x^2}{a^2}\right)} e^{\left(-\frac{3y^2}{b^2}\right)} e^{\left(-\frac{3z^2}{c^2}\right)} \tag{6.4}$$

Where x ,y and z represent the local positioning of the double ellipsoid model, precisely aligned with the orientation of the welded pipe. The parameters $a, b, c_r and c_f$ are essential characteristics defining the welding heat source, and these values are obtained through measurements conducted in the actual welding zone which are presented in Table 6.4.

Table 6.4 Heat source parameters measured from real welding zone

Parameter	Pass 1	Pass 2	Pass 3
c_f(mm)	1	2	2
c_r(mm)	6	7	8
a(mm)	2.5	4	4.5
b(mm)	4.5	4.5	4
f_f	0.28	0.44	0.4
f_r	1.72	1.56	1.6

f_f and f_r represent the fractions of heat deposited in the front and rear quadrants, respectively, with the constraint $f_f + f_r = 2$. To maintain continuity in the equations when x=1, the following conditions must be satisfied:

$$f_f = \frac{2c_f}{c_f + c_r} \tag{6.5}$$

$$f_r = \frac{2c_r}{c_f + c_r} \tag{6.6}$$

Q represents the power of the welding heat source and is calculated using the following equation:

$$Q = I \cdot V \cdot \eta \tag{6.7}$$

Where I (A), V (V), and η are welding current, Arc voltage and welding efficiency.

To simulate the heat source movement, a set of parametric equations were used. Figure 6.2 illustrates a set of parametric equations defining the path of a heat source over time on a cylindrical geometry. The image on the left Figure 6.2 illustrates a cylindrical pipe with the coordinate system axes (X, Y, Z) and the heat source's trajectory components (C_1, C_2, C_3). The image on the right Figure 6.2 depicts a top-down view of the cylinder's cross-section, highlighting the radial position (R) of the heat source and its angular position (θ) with respect to the central axis (figure 6.2). These equations describe a three-dimensional path along the surface of a cylinder, factoring in the heat source's linear and angular displacements as a function of time:

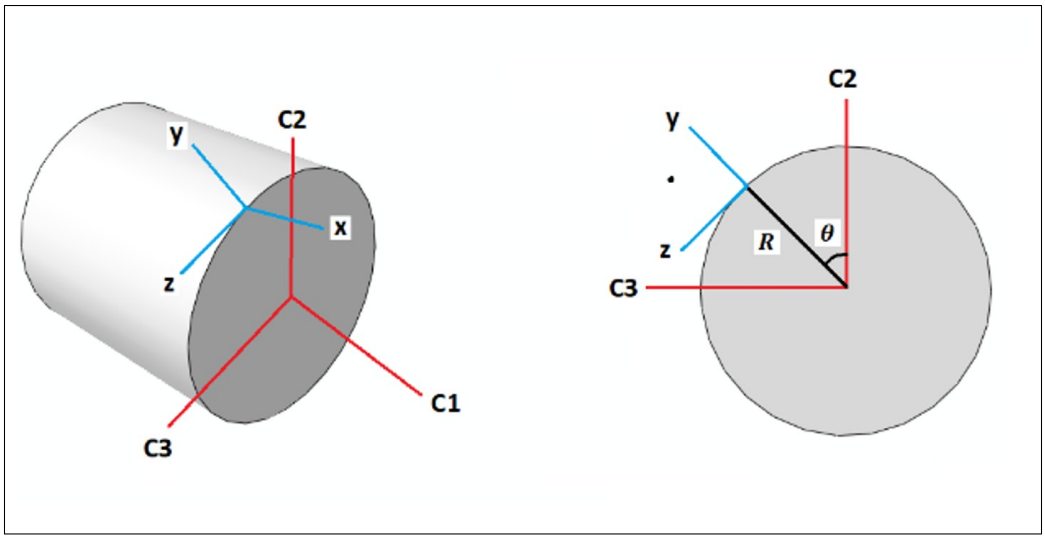

Figure 6.2 Parametric visualization of a moving heat source in cylindrical welding simulation

$$C_1 = x \tag{6.8}$$

$$C_2 = (R + y)\cos(\theta) - z\sin(\theta) \tag{6.9}$$

$$C_3 = (R + y)\sin(\theta) - z\cos(\theta) \tag{6.10}$$

The angle (θ) evolves over time as the heat source orbits the cylinder's surface, with its rate of change defined by the angular velocity (ω) and the radius (R), encapsulating the rotational aspect of the path.

$$\theta = \omega t = \frac{V}{R}t \tag{6.11}$$

(y_1), (y_2), and (y_3) indicate the lateral position of the heat source at different radial distances (R_1, R_2, R_3) from the central axis.

$$x = C_1 \tag{6.12}$$

$$y_1 = C_2 \cos(\theta) + C_3 \sin(\theta) - R_1 \tag{6.13}$$

$$y_2 = C_2 \cos(\theta) + C_3 \sin(\theta) - R_2 \tag{6.14}$$

$$y_3 = C_2 \cos(\theta) + C_3 \sin(\theta) - R_3 \tag{6.15}$$

$$z = C_3 \cos(\theta) + C_2 \sin(\theta) \tag{6.16}$$

The imposed boundary conditions in our simulation model accommodate both convection and radiation phenomena. Notably, radiation losses take precedence at elevated temperatures near the weld, while convection losses become more influential at lower temperatures, particularly away from the welding arc. To effectively capture this dual influence, a consolidated boundary condition, as suggested by [23], has been implemented. This combined boundary condition holistically considers both convection and radiation effects, resulting in the formulation of the temperature-dependent heat transfer coefficient, denoted as h, as expressed in Equations below (Obeid, Alfano et al. 2018, Asadi, Alimohammadi et al. 2021).

$$h = 0.0668T \quad \mathrm{W/m^2\,^\circ C} \quad \text{for } 0 < T < 500^\circ\mathrm{C} \tag{6.17}$$

$$h = 0.231T - 82.1 \quad \mathrm{W/m^2\,^\circ C} \quad \text{for } T > 500^\circ\mathrm{C} \tag{6.18}$$

6.3.3 Thermophysical Properties of 316L Stainless Steel Calculations

The solidus temperature and liquidus temperature, calculated using FactSage, were determined to be 1423°C and 1440°C, respectively. To account for latent heat effects within this temperature range, a value of 270 $\mathrm{kJ\,kg^{-1}}$ was assumed (Deng, Liang & Murakawa, 2007; Venkatkumar & Ravindran, 2019; Xu *et al.*, 2019).

The thermophysical properties of 316L stainless steel—including thermal conductivity, specific heat capacity (Cp), and thermal diffusivity—were experimentally measured using a Laser Flash Analysis (LFA1000) system over the temperature range of 25°C to 1100°C. A total of five samples were tested to ensure repeatability. For each temperature point, six measurements of thermal diffusivity and approximately 60 calculations of Cp were averaged to enhance statistical reliability. As illustrated in Figure 6.3, thermal conductivity increased steadily from 14 W/m·K at 25°C to 38.1 W/m·K at 1000°C. Cp remained relatively stable between 0.44 and 0.55 J/g·K up to 500°C, after which it rose significantly, reaching a peak value of 0.89 J/g·K at 1000°C. A similar increasing trend was observed in thermal diffusivity, which rose from 0.033 cm^2/s at room temperature to about 0.056 cm^2/s at 1000°C (Figure 6.3). Thermal diffusivity (α) was calculated using the relationship:

$$\alpha = \frac{\lambda}{\rho C_P} \tag{6.19}$$

To complete the temperature range required for numerical modeling, thermophysical properties between 1100°C and 1500°C were extrapolated based on values reported in the literature (Mills, 2002a).

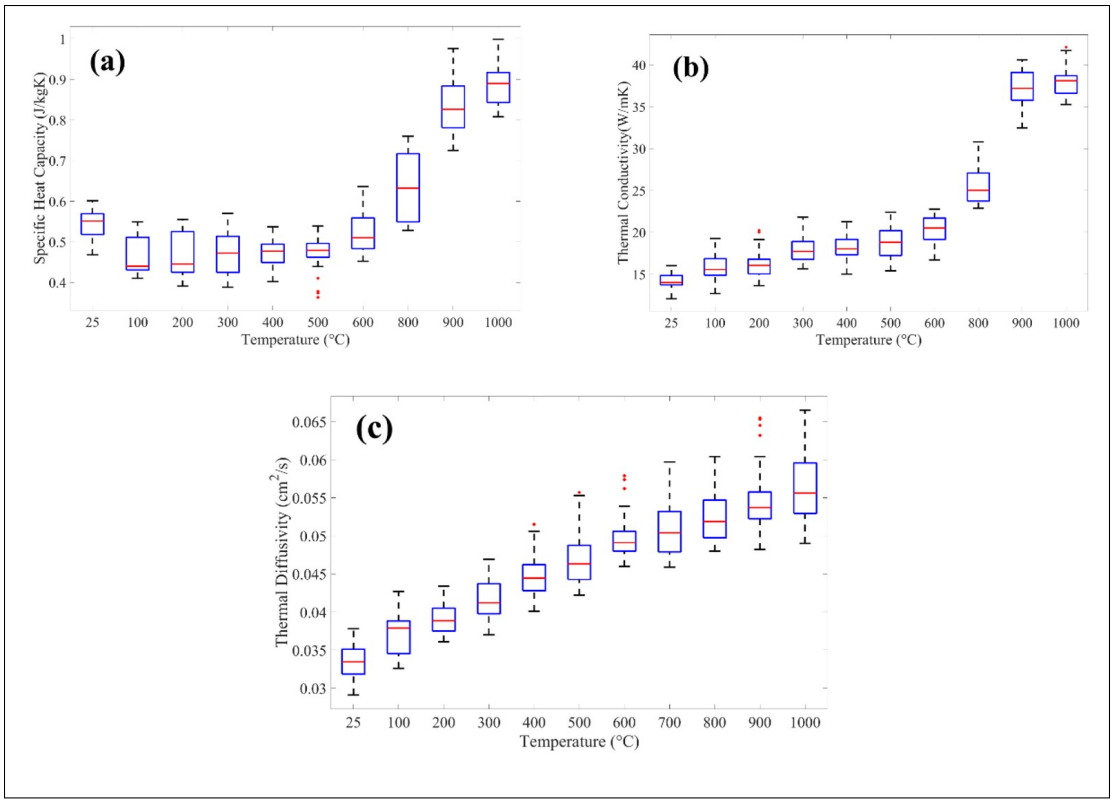

Figure 6.3 Thermophysical Properties of 316L Stainless: (a) specific heat capacity, (b) thermal conductivity, (c) thermal diffusivity

6.3.4 CFD model for weld simulation

6.3.4.1 Torch Model

Before conducting the actual pipe welding simulation, a preliminary model was developed in ANSYS Fluent to validate the surface torch behavior against results reported in the literature (Bitharas *et al.*, 2018). This validation aimed to ensure accurate representation of arc plasma behavior, temperature distribution, and especially oxygen entrainment, which is the key focus of the present study.

The boundary conditions included an argon inlet at 300 K with a flow rate of 6 L/min, an ambient air backflow outlet, and electric potentials of 13 V and 0 V to simulate cathode and anode

walls, respectively. The mixture properties of argon and air were defined using temperature-dependent data: density (ideal gas law), C_p (mixing law), thermal conductivity, viscosity, mass diffusivity, and electrical conductivity, several of which were implemented via user-defined functions (UDFs).

The simulation employed the standard k-ε turbulence model, along with the Magneto-Hydrodynamic (MHD) model to account for Lorentz force ($F_{\text{mag}} = \mathbf{J} \times \mathbf{B}$), Joule heating ($q_{\text{joule}} = \mathbf{J} \cdot \mathbf{E}$), and scalar magnetic field effects. Radiation heat loss was included using a volumetric source term in the energy equation.

This setup enabled comparison of oxygen concentration distributions with the published results. As shown in Figure 6.4, the predicted radial profile of O_2 concentration closely matches the literature data. This validation confirms that the numerical model accurately captures oxygen distribution and magnitude, validating the accuracy of oxygen distribution prediction and provides confidence in its application to the actual pipe welding case.

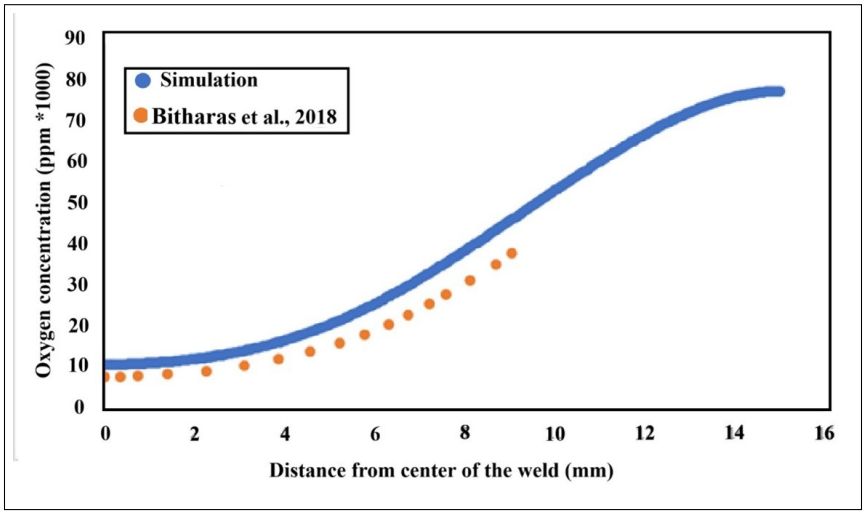

Figure 6.4 Comparison of oxygen concentration as a function of distance from the torch centerline between simulation results and data from (Bitharas *et al.*, 2018).

6.3.4.2 Weld pipe model

In this study, a three-dimensional CFD model was developed to investigate the distribution of oxygen in the backing gas during the GTAW of two cylindrical pipes. The simulation domain consists of two coaxial cylindrical pipes with a gap at the weld joint. The domain was enclosed in a computational box to account for the surrounding environment. The torch was positioned above the weld seam, and its orientation was varied to simulate different angular positions of the weld. Specifically, five torch orientations were analyzed: 0°, 90°, 180°, 270°, and 355°, corresponding to a full rotation around the pipe circumference. Each of these configurations was tested under four different purge gas oxygen contents: 50 ppm, 200 ppm, 500 ppm, and 5000 ppm.

The computational setup was implemented in ANSYS Fluent 2025 R1 using a steady-state solver. The flow field and temperature distribution were solved simultaneously with the oxygen transport to capture the coupling between thermal and mass transport in the weld zone. The model includes two major inlets and several wall boundaries. The argon inlet, located at the torch, introduces pure argon gas at a flow rate of 0.00038 kg/s and a temperature of 296 K (Figure 6.5 (a-1)). This inlet mimics the protective shielding gas delivered through the torch. The purge inlet introduces a gas mixture containing argon and oxygen at the same flow rate of 0.00038 kg/s, but at a slightly lower temperature of 289.817 K (Figure 6.5 (a-3)). This inlet is responsible for protecting the root side of the weld from atmospheric contamination. Both inlets are electrically insulated, with zero flux conditions applied to the electric potential.

The outlet boundary is defined with zero-gauge pressure and allows for backflow composed of 79% nitrogen and 21% oxygen at 300 K (Figure 6.4 (a-2)). Like the inlets, it is electrically insulated. The cathode wall, representing the electrode surface, is assigned a constant potential of 13 V and a no-slip velocity condition (Figure 6.5 (b-4,5)). In contrast, the opposing anode wall is grounded at 0 V and also uses a no-slip condition (Figure 6.5 (b-6)). All other walls in the domain are treated as non-slip surfaces with zero electric flux, ensuring electrical insulation. The detailed boundary setup and domain configuration are illustrated in Figure 6.5.

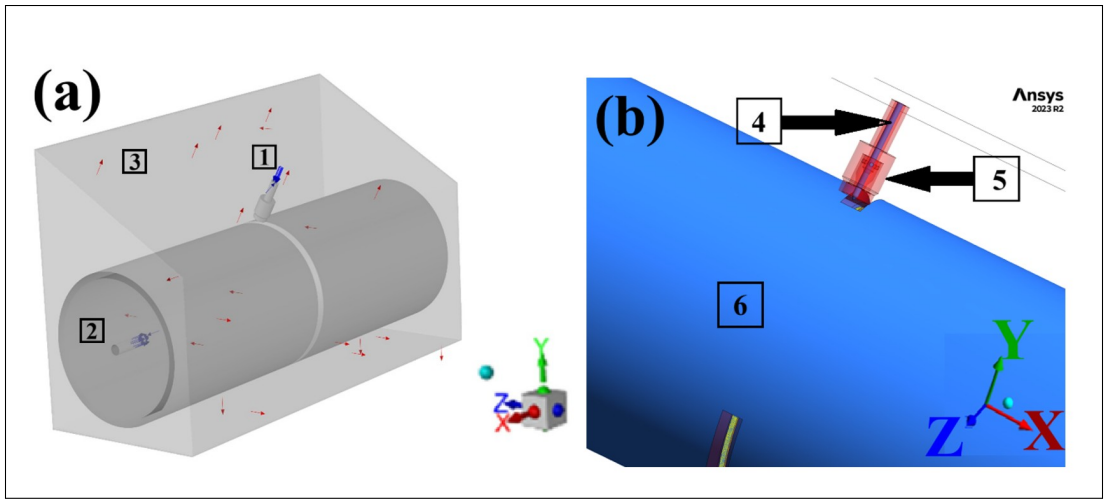

Figure 6.5 (a) Geometric configuration of the 3D simulation domain showing the two coaxial cylindrical pipes being welded, (b) Close-up view of the torch region near the weld joint in the 3D computational model. The figure highlights the inlet conditions

The mesh was generated with a physics preference set to CFD and a solver preference assigned to ANSYS Fluent. For the overall mesh statistics, the final model comprised 1,294,398 nodes and 7,337,530 elements in the medium mesh. Hex-dominant meshing techniques were applied, utilizing the Quad Dominant method for sheet bodies and the Sweep method for sweepable regions. To evaluate mesh sensitivity, coarse, medium, and fine mesh configurations were compared. The coarse mesh contained approximately 4,402,518 million cells, while the fine mesh had about 11,006,295 million cells. Since the medium mesh provided results consistent with the fine mesh but with significantly reduced computational demand, it was selected for all subsequent simulations. The meshed geometry and local refinement around the nozzle are illustrated in Figure 6.6.

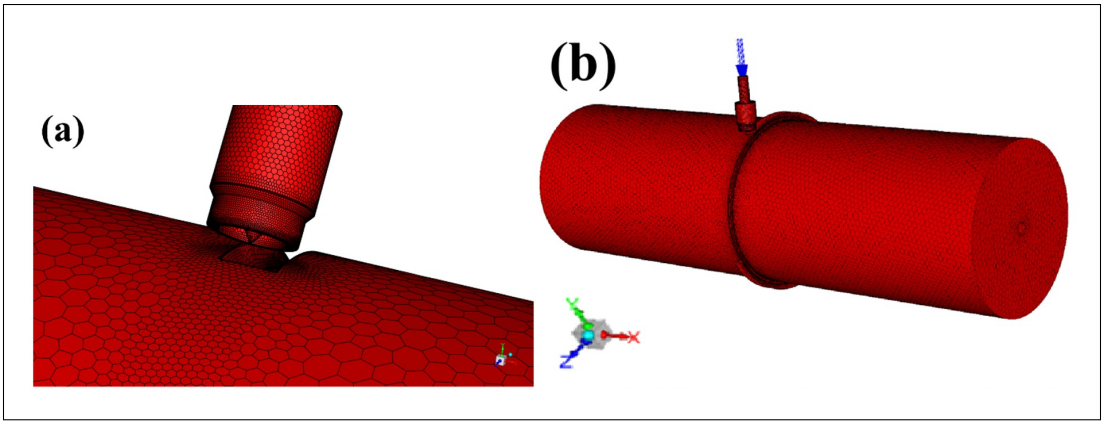

Figure 6.6 Mesh structure used for the CFD model: (a) close-up view of the local mesh refinement around the nozzle and weld root area; (b) overall view of the meshed geometry for the entire pipe assembly

In the present model, the plasma is treated as a multicomponent gas mixture, where the mass fractions of individual species are spatially distributed. It is assumed that the system is in local thermodynamic equilibrium (LTE), implying that the electron temperature is equal to that of the heavy species. This assumption is supported by experimental investigations conducted by Valensi et al. (Bitharas *et al.*, 2018), justifying the adoption of a single temperature field for all components in the plasma. As a result, the temperature-dependent thermophysical properties of the plasma—including density, specific heat, viscosity, and both thermal and electrical conductivity—were evaluated over a broad temperature range (300 K to 30,000 K), considering the influence of air species' mass fractions (Murphy, 1995).

The thermodynamic and transport properties were calculated using the Chapman–Enskog formulation (Present, 1968). Specifically, updates related to argon and nitrogen species were included based on the works of Murphy and Tam (Murphy & Tam, 2014) and Buchowiecki (Buchowiecki & Szabo, 2022). The governing set of non-linear partial differential equations, along with associated boundary conditions, are presented in the following sections. These equations were solved numerically using a hybrid approach combining Newton–Raphson iterations and the double dogleg method (Chen, Li, Huang, Li & Liu, 2022). Unless otherwise noted, the simulations used baseline welding parameters, as listed in Table 6.2.

6.3.4.3 Governing Equations

The simulation framework employs a set of coupled partial differential equations (PDEs) that govern fluid dynamics, electromagnetics, heat transfer, and species transport, expressed in vector form for generality. Vector quantities are shown in bold, and temperature- and composition-dependent properties are denoted in italics.

The fluid flow is modeled using the compressible Navier–Stokes equations. Conservation of momentum is expressed as:

$$\rho(\mathbf{u} \cdot \nabla \mathbf{u}) = \nabla \cdot [-p + \mu(\nabla \mathbf{u} + (\nabla \mathbf{u})^{\mathrm{T}})] + \mathbf{B} \times \mathbf{J} + \rho \mathbf{g} \tag{6.20}$$

where ρ is the fluid density (kg/m^3), $\mathbf{u}$ is the velocity vector (m/s), p is the static pressure (Pa), μ is the dynamic viscosity (Pa·s), $\mathbf{B}$ is the magnetic flux density (T), $\mathbf{J}$ is the electric current density (A/m^2), and $\mathbf{g}$ is the gravitational acceleration vector (m/s^2). The right-hand side of the equation includes the Lorentz force ($\mathbf{B} \times \mathbf{J}$) and gravitational force ($\rho \mathbf{g}$) acting on the fluid. The term $\nabla \mathbf{u} + (\nabla \mathbf{u})^{\mathrm{T}}$ corresponds to the symmetric part of the velocity gradient tensor, ensuring accurate viscous stress representation (Bitharas *et al.*, 2018).

Mass conservation is enforced through the continuity equation:

$$\nabla \cdot (\rho \mathbf{u}) = 0 \tag{6.21}$$

which ensures incompressible flow characteristics are preserved under steady-state conditions.

To capture the effects of turbulence and enhance numerical stability within the plasma jet, the standard two-equation k–ε turbulence model was integrated into the governing system alongside the Navier–Stokes equations.

The electric field distribution within the arc region is obtained by solving the current continuity equation:

$$\nabla \cdot \mathbf{J} = 0 \tag{6.22}$$

The magnetic field induced by current flow is modeled using a gauged form of Ampère's law, written as:

$$\nabla \times (\nabla \times \mathbf{A}) = \mu_0(\mathbf{J} + \nabla(1/\mu_0\Psi)) \tag{6.23}$$

where $\mathbf{A}$ is the magnetic vector potential (Wb/m), μ_0 is the magnetic permeability of free space (H/m), and Ψ is the scalar Coulomb gauge function, which does not influence observable physical fields but helps uniquely define $\mathbf{A}$ (Bitharas *et al.*, 2018). This is ensured by the application of the Coulomb gauge condition:

$$\nabla \cdot \mathbf{A} = 0 \tag{6.24}$$

Electric and magnetic fields are subsequently derived from their potentials. The current density is obtained using Ohm's law:

$$\mathbf{J} = -\sigma \nabla V \tag{6.25}$$

where σ is the electrical conductivity (S/m) and V is the electric potential (V). The magnetic flux density is given by:

$$\mathbf{B} = \nabla \times \mathbf{A} \tag{6 26}$$

and the electric field intensity is defined as:

$$\mathbf{E} = -\nabla V \tag{6 27}$$

Thermal transport within the arc plasma is governed by an energy conservation equation accounting for convection, conduction, Joule heating, and radiation:

$$\rho c(\mathbf{u} \cdot \nabla T) = \nabla \cdot (k \nabla T) + \mathbf{J} \cdot \mathbf{E} + \mathbf{J} \cdot \nabla T - \frac{\varepsilon_p}{2k_e} \cdot \left(\frac{T^4}{\pi}\right) \tag{6 28}$$

In this equation, c is the specific heat capacity at constant pressure (J/kg·K), T is temperature (K), k is thermal conductivity (W/m·K), ε_p is the radiative emission coefficient (W/m^3·K^4), and k_e is Boltzmann's constant (eV/K). The terms on the right-hand side respectively represent conductive heat transfer, Joule heating from electric current, thermoelectric contributions, and radiative losses, the latter being computed only within the plasma zone based on temperature-dependent ε_p values (Bitharas *et al.*, 2018).

To evaluate mixing behavior and contamination from ambient air, species transport equations were solved for argon and air. The convective-diffusive mass transport equation for the species mass fraction ω_i is written as:

$$\nabla \cdot [\rho(D_i^o \nabla \omega_i + D_i^T \nabla T/T)] + \rho \mathbf{u} \cdot \nabla \omega_i = 0 \tag{6 29}$$

where ω_i is the mass fraction of species i, D_i^o is the molecular diffusion coefficient (m²/s), D_i^T is the thermal diffusion coefficient (m²/s), and T is the local temperature. The equation is explicitly solved for ω_2 (air), with the mass fraction of argon (ω_1) calculated by difference from unity (Bitharas *et al.*, 2018).

To simulate turbulent mixing of gas species, the effective diffusion coefficient is enhanced by adding a turbulent component, defined as:

$$D_i = \frac{\mu_t}{Sc_t} \tag{6 30}$$

where μ_t is the turbulent kinematic viscosity (m^2/s) and Sc_t is the turbulent Schmidt number (dimensionless). A value of $Sc_t = 0.2$ is adopted, consistent with experimental studies of turbulent jet mixing by He et al. (He & Hou, 1999).

6.3.5 Validation of the simulations

In this study, the temperature distribution inside the pipe during welding was calculated using a FEM, while the surrounding oxygen concentration was captured through a CFD simulation. These results were then used to develop a non-isothermal oxidation model to estimate oxide growth in the HAZ of 316L stainless steel during welding. The model takes into account the time-dependent temperature history obtained from the first welding pass. For oxygen partial pressure near the weld root, either assumed values based on purging conditions or data from the CFD simulation were used to represent the local environment and predict oxide thickness.Oxidation kinetics are formulated using the extent of conversion, $\alpha(t)$, which quantifies the fraction of metal that has been oxidized. The rate of oxidation is governed by an Arrhenius-type equation in the form (Sato *et al.*, 2002; Vyazovkin *et al.*, 2011; Kang *et al.*, 2014; Guo *et al.*, 2015; Bielsa, Zaki, Arias & Faik, 2021; Gamisch, Huber, Gaderer & Dawoud, 2022):

$$\frac{d\alpha}{dt} = AP_{O_2}^n \exp\left(\frac{-E_a}{RT}\right) f(\alpha)(1-\alpha)^2 \tag{6.1}$$

where $A(\alpha)$ and $E_a(\alpha)$ are the pre-exponential factor and activation energy interpolated from thermogravimetric analysis (TGA) based on α-dependent iso-conversional results. $P(O_2)$ is

the oxygen partial pressure (in atm), n is the reaction order with respect to oxygen, taken as 2 to reflect parabolic oxidation behavior observed in many stainless steels. R is the universal gas constant (8.314 J/mol·K), and T is the instantaneous temperature in Kelvin. The reaction model $f(\alpha) = (1 - \alpha)^2$ corresponds to the F2 model, appropriate for solid-state reactions in which the reactive interface shrinks as oxidation progresses. Oxidation is considered to initiate only above 1100 K, as observed from TGA data.

This model directly calculates oxide thickness using stoichiometric relations based on the extent of oxidation. The oxide thickness $x(t)$ is given by:

$$x(t) = \frac{\alpha(t) \cdot M_{ox}}{\rho_{ox}} \tag{6.2}$$

where M_{ox} is the effective molar mass of the oxide scale and ρ_{ox} is its effective density. These thermophysical parameters were calculated using phase fraction results obtained from FactSage equilibrium simulations in the temperature range of 827 °C and 1097°C. The oxide scale in this study primarily consists of a mixture of spinel and corundum phases. The temperature-dependent percentage of each oxide was extracted from FactSage, and the effective molar mass and density were computed as weighted averages based on these fractions. For instance, if the oxide layer consists of 60% spinel (such as $(Fe,Cr)_3O_4$) and 40% corundum ($(Fe,Cr)_2O_3$), the effective molar mass and density are calculated as weighted averages. Typical values for these phases are $M_{spinel} \approx 0.174$ kg/mol with $\rho_{spinel} \approx 4900$ kg/m³, and $M_{corundum} \approx 0.153$ kg/mol with $\rho_{corundum} \approx 5250$ kg/m³.

A forward Euler numerical integration method is applied to solve the model iteratively over time using the supplied simulation data. This framework enables direct prediction of oxide thickness as a function of time, temperature, and oxygen availability, and is especially suited for modeling oxidation under rapid, transient heating conditions like those encountered in welding processes.

6.4 Results and discussion

6.4.1 SEM and XRD Characterization of Oxide Layers

6.4.1.1 Effect of Oxygen Content on Oxide Layer Thickness at a Fixed Distance

Our Previous study shows cross-sectional SEM images of oxide layers at a constant distance from the fusion zone, formed under different oxygen concentrations: 500 ppm, and 5000 ppm. The oxide layer thickness increases markedly with higher oxygen content. At 500 ppm, a thin oxide layer is present, while at 5000 ppm, a thicker layer is observed. This trend indicates that higher oxygen partial pressures accelerate oxide formation.

6.4.1.2 Oxide Composition at Fixed Distance for Different Oxygen Levels (EDS)

EDS analysis from our previous study for oxide layers at a fixed distance from the fusion zone for 500, and 5000 ppm oxygen shows :

- At 500 ppm, the oxide layer mainly consists of Chromium, forming a protective passive layer.

These compositional shifts explain why the color intensity increases with oxygen concentration: iron oxides contribute to darker zone, while chromium oxides are associated with the other colors.

6.4.1.3 XRD Patterns at Different Distances (5000 ppm)

6.7 displays XRD patterns from various distances within the discoloration zone under 5000 ppm oxygen.

- Near the fusion zone, strong peaks of FeO, Fe_3O_4, and Cr_2O_3 are identified, indicating the formation of complex oxides.
- At greater distances, FeO peaks diminish, while Cr_2O_3 remains prevalent, showing a gradual shift to chromium-rich oxides in lower-temperature regions.

These results confirm a strong correlation between oxide layer thickness, composition, and the discoloration color spectrum observed visually. The SEM and XRD findings validate the above analysis based on optical interference theory and provide a microstructural basis for the visual discoloration patterns.

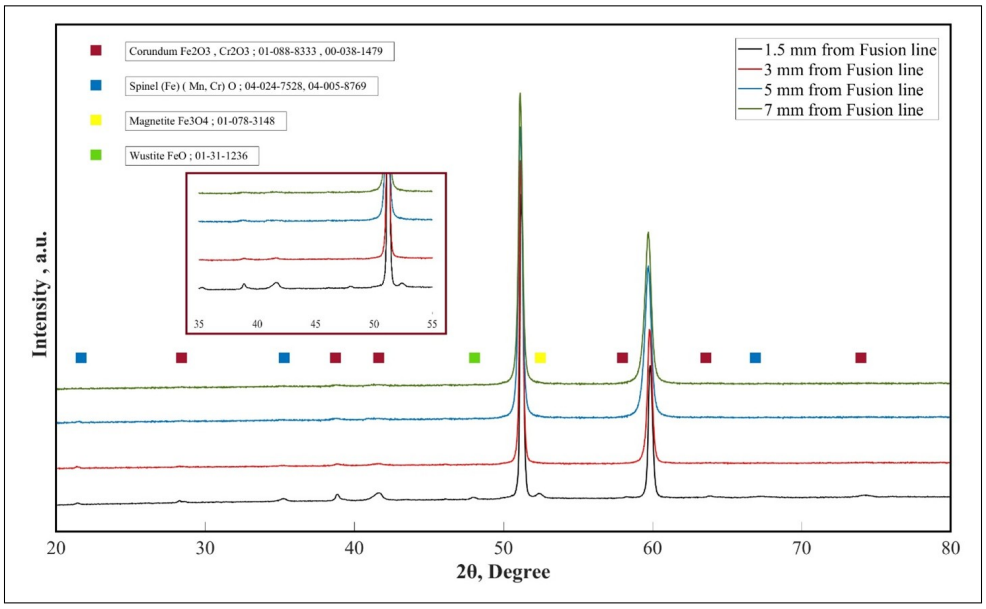

Figure 6.7 XRD pattern under 5000 ppm oxygen condition in different location of discoloration

6.4.2 Thermodynamic Predictions of Oxide Formation Using FactSage

To complement the experimental observations, thermodynamic simulations were conducted using FactSage to predict oxide formation at equilibrium under varying temperature conditions. The results provide insights into the expected oxide phases at different zones of the weld, correlating with the temperature gradients and discoloration patterns.

The simulations were carried out at 800°C, 900°C, 1000°C, 1100°C, 1200°C, 1300°C, 1400°C, 1450°C, and 1500°C, as shown in Figures 6.8 and 6.9 . All calculations were performed under equilibrium conditions, which serve as predictive tools rather than exact reflections of the experimental environment.

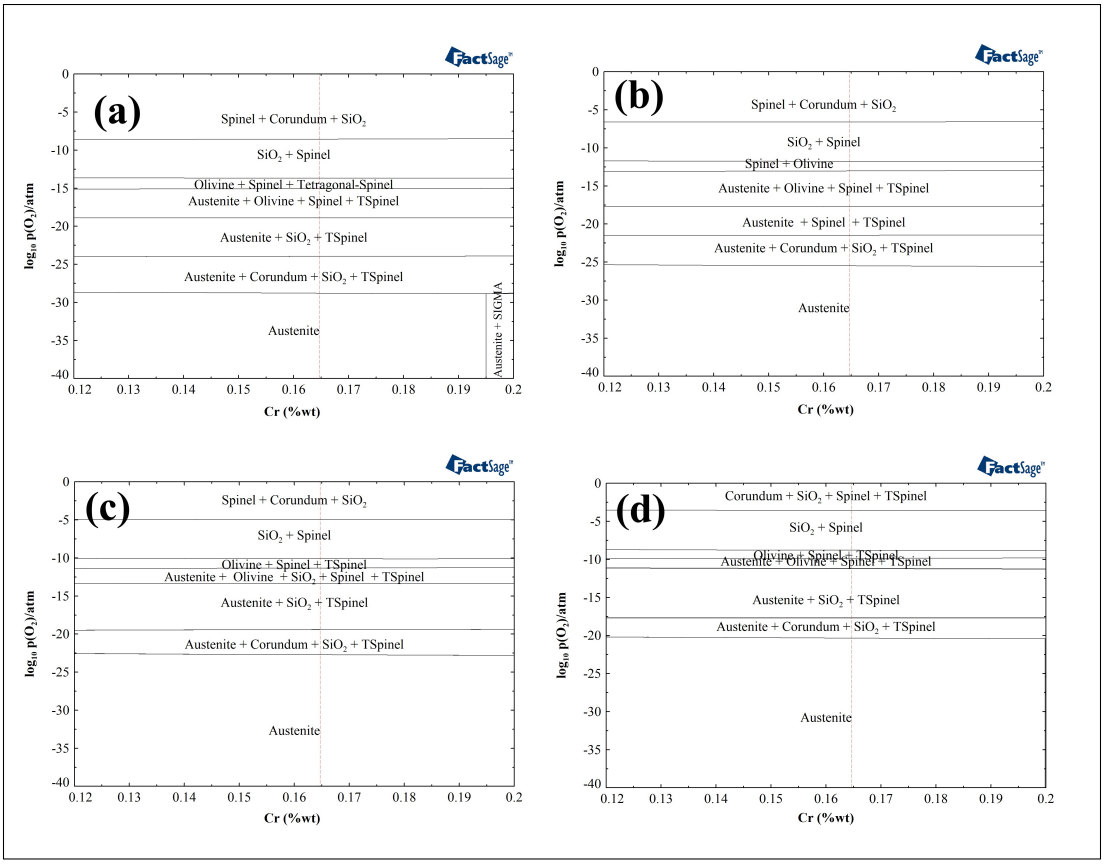

Figure 6.8 FactSage predicted oxide phase distribution on 316L stainless steel surfaces exposed to varying temperature: (a) 800 °C, (b) 900 °C, (c) 1000 °C, (d) 1100 °C

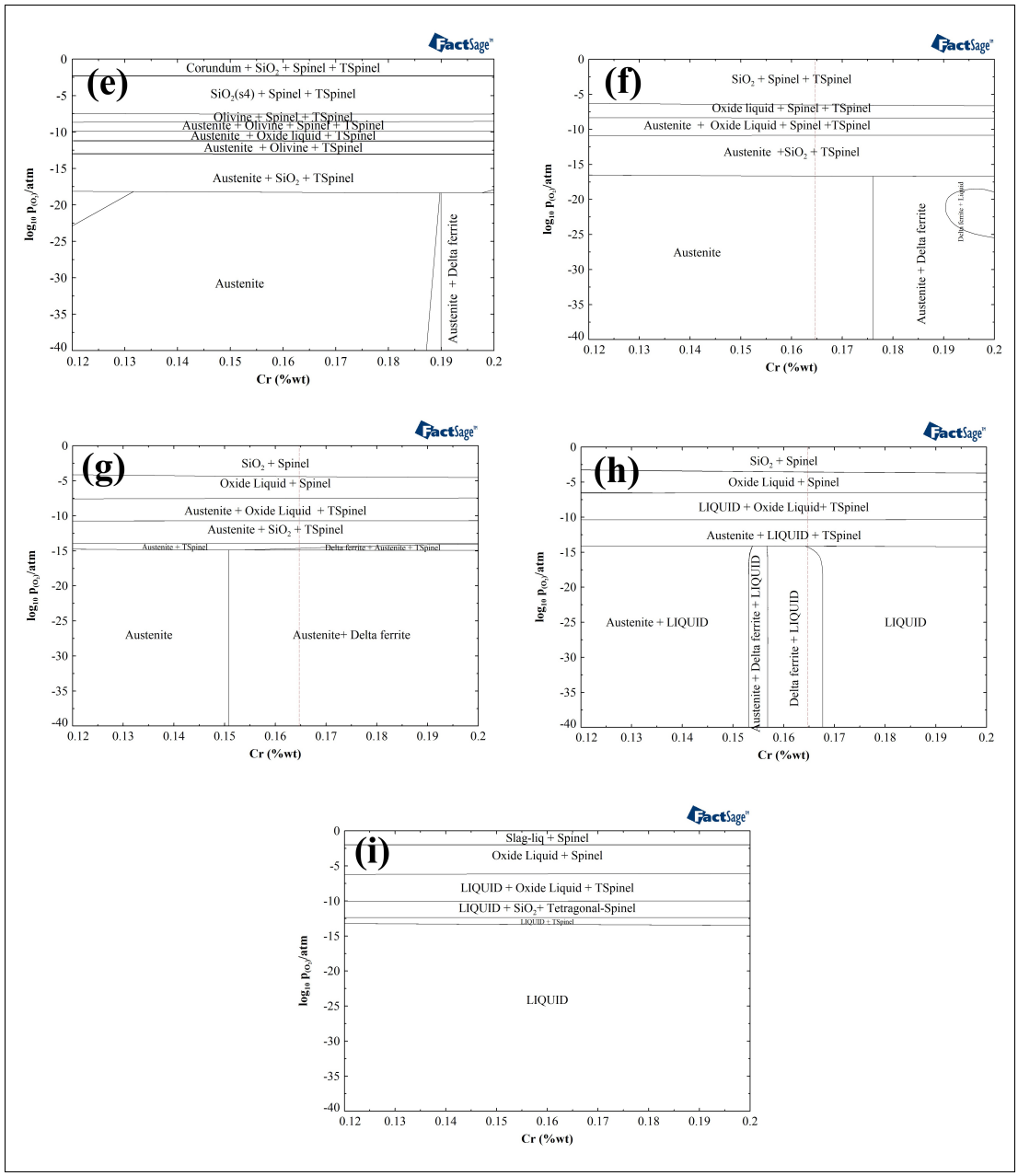

Figure 6.9 FactSage predicted oxide phase distribution on 316L stainless steel surfaces exposed to varying temperature: (e) 1200 °C, (f) 1300 °C, (g) 1400 °C, (h) 1450 °C, and (i) 1500 °C

6.4.2.1 Oxide Phase Evolution with Temperature

- Below 1200°C: The oxide scale consists of corundum (α-Al_2O_3) and t-spinel (Cr_2O_3-based spinel) in the inner layer, and a mixture of corundum, spinel, and t-spinel in the outer layer.
- At 1200°C: The inner layer transitions to t-spinel only, while the outer layer retains spinel, t-spinel, and corundum phases.
- 1300°C: The outer oxide layer simplifies to spinel + t-spinel, indicating a shift towards iron-rich spinel phases. The substrate begins to transform from austenite to austenite + ferrite.
- 1400°C: The oxide structure becomes dominated by spinel, while the metal substrate continues to evolve towards ferrite.
- 1450°C: At the mushy zone between the solidus (1420°C) and liquidus (1440°C), the metal is a mixture of ferrite + liquid, and the oxide layer transitions to a single-phase oxide liquid.
- 1500°C: Complete melting occurs, with both metal and oxide present as liquid.

6.4.2.2 Formation of Oxide Liquid and Dark Discoloration

At temperatures above 1300°C, a single-phase oxide liquid forms, which is likely the cause of the dark zones observed experimentally in the 5000 ppm oxygen condition. Based on previous studies, this oxide liquid is primarily composed of FeO (Maroufkhani, Hakimian et al. 2023).

The appearance of this oxide liquid in the high-temperature regions explains the intense black discoloration near the fusion zone in high-oxygen environments, as previously shown in Figures 6.8 and 6.9.

The FactSage predictions align well with the SEM and XRD findings:

- The formation of FeO at higher temperatures (near the weld) explains the thicker and darker oxide layers observed experimentally.
- The transition from mixed oxides to spinel-only structures at elevated temperatures matches the compositional changes detected in EDS and XRD data.
- The thermodynamic prediction of oxide liquid formation is consistent with the blackened areas in the discoloration zone, particularly for 5000 ppm oxygen.

The thermodynamic based simulations confirm that temperature influences both the oxide phase formation and visual appearance of the weld zone, supporting the interpretations derived from both the visual and microstructural analyses, as reported in Figures 6.8 and 6.9.

6.4.3 Oxygen Distribution Results

To evaluate the transient behavior of oxygen distribution during orbital pipe welding, simulations were conducted for 90°, 180°, 270°, and 355°angular positions of the welding torch representing the early, intermediate, and final stages of the circumferential weld process. While the presented data correspond to the 5000 ppm case, simulations performed at lower oxygen concentrations (50, 200, and 500 ppm) revealed similar trends across all angular positions.

Figure 6.10 presents 3D streamline visualizations of the mass fraction of O_2 in the pipe at the four torch angles. At 90° (6.10a), the oxygen is moderately distributed with partial dilution near the weld area. At 180° (6.10b), a noticeable increase in oxygen concentration is observed, particularly around the torch side and upper region of the pipe interior, suggesting insufficient shielding effectiveness at this stage. In contrast, by 270° (6.10c), oxygen concentration has decreased, indicating the improvement in coverage due to the increasing enclosed geometry and potentially better gas confinement. At 355° (6.10d), very low levels of oxygen are observed throughout the domain, reflecting effective protection due to the nearly enclosed geometry and stable gas flow pattern.

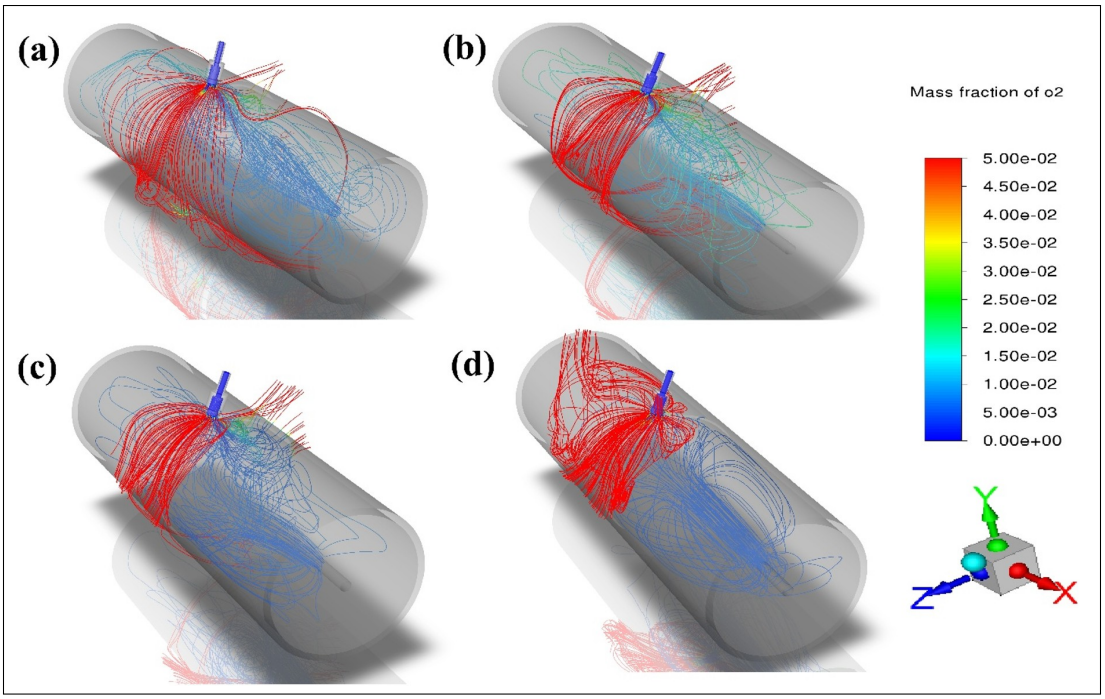

Figure 6.10 Streamline plots colored by oxygen mass fraction at various torch angular positions during circumferential pipe welding with 5000 ppm (mass fraction = 0.005) O: (a) 90 °, (b) 180 °, (c) 270 °, and (d) 355 °.

Figure 6.11 provides a longitudinal cross-section (YZ plane) view of the mass fraction of O_2 at the same angular positions. here again it can be seen that at 180°, ambient oxygen ingress into the pipe is more pronounced than at 270° and 355°. The oxygen-rich zones correspond to regions directly exposed to the environment, whereas areas downstream of the weld torch show gradual dilution. These results confirm that during the early-to-mid welding stages, especially at 180°, transient turbulence and incomplete shielding coverage may lead to localized oxidation risk.

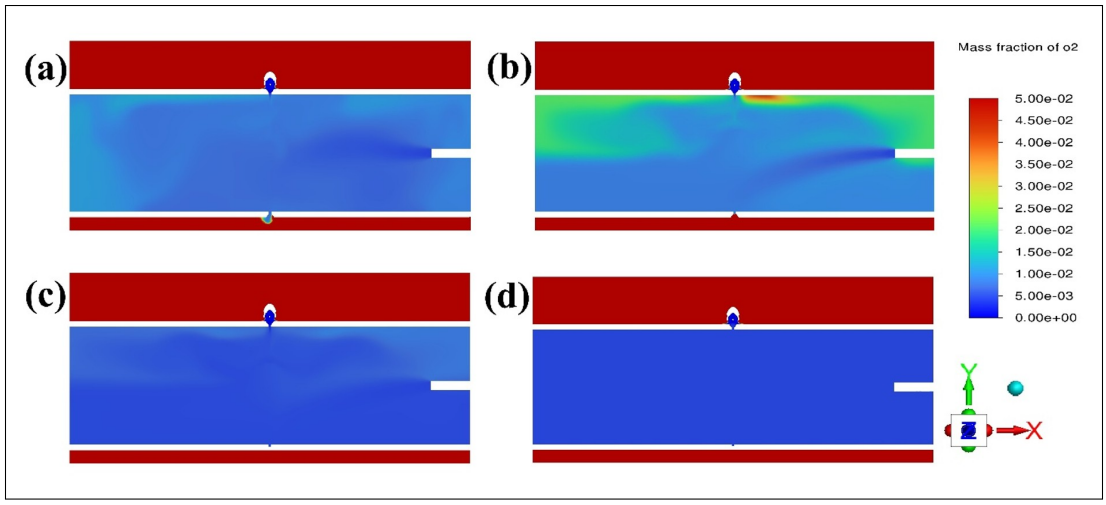

Figure 6.11 Longitudinal (XY plane) contour plots of O_2 mass fraction at (a) 90 °, (b) 180 °, (c) 270 °, and (d) 355 ° angular positions

6.12 displays cross-sectional (XY plane) contours of O_2 mass fraction near the weld seam. The analysis highlights that the intrusion of oxygen is significantly higher at 90° and 180° with considerable penetration at the upper pipe region. As the weld progresses, the oxygen mass fraction decreases substantially, reaching minimal values at 355°, where the torch approaches the closing segment of the weld path and the oxygen level reaches the targeted value of 5000ppm.

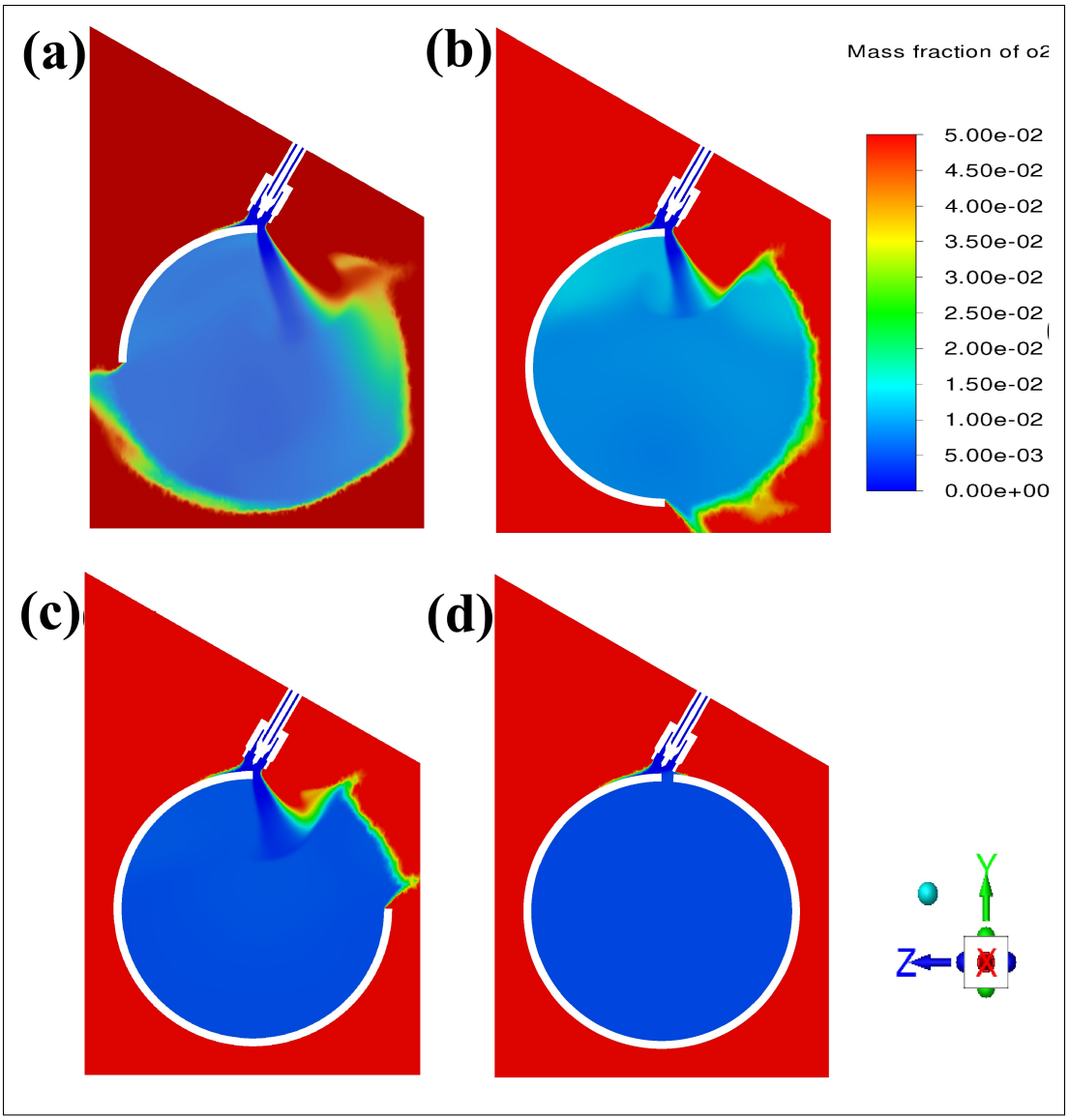

Figure 6.12 Cross-sectional (YZ plane) contours of oxygen mass fraction at: (a) 90°, (b) 180°, (c) 270°, and (d) 355°

6.13 (a) illustrates the 3D model with the black reference line indicating the extraction path used to probe oxygen mass fraction for quantitative comparison. Figure6.13 (b) shows a cross-sectional view of the same line path used for mass fraction extraction in the simulation domain.

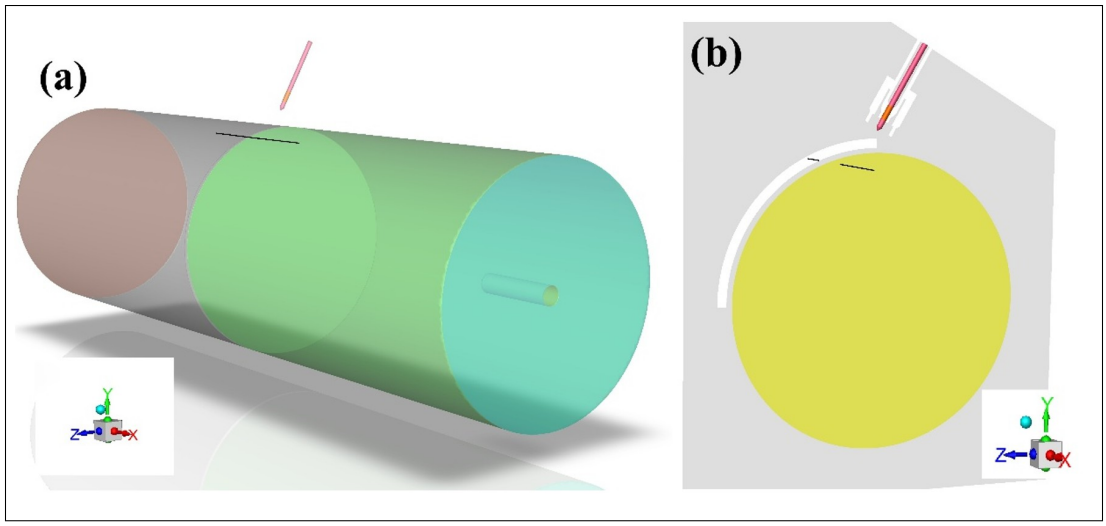

Figure 6.13 (a) 3D representation of the pipe with black line indicating the sampling path for extracting oxygen mass fraction along a consistent cross-section,(b) 2D cross-sectional view of the pipe and torch

As it is shown in Figure 6.14, the observed trend in oxygen mass fraction—rising from 90° to a peak at 180°, then decreasing toward 270° and 355°—is influenced by both shielding and backing gas interactions, torch position, and pipe geometry during welding. At 90°, moderate oxygen presence occurs as the welding process begins and the protective gas coverage is not yet fully established. By 180°, although shielding gas is active, the backing gas flow has not yet fully stabilized along the inner pipe surface, resulting in poor oxygen displacement and the highest recorded oxygen concentration. The rise in oxygen mass fraction from 90° to 180° is primarily attributed to arc-induced turbulence and natural convection inside the pipe, especially as the arc reaches the topmost position (180°). At this stage, the buoyant forces from high temperatures cause oxygen-laden air to recirculate upward, making it more difficult for the shielding and backing gas to maintain a stable, protective environment. This leads to oxygen accumulation near the weld root. Between 180° and 270°, as welding progresses downward along the pipe wall, gravitational forces and improved confinement of both shielding and backing gases help suppress turbulent recirculation and enhance purging efficiency, thereby reducing oxygen ingress. Hence, the observed peak at 180° followed by a decreasing trend is a direct consequence of the interplay between thermal buoyancy, turbulence, and gas flow

behavior within the pipe geometry. As welding progresses to 270° and 355°, the combined effects of the shielding and backing gases become more effective—especially due to increased confinement inside the pipe and more developed purging flow—significantly reducing oxygen ingress. The same pattern was consistently observed in all oxygen input scenarios (50, 200, 500, and 5000 ppm), confirming the critical role of both shielding and backing gases in achieving optimal protection in the later stages of pipe welding.

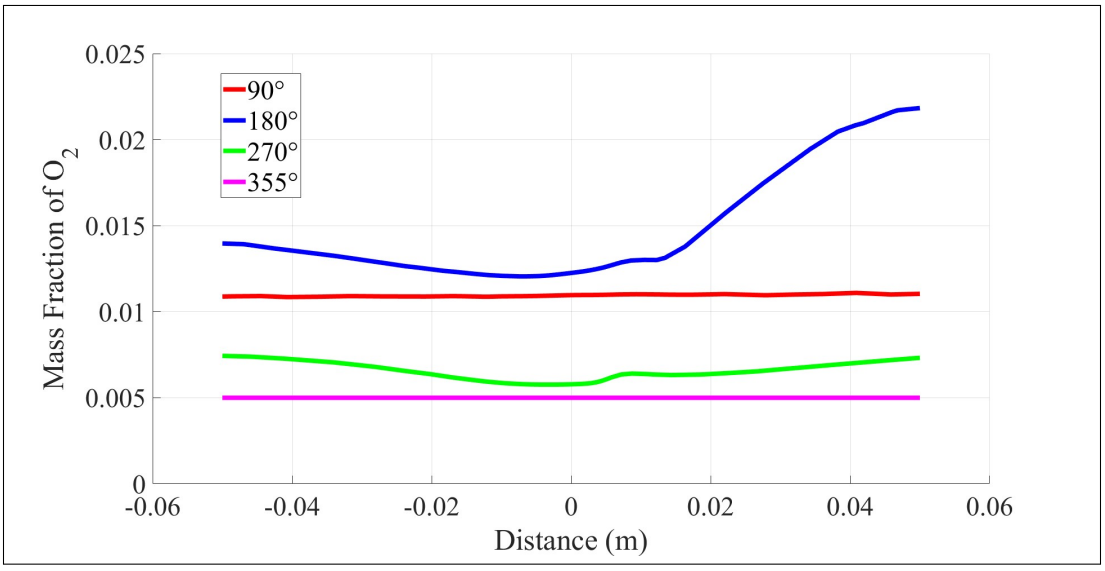

Figure 6.14 Mass fraction of O_2 vs. distance along the probe line beneath the weld torch for 5000 ppm oxygen case at four angular positions

Figure 6.15 shows the mass fraction of oxygen along the defined path at the 90° and 270° angular positions for four different backing gas oxygen contents: 50, 200, 500, and 5000 ppm. Despite the increasing inlet oxygen concentration, the mass fractions for 50, 200, and 500 ppm remain remarkably close, with the 500 ppm case even slightly lower than the 50 ppm case at 90°. This counterintuitive result highlights that oxygen distribution is not solely governed by the inlet concentration but is also highly sensitive to localized flow patterns and shielding efficiency. One plausible explanation for the slightly higher oxygen fraction in the 50 ppm case is the lower buoyancy-driven flow, which reduces the upward momentum that helps displace oxygen,

leading to longer residence time near the probe line. Additionally, minor variations in turbulence intensity and localized diffusion paths can enhance oxygen retention under low-inlet conditions.

This interpretation is further examined by comparing the 270° results shown in the same figure. While the general expectation was that oxygen levels would decrease due to improved confinement and stabilized gas flow in later welding stages, the plot reveals that at 270°, the oxygen mass fraction actually increases in the order of 50 ppm < 200 ppm < 500 ppm — which aligns more intuitively with the inlet concentrations, unlike the 90° case. However, it is important to note that all three simulated cases (50, 200, and 500 ppm) still show higher oxygen mass fractions than what would be expected from their nominal input levels. This suggests that even at later stages, full purging is not entirely achieved for lower ppm conditions, and some oxygen accumulation or recirculation persists due to incomplete displacement, boundary layer effects, or flow separation near the weld root.

Interestingly, the 5000 ppm case at 270° shows a clear drop in mass fraction compared to its value at 90°, and approaches the expected oxygen level more closely than the lower ppm cases. This behavior supports the notion that at high oxygen concentrations, the mass fraction becomes increasingly dominated by the inlet condition, and the saturation effect overwhelms the influence of local turbulence or confinement. Therefore, although the trend at 270° is more consistent with ppm magnitude, the consistently elevated levels for 50–500 ppm, compared to their ideal values, underscore the significance of transient flow behavior and imperfect shielding in practical welding environments.

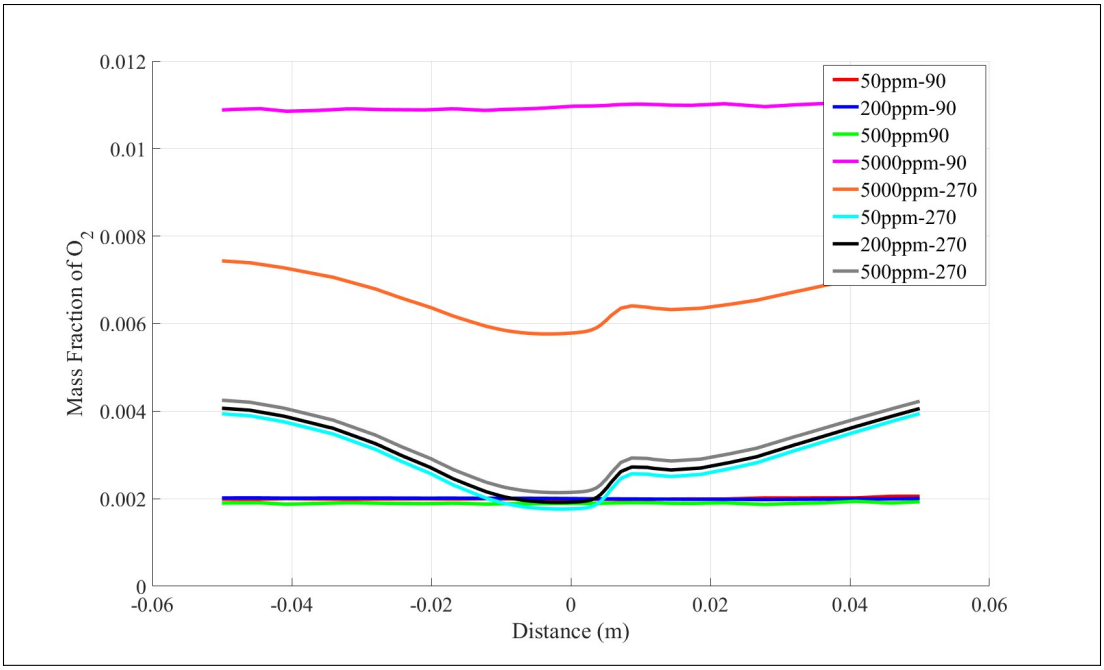

Figure 6.15 Mass fraction of oxygen along the defined path at 90° and 270° angular position for varying oxygen concentrations in the backing gas (50, 200, 500, and 5000 ppm)

6.4.4 Computational Thermal Analysis of the Welding Process

The simulated welding sequence begins at the circumferential angle $\theta = 0°$, proceeds along the pipe's perimeter, and concludes at the same point, completing a full circular pass, as illustrated in Figure 6.16. The welding direction is indicated by an arrow for clarity. The corresponding temperature distribution during welding is also shown in the same figure. The simulation predicts a peak temperature in the weld pool region for first pass of approximately 3098 °C. This temperature rise confirms the accurate calibration of the heat source model and validates the simulation's ability to realistically represent the thermal behavior during the welding process.

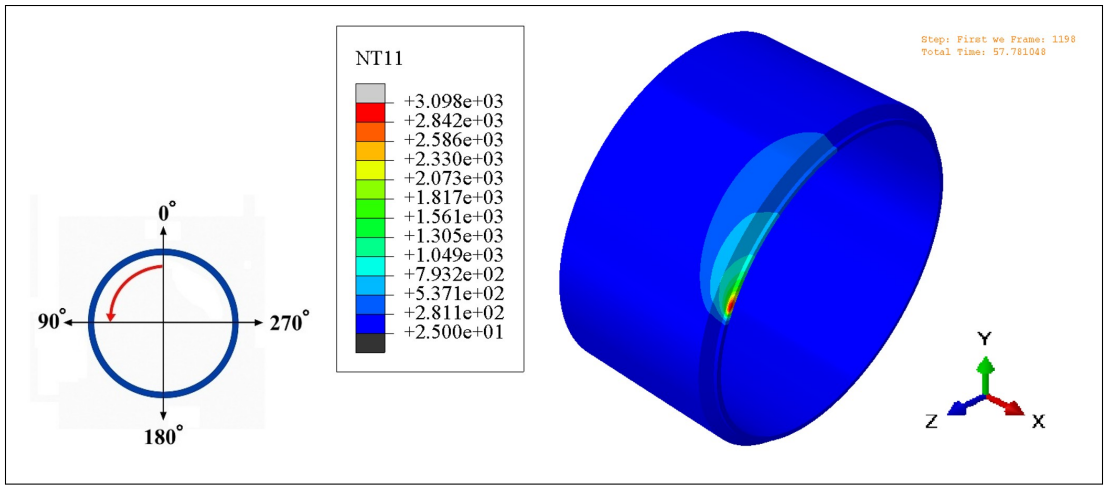

Figure 6.16 Temperature distribution during the first welding pass on the inner surface of a 316L stainless steel pipe and schematic representation of the welding direction on the pipe's circumference, indicating the torch movement from 0° to 180°

Figure 6.17 illustrates the simulated thermal cycles recorded at three circumferential locations—90°, 180°, and 270°—each situated 1 mm away from the fusion line on the inner surface of the pipe. These locations were selected to evaluate temperature variations as the heat source travels around the circumference during the welding process. The results reflect the evolution of temperature over time.

Each curve represents the local temperature response corresponding to a specific angular position. The results reveal that while minor differences in peak temperature and heating duration exist, the overall thermal profiles remain comparable across all three positions. The observed peak temperatures at 90°, 180°, and 270° show high consistency, suggesting a stable heat input during torch movement. Furthermore, the cooling rates after each pass follow similar decay trends, indicating symmetrical thermal behavior around the pipe's circumference.

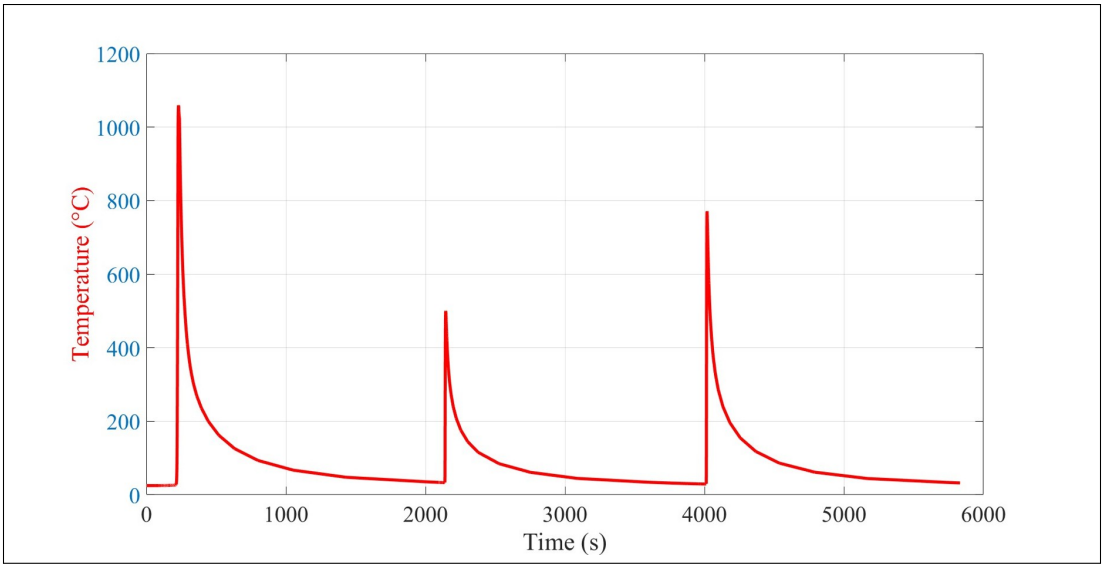

Figure 6.17 Temperature during welding in 1 mm from fusion zone at: 90°, 180°, 270°

6.4.5 Model Validation Through Oxide Growth Prediction

To validate the accuracy of the numerical model, oxidation behavior was simulated at the location 270° circumferentially and 1.5 mm from the fusion line, using 5000 ppm oxygen concentration, as determined from the oxygen distribution simulation. Based on prior experimental studies, oxidation initiates above 827 °C, which means the oxide layer predominantly forms during the first welding pass. Since the second and third passes do not significantly raise the temperature above this threshold at this location, their effect on oxidation is negligible and was thus excluded from the simulation. From the results reported in Figure 6.14, the oxygen content present in this region is 6500 ±900 ppm.

The temperature–time profile (Figure 6.18a) from the thermal simulation was coupled with oxidation kinetics to predict the oxide thickness. The model incorporated the percentage of spinel and corundum phases at each temperature, as extracted from FactSage equilibrium simulations, to calculate effective thermophysical parameters. The resulting oxide thickness, shown in Figure 6.18b, reaches a maximum of 4.16± 1.01 μm, which is in good agreement with the measurements made by electron microscopy. This confirms the robustness of the

simulation framework in predicting oxidation behavior under realistic thermal and chemical conditions.

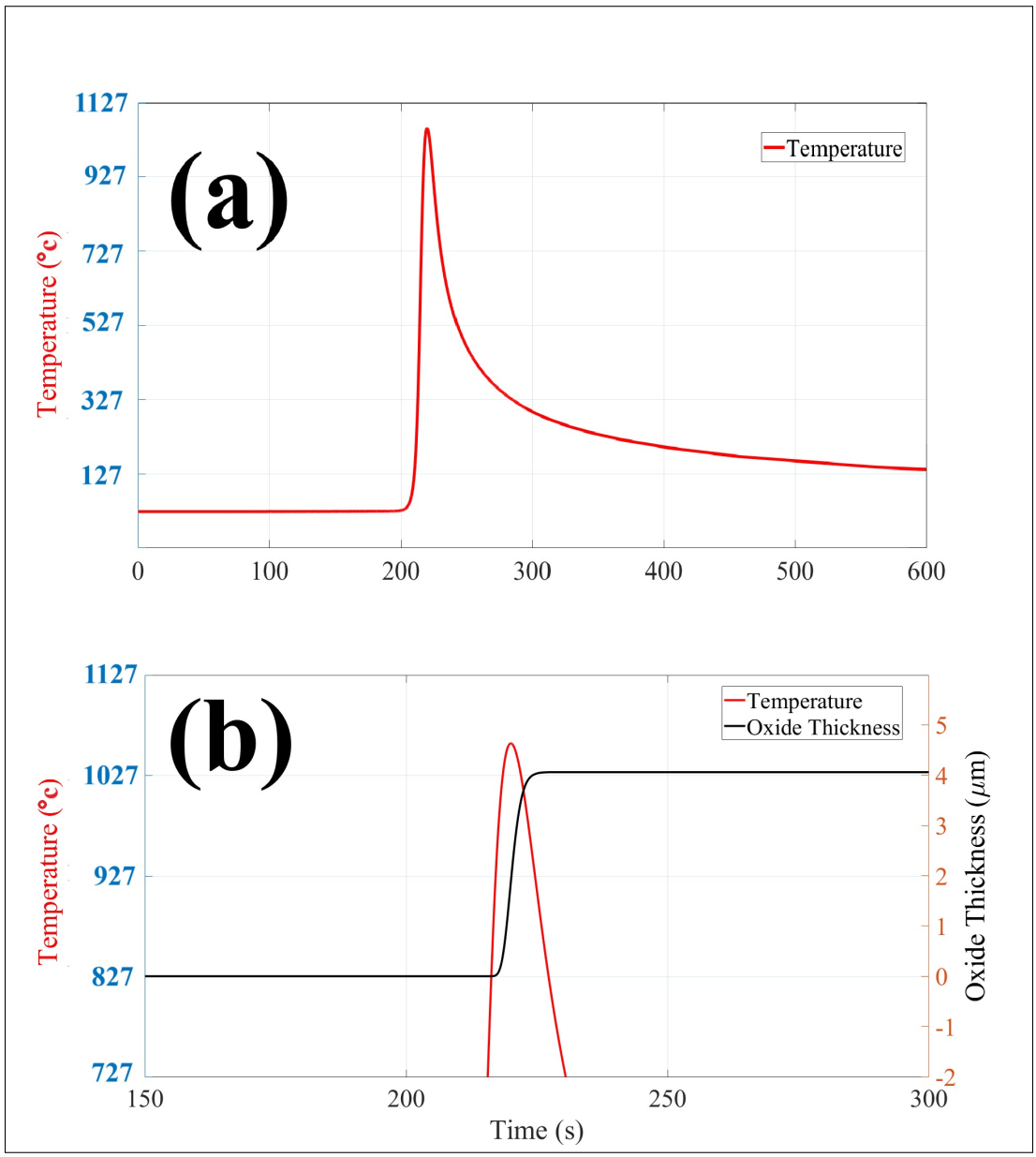

Figure 6.18 (a) Peak temperature for the root pass of welding, (b) Oxide growth prediction

6.5 Conclusion

This study systematically investigated the oxidation behavior in the discoloration zone of 316L stainless steel pipe welds subjected to different oxygen concentrations in the backing gas during orbital GTAW welding. Using a combination of experimental observations and numerical simulations, the influences of thermal gradients, gas flow behavior, and oxygen availability on the formation, thickness, and composition of oxide layers in different sections of the weld root were determined and quantified.

The findings highlight key phenomena responsible for discoloration, which directly impact the weld quality and corrosion resistance. The spatial evolution of oxidation during welding was characterized and validated through visual inspection, SEM/XRD analyses, FEM thermal simulations, and oxygen mass fraction predictions via CFD. The following key findings were drawn:

- Oxidation severity increases with backing gas oxygen content, as evidenced by broader and darker discoloration zones at 5000 ppm.
- The highest oxygen ingress occurs near the 180° torch position, where upward thermal convection and incomplete shielding/backing gas coverage led to increased oxygen accumulation.
- Despite varying oxygen concentrations (50, 200, 500, 5000 ppm), the same spatial distribution trend is maintained, indicating the dominant influence of torch position and flow dynamics on oxygen behavior rather than concentration alone.
- Microstructural and phase analyses show a shift from chromium-rich oxides (Cr_2O_3, spinels) at lower oxygen levels to iron-rich oxides (FeO) at higher temperatures and oxygen content, explaining the difference in discoloration at higher ppm values.
- Thermodynamic and FEM simulations confirm that regions exposed to temperatures above 1300°C are prone to oxide liquid formation, matching experimental observations of blackened discoloration at 5000 ppm.

Together, these insights underscore the critical importance of precise control of oxygen content and flow stability throughout the orbital welding process, especially to prevent oxidation in vulnerable root areas of stainless-steel pipelines.

Acknowledgment

The authors gratefully acknowledge the generous support and collaboration of PCL Construction, whose material provision and partnership were instrumental to the success of this research. Special thanks are owed to Mohammad Saadati for his valuable expertise and assistance in conducting the electron microscopy analyses. The authors also wish to recognize Morteza Sadeghifar for his essential contribution to the Abaqus simulations. This work was carried out with the support of PCL Construction, located in Edmonton, Alberta, Canada, and was financially supported by the Natural Sciences and Engineering Research Council of Canada (NSERC) under Grant Number CRD 542299-19.

CONCLUSION AND RECOMMENDATIONS

CONCLUSION

This thesis investigated the oxidation behavior, oxide layer formation, and pitting corrosion resistance in AISI 316L stainless steel welds, with emphasis on the discoloration zone formed during orbital GTAW. The research uniquely combined experimental characterization, electrochemical analysis, thermodynamic modeling, kinetic assessment, and finite element simulation.

The main original contributions and key findings of this work are:

1. A new correlation between oxygen content in the backing gas and oxide morphology was established, showing that:
   - Increasing oxygen levels from 50 to 5000 ppm results in more intense and extensive discoloration.
   - At 5000 ppm, a porous iron oxide-rich outer layer forms, reducing the protectiveness of the passive film and compromising corrosion resistance.
   - Welding with 500 ppm oxygen results in a more compact, Cr-rich oxide film and superior pitting resistance.
2. Surface roughness was identified as a critical pre-weld condition influencing post-weld corrosion resistance:
   - Smoother surfaces (60 grit) promoted more uniform microstructures with lower grain boundary misorientation.
   - Rougher surfaces (40 grit) led to thicker oxide layers with Cr-Mn enrichment but also higher localized strain accumulation and pit initiation resistance.
3. A dual mechanism of pit initiation and propagation was revealed, depending on oxide morphology and surface condition:
   - Smoother surfaces had thinner oxide films, more prone to pit initiation but more resistant to propagation due to lower grain boundary density.

- Rougher surfaces exhibited thicker oxides that delayed initiation but supported deeper pit growth once initiated.

4. The interaction between surface condition and oxygen concentration was quantitatively linked to corrosion behavior:
   - At high oxygen levels (5000 ppm), surface defects such as micro-holes facilitated chloride ingress and accelerated localized corrosion.
   - An optimal combination was identified: 500 ppm oxygen with 40 grit surface finish offered the best corrosion performance.
5. A comprehensive kinetic analysis using TGA and multiple model-free and model-fitting methods was conducted, leading to:
   - Determination of activation energies in the range of 203–239 kJ/mol depending on the kinetic model.
   - Identification of second- and third-order reaction models as most representative of the oxidation mechanism.
   - Extraction of transition-state thermodynamic parameters confirming the solid-state nature of oxidation.
6. Thermodynamic modeling using FactSage confirmed oxide phase transitions:
   - Formation of Cr-rich spinels at lower temperatures and Fe-rich oxides at higher temperatures.
   - Good agreement between modeled and experimental oxide compositions validated the predictive models.
7. Finite element thermal and fluid flow simulations identified oxidation hot-spots:
   - The highest oxidation occurred at torch positions around 180°, due to localized heat accumulation and shielding inefficiencies.
   - Simulations revealed that oxidation severity is governed more by thermal/fluid dynamics than oxygen concentration alone.
8. This research challenges the adequacy of visual inspection standards (e.g., AWS D18.1 and D18.2):

- Welds with acceptable visual appearance may still exhibit inferior corrosion resistance depending on oxide composition and structure.
- The study provides a scientific basis for supplementing visual standards with electrochemical and microstructural assessments.

9. A new integrated framework was proposed to optimize GTAW process parameters:
   - Simultaneous control of oxygen content and surface preparation can minimize discoloration while maximizing corrosion resistance.
   - This strategy is transferable to other alloys and welding conditions for applications requiring high corrosion resistance.

These contributions provide a deeper understanding of the mechanisms driving oxidation and corrosion in GTAW-welded 316L stainless steel, offering practical guidelines for improving weld quality and durability in corrosive environments.

RECOMMENDATIONS AND FUTURE WORK

1. **Investigate Different Welding Methods:** Expand the scope to include welding techniques such as Gas Metal Arc Welding (GMAW) and Flux-Cored Arc Welding (FCAW), which may offer different oxide formation characteristics.
2. **Optimize Oxygen Content in Backing Gas:** Perform a finer analysis of oxygen concentrations between 500 and 5000 ppm to determine the precise threshold at which corrosion resistance begins to decline, and to propose a cost-effective purity range for industrial use.
3. **Analyze Combined Effects on Weld Pool Behavior:** Examine the interactive effects of welding methods and oxygen content on the weld pool's thermal profile, microstructure, and metallurgical phases using in situ diagnostics and post-weld analysis.
4. **Perform Controlled Laboratory Welds:** Conduct all future welding experiments under tightly controlled laboratory conditions, integrating real-time thermal measurement tools (e.g., thermocouples and infrared cameras) to improve model accuracy and experimental repeatability.

These recommendations not only build on the findings of this research but also provide a clear path forward for developing more practical, corrosion-based acceptance criteria and improved welding procedures for critical stainless steel applications.

BIBLIOGRAPHY

Abiodun, A. O., Ayoola, O. M., Olajire, T. O., Oluwajire, O. E. & Abidakun, O. J. (2020). A Detailed Comparison of Various Steel Types-Stainless Steel, Structural Steel and Aluminum Steel. *International Journal of Scientific Research in Science, Engineering and Technology*, 103-109.

Abood, T. H. (2008). *The influence of various parameters on pitting corrosion of 316L and 202 stainless steel*. (Journal Article, Department of chemical Engineering of the University of Technology. University of Technology).

Aghuy, A. A., Zakeri, M., Moayed, M. H. & Mazinani, M. (2015). Effect of grain size on pitting corrosion of 304L austenitic stainless steel. *Corrosion Science*, 94, 368-376. doi: https://doi.org/10.1007/s10853-022-07888-0.

Agilan, M., Venkateswaran, T., Sivakumar, D. & Pant, B. (2014). Effect of heat input on microstructure and mechanical properties of inconel-718 EB Welds. *Procedia Materials Science*, 5, 656-662.

Agnihotri, N. & Mondal, M. K. (2023). Thermal analysis, kinetic behavior, reaction modeling, and comprehensive pyrolysis index of soybean stalk pyrolysis. *Biomass Conversion and Biorefinery*, 1-16. doi: https://doi.org/10.1007/s13399-023-03807-8.

Ahmad, Z. (2006). *Principles of corrosion engineering and corrosion control*. Elsevier.

Airaksinen, S. (2024). *Oxide scale formation of stainless steel in transition of annealing and reheating towards fossil-free methods*. (Ph.D. thesis, Oulun yliopisto).

Akahira, T. (1971). Trans. Joint convention of four electrical institutes. *Res. Rep. Chiba Inst. Technol.*, 16, 22-31.

Alhulaybi, Z., Dubdub, I., Al-Yaari, M., Almithn, A., Al-Naim, A. F. & Aljanubi, H. (2022). Pyrolysis kinetic study of polylactic acid. *Polymers*, 15(1), 12. doi: https://doi.org/10.3390/polym15010012.

Almaghrabi, M., Alqurshi, A., Jadhav, S. A., Mazzacuva, F., Cilibrizzi, A., Raimi-Abraham, B. & Royall, P. G. (2023). Evaluating thermogravimetric analysis for the measurement of drug loading in mesoporous silica nanoparticles (MSNs). *Thermochimica Acta*, 730, 179616.

Ambade, S. P., Sharma, A., Patil, A. P. & Puri, Y. M. (2021). Effect of welding processes and heat input on corrosion behaviour of Ferritic stainless steel 409M. *Materials Today: Proceedings*, 41, 1018-1023.

Aramaki, K. (2001). Effects of organic inhibitors on corrosion of zinc in an aerated 0.5 M NaCl solution. *Corrosion Science*, 43(10), 1985-2000. doi: https://doi.org/10.1016/S0010-938X(00)00174-8.

Arora, H., Singh, R. & Brar, G. S. (2020). Numerical simulation on residual stresses of stainless steel SS-304 thin welded pipe. *Measurement and Control*, 53(7-8), 1183-1193.

Asadi, P., Alimohammadi, S., Kohantorabi, O., Soleymani, A. & Fazli, A. (2021). Numerical investigation on the effect of welding speed and heat input on the residual stress of multi-pass TIG welded stainless steel pipe. *Proceedings of the Institution of Mechanical Engineers, Part B: Journal of Engineering Manufacture*, 235(6-7), 1007-1021.

Asteman, H., Svensson, J.-E., Norell, M. & Johansson, L.-G. (2000). Influence of water vapor and flow rate on the high-temperature oxidation of 304L; effect of chromium oxide hydroxide evaporation. *Oxidation of metals*, 54, 11-26.

ASTM, G. (2014). Standard reference test method for making potentiodynamic anodic polarization measurements. *West Conshohocken (PA): ASTM International*, 1-4.

ASTM, G. (2020). AWS D18.2:2020; Guide to Weld Discoloration Levels on Inside of Austenitic Stainless Steel Tube. *American Welding Society : Doral, FL, USA*, 1-4.

Aswal, V., Jain, J. K., Singhal, T. S., Agrawal, R. & Kumar, S. (2020). *Effect of Process Parameters on Weld Bead Geometry, Microstructure, and Mechanical Properties in Submerged Arc Welding*. Conference Proceedings presented in Recent Advances in Smart Manufacturing and Materials: Select Proceedings of ICEM 2020 (pp. 403-412).

Atkinson, A. (1985). Transport processes during the growth of oxide films at elevated temperature. *Reviews of Modern Physics*, 57(2), 437.

Aumpiem, A. & Prateepasen, A. (2017). The relation of oxygen value, heat tint and pitting corrosion in super duplex pipe. *Proceedings of 3rd International Conference on Mechanical and Production Engineering*.

Avelar, A. M., Giovedi, C., Abe, A. Y. & Mourão, M. B. (2020). Oxidation of AISI 304L and 348 stainless steels in water at high temperatures. *Materials Research*, 23, e20200373.

Avery, R. E. (2000). *Sanitary Welding Standards*. Conference Proceedings presented in ASME Citrus Engineering Symposium (pp. 53-63).

Ayvaz, S., Aydın. & Bahçepınar, A. (2023). Effect of shot blasting on the boriding kinetics of AISI 316L stainless steel. *Protection of Metals and Physical Chemistry of Surfaces*, 59(4), 671–678. doi: 10.1134/S2070205123040029.

Azuma, S., Kudo, T., Miyuki, H., Yamashita, M. & Uchida, H. (2004). Effect of nickel alloying on crevice corrosion resistance of stainless steels. *Corrosion Science*, 46(9), 2265-2280.

Baba, S. A., Yadav, K. & Sharma, V. K. (2013). Kinetics and modeling of pyrolytic decomposition of sawdust and rice husk. *Bioresource technology*, 130, 663-671.

Babu, N. K., Talari, M. K., Zheng, S., Dayou, P., Jerome, S. & Muthupandi, V. (2013). Arc Welding. In Nee, A. (Ed.), *Handbook of Manufacturing Engineering and Technology* (pp. 1-19). London: Springer London. doi: 10.1007/978-1-4471-4976-7_53-1.

Balasko, T., Batic, B. s. & Burja, J. (2025). Influence of the Cooling Rate on the Wüstite Content in Oxide Layers Formed During High-Temperature Oxidation of Hot-Worked Tool Steel with High Thermal Conductivity. *High Temperature Corrosion of Materials*, 102(1), 1-14.

Bale, C. W., Chartrand, P., Degterov, S., Eriksson, G., Hack, K., Mahfoud, R. B., Melançon, J., Pelton, A. & Petersen, S. (2002). FactSage thermochemical software and databases. *Calphad*, 26(2), 189–228.

Balusamy, T., Kumar, S. & Narayanan, T. S. (2010). Effect of surface nanocrystallization on the corrosion behaviour of AISI 409 stainless steel. *Corrosion Science*, 52(11), 3826-3834. doi: https://doi.org/10.1016/j.corsci.2010.07.004.

Bard, A. J., Faulkner, L. R. & White, H. S. (2022). *Electrochemical methods: fundamentals and applications*. John Wiley & Sons.

Bedoya-Zapata, A. D., Franco-Rendon, C. M., Leon-Henao, H., Santa, J. F. & Barrada, J. E. G. (2021). Failure analysis of a welded stainless-steel piping system with premature pitting. *Engineering Failure Analysis*, 119, 104986. doi: https://doi.org/10.1016/j.engfailanal.2020.104986.

Behnamian, Y., Mostafaei, A., Kohandehghan, A., Zahiri, B., Zheng, W., Guzonas, D., Chmielus, M., Chen, W. & Luo, J. L. (2017). Corrosion behavior of alloy 316L stainless steel after exposure to supercritical water at 500 C for 20,000 h. *The Journal of Supercritical Fluids*, 127, 191-199.

Bellezze, T., Giuliani, G. & Roventi, G. (2018). Study of stainless steels corrosion in a strong acid mixture. Part 1: cyclic potentiodynamic polarization curves examined by means of an analytical method. *Corrosion Science*, 130, 113–125.

Bergquist, E.-L., Huhtala, T. & Karlsson, L. (2011). The effect of purging gas on 308L TIG root pass ferrite content. *Welding in the World*, 55(3), 57-64. doi: https://doi.org/10.1007/BF03321287.

Bhandari, J., Khan, F., Abbassi, R., Garaniya, V. & Ojeda, R. (2015). Modelling of pitting corrosion in marine and offshore steel structures–A technical review. *Journal of Loss Prevention in the Process Industries*, 37, 39-62.

Bielsa, D., Zaki, A., Arias, P. L. & Faik, A. (2021). Development of a kinetic reaction model for reduction and oxidation of Si doped Mn2O3 for thermochemical energy storage in concentrated solar power plants. *Journal of Energy Storage*, 43, 103271.

Bilbao, R., Millera, A., Arauzo, J., Salvador, M. L. & Munt, J. (1996). Kinetic models for the thermal degradation of polyvinyl chloride. *Thermochimica acta*, 275, 1-12.

Binninger, T., Mohamed, R., Waltar, K., Fabbri, E., Levecque, P., Kötz, R. & Schmidt, T. J. (2015). Thermodynamic explanation of the universal correlation between oxygen evolution activity and corrosion of oxide catalysts. *Scientific reports*, 5(1), 12167.

Birks, N. (2006). *Introduction to the high temperature oxidation of metals*. Cambridge Univ.

Bitharas, I., McPherson, N., McGhie, W., Roy, D. & Moore, A. J. (2018). Visualisation and optimisation of shielding gas coverage during gas metal arc welding. *Journal of Materials Processing Technology*, 255, 451-462.

Bittel, J., Sjodahl, L. & White, J. (1969). Oxidation of 304L stainless steel by steam and by air. *Corrosion*, 25(1), 7-14.

Borchardt, H. J. & Daniels, F. (1956). The application of differential thermal analysis to the study of reaction kinetics. *Journal of the American Chemical Society*, 79(1), 41-46.

Briant, C. (1985). Grain boundary segregation of phosphorus in 304L stainless steel. *Metallurgical Transactions A*, 16, 2061-2062.

Brown, M., Maciejewski, M., Vyazovkin, S., Nomen, R., Sempere, J., Burnham, A. K., Opfermann, J., Strey, R., Anderson, H. & Kemmler, A. (2000). Computational aspects of kinetic analysis: Part A: The ICTAC kinetics project—data, methods and results. *Thermochimica Acta*, 355(1-2), 125–143. doi: 10.1016/S0040-6031(00)00453-5.

Brylewski, T., Miruszewski, T., Kaczmarek, W. & Moskal, A. (2004). Oxidation resistance of austenitic and ferritic stainless steels in air and oxygen. *Journal of Achievements in Materials and Manufacturing Engineering*, 13(1), 295–302.

Buchowiecki, M. & Szabo, P. (2022). Transport coefficients of plasmas in mixtures of nitrogen and hydrogen. *Plasma Sources Sci Technol*, 31, 045010.

Buscail, H., El Messki, S., Riffard, F., Perrier, S., Cueff, R. & Issartel, C. (2008). Role of molybdenum on the AISI 316L oxidation at 900 C. *Journal of materials science*, 43(21), 6960-6966.

Buscail, H., El Messki, S., Riffard, F., Perrier, S. & Issartel, C. (2011). Effect of pre-oxidation at 800°C on the pitting corrosion resistance of the AISI 316L stainless steel. *Oxidation of Metals*, 75(1), 27–39. doi: 10.1007/s11085-010-9225-3.

Cai, J. & Liu, R. (2007). New distributed activation energy model: numerical solution and application to pyrolysis kinetics of some types of biomass. *Bioresource technology*, 98(17), 3283-3289.

Cai, J. & Liu, R. (2008). Study on the pyrolysis of four biomass materials using TG–FTIR and kinetic analysis. *Journal of Analytical and Applied Pyrolysis*, 82(2), 332-339.

Cai, J., Chen, P. & He, Y. (2018). Pyrolysis simulation of lignin based on a new kinetic model. *Energy Conversion and Management*, 157, 385-393.

Cao, X. & Jahazi, M. (2009). Effect of welding speed on butt joint quality of Ti–6Al–4V alloy welded using a high-power Nd: YAG laser. *Optics and Lasers in Engineering*, 47(11), 1231-1241.

Capart, R., Vanderghem, C., Goffin, D., Paquot, M. & Blecker, C. (2004). Thermal degradation kinetics of wheat bran hemicelluloses by thermogravimetric analysis. *Thermochimica Acta*, 423(1-2), 1-9.

Cardoso, J. L., Silva Nunes Cavalcante, A. L., Araujo Vieira, R. C., de Lima-Neto, P. & Gomes da Silva, M. J. (2016). Pitting corrosion resistance of austenitic and superaustenitic stainless steels in aqueous medium of NaCl and H2SO4. *Journal of Materials Research*, 31(12), 1755–1763. doi: 10.1557/jmr.2016.198.

Celik, S. & Ersozlu, I. (2020). Dynamic recrystallization of friction welded AISI 316 stainless steel joints. *Materials Testing*, 62(11), 1126-1130. doi: https://doi.org/10.3139/120.111600.

Chandra-Ambhorn, S., Saranyachot, P. & Thublaor, T. (2019). High temperature oxidation behaviour of Fe–15.7 wt.% Cr–8.5 wt.% Mn in oxygen without and with water vapour at 700 ºC. *Corrosion Science*, 148, 39–47.

Chandra-Ambhorn, S. & Saranyachot, P. (2019). Effect of the H2 content in shielding gas on the microstructure and oxidation resistance of oxidation resistance of Fe–15.7 wt.% Cr–8.5 wt.% Mn steels. *Journal of Materials Processing Technology*, 268, 18-24.

Chen, D., Yin, L., Wang, H. & He, P. (2008). Pyrolysis technologies for municipal solid waste: A review. *Waste Management*, 28(12), 2730-2740.

Chen, J., Xiao, Q., Lu, Z., Ru, X., Peng, H., Xiong, Q. & Li, H. (2017). Characterization of interfacial reactions and oxide films on 316L stainless steel in various simulated PWR primary water environments. *Journal of Nuclear Materials*, 489, 137-149. doi: https://doi.org/10.1016/j.jnucmat.2017.03.029.

Chen, J., Lee, H. B., Jeong, C., Xiao, Q., Jang, K., An, T. & Jang, C. (2024). Oxidation behavior of the directed energy deposited 316L stainless steel in supercritical carbon dioxide environment: Effect of post-manufacturing heat treatment. *Additive Manufacturing*, 81, 103998.

Chen, Y., Li, Y., Huang, Y., Li, M. & Liu, Y. (2022). An efficient algorithm based on Broyden's and generalized-α method for large scale flexible multi-body systems. *Applied Mathematical Modelling*, 106, 742-755.

Chen, Y., Wang, W., Chen, X. & Zhang, Z. (2014). Oxidation behavior of 316L stainless steel at 700–900 °C in air and steam environments. *Corrosion Science*, 85, 54–60. doi: 10.1016/j.corsci.2014.03.020.

Cheng, X., Zhang, P., Zhou, X., Zhang, W. & Wang, W. (2021). Oxidation behavior and mechanism of 316L stainless steel at 700–900 °C in water vapor. *Corrosion Science*, 187, 109508. doi: 10.1016/j.corsci.2021.109508.

Chiang, Y.-M. (1997). DB III, and WD Kingery, Physical Ceramics [Generic]. John Wiley & Sons.

Chilingar, G. V., Mourhatch, R. & Al-Qahtani, G. D. (2013). *The fundamentals of corrosion and scaling for petroleum & environmental engineers*. Elsevier.

Choi, W., Shin, H.-C., Kim, J. M., Choi, J.-Y. & Yoon, W.-S. (2020). Modeling and applications of electrochemical impedance spectroscopy (EIS) for lithium-ion batteries. *Journal of Electrochemical Science and Technology*, 11(1), 1-13.

Chong, C. T., Mong, G. R., Ng, J.-H., Chong, W. W. F., Ani, F. N., Lam, S. S. & Ong, H. C. (2019). Pyrolysis characteristics and kinetic studies of horse manure using thermogravimetric analysis. *Energy Conversion and Management*, 180, 1260–1267. doi: 10.1016/j.enconman.2018.11.049.

Chuaiphan, W. & Srijaroenpramong, L. (2014). Effect of welding speed on microstructures, mechanical properties and corrosion behavior of GTA-welded AISI 201 stainless steel sheets. *Journal of Materials Processing Technology*, 214(2), 402–408.

Coats, A. & Redfern, J. (1965). Kinetic parameters from thermogravimetric data. II. *Journal of Polymer Science Part B: Polymer Letters*, 3(11), 917–920.

Coats, A. W. & Redfern, J. P. (1964). Kinetic parameters from thermogravimetric data. *Nature*, 201, 68–69.

Comotti, I. M., Trueba, M. & Trasatti, S. P. (2013). The pit transition potential in the repassivation of aluminium alloys. *Surface and interface analysis*, 45(10), 1575–1584.

Costa, E. M., Dedavid, B. A., Santos, C. A., Lopes, N. F., Fraccaro, C., Pagartanidis, T. & Lovatto, L. P. (2023). Crevice corrosion on stainless steels in oil and gas industry: A review of techniques for evaluation, critical environmental factors and dissolved oxygen. *Engineering Failure Analysis*, 144, 106955.

Criado, J. M., Ortega, A., Malek, J. & Koga, N. (1978). A new method for the kinetic analysis of solid state reactions. *Thermochimica Acta*, 27, 25-30.

Dai, P., Wang, Y., Li, S., Lu, S., Feng, G. & Deng, D. (2020). FEM analysis of residual stress induced by repair welding in SUS304 stainless steel pipe butt-welded joint. *Journal of Manufacturing Processes*, 58, 975–983.

Dak, G. & Pandey, C. (2022). Study on effect of weld groove geometry on mechanical behavior and residual stresses variation in dissimilar welds of P92/SS304L steel for USC boilers. *Archives of Civil and Mechanical Engineering*, 22(3), 140.

De Blasio, C., Noreña, H. L. & Gil, A. (2019). Kinetic analysis of the thermal decomposition of stainless steel using thermogravimetric analysis. *Journal of Thermal Analysis and Calorimetry*, 136(1), 395–406. doi: 10.1007/s10973-018-7896-9.

Demirci, S., Kıran Yıldırım, B., Tünçay, M. M., Kaya, N. & Dikici, T. (2024). Non-isothermal Kinetic Analysis of High Temperature Oxidation of Additively Manufactured Ti-6Al-4V Alloy. *Journal of Materials Engineering and Performance*, 1–12. doi: 10.1007/s11665-024-09299-z.

Deng, D., Liang, W. & Murakawa, H. (2007). Determination of welding deformation in fillet-welded joint by means of numerical simulation and comparison with experimental measurements. *Journal of Materials Processing Technology*, 183(2-3), 219-225.

Dhawan, S. K., Bhandari, H., Ruhi, G., Bisht, B. M. S. & Sambyal, P. (2020). *Corrosion preventive materials and corrosion testing*. CRC Press.

Di Benedetti, M., Loreto, G., Matta, F. & Nanni, A. (2013). Acoustic emission monitoring of reinforced concrete under accelerated corrosion. *Journal of Materials in Civil Engineering*, 25(8), 1022-1029.

Driscoll, T. & Needham Jr, P. (1979). The oxidation of Fe-Cr surface and bulk alloys at 300° C. *Oxidation of Metals*, 13(3), 283-298.

Dudziak, T., Buzolin, R., Rzad, E., Wójcicki, M., Kateusz, F., Arneitz, S. & Polkowska, A. (2023). Effect of 316L Stainless Steel Fabrication on Oxidation Resistance, Surface Morphology, and Hot Tensile Behavior. *Journal of Materials Engineering and Performance*, 32(22), 10443-10454.

Dunning, J., Alman, D. & Rawers, J. (2002). Influence of silicon and aluminum additions on the oxidation resistance of a lean-chromium stainless steel. *Oxidation of Metals*, 57(5), 409-425.

Esmailzadeh, S., Aliofkhazraei, M. & Sarlak, H. (2018). Interpretation of cyclic potentiodynamic polarization test results for study of corrosion behavior of metals: a review. *Protection of metals and physical chemistry of surfaces*, 54, 976-989.

Ezuber, H., Alshater, A., Nisar, S., Gonsalvez, A. & Aslam, S. (2018). Effect of surface finish on the pitting corrosion behavior of sensitized AISI 304 austenitic stainless steel alloys in 3.5 *Surface Engineering and Applied Electrochemistry*, 54, 73-80. doi: https://doi.org/10.3103/S1068375518010039.

Ezuber, H., Alshater, A. & Abulhasan, M. (2017). Role of thiosulfate in susceptibility of AISI 316L austenitic stainless steels to pitting corrosion in 3.5% sodium chloride solutions. *Surface Engineering and Applied Electrochemistry*, 53, 493-500.

Fatahi Amirdehi, A., Gholipour, S. M., Pourazadi, E., Dadkhah, N. & Jafari, E. (2024). Thermogravimetric and kinetic analysis of high-temperature oxidation behavior of 316L stainless steel. *Materials Chemistry and Physics*, 305, 127797. doi: 10.1016/j.matchemphys.2023.127797.

Fattah-Alhosseini, A. (2016). Passivity of AISI 321 stainless steel in 0.5 M 0.5 M H_2SO_4 solution studied by Mott–Schottky analysis and the point defect model. *Arabian Journal of Chemistry*, 9, S1342–S1348. doi: 10.1016/j.arabjc.2013.12.015.

Fattah-Alhosseini, A. & Vafaeian, S. (2016). Influence of grain refinement on the electrochemical behavior of AISI 430 ferritic stainless steel in an alkaline solution. *Applied Surface Science*, 360, 921-928. doi: https://doi.org/10.1016/j.apsusc.2015.11.085.

Fazlioglu-Yalcin, B., Hilse, M. & Engel-Herbert, R. (2024). Thermogravimetric study of metal–organic precursors and their suitability for hybrid molecular beam epitaxy. *Journal of Materials Research*, 39(3), 436–448. doi: 10.1557/s43578-024-01240-w.

Fazlioglu-Yalcin, B., Hilse, M. & Engel-Herbert, R. (2024). Thermogravimetric study of metal–organic precursors and their suitability for hybrid molecular beam epitaxy. *Journal of Materials Research*, 39(3), 436–448. doi: 10.1557/s43578-023-01237-w.

Fehlner, F. P. (1970). *Oxide Films: An Approach to the Study of Reaction Mechanisms*. New York: Academic Press.

Feng, X., Zhang, S., Liu, P. & Kuang, W. (2023). The structure dependence of grain boundary passivation of Alloy 690 in high temperature water. *Acta Materialia*, 261, 119368. doi: https://doi.org/10.1016/j.actamat.2023.119368.

Fernandez, A., Zalazar-García, D., Torres, E., Torres-Sciancalepore, R., Parthasarathy, P., McKay, G., Fouga, G., Mazza, G. & Rodriguez, R. (2024). Assessment of the use of biochar from the slow pyrolysis of walnut and almond shells as an energy carrier. *Energy Sources, Part A: Recovery, Utilization, and Environmental Effects*, 46(1), 15379-15394.

Finšgar, M. & Milošev, I. (2010). Corrosion behaviour of stainless steels in aqueous solutions of methanesulfonic acid. *Corrosion science*, 52(7), 2430–2438.

Flynn, J. H. & Wall, L. A. (1966). General Treatment of the Thermogravimetry of Polymers. *Journal of Research of the National Bureau of Standards, Section A: Physics and Chemistry*, 70A(6), 487–523. doi: 10.6028/jres.070A.043.

Folkhard, E. (2012). *Welding metallurgy of stainless steels*. Springer Science & business media.

Fontana, M. G. (1986). *Corrosion engineering*. McGraw Hill Book Co., New York, NY.

Fontana, M. G., Greene, N. D. & Klerer, J. (1968). Corrosion engineering. *Journal of The Electrochemical Society*, 115(5), 142C.

Frankel, G. (1998). Pitting corrosion of metals: a review of the critical factors. *Journal of the Electrochemical society*, 145(6), 2186.

Friedman, H. L. (1964). Kinetics of thermal degradation of char-forming plastics from thermogravimetry. Application to a phenolic plastic. *Journal of Polymer Science Part C: Polymer Symposia*, 6(1), 183-195.

Gajera, B., Tyagi, U., Sarma, A. K. & Jha, M. K. (2023). Pyrolysis of cattle manure: Kinetics and thermodynamic analysis using TGA and artificial neural network. *Biomass Conversion and Biorefinery*, 1–17. doi: 10.1007/s13399-023-01237-0.

Galvele, J. (1981). Transport processes in passivity breakdown—II. Full hydrolysis of the metal ions. *Corrosion Science*, 21(8), 551-579.

Gamisch, B., Huber, L., Gaderer, M. & Dawoud, B. (2022). On the kinetic mechanisms of the reduction and oxidation reactions of iron oxide/iron pellets for a hydrogen storage process. *Energies*, 15(21), 8322.

Gao, S., Hu, Z., Duchamp, M., Krishnan, P. S. R., Tekumalla, S., Song, X. & Seita, M. (2020). Recrystallization-based grain boundary engineering of 316L stainless steel produced via selective laser melting. *Acta Materialia*, 200, 366-377. doi: https://doi.org/10.1016/j.actamat.2020.09.015.

Gao, Z., Wang, R., Li, J., Xu, L. & Qiao, L. (2022). Effect of cold rolling on the pitting corrosion of 316L and 304 austenitic stainless steels. *Journal of Materials Science*, 57(43), 20503-20520. doi: https://doi.org/10.1007/s10853-022-07888-0.

Garcia, J. H. N., Santos, N. F. d., Esteves, L., Campos, W. R. d. C. & Rabelo, E. G. (2019). Corrosion behavior of 316L and alloy 182 dissimilar weld joint with post-weld heat treatment. *Matéria (Rio de Janeiro)*, 24, e12471. doi: https://doi.org/10.1590/S1517-707620190003.0787.

Geffroy, P.-M., Guironnet, L., Bouwmeester, H. J., Chartier, T., Grenier, J.-C. & Bassat, J.-M. (2019). Influence of oxygen partial pressure on the oxygen diffusion and surface exchange coefficients in mixed conductors. *Journal of the European Ceramic Society*, 39(1), 59–65.

Gholizadeh, S., Yuen, S. C. K. & George, S. (2024). Post-localized blast experimental investigation of mechanical properties and microstructural evolutions in austenitic stainless steel 316L. *Materialia*, 38, 102263.

Goldak, J. A. & Akhlaghi, M. (2005). *Computational welding mechanics*. Springer Science & Business Media.

Gronli, M. G., Antal,Jr, M. J. & Varhegyi, G. (2002). A round-robin study of cellulose pyrolysis kinetics by thermogravimetry. *Industrial and Engineering Chemistry Research*, 41(17), 4201-4208.

Guo, D., Hu, M., Pu, C., Xiao, B., Hu, Z., Liu, S., Wang, X. & Zhu, X. (2015). Kinetics and mechanisms of direct reduction of iron ore-biomass composite pellets with hydrogen gas. *International journal of hydrogen energy*, 40(14), 4733-4740.

Guo, P., Zhang, P., Zhang, J., Yue, F., Nie, X., Chi, R. & Fu, M. (2025). Influence of Surface Roughness on the Corrosion Behavior of ENiCrFe-7 Weld Overlay Cladding Materials. *Journal of Materials Engineering and Performance*, 1–9.

Ha, H.-Y., Lee, T.-H., Bae, J.-H. & Chun, D. W. (2018). Molybdenum Effects on Pitting Corrosion Resistance of FeCrMnMoNC Austenitic Stainless Steels. *Metals*, 8(8), 1-8. doi: 10.3390/met8080653.

Ha, H.-Y., Kim, K.-W., Park, S.-J., Lee, T.-H., Park, H., Moon, J., Hong, H.-U. & Lee, C.-H. (2022). Effects of Cr on pitting corrosion resistance and passive film properties of austenitic Fe–19Mn–12Al–1.5 C lightweight steel. *Corrosion Science*, 206, 110529.

Habib, K., Damra, M., Saura, J., Cervera, I. & Bellés, J. (2011). Breakdown and Evolution of the Protective Oxide Scales of AISI 304 and AISI 316 Stainless Steels under High-Temperature Oxidation. *International Journal of Corrosion*, 2011(1), 824676. doi: https://doi.org/10.1155/2011/824676.

hai XIA, D., zhe SONG, S., hui WANG, J., chao BI, H., xuan JIANG, Y. & wen HAN, Z. (2012). Corrosion behavior of tinplate in NaCl solution. *Transactions of Nonferrous Metals Society of China*, 22(3), 717-724. doi: https://doi.org/10.1016/S1003-6326(11)61236-3.

Hakimian, S., Pourrahimi, S., Bouzid, A. & Hof, L. (2023). Application of machine learning for the classification of corrosion behavior in different environments for material selection of stainless steels. *Computational Materials Science*, 228, 112352. doi: 10.1016/j.commatsci.2023.112352.

Hao, Y.-w., Deng, B., Zhong, C., Jiang, Y.-m. & Li, J. (2009). Effect of surface mechanical attrition treatment on corrosion behavior of 316 stainless steel. *Journal of iron and steel research international*, 16(2), 68-72. doi: https://doi.org/10.1016/S1006-706X(09)60030-3.

Hart, E. (1957). On the role of dislocations in bulk diffusion. *Acta metallurgica*, 5(10), 597. doi: https://doi.org/10.1016/0001-6160(57)90127-X.

He, W. & Hou, P. Y. (1999). Oxidation of 316 stainless steel in O2–H2O mixtures at 600 °C and 800 °C. *Oxidation of Metals*, 52(5–6), 337–368. doi: 10.1023/A:1018836106902.

He, Y., Chang, C., Li, P., Han, X., Li, H., Fang, S., Chen, J. & Ma, X. (2018). Thermal decomposition and kinetics of coal and fermented cornstalk using thermogravimetric analysis. *Bioresource Technology*, 259, 294–303. doi: 10.1016/j.biortech.2018.03.051.

Hernández, H. H., Reynoso, A. R., González, J. T., Morán, C. G., Hernández, J. M., Ruiz, A. M., Hernández, J. M. & Cruz, R. O. (2020). Electrochemical impedance spectroscopy (EIS): A review study of basic aspects of the corrosion mechanism applied to steels. *Electrochemical impedance spectroscopy*, 137-144.

Hoar, T. (1967). The production and breakdown of the passivity of metals. *Corrosion Science*, 7(6), 341-355.

Hong, T. & Nagumo, M. (1997). Effect of surface roughness on early stages of pitting corrosion of type 301 stainless steel. *Corrosion science*, 39(9), 1665-1672. doi: https://doi.org/10.1016/S0010-938X(97)00072-3.

Hou, P., Chen, X., Liu, W. & Song, X. (2010). Oxidation behavior of 316L stainless steel in steam at 600–800 °C. *Journal of Materials Science and Technology*, 26(7), 577–582. doi: 10.1016/S1005-0302(10)60100-7.

Huang, X., Xiao, K., Fang, X., Xiong, Z., Wei, L., Zhu, P. & Li, X. (2020). Oxidation behavior of 316L austenitic stainless steel in high temperature air with long-term exposure. *Materials Research Express*, 7(6), 066517.

Huang, X., Li, X., Zhan, Z., Xiao, K., Fang, X. & Li, Z. (2022). Effect of Long-Term Pre-oxidation on the Corrosion Rate of 316L Stainless Steel in a High-Temperature Water Environment. *Journal of Materials Engineering and Performance*, 31(10), 7935-7944.

Huidobro, J. A., Iglesias, I., Alfonso, B. F., Espina, A., Trobajo, C. & Garcia, J. R. (2016). Reducing the effects of noise in the calculation of activation energy by the Friedman method. *Chemometrics and Intelligent Laboratory Systems*, 151, 146–152. doi: 10.1016/j.chemolab.2016.01.007.

Humphreys, F. J. & Hatherly, M. (2012). *Recrystallization and related annealing phenomena*. elsevier.

Jaffré, K., Ter-Ovanessian, B., Abe, H., Mary, N., Normand, B. & Watanabe, Y. (2021a). Effect of mechanical surface treatments on the surface state and passive behavior of 304L stainless steel. *Metals*, 11(1), 135. doi: https://doi.org/10.3390/met11010135.

Jaffré, K., Ter-Ovanessian, B., Abe, H., Mary, N., Normand, B. & Watanabe, Y. (2021b). Effect of mechanical surface treatments on the surface state and passive behavior of 304L stainless steel. *Metals*, 11(1), 135.

Jepson, M. A. E. (2008). *Oxidation of austenitic and duplex stainless steels during primary processing*. (Ph.D. thesis, Loughborough University).

Ji, Y., Hao, L., Wang, J. & Ke, W. (2025). EIS investigation on surface roughness induced oxide film evolution on 304 SS in simulated secondary circuit water of PWR system. *Journal of Materials Science*, 60(12), 5511–5532.

Jones, D. A. (1996). *Principles and prevention of corrosion*. Prentice Hall.

Kabir, A., Koszelow, D., Miruszewski, T., Tinti, V. B., Esposito, V., Kern, F. & Molin, S. (2024). Assessment of High-Temperature Oxidation Properties of 316L Stainless Steel Powder and Sintered Porous Supports for Potential Solid Oxide Cells Applications. *Advances in Science and Technology Research Journal*, 18(5), 10-18.

Kadoi, K. & Shinozaki, K. (2017). Effect of chemical composition on susceptibility to weld solidification cracking in austenitic weld metal. *Metallurgical and Materials Transactions A*, 48, 5860-5869.

Kang, K.-S., Kim, C.-H., Bae, K.-K., Cho, W.-C., Jeong, S.-U., Lee, Y.-J. & Park, C.-S. (2014). Reduction and oxidation properties of Fe2O3/ZrO2 oxygen carrier for hydrogen production. *Chemical Engineering Research and Design*, 92(11), 2584-2597.

Kazemipour, M. (2020). *Corrosion evaluation of 13Cr (AISI 420) stainless steel: synergic effects of environmental factors and microstructure*. (Thesis, Memorial University of Newfoundland).

Kennedy, J. A. & Clark, S. M. (1997). A new method for the analysis of non-isothermal DSC and diffraction data. *Thermochimica Acta*, 307(1), 27–35. doi: 10.1016/S0040-6031(96)02962-0.

Khafaji, N. Y., Demir, A. G., Vitali, L., Fustinoni, D., Niro, A., Previtali, B. & Taha, Z. A. (2017). Optical characterization of laser coloured titanium under different processing atmospheres. *Surface and Coatings Technology*, 321, 156-163.

Khanna, A. S. (2005). High temperature oxidation. In *Handbook of environmental degradation of materials* (pp. 105-152). Elsevier.

Khanna, A. S. (2002). *Introduction to high temperature oxidation and corrosion*. ASM international.

Khattar, N., Ahlawat, V., Sharma, P., Berar, U. & Diwan, P. (2023). Optimization of compression parameters of UHMWPE through thermal stability. *Materials Chemistry and Physics*, 307, 128220. doi: 10.1016/j.matchemphys.2023.128220.

Kim, B., Lee, C., Kim, J. & Lee, J. (2024). Corrosion Assessment and Quantification of Discoloration in the Weld Root Bead and Heat-Affected Zone of Stainless Steel Pipe Weldments. *ISOPE International Ocean and Polar Engineering Conference*, pp. ISOPE–I.

Kim, J.-H., Kim, B. K., Kim, D.-I., Choi, P.-P., Raabe, D. & Yi, K.-W. (2015). The role of grain boundaries in the initial oxidation behavior of austenitic stainless steel containing alloyed Cu at 700 C for advanced thermal power plant applications. *Corrosion Science*, 96, 52-66. doi: https://doi.org/10.1016/j.corsci.2015.03.014.

Kim, S.-T. & Park, Y.-S. (2009). Effects of copper and sulfur additions on machinability behavior of high performance austenitic stainless steel. *Metals and Materials International*, 15, 221-230.

Kimbrel, K. (2011). Determining Acceptable Levels of Weld Discoloration on Mechanically Polished and Electropolished Stainless Steel Surface. *Pharmaceutical Engineering*, 31(6), 1-7.

Kissinger, H. E. (1957). Reaction kinetics in differential thermal analysis. *Analytical Chemistry*, 29(11), 1702-1706.

Klapper, H. S., Stevens, J. & Wiese, G. (2013). Pitting corrosion resistance of CrMn austenitic stainless steel in simulated drilling conditions—Role of pH, temperature, and chloride concentration. *Corrosion*, 69(11), 1095-1102.

Kofstad, P. (1988). High temperature corrosion [Generic]. Elsevier Appl. Sci. Publ.

Kofstad, P. (2012). Mass Transport Phenomena in Oxidation of Metals. In *Mass Transport Phenomena in Ceramics* (pp. 383-407). Springer.

Kumar, S., Nath, S. & Kumar, V. (2015). Effect of single and multiple thermal cycles on microstructure and mechanical properties of simulated HAZ in low carbon bainitic steel. *Materials Performance and Characterization*, 4(3), 365-380.

Kumar, S. & Shahi, A. (2011). Effect of heat input on the microstructure and mechanical properties of gas tungsten arc welded AISI 304 stainless steel joints. *Materials & Design*, 32(6), 3617-3623.

Kumar, S., Shahi, A., Sharma, V. & Malhotra, D. (2021). Effect of welding heat input and post-weld thermal aging on the sensitization and pitting corrosion behavior of AISI 304L stainless steel butt welds. *Journal of Materials Engineering and Performance*, 30(3), 1619–1640.

Kurtulmus, M., Yukler, A., Bilici, M. K. & Catalgol, Z. (2015). Effects of welding current and arc voltage on FCAW weld bead geometry. *IJRET: International Journal of Research in Engineering and Technology*, 4(9), 23-28.

Laidler, K. J. (1984). The development of the Arrhenius equation. *Journal of chemical Education*, 61(6), 494.

Lasia, A. (2002). Electrochemical impedance spectroscopy and its applications. In *Modern aspects of electrochemistry* (pp. 143-248). Springer.

Lawson, B. J. (2019). *Compositional Optimization, Mechanical Properties, and Tempering Response in Type 410 Stainless Steel Welds*. (Thesis).

Li, J., Li, H., Zhao, G., Zhou, C., Ma, L. & Liu, H. (2020). Insights into the high-temperature oxidation behavior of austenitic stainless steel and influence of copper on it. *Journal of Materials Engineering and Performance*, 29(6), 3661–3669.

Li, M. (2020). *Galvanic Corrosion of Carbon Steel-Stainless Steel Welds*. (Thesis).

Li, M., Zou, D., Li, Y. & Tong, L. (2023). Effect of cooling rate on pitting corrosion behavior of 904L austenitic stainless steel in a simulated flue gas desulfurization solution. *Metals and Materials International*, 29(3), 730-747. doi: https://doi.org/10.1007/s12540-022-01255-z.

Li, Y., Luo, Y., Li, J., Song, D., Xu, B. & Chen, X. (2021). Ferrite formation and its effect on deformation mechanism of wire arc additive manufactured 308 L stainless steel. *Journal of Nuclear Materials*, 550, 152933.

Li, Y., Liu, Q., Fang, S., Xu, J. & Liu, Z. (2019). Pyrolysis kinetics and thermal behavior of lignin-rich biomass in a fixed bed reactor. *Journal of Thermal Analysis and Calorimetry*, 135, 1453–1464.

Li, Z., Mei, K., Dong, J., Yang, Y., Sun, J. & Luo, Z. (2024). An investigation on the wear and corrosion resistance of AlCoCrFeNi high-entropy alloy coatings enhanced by Ti and Si. *Surface and Coatings Technology*, 487, 130949. doi: https://doi.org/10.1016/j.surfcoat.2024.130949.

Ling, L., Liu, T., Lu, Y. & Guo, P. (2019). Investigation of the oxides film on 304L base metal produced during welding process without inert gas shielding. *Applied Surface Science*, 465, 780–786.

Liu, X., Zhang, H., Tong, H., Sui, Y., Li, X. & Hou, J. (2024). Effect of surface roughness on the corrosion behavior of 304 stainless steel in seawater. *Journal of Materials Engineering and Performance*, 1–11.

Lobb, R. C. & Evans, H. E. (1981). Formation of protective oxide film on chromium-depleted stainless steel. *Metal Science*, 15(6), 267–274. doi: 10.1179/030634581790426714.

Loto, R. T. (2017). Study of the corrosion behaviour of S32101 duplex and 410 martensitic stainless steel for application in oil refinery distillation systems. *Journal of Materials Research and Technology*, 6(3), 203-212. doi: https://doi.org/10.1016/j.jmrt.2016.11.001.

Luo, H., Xu, M., Wang, F. & Xiao, Y. (2011). Effect of grain boundary character distribution on intergranular corrosion resistance of austenitic stainless steel. *Corrosion Science*, 53(4), 1525-1531. doi: https://doi.org/10.1016/j.corsci.2010.12.021.

Luo, W., Lei, Y., Fu, H., Lin, J., Zhao, J., Chen, J. & Xu, H. (2020). Microstructural characterization and mechanical properties of 308L stainless steel fabricated by wire arc additive manufacturing. *Materials Science and Engineering: A*, 778, 139001. doi: https://doi.org/10.1016/j.msea.2020.139001.

Macdonald, J. R. (1992). Impedance spectroscopy. *Annals of biomedical engineering*, 20, 289-305.

Macdonald, J. R., Johnson, W. B., Raistrick, I., Franceschetti, D., Wagner, N., McKubre, M., Macdonald, D., Sayers, B., Bonanos, N. & Steele, B. (2018). *Impedance spectroscopy: theory, experiment, and applications*. John Wiley & Sons.

Macleod, H. A. & Macleod, H. A. (2010). *Thin-film optical filters*. CRC press.

Malek, J. (1992). The kinetic analysis of non-isothermal data. *Thermochimica Acta*, 200, 257–269.

Malik, A. M., Qureshi, E. M., Dar, N. U. & Khan, I. (2008). Analysis of circumferentially arc welded thin-walled cylinders to investigate the residual stress fields. *Thin-Walled Structures*, 46(12), 1391-1401.

Mansfeld, F. (1995). Use of electrochemical impedance spectroscopy for the study of corrosion protection by polymer coatings. *Journal of applied electrochemistry*, 25(3), 187-202.

Mao, H.-h., Qi, X., Cao, J., An, L.-c. & Yang, Y.-t. (2017). Effect of Si on high temperature oxidation of 30Cr13 stainless steel. *Journal of Iron and Steel Research International*, 24(5), 561-568.

Maroufkhani, M., Hakimian, S., Khodabandeh, A., Radu, I., Hof, L. A. & Jahazi, M. (2023). Influence of oxygen content in the protective gas on pitting corrosion resistance of a 316l stainless steel weld joint. *Materials*, 16(17), 5968.

Maroufkhani, M., Khodabandeh, A., Radu, I., Moosavi-Khoonsari, E. & Jahazi, M. (2025). Thermodynamic and kinetic analyses of high temperature oxidation of 316L stainless steel. *Results in Materials*, 28, 100774. doi: https://doi.org/10.1016/j.rinma.2025.100774.

Marquez, C., Gravier, S., Prokhorov, E., Chmielarz, T. & Sánchez, M. (2023). Weld discoloration and passivation of 316L stainless steel welded joints for the food industry: influence of the heat input and the shielding gas. *Materials and Corrosion*, 74(8), 1097-1113. doi: https://doi.org/10.1002/maco.202213369.

Martin, J. (2006). *Materials for engineering*. Woodhead Publishing.

Messinese, E., Casanova, L., Paterlini, L., Capelli, F., Bolzoni, F., Ormellese, M. & Brenna, A. (2022). A Comprehensive Investigation on the Effects of Surface Finishing on the Resistance of Stainless Steel to Localized Corrosion. *Metals*, 12(10), 1751.

Mills, K. C. (2002a). *Recommended values of thermophysical properties for selected commercial alloys*. Woodhead Publishing.

Mills, K. C. (2002b). *Recommended values of thermophysical properties for selected commercial alloys*. Woodhead publishing.

Mills, K. C. (2002c). *Recommended values of thermophysical properties for selected commercial alloys*. Woodhead publishing.

Miranda-Pérez, A. F., Rodríguez-Vargas, B. R., Calliari, I. & Pezzato, L. (2023). Corrosion Resistance of GMAW Duplex Stainless Steels Welds. *Materials*, 16(5), 1-5. doi: 10.3390/ma16051847.

Mohammed, G. R., Ishak, M., Aqida, S. N. & Abdulhadi, H. A. (2017). Effects of heat input on microstructure, corrosion and mechanical characteristics of welded austenitic and duplex stainless steels: A review. *Metals*, 7(2), 39.

Morales, E. V., Cruz-Crespo, A., Pozo-Morejón, J. A., Oria, J. V., Araujo, L. S. & Bott, I. S. (2024). Microstructural characteristics of different heat-affected zones in welded joints of UNS S32304 duplex stainless steel using the GMAW process: analysis of the pitting corrosion resistance. *Corrosion Reviews*, 42(1), 93-105.

Mouginot, R. & Hänninen, H. (2013). *Microstructures of nickel-base alloy dissimilar metal welds*. (Ph.D. thesis, Aalto University).

Murphy, A. B. (1995). Transport coefficients of air, argon-air, nitrogen-air, and oxygen-air plasmas. *Plasma chemistry and plasma processing*, 15, 279-307.

Murphy, A. B. & Tam, E. (2014). Thermodynamic properties and transport coefficients of arc lamp plasmas: argon, krypton and xenon. *Journal of Physics D: Applied Physics*, 47(29), 295202.

Nasiri, A. M. & Clark, J. P. (2012). An investigation of pitting corrosion resistance in welded austenitic stainless steel pipe. *Corrosion Science*, 63, 323-333. doi: https://doi.org/10.1016/j.corsci.2012.06.010.

Nateghi, E. & Volukola, A. G. (2016). Experimental and numerical investigation into effect of weld configuration geometry on distribution of residual stress and temperature in the welded parts of stainless steel. *The International Journal of Advanced Manufacturing Technology*, 87, 2391-2404.

Nezakat, M., Akhiani, H., Penttilä, S. & Szpunar, J. (2016). Oxidation behavior of austenitic stainless steel 316L and 310S in air and supercritical water. *Journal of Nuclear Engineering and Radiation Science*, 2(2), 021008.

Nishimoto, K., Saida, K., Kiuchi, K. & Nakayama, J. (2011). Influence of minor and impurity elements on hot cracking susceptibility of extra high-purity type 310 stainless steels. *Hot cracking phenomena in welds III*, 183-208.

Nishimoto, M., Muto, I., Sugawara, Y. & Hara, N. (2021). Cerium addition to CaS inclusions in stainless steel: Insolubilizing water-soluble inclusions and improving pitting corrosion resistance. *Corrosion Science*, 180, 109222.

Nowak, W. J. (2020). Effect of surface roughness on oxidation resistance of stainless steel AISI 316Ti during exposure at high temperature. *Journal of Materials Engineering and Performance*, 29(12), 8060-8069.

Obeid, O., Alfano, G., Bahai, H. & Jouhara, H. (2018). Numerical simulation of thermal and residual stress fields induced by lined pipe welding. *Thermal Science and Engineering Progress*, 5, 1-14.

Olsson, C.-O. & Landolt, D. (2003). Passive films on stainless steels—chemistry, structure and growth. *Electrochimica acta*, 48(9), 1093-1104.

Orazem, M. E. & Tribollet, B. (2008). Electrochemical impedance spectroscopy. *New Jersey*, 1(906), 383-389.

Ostovan, F., Shafiei, E., Toozandehjani, M., Mohamed, I. F. & Soltani, M. (2021). On the role of molybdenum on the microstructural, mechanical and corrosion properties of the GTAW AISI 316 stainless steel welds. *Journal of Materials Research and Technology*, 13, 2115-2125.

Osório, W. R., Rosa, D. M. & Garcia, A. (2012). Electrochemical behaviour of a Pb–Sb alloy in 0.5 M NaCl and 0.5 M H2SO4 solutions. *Materials & Design*, 34, 660-665.

Ozawa, T. (1965). A new method of analyzing thermogravimetric data. *Bulletin of the Chemical Society of Japan*, 38(11), 1881–1886.

Pandey, P., Singh, M., Rathi, R. & Verma, J. (2024). Analysis and optimization of welding techniques for austenitic stainless steel using grey relational analysis. *International Journal on Interactive Design and Manufacturing (IJIDeM)*, 18(8), 5951-5959. doi: https://doi.org/10.1007/s12008-023-01456-0.

Panmongkol, P. & Phung-on, I. (2021). Effect of backing gas mixtures on corrosion properties of stainless steel grade 304 weld metal by autogenous GTAW. *Journal of Materials Research and Technology*, 11, 1559–1570.

Park, J.-H., Park, T.-W. & Kim, C.-S. (2007). Oxidation of 316L stainless steel at high temperatures in dry and wet air. *Materials Science and Engineering: A*, 449–451, 525–528. doi: 10.1016/j.msea.2006.02.276.

Parsian, A., Akbari, M., Karimipour, A., Rafiei, M. & Razzaghi, M. M. (2025). Experimental Investigation of Temperature Field, Fusion Zone Microstructure and Mechanical Properties During Dissimilar Laser Welding of Nickel-Base Alloy and Duplex Stainless Steel. *JOM*, 77(1), 193-210.

Pate, D., Singh, H. & Sidhu, B. S. (2020). Hot corrosion behavior of Fe–Cr–Al–Y and Co–Cr–Al–Y coatings in the presence of Na2SO4–60*Journal of Thermal Spray Technology*, 29, 2387–2400. doi: https://doi.org/10.1007/s11666-020-01130-6.

Paulraj, P. & Garg, R. (2016). Effect of welding parameters on pitting behavior of GTAW of DSS and super DSS weldments. *Engineering Science and Technology, an International Journal*, 19(2), 1076–1083.

Pedrotti, L. S. (2008). Basic physical optics. *Fundamentals of photonics*, 1, 152-154.

Perez, N. (2016). Corrosivity and passivity. In *Electrochemistry and Corrosion Science* (pp. 199–264). Springer.

Perron, A., Toffolon-Masclet, C., Ledoux, X., Buy, F., Guilbert, T., Urvoy, S., Bosonnet, S., Marini, B., Cortial, F. & Texier, G. (2014). Understanding sigma-phase precipitation in a stabilized austenitic stainless steel (316Nb) through complementary CALPHAD-based and experimental investigations. *Acta Materialia*, 79, 16-29.

Pinto, F. C., Aota, L. S., Souza Filho, I. R., Raabe, D. & Sandim, H. R. Z. (2022). Recrystallization in non-conventional microstructures of 316L stainless steel produced via laser powder-bed fusion: effect of particle coarsening kinetics. *Journal of Materials Science*, 57, 9576–9598. doi: 10.1007/s10853-021-06859-1.

Popescu, C., Vasile, C., Lisa, G. & Craciun, G. (2016). Thermogravimetric analysis of polymeric materials. *Environmental Engineering and Management Journal*, 15(3), 665–673.

Potgieter, J., Olubambi, P., Cornish, L., Machio, C. & Sherif, E.-S. M. (2008). Influence of nickel additions on the corrosion behaviour of low nitrogen 22% Cr series duplex stainless steels. *Corrosion Science*, 50(9), 2572-2579.

Prado, L. H., Anastasiou, E. & Virtanen, S. (2021). Corrosion behavior of anodic self-ordered porous oxide layers on stainless steel. *Journal of The Electrochemical Society*, 168(2), 021507.

Pratt, A., Lari, L., Hovorka, O., Shah, A., Woffinden, C., Tear, S. P., Binns, C. & Kröger, R. (2014). Enhanced oxidation of nanoparticles through strain-mediated ionic transport. *Nature materials*, 13(1), 26-30.

Praveen, R., Rajendran, N. & Rajagopal, G. (2020). Study on the pitting corrosion behavior of 316L stainless steel weldments in artificial seawater. *Materials Today: Proceedings*, 27, 1717-1721. doi: https://doi.org/10.1016/j.matpr.2020.02.245.

Present, R. (1968). Chapman–Enskog method in chemical kinetics. *The Journal of Chemical Physics*, 48(11), 4875-4877.

Rajabi, A., Mashreghi, A. & Hasani, S. (2020). Non-isothermal kinetic analysis of high temperature oxidation of Ti–6Al–4V alloy. *Journal of Alloys and Compounds*, 815, 151948. doi: 10.1016/j.jallcom.2019.151948.

Ravisankar, A., Velaga, S. K., Rajput, G. & Venugopal, S. (2014). Influence of welding speed and power on residual stress during gas tungsten arc welding (GTAW) of thin sections with constant heat input: A study using numerical simulation and experimental validation. *Journal of Manufacturing Processes*, 16(2), 200–211. doi: 10.1016/j.jmapro.2013.12.006.

Revie, R. W. (2011). *Uhlig's corrosion handbook*. John Wiley & Sons.

Revis, J. R., Tiedeman, D. R., Koury, D. M., Madsen, C., Christ, J. M. & McIlroy, D. N. (2021). Colorimetry analysis of weld oxidation on stainless steel 316L with argon and nitrogen shield gases. *Journal of Manufacturing and Materials Processing*, 5(4), 109. doi: https://doi.org/10.3390/jmmp5040109.

Rizk, T., Di Schino, A., Kaptay, G. & Soliman, M. (2023). Recent trends in the modeling of stainless steel corrosion and passivation using computational methods: A review. *Metals*, 13(2), 309. doi: https://doi.org/10.3390/met13020309.

Roberge, P. R. (2000). Handbook of Corrosion Engineering [Generic]. McGraw-Hill.

Ropo, M., Punkkinen, M., Kuopanportti, P., Yasir, M., Granroth, S., Kuronen, A. & Kokko, K. (2021). Oxygen adsorption on (100) surfaces in Fe–Cr alloys. *Scientific Reports*, 11(1), 6046.

Saadatkhah, N., Carillo Garcia, A., Ackermann, S., Leclerc, P., Latifi, M., Samih, S., Patience, G. S. & Chaouki, J. (2020). Experimental methods in chemical engineering: Thermogravimetric analysis—TGA. *The Canadian Journal of Chemical Engineering*, 98(1), 34–43. doi: 10.1002/cjce.23632.

Sabioni, A. S., Ramos, R. B., Ji, V., Jomard, F., Macedo, W. d. A., Gastelois, P. L. & Trindade, V. (2012). About the role of chromium and oxygen ion diffusion on the growth mechanism of oxidation films of the 304 austenitic stainless steel. *Oxidation of Metals*, 78(3–4), 211–220. doi: 10.1007/s11085-012-9301-y.

Sadeghian, M., Shamanian, M. & Shafyei, A. (2014). Effect of heat input on microstructure and mechanical properties of dissimilar joints between super duplex stainless steel and high strength low alloy steel. *Materials & Design*, 60, 678-684.

Saeki, I., Konno, H. & Furuichi, R. (1996). The initial oxidation of type 430 stainless steel in O_2–H_2O–N_2 atmospheres at 1273 K. *Corrosion Science*, 38(1), 19-31.

Sahoo, S. K., Kumar, M. & Karak, S. K. (2023). Fugacity, Activity, Equilibrium Constant and Ellingham Diagram. In *Fundamentals of Metallurgical Thermodynamics* (pp. 125-165). Springer.

Salah-Rousset, N. B., Chaouachi, M. & Chellouf, A. (1996). Role of surface finishing on pitting corrosion of a duplex stainless steel in seawater. *Journal of materials engineering and performance*, 5(2), 225–231.

Sander, T., Kelm, M., Kolb, M., Kirchgaßner, W., Golle, R. & Reiners, H. (2021). Simulation and experimental validation of the residual stress and distortion behavior of large-diameter longitudinally welded steel pipes. *Materials*, 14(15), 4184. doi: https://doi.org/10.3390/ma14154184.

Sanni, O. S. & Popoola, A. P. I. (2021). Corrosion inhibition effect of a non-toxic waste compound on stainless steel in 0.5 molar concentration of sulfuric acid. *Journal of Bio- and Tribo-Corrosion*, 7(3), 88. doi: 10.1007/s40735-021-00625-z.

Sato, I., Takaki, M., Arima, T., Furuya, H., Idemitsu, K., Inagaki, Y., Momoda, M. & Namekawa, T. (2002). Oxidation behavior of modified SUS316 (PNC316) stainless steel under low oxygen partial pressure. *Journal of Nuclear Materials*, 304(1), 21-28. doi: https://doi.org/10.1016/S0022-3115(02)00874-9.

Schwedersky, M. B., da Rosa, A. F., Okuyama, M. P. & e Silva, R. H. G. (2021). Limitations of the Schlieren technique for shielding gas flow visualization in arc welding processes. *Welding in the World*, 65(6), 1097-1105.

Sedriks, A. J. (1996). Corrosion of stainless steels. *John Wiley & Sons google schola*, 2, 3410-3413.

Sengupta, R., Mazumder, S., Maity, S., Lahiri, A. K. & Kumar, S. (2020). Corrosion behavior of GTAW and SMAW welded 316L stainless steel in nitric acid medium. *Materials Today: Proceedings*, 33, 4657-4661. doi: https://doi.org/10.1016/j.matpr.2020.04.291.

Sharifitabar, M., Shamanian, M., Kermanpur, A., Karimzadeh, F. & Sadeghi, M. (2011). Effect of welding speed on microstructure and mechanical properties of austenitic stainless steel clad plates manufactured by gas tungsten arc welding (GTAW). *Journal of Materials Engineering and Performance*, 20, 561–568. doi: https://doi.org/10.1007/s11665-010-9715-1.

Sharma, P., Diwan, P. & Pandey, O. (2019). Impact of environment on the kinetics involved in the solid-state synthesis of bismuth ferrite. *Materials Chemistry and Physics*, 233, 171–179. doi: 10.1016/j.matchemphys.2019.05.033.

Sheir, L., Jarman, R. & Burstein, G. (1994). Corrosion: metal/environment reactions. *Newnes-Butterworths Lond*, 8, 3-8.

Shen, S. (2011). *The Effects of Heat Input on Tensile and Fatigue Properties of Submerged Arc Welded ASTM A709 Grade 50 Steel*. (Master's thesis, University of Saskatchewan).

Shen, Y., Wang, Y., Liu, X., Zheng, Y. & Du, C. (2019). Corrosion behavior of 316L stainless steel welds in simulated pressurized water reactor primary water: The effect of microstructure and residual stress. *Corrosion Science*, 149, 95–108. doi: https://doi.org/10.1016/j.corsci.2019.01.015.

Shirali, A. & Mills, K. (1993). The effect of welding parameters on penetration in GTA welds. *WELDING JOURNAL-NEW YORK-*, 72, 347-s.

Shirwaikar, C. & GP, R. (1975). *Purging with nitrogen in the welding of austenitic stainless steels*. Inist-CNRS.

Siddiqi, M. A., Siddiqui, R. A. & Atakan, B. (2007). Thermal stability, sublimation pressures and diffusion coefficients of some metal acetylacetonates. *Surface and Coatings Technology*, 201(22–23), 9055–9059. doi: 10.1016/j.surfcoat.2007.03.035.

Simms, H. G. (2011). *Oxidation behaviour of austenitic stainless steels at high temperature in supercritical plant*. (Thesis, University of Birmingham).

Singh, R. (2021). *Applied welding engineering: processes, codes, and standards*. Butterworth-Heinemann.

Singh, V., Pramanik, A., Basak, A. K. & Chattopadhyay, K. (2020). Evaluation of pitting corrosion of 316L stainless steel weldment in chloride environment: Influence of shielding gases and welding processes. *Journal of Materials Research and Technology*, 9(6), 15052–15066. doi: https://doi.org/10.1016/j.jmrt.2020.10.012.

Siri, C., Popa, I., Vion, A., Langlade, C. & Chevalier, S. (2020). Impact of selective laser melting additive manufacturing on the high temperature behavior of AISI 316L austenitic stainless steel. *Oxidation of Metals*, 94, 527–548. doi: 10.1007/s11085-020-09981-3.

Smith, P. (2005). *Piping Materials Guide*. Elsevier.

Smola, G., Gawel, R., Kyziol, K., Miszczak, M. & Grzesik, Z. (2019). Influence of nickel on the oxidation resistance at high temperatures of thin chromium coatings. *Oxidation of Metals*, 91, 625-640.

Sonar, T., Ivanov, M., Trofimov, E., Tingaev, A. & Suleymanova, I. (2024). A comprehensive review on fusion welding of high entropy alloys–processing, microstructural evolution and mechanical properties of joints. *International Journal of Lightweight Materials and Manufacture*, 7(1), 122-183.

Sridhar, P., Biswas, P. & Mahanta, P. (2020). Effect of process parameters on bead geometry, tensile and microstructural properties of double-sided butt submerged arc welding of SS 304 austenitic stainless steel. *Journal of the Brazilian Society of Mechanical Sciences and Engineering*, 42, 1-15.

Sridhar, R., Kumar, P., Varma, V. K., Bhaduri, A. K. & Rodriguez, P. (2013). Influence of surface oxides on the corrosion behavior of type 316LN stainless steel weld metal in boiling nitric acid medium. *Journal of Nuclear Materials*, 433, 97–101. doi: https://doi.org/10.1016/j.jnucmat.2012.09.012.

Starink, M. J. (2003). The determination of activation energy from linear heating rate experiments: a comparison of the accuracy of isoconversion methods. *Thermochimica Acta*, 404(1–2), 163–176.

Steigerwald, R. (1968). Electrochemistry of corrosion. *Corrosion*, 24(1), 1-10.

Stewart, M. (2021). *Surface Production Operations: Volume 5: Pressure Vessels, Heat Exchangers, and Aboveground Storage Tanks: Design, Construction, Inspection, and Testing*. Gulf professional publishing.

Strehblow, H.-H. (2002). Mechanisms of pitting corrosion. In *Corrosion mechanisms in theory and practice* (pp. 252-295). CRC Press.

Sudhakaran, R., VeL Murugan, V., Senthil Kumar, K., Jayaram, R., Pushparaj, A., Praveen, C. & Venkat Prabhu, N. (2011). Effect of welding process parameters on weld bead geometry and optimization of process parameters to maximize depth to width ratio for stainless steel gas tungsten arc welded plates using genetic algorithm. *European Journal of Scientific Research*, 62(1), 76-94.

Sugumaran, V., Kamalakkannan, A. & Subramanian, B. (2023). Extricating the effect of sodium monovalent cation in the crystallization kinetics of bioactive glass and its influence on bioactivity. *Materials Chemistry and Physics*, 305, 127897. doi: 10.1016/j.matchemphys.2023.127897.

Sun, L., Guo, Y. & Feng, J. (2019). Finite element modeling and experiment of GTAW arc and weld pool for stainless steel with moving arc heat source. *International Journal of Heat and Mass Transfer*, 138, 984–996. doi: https://doi.org/10.1016/j.ijheatmasstransfer.2019.04.091.

Suresh, G., Parida, P. K., Bandi, S. & Ningshen, S. (2019). Effect of carbon content on the low temperature sensitization of 304L SS and its corrosion resistance in simulated ground water. *Materials Chemistry and Physics*, 226, 184-194.

Szklarska-Smialowska, Z. (1999). Pitting corrosion of aluminum. *Corrosion science*, 41(9), 1743–1767.

TABAN, E., KALUC, E. & AYKAN, T. (2014). Effect of the Purging Gas on Properties of 304H GTA Welds: Experiments measured the effects of various purging gases on the microstructural, corrosion, tensile, bend, and impact toughness properties of stainless steel weld metal. *Welding journal*, 93(4), 1-4.

Taheri, H., Soltanieh, M., Fattahi, M., Shamanian, M., Malekan, M. & Shahverdi, H. R. (2021). Microstructure and corrosion behavior of autogenous GTAW 316L welds with different arc energies in nitric acid and sodium chloride media. *Journal of Materials Engineering and Performance*, 30, 4605–4618. doi: https://doi.org/10.1007/s11665-021-05783-z.

Tandon, V., Thombre, M. A., Patil, A. P., Taiwade, R. V. & Vashishtha, H. (2020). Effect of heat input on the microstructural, mechanical, and corrosion properties of dissimilar weldment of conventional austenitic stainless steel and low-nickel stainless steel. *Metallography, Microstructure, and Analysis*, 9, 668-677.

Tang, Y., Dai, N., Wu, J., Jiang, Y. & Li, J. (2019a). Effect of surface roughness on pitting corrosion of 2205 duplex stainless steel investigated by electrochemical noise measurements. *Materials*, 12(5), 738.

Tang, Y., Dai, N., Wu, J., Jiang, Y. & Li, J. (2019b). Investigation of influence of surface roughness on pitting corrosion of duplex stainless steel 2205 using various electrochemical techniques. *International Journal of Electrochemical Science*, 14(7), 6790–6813.

Tarak, F. (2013). *Residual Stresses Due to Circumferential Girth Welding of Austenitic Stainless Steel Pipes*. Lehigh University.

Tavares, S. S. M., Abreu, H. F. G., Netto, J. M., Silva, M. B. & Farias, J. P. (2020). Influence of welding processes and filler metals on the pitting corrosion resistance of AISI 316L stainless steel welds. *Corrosion Science*, 170, 108677. doi: https://doi.org/10.1016/j.corsci.2020.108677.

Testing, A. S. f. & Materials. (2009). Standard Test Method for Conducting Cyclic Potentiodynamic Polarization Measurements for Localized Corrosion Susceptibility of Iron-, Nickel-, Or Cobalt-Based Alloys: Designation: G61-86 (Reapproved 2009). *ASTM*.

Ting, J., Li, W., Huang, J., Li, J., Yang, Y., Guo, L. & Liao, B. (2019). Effects of surface oxidation on corrosion behavior of 316L stainless steel weldment in simulated pressurized water reactor primary water. *Journal of Materials Research and Technology*, 8(6), 5472–5484. doi: https://doi.org/10.1016/j.jmrt.2019.09.035.

Tobler, R. & Reed, R. (1981). Tensile and fracture properties of manganese-modified AISI 304 type stainless steel. In *Advances in Cryogenic Engineering Materials* (pp. 83-92). Springer.

Trethewey, K. (1995). *Corrosion for Science and Engineering*. U.S. Department of Energy Office of Scientific and Technical Information.

Trigwell, S. & Selvaduray, G. (2005). Effects of welding on the passive oxide film of electropolished 316L stainless steel. *Journal of Materials Processing Technology*, 166(1), 30–43.

Trillo, E., Beltran, R., Maldonado, J., Romero, R., Murr, L., Fisher, W. & Advani, A. (1995). Combined effects of deformation (strain and strain state), grain size, and carbon content on carbide precipitation and corrosion sensitization in 304 stainless steel. *Materials Characterization*, 35(2), 99-112.

Tsay, L. W., Wang, J. Y., Chiang, M. F. & Chen, C. (2002). Microstructure and pitting corrosion of gas tungsten arc welds of AISI 316L stainless steel. *Corrosion Science*, 44, 1029–1046. doi: https://doi.org/10.1016/S0010-938X(01)00119-5.

Tsuei, H.-E. (2000). *Analysis and modelling of weld metal mechanical properties in flux cored arc welded steels*. (Ph.D. thesis, University of Wollongong).

Tsurkan, V., Von Nidda, H.-A. K., Deisenhofer, J., Lunkenheimer, P. & Loidl, A. (2021). On the complexity of spinels: Magnetic, electronic, and polar ground states. *Physics Reports*, 926, 1-86.

Uhlig, H. H. & Revie, R. W. (1985). *Corrosion and corrosion control*. John Wiley and Sons, Inc., New York, NY.

Uhlig, H. (1978). HISTORY OF PASSIVITY, EXPERIMENTS, AND THEORIES. *H. H. Uhlig, MIT, Cambridge, Passivity of Metals, Frankenthal and Kruger(eds.), The Electrochemical Soc., Princeton, NJ*, 1-28.

Unnikrishnan, R., Idury, K. S., Ismail, T., Bhadauria, A., Shekhawat, S., Khatirkar, R. K. & Sapate, S. G. (2014). Effect of heat input on the microstructure, residual stresses and corrosion resistance of 304L austenitic stainless steel weldments. *Materials characterization*, 93, 10-23.

Us, H. (2016). *Oxidation behavior of very high temperature reactor (VHTR) candidate materials: 316L stainless steel, Alloy 617, and Incoloy-800H*. (Thesis).

Valiente Bermejo, M. A., Karlsson, L., Svensson, L.-E., Hurtig, K., Rasmuson, H., Frodigh, M. & Bengtsson, P. (2015). Effect of shielding gas on welding performance and properties of duplex and superduplex stainless steel welds. *Welding in the World*, 59, 239-249.

van der Geest, J. W., Visser, R., de Keijzer, T. H. & van Eekelen, P. M. C. (2013). Oxidation of stainless steel in humid environments: A thermogravimetric analysis. *Thermochimica Acta*, 559, 1–7. doi: 10.1016/j.tca.2013.02.019.

Venkatkumar, D. & Ravindran, D. (2019). Effect of boundary conditions on residual stresses and distortion in 316 stainless steel butt welded plate. *High Temperature Materials and Processes*, 38(2019), 827-836.

Vyazovkin, S. (2002). A unified approach to kinetic processing of nonisothermal data. *International Reviews in Physical Chemistry*, 22(2), 231–260.

Vyazovkin, S. (2024). Misinterpretation of Thermodynamic Parameters Evaluated from Activation Energy and Preexponential Factor Determined in Thermal Analysis Experiments. *Thermo*, 4(3), 373–381. doi: 10.3390/thermo4030026.

Vyazovkin, S. & Wight, C. A. (2000). Model-free and model-fitting approaches to kinetic analysis of isothermal and nonisothermal data. *Thermochimica Acta*, 340–341, 53–68.

Vyazovkin, S., Burnham, A. K., Criado, J. M., Pérez-Maqueda, L. A., Popescu, C. & Sbirrazzuoli, N. (2011). ICTAC Kinetics Committee recommendations for performing kinetic computations on thermal analysis data. *Thermochimica acta*, 520(1-2), 1-19.

Vázquez, M. V., Blanco, M. D., Figueroa, R. P., Varela, E. B., Riveros, O. J., Cerda, M. C. & Bravo, I. M.-V. (2024). Kinetic study of Cu_2S–FeS mixtures in an oxidative environment by thermogravimetric and thermodynamic analysis. *Materials Chemistry and Physics*, 311, 128548. doi: 10.1016/j.matchemphys.2023.128548.

Wallace, W., Hoeppner, D. & Kandachar, P. (1985). Aircraft corrosion: causes and case histories. *AGARD*.

Wang, C., Feng, J., Zhang, Z., Zhang, Y. & Sun, L. (2021). Improved model for simulating GTAW arc plasma and weld pool in 316L stainless steel welding with Ar-He mixed shielding gas. *International Journal of Heat and Mass Transfer*, 172, 121155. doi: https://doi.org/10.1016/j.ijheatmasstransfer.2021.121155.

Wang, C., Liu, Y., Wu, H., Liu, Y., Zhang, P. & Li, Z. (2024a). Texture-Type Analysis of Fe2O3 and Fe3O4 Oxide Layers on the Surface of High-Strength Steel. *Journal of Materials Engineering and Performance*, 33(2), 978-986.

Wang, J., Xue, H., Zhao, Y., Zhang, T. & Wang, F. (2024b). Effect of surface roughness on the corrosion of HP-13Cr stainless steel in the dynamic aggressive oilfield environment. *Metals*, 14(3), 280.

Wang, J., Xue, H., Zhao, Y., Zhang, T. & Wang, F. (2024c). Effect of Surface Roughness on the Corrosion of HP-13Cr Stainless Steel in the Dynamic Aggressive Oilfield Environment. *Metals*, 14(3), 280.

Wang, Q., Chen, S. & Rong, L. (2020). δ-ferrite formation and its effect on the mechanical properties of heavy-section AISI 316 stainless steel casting. *Metallurgical and Materials Transactions A*, 51, 2998-3008.

Wang, S., Sun, M., Xu, Y., Long, K. & Zhang, Z. (2018). Enhanced localized and uniform corrosion resistances of bulk nanocrystalline 304 stainless steel in high-concentration hydrochloric acid. *Journal of Materials Science and Technology*, 34(12), 2498–2506. doi: 10.1016/j.jmst.2018.08.015.

Wang, Z., Xu, Z., Zhang, Y., Zhang, X., Shao, L. & Wang, J. (2017). Thermal decomposition behavior and kinetics of ammonium perchlorate under nonisothermal conditions. *Journal of Hazardous Materials*, 325, 147–154.

Wei, L., Wang, Y., Misra, R. & Chen, J. (2024). Understanding the high-temperature oxidation resistance of heat-resistant austenitic stainless steel with gradient nanostructure. *Corrosion Science*, 231, 111966. doi: 10.1016/j.corsci.2024.111966.

Wessman, S., Hertzman, S., Pettersson, R., Lagneborg, R. & Liljas, M. (2008). On the effect of nickel substitution in duplex stainless steel. *Materials Science and Technology*, 24(3), 348-355.

West, J. M. (1986). *Basic corrosion and oxidation*. U.S. Department of Energy Office of Scientific and Technical Information.

White, J. L., Scherrer, R. A. & Vassallo, A. M. (2001). Thermal decomposition mechanisms of ammonium nitrate and ammonium perchlorate: a comparative study using infrared spectroscopy and mass spectrometry. *Thermochimica Acta*, 367–368, 129–139.

Wu, X., Ma, X., Lu, Q., Liu, X. & Liu, M. (2021). Kinetic study on pyrolysis of lignocellulosic biomass and its model components based on thermogravimetric analysis. *Bioresource Technology*, 321, 124512.

Xiao, J., Liu, J., Tang, B., Ma, Y., Zheng, H. & Wang, X. (2021). Corrosion behavior of 316L stainless steel weldments fabricated by GTAW and laser welding in simulated PWR primary water. *Corrosion Science*, 190, 109678. doi: https://doi.org/10.1016/j.corsci.2021.109678.

Xiao, P., Orme, C. A., Qiu, S. R., Pham, T. A., Cho, S., Bagge-Hansen, M. & Wood, B. C. (2025). Atomic-scale understanding of oxide growth and dissolution kinetics of Ni-Cr alloys. *Nature Communications*, 16(1), 341.

Xiao, Y., Wang, C., Zhang, Y., Liu, X., Qin, C., Wang, Z., Lin, X., Wang, J., Wang, L. & He, F. (2024). Recovery-assisted abnormal grain evolution of selective laser-melted 316L stainless steel at intermediate temperatures. *Metallurgical and Materials Transactions A*, 55(11), 4613–4622. doi: 10.1007/s11661-024-05800-2.

Xie, B., Sun, M., Xu, B., Wang, C., Jiang, H., Li, D. & Li, Y. (2019). Oxidation of stainless steel in vacuum and evolution of surface oxide scales during hot-compression bonding. *Corrosion Science*, 147, 41–52.

Xiuming, Y., Yanliang, H., Yadav, A. P., Wenjuan, Q. & De Marco, R. (2015). Study on the temperature dependence of pitting behaviour of AISI 4135 steel in marine splash zone. *Electrochemistry*, 83(7), 541-548.

Xu, H., Guo, X., Lei, Y., Lin, J., Fu, H., Xiao, R., Huang, T. & Shin, Y. C. (2019). Welding deformation of ultra-thin 316 stainless steel plate using pulsed laser welding process. *Optics & Laser Technology*, 119, 105583.

Xu, W., Li, S., Whitely, N. & Pan, W.-P. (2005). Fundamentals of TGA and SDT. *Thermal Analysis: Fundamentals and Applications to Material Characterization*, pp. 1–7.

Yalamaç, E. (2010). *Sintering, co-sintering and microstructure control of oxide based materials: Zirconia, alumina, spinel, alumina-zirconia and spinel-alumina*. (Thesis, Izmir Institute of Technology (Turkey)).

Yamamoto, K., Takayama, T., Minamino, Y., Koizumi, Y., Tokunaga, T. & Hagihara, K. (2023). Modification of grain boundary microstructure by controlling dissolution behavior of θ particles in Cr-containing hypereutectoid steel. *Materials Characterization*, 205, 113241. doi: 10.1016/j.matchar.2023.113241.

Yamauchi, A., Kurokawa, K. & Takahashi, H. (2003). Evaporation of Cr 2 O 3 in atmospheres containing H 2 O. *Oxidation of metals*, 59, 517-527.

Yan, L., Zhao, Z., Zhao, Y., Wei, Z., Zhang, M. & Zhao, G. (2022). Study on pyrolysis behavior and kinetics of rubber wood sawdust using thermogravimetric analysis. *Energy Reports*, 8, 1110–1118.

Yang, J., Wang, L., Song, Z., Yang, H., Chen, H. & Chen, H. (2020). Kinetic study on co-pyrolysis of oily sludge and sawdust using thermogravimetric analysis and artificial neural network models. *Renewable Energy*, 162, 1776–1787.

Yang, X., Chen, H., Zhu, Z., Cai, C. & Zhang, C. (2019). Effect of shielding gas flow on welding process of laser-arc hybrid welding and MIG welding. *Journal of Manufacturing Processes*, 38, 530-542.

Yang, Y., Ding, L., Xu, L. & Tsai, Y.-T. (2021). Effect of metal chloride on thermal decomposition of nitrocellulose. *Case Studies in Thermal Engineering*, 28, 101667. doi: 10.1016/j.csite.2021.101667.

Yang, Y., Wang, Z., Tan, H., Hong, J., Jiang, Y., Jiang, L. & Li, J. (2012). Effect of a brief post-weld heat treatment on the microstructure evolution and pitting corrosion of laser beam welded UNS S31803 duplex stainless steel. *Corrosion Science*, 65, 472–480.

Yin, X., Wang, Z., Zhao, Y., Shao, Y., Wei, X. & Yu, G. (2020). Pyrolysis behavior and kinetic analysis of co-pyrolysis of cotton stalk and waste tires using TGA. *Renewable Energy*, 162, 1402–1413.

Young, D. J. (2008). *High temperature oxidation and corrosion of metals*. Elsevier.

Yuen, W. & Chen, R. (2010). Short-time Oxidation Behavior of Low-carbon, Low-silicon Steel in Air at 850–1,180° C—III: Mixed Linear-and-Parabolic to Parabolic Transition Determined Using Local Mass-Transport Theories. *Oxidation of metals*, 74(5), 255-274.

Zakeri, M., Naghizadeh, M., Nakhaie, D. & Moayed, M. H. (2016). Pit transition potential and repassivation potential of stainless steel in thiosulfate solution. *Journal of The Electrochemical Society*, 163(6), C275.

Zangeneh, S., Lashgari, H. & Sharifi, H. (2020). Fitness-for-service assessment and failure analysis of AISI 304 demineralized-water (DM) pipeline weld crack. *Engineering Failure Analysis*, 107, 104210.

Zeng, K., Liu, Y., Yang, X., Li, H., Wu, T. & Zhang, Y. (2021). Pyrolysis behavior and kinetics of corncob and pine sawdust under different heating rates using TGA and artificial neural networks. *Fuel*, 292, 120293.

Zhang, L., Yang, G., Zhang, W., Xu, Y., Du, C. & Li, X. (2019). Corrosion behavior of autogenous GTAW joints of 316L stainless steel in high-temperature water. *Corrosion Science*, 150, 17–27. doi: https://doi.org/10.1016/j.corsci.2019.02.026.

Zhang, R., Sur, D., Li, K., Witt, J., Black, R., Whittingham, A., Scully, J. R. & Hattrick-Simpers, J. (2024). Bayesian assessment of commonly used equivalent circuit models for corrosion analysis in electrochemical impedance spectroscopy. *npj Materials Degradation*, 8(1), 120.

Zhang, W., Liu, J., Xue, Q., Wang, J. & Zhou, M. (2020). Co-pyrolysis characteristics and kinetics of oily sludge and corn stalk using TGA and kinetic model fitting. *Energy Sources, Part A: Recovery, Utilization, and Environmental Effects*, 42(4), 491–500.

Zhao, G., Tian, Y., Li, H., Ma, L., Li, Y. & Li, J. (2024). Microstructure evolution and dynamic recrystallization mechanisms of 316L stainless steel during hot deformation. *Archives of Civil and Mechanical Engineering*, 24(1), 35. doi: 10.1007/s43452-024-00180-5.

Zhao, M., Wu, H., Lu, J., Sun, G. & Du, L. (2022). Effect of grain size on mechanical property and corrosion behavior of a metastable austenitic stainless steel. *Materials Characterization*, 194, 112360.

Zhao, Y., Chen, P., Wen, W., Deng, Y., Peng, K. & Liu, Y. (2023). Effect of Mn content on the high-temperature oxidation behaviors of Mn-substituted-for-Ni alumina-forming austenitic stainless steel. *Corrosion Science*, 223, 111294. doi: 10.1016/j.corsci.2023.111294.

Zhou, C., Wu, S., Cheng, J., Wang, W. & Liu, G. (2017). Thermogravimetric analysis and kinetic study on pyrolysis of waste tires using Coats–Redfern method. *Journal of Thermal Analysis and Calorimetry*, 128, 1125–1135.

Zhou, G., Unocic, K. A., Wang, C., Shan, Z., Haigh, S. J. & Yang, J. C. (2023). Revealing atomic-to-nanoscale oxidation mechanisms of metallic materials. *MRS Bulletin*, 48(8), 852-863.

Zhou, Y., Zhang, S., Zhang, L., Du, C. & Li, X. (2020). Effects of welding heat input on corrosion behavior of 316L stainless steel in high temperature water. *Corrosion Science*, 170, 108693. doi: https://doi.org/10.1016/j.corsci.2020.108693.

Zhou, Y., Zhang, S., Zhang, L., Du, C. & Li, X. (2022). Influence of laser power on corrosion behavior of 316L stainless steel welds in simulated pressurized water reactor primary water. *Corrosion Science*, 195, 109960. doi: https://doi.org/10.1016/j.corsci.2021.109960.

Zhou, Z., Chen, Y., Chen, X., Jin, B. & Li, G. (2018). Co-pyrolysis characteristics and kinetics of waste cartons and waste plastics by thermogravimetric analysis. *Energy Conversion and Management*, 165, 92–100.

Zhu, X., Fan, Y., Yang, T. & Shi, X. (2018). Kinetic analysis of pyrolysis characteristics of lignocellulosic biomass using iso-conversional and model-fitting methods. *Energy Conversion and Management*, 180, 360–367.

Zou, D., Wang, Z., Ma, L. & Cheng, Y. (2016). Effect of heat input on pitting corrosion resistance of GTAW welded AISI 316L stainless steel joints. *Corrosion Science*, 111, 835–845. doi: https://doi.org/10.1016/j.corsci.2016.06.008.

Zou, H., Chen, S., Li, Y., Zhou, J., Li, Y., Shi, X. & Wang, J. (2021). Co-pyrolysis characteristics and kinetics of waste polyethylene and wheat straw blends using thermogravimetric analysis. *Renewable Energy*, 177, 346–356.